The Government of
The Republic of the Union of Myanmar
Ministry of Education

Department of Higher Education

Universities Research Journal

Vol. 13, No. 1 September, 2022

The Government of
The Republic of the Union of Myanmar
Ministry of Education

Department of Higher Education

Universities Research Journal

Vol. 13, No. 1 September, 2022

Universities Research Journal 2020
Vol.13, No. 1

Chemistry, Physics, Industrial Chemistry, Computer Science, Marine Science

Editorial Board

Editors

Contents

Chemistry

Page

Physics

Preparation, Characterization and Determination of Antimicrobial Activity of Cupric Oxide (CuO) Nanoparticles Using Oxalic Acid

Toe[1] & Yi Yi Myint[2]

Abstract

The present research deals with a study on the synthesis and characterization of cupric oxide nanoparticles. The nanoparticles were synthesized by sol-gel method using oxalic acid. Magnesium nitrate and copper nitrate were used to obtain homogeneous solution. The gel powder was dried in an oven at temperature of 105 ℃ to obtain weight. The resulting sample was thermally heated in muffle furnace at temperature of 500 ˚C for four hours to get required nanoparticles. The prepared nanoparticles were characterized by Energy Dispersive X-ray Fluorescence (EDXRF) and X-ray powder diffraction (XRD). Then determination of antimicrobial activity of the nanoparticle was carried out by Agar Well Diffusion Method. According to the XRD analyzed data, the the average crystallite sizes of CuO nanoparticle was 22.08 nm.

Keywords : Cupric oxide nanoparticle, sol-gel method, XRD and EDXRF

Introduction

Metal oxide nanoparticles, such as copper oxide (CuO), have attracted attention mostly because of their antimicrobial and biocide properties and they may be used in many biomedical applications (Nation, S. 2015). Copper oxide is a semiconductor metal with unique optical, electrical and magnetic properties and it has been used for various applications, such as the development of super capacitors, near-infrared filters, in magnetic storage media, sensors, catalysis, semiconductors, etc. (Zhang, Q. 2014). One of the most important parameters in the synthesis of these nanoparticles is the control of particle size, morphology and crystallinity and in order to achieve this goal, different synthesis methods were developed; some of the most investigated approaches include the sonochemical method, the sol-gel method, laser ablation, the electrochemical method, chemical precipitation and surfactant-based

[1] Lecturer, Department of Chemistry, University of Magway
[2] Professor, Department of Chemistry, University of Mandalay

techniques (Khashan, K. 2016). Other methods for the synthesis of CuO NPs have been developed; such as hydrothermal approach

(Abromov, O. 2009), thermal oxidation method (Zhang, Q. 2014), alcohol-thermal synthesis (Premkumar, T. 2006), liquid ammonia (Sun, L. 2005) and microwave-assisted synthesis (Karunakaran, C. 2013).

The sol-gel technique is a simple and relatively fast method and therefore it is widely used in the design of nanoparticles (Jayaprakash, J. 2014). This method is applied often as it ensures the rigorous control of the nanoparticle size. The method was optimized in order to obtain nanoparticles with dimensions ranging between 10 and 40 nm. Karthik et al. synthesized CuO NPs with dimensions of 25 nm by a sol-gel method (Karthik, K. 2011). The physical properties of CuO NPs also depend on the applied sol-gel method and the calcination time (Suleima, M. 2013). Moreover, in the case of sol-gel method, the size of nanoparticles is proportionally related with the temperature, physical conditions are very important for the design of functional nanoparticles using this approach (Nithya, K. 2014). CuO nanoparticles are mainly utilized as antimicrobial agents. They are used in hospitals due to their antimicrobial ability to kill more than 99.9% of Gram-positive and negative bacteria within 2 h of exposure, if a suitable dose is applied. Studies reported that the utilization of CuO reduces the occurrence of hospital-acquired infections and the costs associated with health care in health care facilities. Bed sheets containing CuO NPs are considered one of the most interesting innovations in medical care, since they reduce microbial attachment and thus microbial infections within hospitals (Lazary, A. 20014). Previous work had demonstrated that CuO NPs also have beneficial effects on the skin. Studies conducted on women who utilized pillowcases and beddings containing CuO NPs revealed an improved aspect of the facial skin and an increase in the foot skin elasticity using socks impregnated with copper oxide nanoparticles (Dykes, P. 2014). Some advantages of using copper-oxide in hospital textiles are: (1) It is effective against both, susceptible and antibiotic resistant microorganisms involved in nosocomial infections; (2) It has wide antifungal spectrum and antibacterial properties (3); It inhibits biofilm or the development of microorganisms in attached communities on the surface of materials coated with CuONPs; (4) It does not cause skin irritation or sensitization; (5) It is safe for humans if used externally and in low amounts (Borkow, G. 2008). This research focuses on the characterization and

antimicrobial activity of prepared cupric oxide nanoparticles, using copper (II) nitrate as a precursor.

Materials and Methods

All chemicals were analytical grade. Magnesium nitrate $Mg(NO_3)_2.6H_2O$, copper nitrate $Cu(NO_3)_2$ and oxalic acid ($C_2H_2O_4$) were Merck product with a purity of 99.99%. Ethylene glycol was product from Applichem, Germany. All solutions were prepared using distilled water during preparation procedures. Various conventional and modern instrumental techniques were used throughout the experimental procedure. These include X-ray Diffraction (XRD) and Energy Dispersive X-ray Fluorescence (EDXRF).

Preparation of Cupric Oxide Nanoparticles

5.12 g of magnesium nitrate $Mg(NO_3)_2.6H_2O$ was dissolved in 50 mL of distilled water to obtain solution A. Solution B was prepared by dissolving 3.8 g of copper nitrate $Cu(NO_3)_2$ in 50 mL of distilled water. The solution A and B were mixed to obtain solution (I). 2.5 gm of oxalic acid was dissolved in 100 mL of distilled water to obtain solution (II). Solution (I) and (II) were mixed together with 10 mL of ethylene glycol to obtain a homogeneous mixture solution. The mixture solution was stirred and heated on a magnetic stirrer hot plate at 70-80 ˚C for 2 hours. The gel-powder was obtained. The gel-powder was dried in an oven at 105 ˚C until constant weight was obtained. The dried as prepared powder was calcined in a muffle furnace at 500 ˚C for 4 hours to obtain cupric oxide (CuO) nanoparticles.

Characterization of Prepared Cupric Oxide Nanoparticles

Crystal structure and phase analysis of prepared cupric oxide nanoparticles were performed by X-ray diffraction (XRD) using Rigaku,

D-Max 2200, Japan in Department of Chemistry, University of Yangon. The relative abundance of elements in the prepared ample were confirmed by using EDXRF 700 spectrometer in Department of Chemistry, Monywa University.

Determination of Crystallite Size and Interatomic Spacing

The crystallite size of prepared cupric oxide can be calculated by using Debye-Scherrer' formula,

$D = 0.9\lambda / \beta \cos\theta$ and interatomic spacing by Bragg's equation $d = \lambda/2\sin\theta$

Where, λ = the wave length of X-rays (1.54056Å for Cu/K-alpha 1)

θ = the diffraction angle

β = full width at half maximum in radian

D = average crystallite size

d = interatomic spacing

Determination of Antimicrobial Activity of Prepared Cupric Oxide Nanoparticles

Table 1. Test microorganisms for Determination of Antimicrobial Activity of Prepared Cupric Oxide Nanoparticle

No	Test Organism	
1	*Bacillus pumilus*	IFO 12102
2	*Baillus subtilus*	IFO 90571
3	*Candida albicans*	NITE 09542
4	*Eschericha coli*	AUH 5436
5	*Staphylococcus aureus*	AUH 8465
6	*Salmonella typhi*	AUH 7943

Chemicals and Reagents

Glucose, yeast extract, peptone, Agar, Distilled water.

Apparatus and Equipments

Autoclave, an incubator, hot plate, Petri-dishes, measuring cylinder, micropipette and clipper.

Screening of Antimicrobial Activity of Crude Extract by Using Agar Well Diffusion Method

Glucose 0.5 g, Yeast extract 0.3 g, Peptone 0.3 g, Agar 1.7 g, 100 mL of distilled water were added in a 250 mL sterile conical flask and heated on hot plate until boil medium. Then, the mouth of the flask was plugged with a piece of cotton wool. This medium was sterilized in an autoclave at 121℃ for 45 minutes. After 45 minutes, a 0.1 mL test organisms were inoculated in to 20 mL of medium agar at about 40℃ and were poured into the sterile petri- dishes at aseptic condition. After the agar became solid, cock borer was used to make the wells (8 mm in diameter). Then extract sample (20 μL) was introduced into the well and they were incubated at room temperature for 24-48 hours. After 24-48 hours of incubation, the clear zones were measured. Clear zone surrounding the wells indicated the presence of antimicrobial active compound in the extracts which inhibit the growth of the test organisms (Collin, 1965).

Results and Discussion

Characterization of Prepared Cupric Oxide Nanoparticle

The prepared CuO nanoparticle was characterized by X-ray Diffraction (XRD) and Energy Dispersive X-ray Fluorescence (EDXRF).

EDXRF Analysis of Prepared Cupric Oxide Nanoparticle

Figure 1 shows EDXRF spectrum of prepared CuO nanoparticle. Result of Prepared CuO Nanoparticles by EDXRF was shown in Table 2.

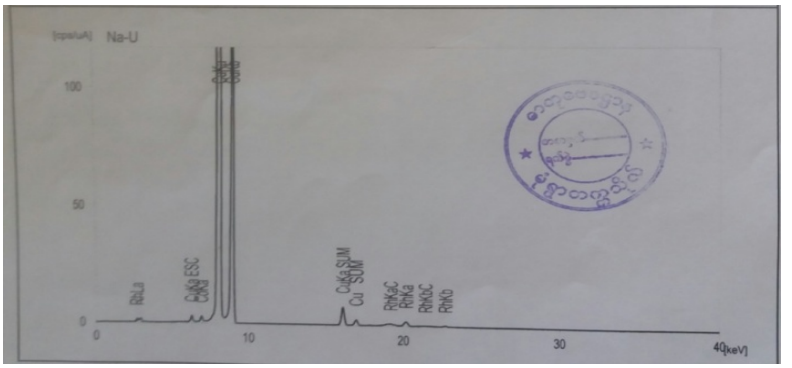

Figure 1. EDXRF spectrum of prepared CuO nanoparticle

Table 2. Results of Prepared CuO Nanoparticles by EDXRF

No	Analyte	Relative abundance (%)
1	Cu	99.908
2	Co	0.092

From the EDXRF data, the amount of copper and cobalt in prepared CuO nanoparticle were found to be 99.908 % and 0.092 % respectively.

XRD Analysis of Prepared Cupric Oxide Nanoparticle

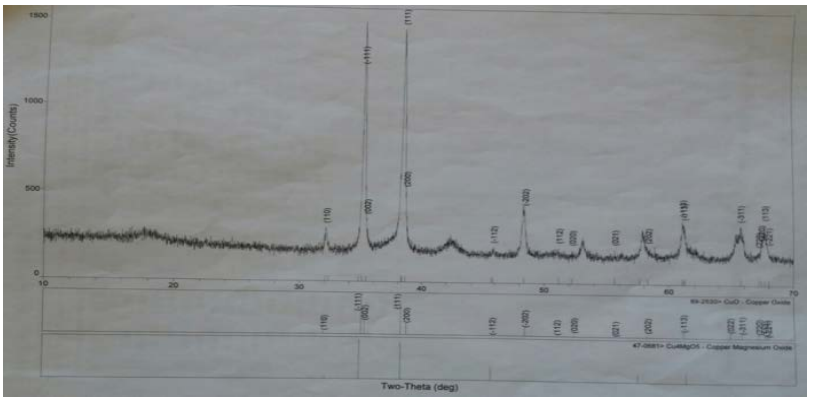

Figure 2. XRD Diffractogram of prepared CuO nanoparticle

Table 3. The Average Particles Size of Prepared CuO Nanoparticle

No	Bragg angle (2θ)	Miller indices (h k l)	(β) radiation	Interplanar spacing d (nm)	Particle size D (nm)
1	32.041	110	0.0057	0.279	25.21
2	35.358	002	0.007	0.254	20.69
3	38.330	111	0.0057	0.235	25.68
4	45.906	-112	0.0052	0.198	28.89
5	48.582	-202	0.0084	0.187	18.01
6	51.142	111	0.0048	0.179	32.24
7	52.204	020	0.0012	0.175	12.61
8	55.631	021	0.0041	0.165	38.51

Range of crystalline size = 12.61 – 38.51 nm

Average particle size = 23.37 nm

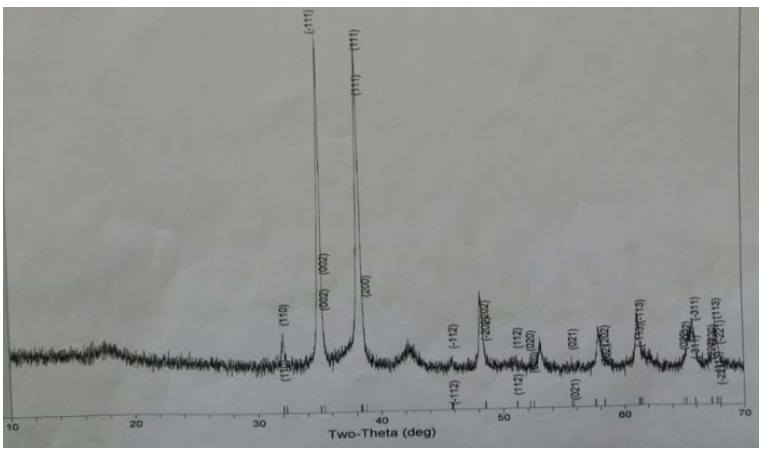

Figure 3. XRD Diffractogram of prepared CuO nanoparticle

Table 4. The phase ID Report of Prepared CuO Nanoparticles

No	Bragg angle (2θ)	Miller indices (h k l)	Area (%)	Inter planar spacing d (nm)	Phase ID
1	32.041	110	7.1	0.279	CuO
2	35.358	002	34.2	0.254	CuO
3	38.330	111	81.3	0.235	CuO
4	45.906	-112	0.1	0.198	CuO
5	51.142	111	2.2	0.179	CuO
6	52.204	020	7.9	0.175	CuO
7	55.631	021	0.6	0.165	CuO
8	58.300	202	9.4	0.158	CuO
9	61.279	-113	14.1	0.151	CuO
10	65.191	002	13.0	0.143	CuO
11	65.929	-311	10.5	0.142	CuO

Phase ID of prepared nanoparticle was CuO.

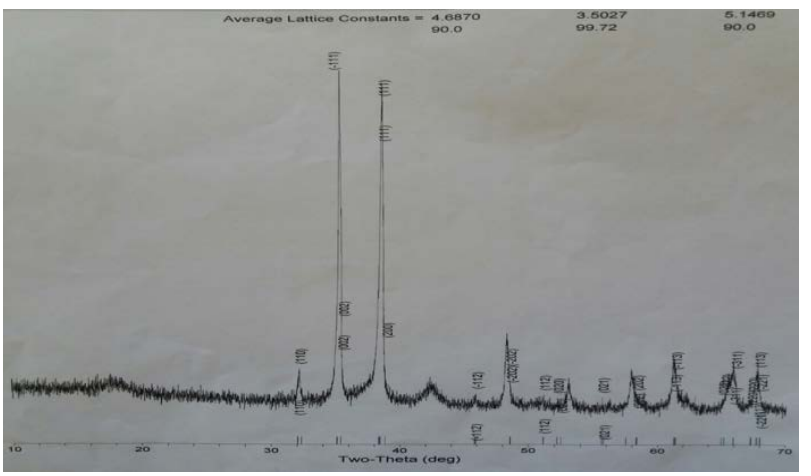

Figure 4. XRD Diffractogram of prepared CuO nanoparticles

Table 5. Lattice Constants from Peak Locations and Miller Indices for Prepared CuO Nanoparticles

No	Bragg angle (2θ)	Miller indices (h k l)	Inter planar spacing d (nm)	a-axis (nm)	b-axis (nm)	c-axis (nm)
1	32.041	110	0.279	0.4687	0.3502	0.5146
2	35.358	002	0.254	0.4867	0.3502	0.5146
3	38.33	111	0.235	0.4867	0.3502	0.5146
4	45.906	-112	0.198	0.4867	0.3502	0.5146
5	48.582	-202	0.187	0.4867	0.3502	0.5146
6	51.142	111	0.179	0.4867	0.3502	0.5146

Average lattice constants calculated from XRD pattern for prepared CuO nanoparticles were a = 0.4687 nm, b = 0.3502 nm, and c = 0.5146 nm The crystal structure is monoclinic.

Determination of Antimicrobial Activities of Prepared Cupric Oxide Nanoparticles

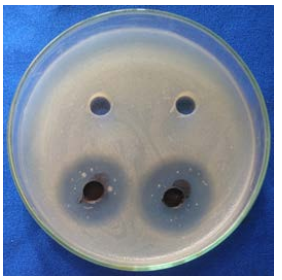

B.subtilis

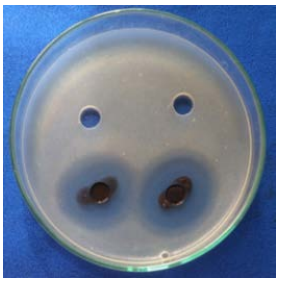

Candida albicans

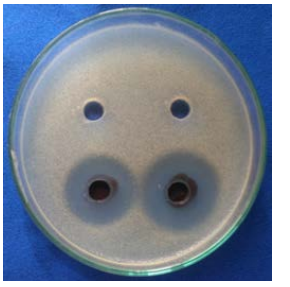

Eschericha coli

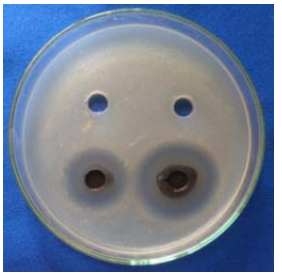

Pseudomonas aeruginosa

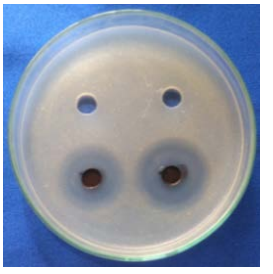

Staphylococcus aureus

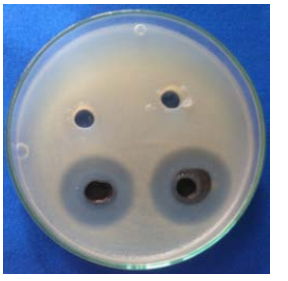

Salmonella typhi

Figure 5. Screening of antimicrobial activities of prepared cupric oxide nanoparticles

In the figure, upper pair of holes of each dish shows the activity of blank solution. Left hole of lower pair in each dish indicates activity of prepared CuO nanoparticles.

Table 6. Results of Screening of Antimicrobial Activity of Prepared CuO Nanoparticles

Sample	**Inhibition zone diameter (mm)**					
	1	2	3	4	5	6
CuO	23.00 (+++)	26.16 (+++)	26.15 (+++)	18.20 (++)	19.38 (++)	27.31 (+++)

Test Organisms

1. *Bacillus subtilis* IFO 90571	(-) No activity
2. *Candida albicans* NITE 09542	(+) low activity, 9-14 mm
3. *Escherichia coli* AUH 5436	(++) medium activity, 15-20mm
4. *Pseudomonas aeruginosa*	(+++) high activity, 21mm - above
5. *Staphylucoccus aureus* AUH 8465	
6. *Salmonella typhi* AUH 7943	

Conclusion

In this research, cupric oxide nanoparticle was synthesized from magnesium nitrate and copper nitrate by sol gel method using oxalic acid. The prepared cupric oxide nanoparticle was characterized by modern sophisticated methods such as EDXRF, XRD. From the EDXRF data the 99.908% of copper was found in CuO nanoparticles. From the XRD results, the average crystallite size of prepared nanoparticles was 22.08 nm. The crystal structure of CuO nanoparticle was monoclinic. The cupric oxide nanoparticle was detected in antimicrobial activity by Agar Well Diffusion Method (Collin, 1965). According to the screening of antimicrobial activities of crude extract by using Agar Well Diffusion Method, prepared CuO nanoparticles showed high activity in *Bacillus subtilis*, *Candida albicans*, *Escherchia coli*, *Staphylococcus aureus* and *Salmonella typhi* but medium activity in *Pseudomonas aeruginosa*

Acknowledgement

I am extremely grateful to Dr Khin Maung Oo, Rector, University of Magway and Professor and Head, Dr Thida Aung, Department of Chemistry, Magway University for their provision and suggestions of the research facilities.

References

Abramov, O., A. Gedanken, Y. Koltypin, N. Perkas, I. Perelshtein, E. Joyce, and T. Mason. (2009). “Pilot scale sonochemical coating of nanoparticles onto textiles to produce biocidal fabrics”. *Surf. Coat Technol*, 204, 718–722

Borkow, G., and J. Gabbay.(2008). “ Biocidal textiles can help fight nosocomial infections”. *Medical* . 70, 990–994

Colin, C. H. (1965).” Microbiallogical Methods”. Butterworth and Co, Publishers Ltd, Landon

Dykes, P.(2014). “Increase in skin surface elasticity in normal volunteer subjects following the use of copper oxide impregnated socks”. *Skin Res. Technol*. 21, 272–277

Jayaprakash, J., N. Srinivasan, and P. Chandrasekaran. (2014). “Surface modifications of CuO nanoparticles using Ethylene diamine tetra acetic acid as a capping agent by sol–gel routine” *Spectrochim. Acta A. Mol. Biomol. Spectrosc*.123, 363–368

Karthik, K.. , N. V. Jaya, M. Kanagaraj, S. Arumugam. (2011). “Temperature-dependent magnetic anomalies of CuO nanoparticles.” *Solid State Commun*. 151, 564–568

Khashan, K.S., G. M. Sulaiman, F. A. Abdulameer.(2016). Synthesis and Antibacterial Activity of CuO Nanoparticles Suspension Induced by Laser Ablation in Liquid”. *Arab. J. Sci. Eng*. 41, 301–310

Karunakaran, C., G. Manikandan, P. Gomathisankar. (2013). “Microwave, sonochemical and combustion synthesized CuO nanostructures and their electrical and bactericidal properties”. *J. Alloys Compd*. 580, 570–57

Lazary, A. I. Weinberg, J.J. Vatine, A. Jefidoff, R. Bardenstein, G. Borkow, N. Ohana.(2014) “Reduction of healthcare-associated infections in a long-term care brain injury ward by replacing regular linens with biocidal copper oxide impregnated linens”. *Int. J. Infect. Dis*. 24, 23–29

Nithya, K.; Yuvasree, P. N. Neelakandeswari, N. Rajasekaran. (2014). “Preparation and Characterization of Copper Oxide Nanoparticles”. *Int. J. ChemTech Res*. 6,2220–2222

Premkumar, T., and K. E. Geckeler.(2006). “A green approach to fabricate CuO nanoparticles*”. J. Phys. Chem. Solids*. 67, 1451–1456

Sun, L. Z. Zhang, Z. Wang, Z. Wu, and H. Dang, H.(2005). “Synthesis and characterization of CuO nanoparticles from liquid ammonia*”. Mater. Res. Bull*, 40, 1024–1027

Zhang, Q. K. Zhang, D. Xu, G. Yang, H. Huang, F. Nie, C. Liu, S. Yang. (2014).”CuO nanostructures: Synthesis, characterization, growth mechanisms, fundamental properties, and applications”. *Prog. Mater. Sci*. 60, 208–337

Study on the Impact of Neutron Irradiated Polyethylene Plastic

Khin Nwe Oo[1] & Sai Pon[2]

Abstract

In this research work, the polyethylene sample was irradiated with neutron for one week by using Am (Be) source. The disruption of polyethylene was studied by Solid State Nuclear Track Detectors (SSNTDs. The damage of neutron irradiated polyethylene was studied by chemical etching methods. The track can be revealed by the optical microscope (OLYMPUS BX- 41). The structure and composition of polyethylene were also studied by Scanning Electron Microscope (SEM) and X-Ray Diffraction (XRD). As an auxiliary study, exposure of sunlight on polyethylene for 50 hours was carried out. Potential damages of polyethylene were also studied.

Keyword: SSNTDs, SEM, XRD

Introduction

The present work is a part of the project on the study of the Solid State Nuclear Track Detectors (SSNTDs). This research work is pioneer studies of neutron irradiated polyethylene by using Am (Be) source. It is essentially materials that are damaged in such a way by energetic particles, the particle tracks can be developed by subsequent etching and observed microscopically.Etchable tracks may be found in almost any type of electrically insulating material, crystalline, glassy or polymeric which has been exposed to ionizing particles. They have never been seen in metals or other good conductor (Fleischer *et al*., 1975).

In this work, the disruption of polyethylene plastic as result of thermal neutron irradiation was studied by using chemical etching methods, SEM, and XRD techniques. Non-irradiated polyethylene sample was used as comparative study.A solid –state nuclear detector (SSNTDs) is a section of a solid material(photographic emulsion, crystal, glass or plastic)which uncovered to nuclear radiation (neutrons or charged particles, intermittently

[1] Associate Professor, Dr., Department of Chemistry, Yangon University of Distance Education

[2] MSc Candidate, Department of Chemistry, University of Yangon

as well gamma rays), etched, and inspected microscopically. The pathways of nuclear particles are imprinted quicker than the body substance, in addition to the range and form of these trails acquiesce knowledge regarding the charge, mass, direction of motion of the particles as well as the energy (Hepburn *et al*., 1980).

The foundation of SSNTDs is that charged particles break the detector within nanometers down the path in such a way that the path can be imprinted persistently more rapidly than the unspoiled substance. Engraving, characteristically for some hours, extends the dent to tapering depths of micrometer dimensions, which can be seen with a microscope. For a known particle, the span of the pathway shows the energy of the particle. The charge can be acquired from the carve rate of the pathway in contrast to that of the main part. Solid state nuclear track detectors or track recording materials are the material that are damaged in such away by incident energetic particles that the particle tracks can be developed by subsequent etching and observed microscope. Track recording materials are classified in three groups such as minerals crystals, glasses and plastics (Green *et al*., 1977).

The most attractive characteristics of the techniques are its simplicity, low cost and ability to provide direct evidence for certain phenomena. And the technique involves simple instrumentation. Further more, the detectors are small, easy to use and unconstructive. They are insensitive to light and X-rays. The registered tracks are permanent record on the detector. Etching of the detector is simple and does not need darkroom facilities. One disadvantage of the SSNTD is the fact that the exposure period is long; generally they should be exposed for periods not less than one month (Durrani *et al*., 1987).With the passage of time the technique of SSNTDs became a powerful scientific tool. Not only this technique system is simple, inexpensive, employs portable electronics but also it has found some unique applications in almost all scientific fields(Katz,1977).

Materials and Methods

Sample Collection

In this research work, the high density polyethylene plastic sample was obtained from Golden Deer plastic Industry at Industrial Zone (2),

South Dagon Township, and Yangon Region. The sample was cut into small pieces with dimension of 1cm × 1cm.

Sample Irradiation

The polyethylene sample (1cm × 1cm) was irradiated with thermal neutron from Am (Be) source which has neutron flux of 10^4 $ncm^{-2}s^{-1}$ supplied by IAEA at the Department of Chemistry, University of Yangon. Irradiating time was one week and source target distance was 3cm.

Sunlight Exposure on Sample

The polyethylene plastic sample (1cm × 1cm) was exposed with sunlight for 50 hours at the Nuclear Laboratory, Department of Chemistry, University of Yangon.

Preparation of Etchant

The $K_2Cr_2O_7$ was weighed into 10g and 35ml of 30% H_2SO_4 was added into the beaker. Then, the solution was stirred with a glass rod until all $K_2Cr_2O_7$ were dissolved.

Procedure of Chemical Etching

In this work, to enlarge the size of particle track in polyethylene plastic, 10g of $K_2Cr_2O_7$: 35ml of 30% H_2SO_4 were used as an etchant. The beaker with an etchant solution was heated in water bath at constant temperature of 65◦C. Then, irradiated polyethylene plastic sample was put into the beaker for 45 min. During heating, the solution in the beaker was occasionally stirred with a glass rod.

Then, the irradiated polyethylene plastic sample was taken out from the beaker and washed with distilled water until the plastic surface was cleaned and dried. The characteristics of polyethylene plastic samples were examined by X-Ray Diffraction **(**XRD**)** and Scanning Electron Microscope (SEM). Track visualization, track photographing, track counting and measuring the length of tracks were performed by using the optical microscope (OLYMPUS BX - 41), attached with digital camera and camera control unit. The microscope consists of eyepiece (40 X) magnification and four lens each with 10, 20, 40, and 100 times magnification. The camera and camera control unit used in this work were camera head and camera control unit DP-12 .Pressing the menu button brings up the menu to photograph the tracks.

Results and Discussion

Assessment of Irradiated Polyethylene by X-Ray Diffraction (XRD)

The non-irradiated and irradiated polyethylene plastic samples were studied by using XRD method to determine the chemical composition and structure of the raw material component. The XRD spectrums of each sample are shown in Figure 1 and 2. From these figures, it was found that there is no change in chemical compositions and structure of irradiated polyethylene plastic compared to that of non-irradiated polyethylene's spectrum. So SSNTDs can detect the radiation without changing the chemical composition etc. Thus, the use of SSNTDs has already become a well-known technique which has been applied in many branches of sciences such as studying in cosmic rays, long-lived radioactive elements, radon concentration in houses, and the age of geological samples.

Assessment of Irradiated Polyethylene by Scanning Electron Microscope (SEM)

In this research work, surface texture of various polyethylene samples such as non-irradiated, irradiated and after etching were studied by Scanning Electron Microscope (SEM).The representative SEM photomicrographs are shown in Figure 3 and 4 respectively. From these observations, it can be found out that there is no similar pattern was observed. Hence, the surface morphology of polyethylene samples differs in each case due to thermal neutron irradiation. Therefore preliminary study on SEM indicates that physical damage is formed.

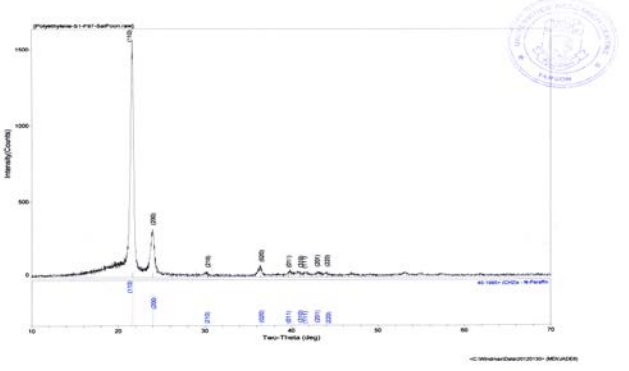

Figure 1. XRD diffractogram of non-irradiated polyethylene plastic

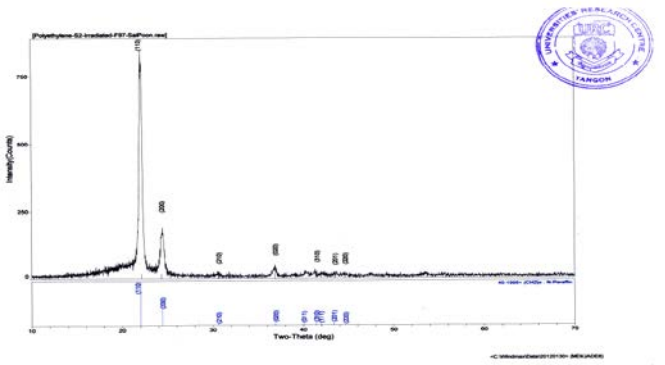

Figure 2. XRD diffractogram of irradiated polyethylene plastic

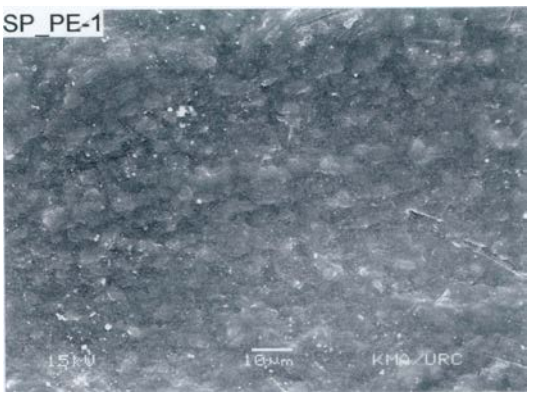

Figure 3. SEM micrograph of non-irradiated polyethylene plastic

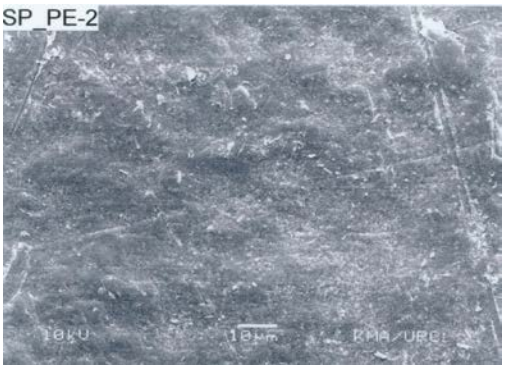

Figure 4. SEM micrograph of irradiated and after etching polyethylene plastic

Assessment of Irradiated Polyethylene by Solid State Nuclear Track Detectors (SSNTDs)

Track caused by irradiated polyethylene was studied by SSNTDs techniques. Etching method was made to enlarge the size of tracks in polyethylene. After etching, the etched tracks were viewed by an Olympus BX - 41 Optical Microscope fitted with Digital camera and display system. The Microscopic photographs are shown in Figure 5.and 6. From these studies, tracks can be observed. Formation of tracks depends on the factors such as irradiation time, neutron flux and high energy. Thus, this research work is initiative study of neutron irradiation of polyethylene by using Am (Be) source.

Assessment on the Damage of Polyethylene by Sunlight

According to the literature, environmental condition that could be damaging to plastic includes exposure to UV, moisture, chemicals, temperature and oxidation. To study the effect of sunlight, the polyethylene sample was exposed on sunlight for 50 hours. From the observations, considerable physical changes are found in exposed polyethylene compared to that of original polyethylene.

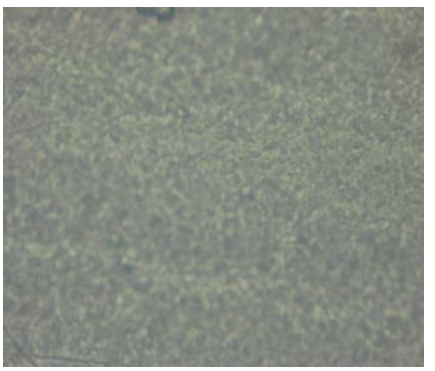

Figure 5. Optical microscopic photo of non-irradiated polyethylene plastic

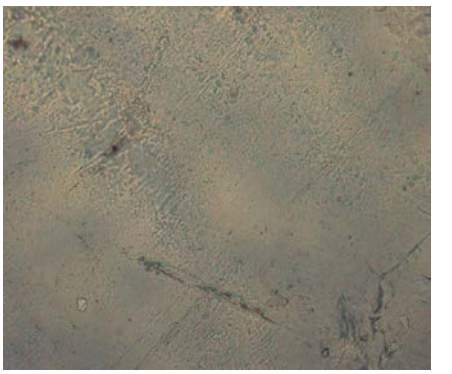

Figure 6. Optical microscopic photo of irradiated polyethylene plastic

Conclusion

The disruption of neutron irradiated polyethylene was studied by Solid State Nuclear Track Detectors (SSNTDs). The structure and composition of polyethylene were also carried out by Scanning Electron Microscope (SEM) and X-Ray Diffraction (XRD). This work had found out that:

From XRD study, there is no distinctive change in chemical composition and structure of irradiated and non-irradiated polyethylene samples as a result of irradiation with thermal neutron from Am (Be) source. Thus, it indicates that the bonds of polyethylene cannot be broken in the case of neutron irradiation for one week. From SEM study, the surface morphology of irradiated polyethylene is found to be different from non-irradiated polyethylene due to the neutron irradiation effect. It indicates that only physical damage is formed but not in chemical change.

From SSNTDs study, track can probably be formed. It shows that disruption of polyethylene was caused by neutron irradiations for one week. As an auxiliary study, exposure of sunlight on polyethylene was carried out for 50 hours. It is found out that there is considerable physical change but not in chemical change between exposed polyethylene and original polyethylene. Thus, it can be concluded that sunlight exposure for 50 hours may cause physical damage. From these observations, Radiation can be detected by using solid state nuclear track detectors such as polyethylene, mica, LR-115, CR-39 and etc. to explore the radon via alpha for environmental safety.

Acknowledgement

I would like to express my profound gratitude to the Department of Higher Education (Lower Myanmar), Ministry of Education, Yangon, Myanmar, for the provision of opportunity to do this research. I would like to express my gratitude to Rector, Dr Ohmar Kyaw, Yangon University of Distance Education, for her generous permission to do this research paper. Thanks also to Pro-rector Dr Khin Thant Sin, Yangon University of Distance Education, for sharing her thoughtful ideas. I would like to express my thanks to Professor Dr Thazin Lwin, Head of the Department of Chemistry, University of Distance Education, for her kind permission, encouragement, for providing the departmental facilities. I am also very thankful to Professor Dr. Yu Yu Myo, Department of Chemistry for her kind encouragement for this research paper.

References

Durrani, S. A., and R. Bull. (1997). *Solid state Nuclear Track Detection Principles, Method and Application*. Oxford: Pergamon, 279-282

Fleischer, R. L., P.B. Price and R. M.Walker. (1975). *Nuclear Tracks in Solid: Principles and Applications*. University of California, Berkeley,1-44

Green, P. F., and S. A. Durrani. (1977). "Annealing Studies of Tracks in Crystals *". J. Nucl. Detection*. 57-59

Hepburn, C., and A. H. Windle. (1980). *Solid State Nuclear Track Detectors*. Cambridge, UK, 279-296

Katz, R. (1977). "Track Structure in Radiobiology and in Radiation Detection". *J. Nucl. Detection*. **2**, 1-28

Determination of Salt Rejection of Cellulose Acetate-Kaolinite Clay-Chitosan Membrane for Sodium Chloride Solution

Khin Kay Thi Han[1], Hnin Yu Wai[2] & Cho Cho[3]

Abstract

This research is concerned with the preparation, characterization and application of cellulose acetate-kaolinite clay-chitosan membranes. The membranes were prepared by using cellulose acetate-kaolinite clay-chitosan and glutaraldehyde as a cross-linker by the casting and autoclaving method. The physicochemical properties (such as pH, moisture content, ash content and bulk density) of samples were determined by conventional methods and these samples were characterized by modern techniques such as EDXRF, FT IR and SEM analyses. The series of cellulose acetate-kaolinite clay- chitosan membranes of 0.3 g (w/v) kaolinite clay, 2 g (w/v) chitosan, and different amounts (1.0 g, 1.5 g, 2.0 g, 2.5 g, 3.0 g) of cellulose acetate (A_1, A_2, A_3, A_4, A_5) were prepared by the solvent evaporating method. The prepared membranes were characterized by physicomechanical properties such as tensile strength, elongation at break (%), and tear strength. It was found that the membrane (A_3) possesses tensile strength (15.4 MPa), elongation at break (8.7 %) and tear strength (25.5 km^{-1}). The degree of swelling for the A_3 membrane 0.5 % in water, 68.8 % in 1% w/v NaCl solution, 62.7 % in 2 % w/v NaCl solution, and 55.3 % in 3 % w/v NaCl solution. According to mechanical properties, the membrane A_3 was to be used as the most suitable membrane for salt rejection. From the experiments, the salt rejection of 0.4 mm membrane A_3 was found to increase with operating run and also membrane A_3 could be used for a higher input salt concentration (5000 mgL^{-1}). It can be found that the salt rejection percent of membrane A_3 was 66.1 % in the fifth operation run.

Keywords: cellulose acetate, kaolinite clay, chitosan, glutaraldehyde, physicomechanical properties

[1] Lecturer, Department of Chemistry, Hpa-an University.
[2] Lecturer, Dr, Department of Chemistry, University of Yangon.
[3] Professor, Dr, Department of Chemistry, University of Yangon.

Introduction

Saline water contains significant amounts of dissolved salt so humans cannot drink it. Fresh water can make from sea water by desalination process. It is using more and more around the world to provide people needed fresh water. Highly hazardous materials released from industries contaminated in water streams. People use various purification techniques for remediating the contaminated water. Among them, membrane technology is tremendous importance in recent years (David, 2012).

The less permeation flux, the more salt concentration. This is due to increase the osmotic pressure difference across the membrane. If feed pressure remains constant, under higher salt concentration results in higher osmotic pressure and this leads to much higher driving force. The increasing in salt concentration in feed water also leads to surface cake or fouling phenomenon on the membrane surface (Marwan, 2006).

Water desalination processes separate dissolved salts and other materials form water. The brackish, seawater, wells, surface (rivers and streams), wastewater and industrial feed and process water may be included in feed water sources. Seawater desalination has the potential to reliable produce enough potable water to support large populations located near the coast. Membrane is an alternative technology of water treatment with filtration principle. Membrane technology is considered to have more advantageous to be applied water treatment because it does not require any necessary chemical additives such as the existing conventional technologies (Baker, 2004).

This work is concerned with the preparation, characterization and application of composite membrane (cellulose acetate-kaolinite clay-chitosan) which were prepared by blending of cellulose acetate-kaolinite clay- chitosan and glutaraldehyde as cross-linker.

Materials and Methods

All chemicals in this work were obtained from British Drug House Chemical Ltd., Poole, England and from the Kanto Co. Ltd., Japan.

Equipment employed in this work consists of lab ware, glassware and other supporting facilities. Some of the instruments used in the

experiment are Blance (BL 210S Satourius Gottingen, Germany), Magnetic stirrer (Bibbysterilini Ltd., United Kingdom), Electric furnace (LDO-080N), Centrifuge (No. 5837, Tokyoseiden Co. Ltd., Tokyo, Japan), Auto clave (0.3 MPa, SP 510, Lecicester Le 67, Laquip, England, Supplied by Labquip), Casting mold (Malamine plate), Cutter (Wallace), Tensile Tester (Tensile Testing Machine, Hournsfied 5000E, England), FT IR spectrophotometer (Shimadzu Perkin Elmer Spectrum GX, Japan), Scanning Electron Microscope (No. JSM- 5610, JEOL: Ltd., Japan) and Energy Dispersive X-Ray Fluorescence (EDXRF (Rigaku, D-Max-2200, Japan).

Collection of samples

Chitosan sample was collected from Shwe Poe Co. Ltd, Hlaing Tharyar Township, Yangon Region and kaolinite clay from Minbu Township, Magway Region and also cellulose acetate from chemical shop.

Characterization of samples

The physicochemical properties (pH, moisture content, ash content and bulk density) of chitosan, kaolinite clay and cellulose acetate were determined by conventional method and their characterizations are characterized by modern techniques such as EDXRF, FT IR and SEM.

Preparation of membrane

In this research, all of the membranes were prepared by blending, casting and by solvent evaporating technique under autoclaving conditions of 121 °C and 0.1 MPa in a time frame of 20 min. Firstly, 2 g of chitosan and
1 % acetic acid were mixed by magnetic stirrer for 3 h to chitosan solution. Each membrane 1 % (w/v) of chitosan solution, 0.3 g of kaolinite clay and cellulose acetate (1.0 g, 1.5 g, 2.0 g, 2.5 g and 3.0 g) was mixed by magnetic stir for 30 min. Then, 0.1 % glutaraldehyde was added as crosslink, put into the 0.1 MPa autoclave for 20 min at 121 °C and poured onto melamine tray. The membranes were kept and dried at room temperature for 15 days and then, they were skimmed off.

Characterization of membranes

The prepared cellulose acetate-kaolinite clay-chitosan membranes were characterized by physicomechanical properties.

Measurement of Salt Rejection of Selected Membrane (A_3)

The salt rejection of membrane A_3 was determined by Fick's Law of diffusion.

Results and Discussion

Determination of Physicochemical Properties of Samples

The results of the physicochemical properties of cellulose acetate, kaolinite clay and chitosan are presented in Table 1. The pH results indicate that the cellulose acetate, kaolinite clay and chitosan are 6.20, 7.17, and 6.70, respectively. The moisture content of cellulose acetate, kaolinite clay and chitosan was 6.24 %, 11.54 % and 20.76 %, respectively. It was found that the moisture content of chitosan is higher than that of cellulose acetate and kaolinite clay. The total ash of kaolinite clay was 13.52 %. The bulk densities of cellulose acetate and kaolinite were 1.32 and 2.72 g cm^{-3}.

Table 1. Physicochemical Properties of Cellulose Acetate, Kaolinite Clay and Chitosan

Sample	pH	Moisture Content (%)	Ash content (%)	Bulk density (g cm^{-3})
Cellulose acetate	6.20	6.24	10.17	1.32
Kaolinite clay	7.17	11.54	13.52	2.72
Chitosan	6.70	20.76	2.14	-

EDXRF Analysis

EDXRF spectrum of kaolinite clay is shown in Figure 1 and the relative abundance of elements is presented in Table 2. From this table, the major elements present in kaolinite clay were found to be 36.28 % Si, 27.31 % K, and 23.09 % Al, respectively.

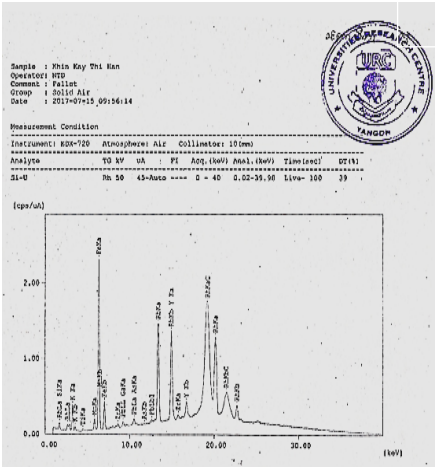

Figure 1. EDXRF spectrum of kaolinite clay

Table 2. Relative Abundance of Elements Present in Kaolinite Clay by EDXRF Spectrometry

Element	Relative Abundance (%)
	Kaolinite clay
Si	36.28
K	27.31
Al	23.09
Rb	5.47
Y	3.52
Mn	1.89
Ti	0.82
Pb	0.53
Ga	0.40
Zn	0.34
Zr	0.17
As	0.16

FT IR Analysis

The FT IR spectra of cellulose acetate, kaolinite clay and chitosan are shown in Figures 2(a), 2(b) and 2(c) and in Table 3.

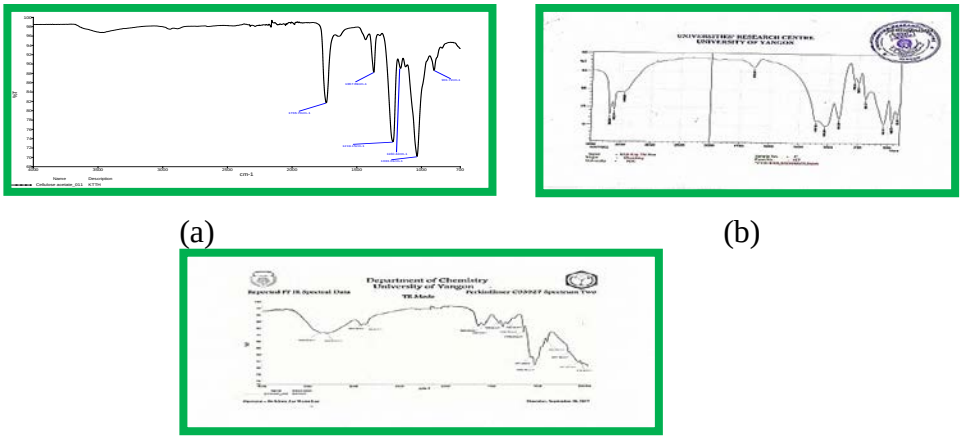

(a) (b)

(c)

Figure 2. FT IR spectra of (a) cellulose acetate, (b) kaolinite clay and (c) chitosan

Table 3. FT IR Band Assignments of Cellulose Acetate, Kaolinite Clay and Chitosan

Wave number (cm^{-1})						Band Assignment
CA	CA*	KC	KC**	CS	CS***	
-	-	3622	3620	-	-	Al-O-H stretching
-	-	-	-	3365	3367	N-H stretching
3337	3335			3240	3247	O-H stretching
2919	2902			2922	2916	C-H stretching
1728	1731			-	-	C=O stretching
-	-	1639	1634	-	-	H-O-H bending
-	-	-	-	1604	1559	C-O-N-H stretching
1437	1430			1335	1335	C-H bending
1160, 1109	1161, 1107			1418,1087	1414,1082	C-O-C stretching
-	-	1107, 1033	1101, 1032	-	-	Si-O stretching
1019	1038	-	-	1071	1048	O-H bending
-	-	910	912	-	-	Al-Al-O-H stretching
				890	896	Saccharide structure of chitosan
-	-	692	693	-	-	Si-O-H stretching

CA= cellulose acetate, KC=kaolinite clay, CS=chitosan

*Huda *et al.* (2019), ** Kumar *et al.* (2013), *** Varma and Vasudevan (2020)

SEM Analysis

The SEM micrographs of chitosan, kaolinite clay and cellulose acetate are shown in Figure 3(a), 3(b) and 3(c). The surface morphology of

cellulose acetate and chitosan was found to be fibrous like nature and that of kaolinite clay was found to be spherical shape like nature distributed.

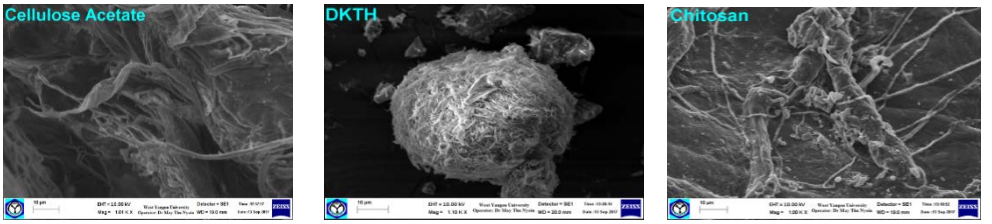

(a) **(b)** **(c)**

Figure 3. SEM micrographs of (a) cellulose acetate, (b) kaolinite clay and (c) chitosan

Determination of Physicomechanical Properties of Prepared Membranes

The results of the physicomechanical properties of membranes are presented in Table 4 and Figure 4. According to this Table, it was found that the tensile strength, elongation at break (%) and tear strength of membrane A_3 are greater than those of other membranes. Among these parameters, tensile strength is more specific than other membranes for determining the qualities. The mechanical properties in terms of thickness, tensile strength, elongation at break and tear strength are important parameters which reveal the nature of membranes. The mechanical properties of the prepared cellulose acetate-kaolinite clay-chitosan membranes depend upon the concentration of cellulose acetate. The thickness of membranes is in the range of 0.12 mm to 0.20 mm. Among these membranes, tensile strength of membrane A_3 is greater than the other membranes. It can also be seen that the percent elongation at break of membrane A_3 is greater than that of the other membranes. The higher the elongation at break of the membrane, the higher the stability of the membrane. From the resulting data, it was found that the tear strength of membrane A_3 possesses the highest value. Therefore, membrane A_3 is selected to determine salt rejection for NaCl solution.

Table 4. Physicomechanical Properties of Prepared Membranes

Properties	Prepared Membranes				
	A_1	A_2	A_3	A_4	A_5
Thickness (mm)	0.12	0.14	0.16	0.18	0.20
Tensile strength (MPa)	12.1	13.5	15.4	11.8	10.3
Elongation at break (%)	6.9	7.0	8.7	6.8	4.1
Tear strength (kN/m)	16.4	20.5	25.5	18.2	12.8

A_1 = Cellulose acetate (1.0 g) + Kaolinite (0.3 g) + Chitosan (2 g)

A_2 = Cellulose acetate (1.5 g) + Kaolinite (0.3 g) + Chitosan (2 g)

A_3 = Cellulose acetate (2.0 g) + Kaolinite (0.3 g) + Chitosan (2 g)

A_4 = Cellulose acetate (2.5 g) + Kaolinite (0.3 g) + Chitosan (2 g)

A_5 = Cellulose acetate (3.0 g) + Kaolinite (0.3 g) + Chitosan (2 g)

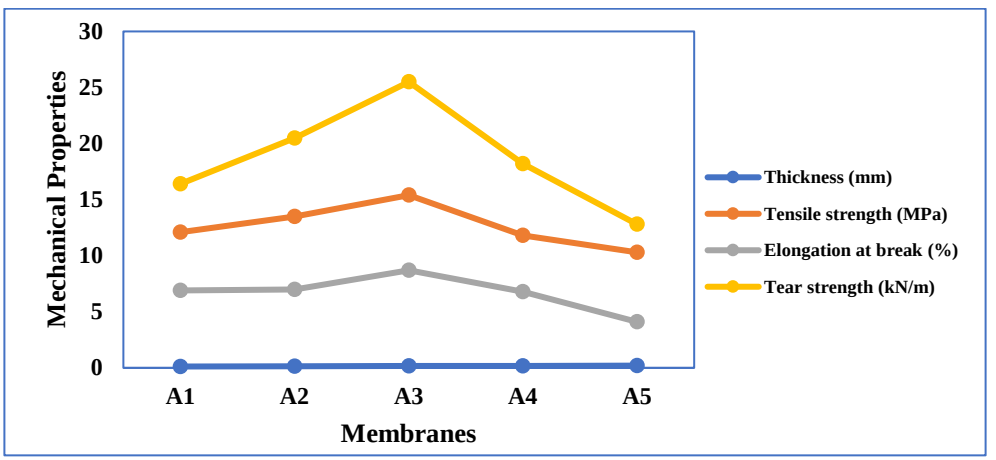

Figure 4. Physicomechanical properties of prepared membranes

Measurement of Swelling Degree of Membranes

The swelling properties of prepared membranes in water and different concentrations of NaCl solutions were presented in Tables 5, 6 and Figure 5. From the resulting data, membrane A_3 possesses the highest degree of swelling in water and 1 % w/v, 2 % w/v and 3 % w/v NaCl solutions.

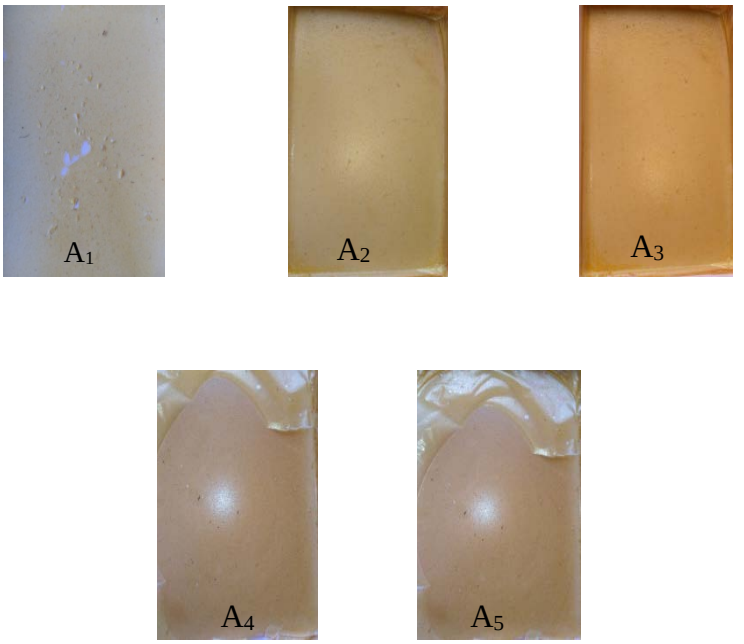

Figure 5. Photographs of prepared membranes

Table 5. Swelling Degree of Membranes (A_1- A_5) in Water

Membranes	Degree of Swelling (%)								
	10 min	20 min	30 min	40 min	50 min	60 min	70 min	80 min	90 min
A_1	40.5	43.6	49.8	52.6	55.3	65.4	62.5	60.4	57.4
A_2	41.2	45.6	50.8	56.8	60.5	66.8	65.5	60.7	59.8
A_3	42.6	44.8	50.6	58.3	61.7	70.5	64.6	61.2	58.5

Membranes	Degree of Swelling (%)								
	10 min	20 min	30 min	40 min	50 min	60 min	70 min	80 min	90 min
A_4	41.3	46.7	51.8	57.4	62.3	67.4	64.0	62.8	57.1
A_5	39.2	41.3	50.8	55.3	59.3	63.4	60.3	58.3	55.3

Immersing time = 90 min

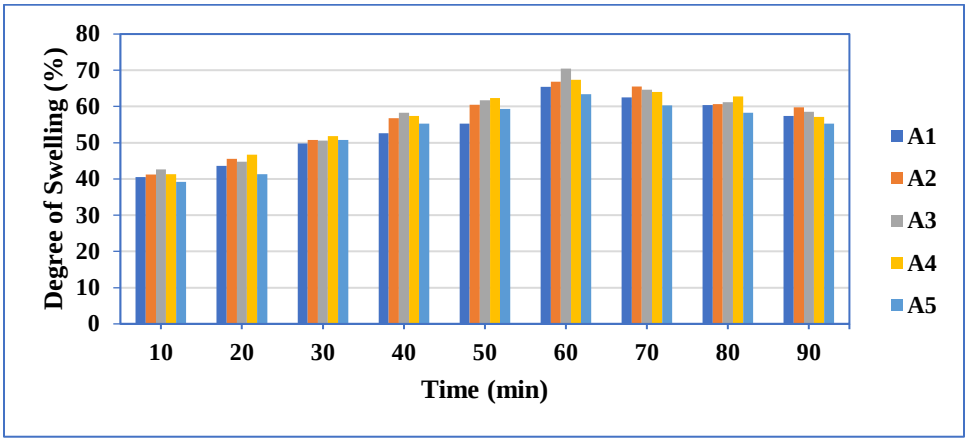

Figure 6. Swelling Degree of Membranes (A_1- A_5) in Water

Table 6. Swelling Degree of Prepared Membranes in Water

Membranes	CA (g)	KC (g)	CS (g)	Swelling (%)	Remark
A_1	1.0	0.3	2.0	65.4	Water deformed membrane
A_2	1.5	0.3	2.0	66.8	Even membrane formed
A_3	2.0	0.3	2.0	70.5	Durable membrane formed
A_4	2.5	0.3	2.0	67.4	Thick membrane formed (brittle)
A_5	3.0	0.3	2.0	63.4	Thick membrane formed (brittle)

Immersion time = 90 min

Table 7. Swelling Degree of Prepared Membranes in Water and Different Salt Solutions

Membranes	Swelling (%)			
	H_2O	NaCl (1% w/v)	NaCl (2% w/v)	NaCl (3% w/v)
A_1	65.4	59.8	52.3	48.3
A_2	66.8	61.4	56.7	50.4
A_3	70.5	68.8	62.7	55.3
A_4	62.4	57.3	52.4	46.0
A_5	60.7	57.3	49.8	40.4

Immersion time = 90 min

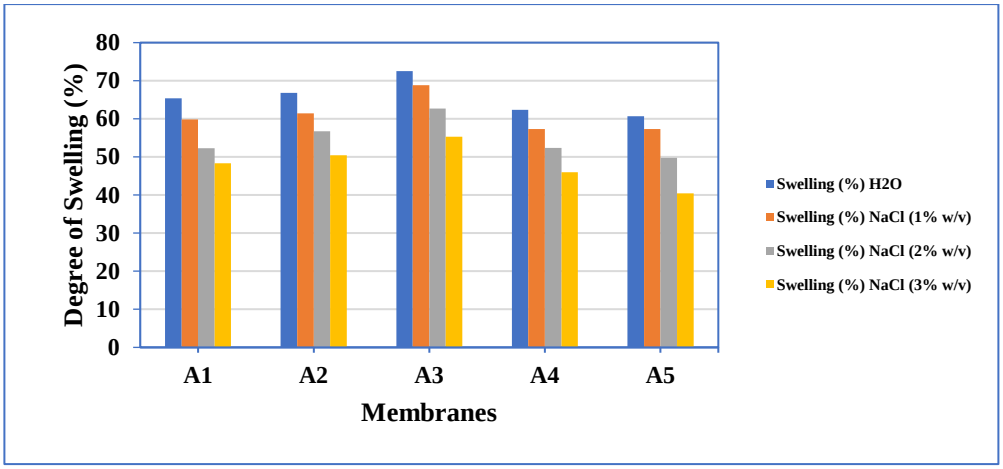

Figure 7. Swelling degree of membranes in water and different concentration of NaCl solutions

Measurement of Salt Rejection of the Selected Membrane (A_3) for Sodium Chloride Solution by using the Effect of Applied Run

Tables 8 and 9 showed the calculated result of permeate flux of chloride ions according to Fick's Law of diffusion equation. The increasing the number of applied operating runs, increases the permeate volume. The lower the permeate flux of chloride ions, the better the performance of salt rejection of the membrane. The permeability of membrane A_3 gives 1.10×10^4 $Lm^{-2}day^{-1}$ in the fifth operation run. It can be seen that the diffusion coefficient of membrane A_3 gives 4.40 $Lm^{-1}day^{-1}$ in the fifth operation run. According to Table 9, it was observed that the salt rejection of membrane A_3 was 66.1 %.

Table 8. Effect of Applied Runs on permeate Flux of Chloride Ions from Sodium Chloride Solution by the Selected Membrane (A_3)

Run	NaCl concentration of feed (mgL^{-1})	NaCl concentration of permeate (mgL^{-1})	Different NaCl concentration of permeate (mgL^{-1})	Collected permeate volume (mL)	Mass of salt ion in the permeate $\times 10^3$ (mg)
1	5000	3860	1140	775	2.992
2	3860	2795	1065	800	2.236
3	2795	1805	990	825	1.528
4	1805	960	845	860	0.826
5	960	325	635	963	0.313

Collected time = 15 min

Thickness of membrane = 0.4×10^{-3} m

Table 9. Effect of Applied Runs on Permeability, Diffusion Coefficient and Salt Rejection of the Selected Membrane (A_3)

Run	NaCl concentration of feed (mg L^{-1})	Permeate flux$\times 10^{7}$ (mg $m^{-2}day^{-1}$)	Permeability $\times 10^{4}$ ($Lm^{-2}day^{-1}$)	Diffusion Coefficient ($Lm^{-1}day^{-1}$)	Salt Rejection (%)
1	5000	10.587	3.51	14.04	22.8
2	3860	7.912	3.11	12.44	27.6
3	2795	5.407	2.55	10.20	35.4
4	1805	2.923	1.99	7.96	46.8
5	960	1.108	1.10	4.40	66.1

Collected time = 15 min

Thickness of membrane = 0.4 x 10^{-3} m

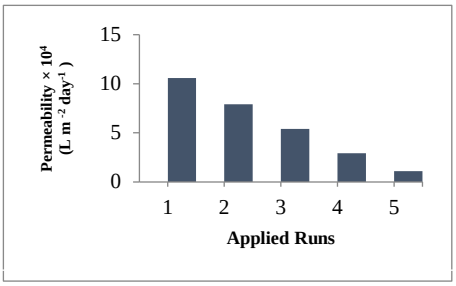

Figure 8(a) Effect of applied runs on permeate flux of the selected membrane (A_3)

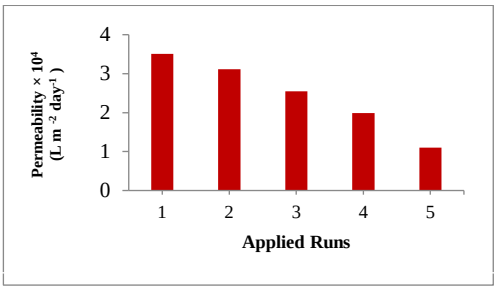

Figure 8(b) Effect of applied runs on permeability of the selected membrane (A_3)

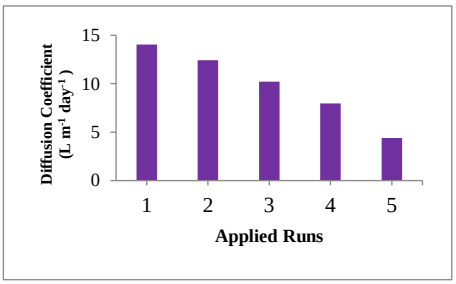

Figure 8(c) Effect of applied runs on diffusion coefficient of the selected membrane (A_3)

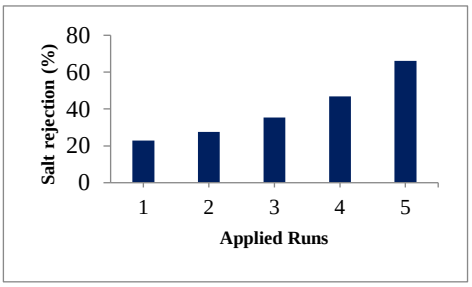

Figure 8(d) Effect of applied runs on salt rejection of the selected membrane (A_3)

Conclusion

In this research, polymer blended membranes consisting of cellulose acetate, kaolinite clay and chitosan were prepared. The various types of cellulose acetate-kaolinite clay-chitosan blended membranes were prepared by blending, casting and by solvent evaporating technique under autoclaving conditions of 121 °C and 0.1 MPa in a time frame of 20 min.

According to the physicomechanical properties such as tensile strength, elongation at break (%) and tear strength, it was found that membrane A_3 sample possesses 15.4 MPa of tensile strength, 8.7 % of elongation at break and 25.5 kNm^{-1} of tear strength. The degree of swelling for A_3 membrane has 70.5 % in water, 68.8 % in 1 % w/v NaCl solution, 62.7 % in 2 % w/v NaCl solution and 55.3 % in 3 % w/v NaCl solution. Membrane A_3 possesses the highest tensile strength, elongation at break, tear strength and swelling degree in water. Therefore, membrane A_3 was chosen to be applied for desalination process. From the effect of applied runs 0.4 mm thickness of membrane A_3, it was found that the salt rejection percent of membrane A_3 was 66.1 % in the fifth operation run. The lower permeate flux, permeability and diffusion coefficient, the better the performance of the membrane and also the salt rejection percent of the membrane.

Acknowledgement

The authors would like to thank Professor and Head, Dr. Ni Ni Than, of the Department of Chemistry, University of Yangon for allowing to carry out this research programme and for allowing the writing of this paper. Special thanks are extended to Dr Khin Thu Thu Min (Professor and Head), the Department of Chemistry, Hpa-an University; and Dr Win Pa Pa, Professor and Head, the Department of Chemistry, Nationalities Youth Resource Development of Degree College.

References

Baker, RW. (2004). Membrane Technology and Applications. Chichester: John Wiley & Sons. Ltd, 2nd edn, 112-135

David, C.T. and C.G. Jeffrey. (2012). “Water Desalination across Nanoporous Graphene”, American Chemical Society, 1-7

Huda, E., Rahmi and Khairon. (2019). “Preparation and characterization of cellulose acetate from cotton”, *IOP Conf. Ser*. *Earth Environ. Sci*., 364, 1-7

Kumar, S., A. K. Panda and R. K. Singh. (2013). “Preparation and Characterization Acids and Alkali Treated Kaolin Clay”, *Bulletin of Chemical Reaction Engineering & Catalysis*, **8**(1), 61-69

Marwan, M.S. and T.C. Owee. (2006). "Drinking Water from Desalination of Seawater: Optimization of Reverse Osmosis System Operating Parameters", *J. Eng. Sci. Technol.*, **1**(2), 203-211

Varma, R. and S. Vasudevan. (2020). “Extraction, Characterization, and Antimicrobial Activity of Chitosan from Horse Mussel *Modiolus modiolus*”, *ACS Ome*ga, 5, 20224-20230

Antioxidant Activity and Sun Protection Factor (SPF) of Sunscreen Lotions of Shells and Roots of *Arachis hypogaea* L. (Peanut)

Ei Ei Thwin*

Abstract

The present research deals with antioxidant activity and sun protection factor (SPF) of shells and roots of peanut (*Arachis hypogaea* L.) was investigated. Extracts from shells and roots of peanut using different solvents were subjected to screening for their possible antioxidant properties by using 2,2'-diphenyl-1-picrylhydrazyl (DPPH) assay. From this investigation, MeOH (IC_{50}= 12.32 μg/mL) and acetone extracts of shells (IC_{50}= 11.01 μg/mL) were potent antioxidant power than that of roots in DPPH radical scavenging activity. The sunscreen lotions containing ethanol extracts of shells and roots of peanut were prepared. The formulated sunscreen lotions were evaluated for sun protection factor (SPF) and the skin irritation test was also performed. In the *in vitro* determination of SPF values, absorbance values were measured by UV spectrophotometer and SPF were calculated by using the equation derived by Mansaur. SPF of shells and roots of peanut exhibited moderate activity (SPF= 8.1 and 6.5). In the skin irritation test, they did not show any sign and symptom of skin irritation on albino rats. The skin irritation test demonstrated that the formulated sun screen lotions containing ethanol extracts of shells and roots of peanut might be considered to be safe and protect the skin from sunburn.

Keyword: antioxidant activity, *Arachis hypogaea* L., shells and roots, skin irritation test, sun protection factor

Introduction

Peanut (*Arachis hypogaea* L.) is a species in the Leguminosae or Fabaceae family. Peanuts are one of the most important legume crops in the semiarid and tropical regions of the world. It is cultivated in Myanmar, Vietnam, the United States, India, Georgia, North and South Carolina, Florida, Virginia and New Mexico. It is both an oilseed crop and a food grain legume. It has been grown for use not only as snack food and cooking oil, but also as material for the production of soap, cosmetics and machine oil (Sim, 2011).

* Lecturer, Dr. Department of Chemistry, University of Magway

On exposure to sunlight human body experiences both beneficial and harmful effects, depending on the length and frequency of exposure, sunlight intensity and the sensitivity of the individual concerned. On exposure to sunrays the first effect produced is erythema of skin, followed by formation of tan. The intensity of erythema [reddening] produced on exposure to sunlight depends on the amount of UV energy absorbed by skin. It usually develops after a latent time period of 2-3 hours and reaches its maximum level within 10-24 hours. The sun emits a wide range of ultraviolet (UV) radiation. All of the harmful UVC (200–280 nm) and most of UVB (280–320 nm) is absorbed by the stratospheric ozone layer. Stratospheric ozone does not affect UVA (320–400 nm) transmission. As the stratospheric ozone layer is depleted the amount of harmful shortwave UV reaching the earth's surface will increase. On the other hand, chances of UV exposure by increased outdoor activity and imprudent use of sun tanning machines increased the risks of unwanted UV effects, such as sunburn, photoaging, skin cancer induction and immune suppression. Solar UV is the most prominent cause of skin cancer (Wilkinson, 1982). In response to this, various herbal formulations and chemicals are being available to block UV rays and to prevent skin damages.

Solar UV radiations at the earth's surface encompass approximately 95-98 % UVA and 2-5 % UVB. The frequency of UVB is fundamentally liable to be absorbed by keratinocytes leading to production of free radicals or reactive oxygen species (ROS) which might cause skin erythema, sunburn, skin cancer and premature ageing (Mishra, 2011). Antioxidants quench free radicals and ROS which might aid photo-protection effect. Herbal sunscreen topical products guard skin from sun's radiations which reduces sunburns with reduced risk of skin harms (Singh, 2017).

There has been increasing interest in the presence and availability of compounds in plant materials. Natural substances extracted from plants have recently been considered as potential sunscreen resources owing to ultraviolet ray absorption and antioxidant activity. In the present work, shells and roots of peanut were chosen to investigate antioxidant activity, to formulate sunscreen lotions and to determine the sun protection factor (SPF) since the bioactivities of these samples have not yet been investigated scientifically in our laboratory.

Sun protection factor (SPF)

A number on a scale for rating the degree of protection can be provided by sunscreens. SPF stands for Sun Protection Factor. SPF numbers on a package can range from as low as 2 to as high as 100. These numbers refer to the product's ability to screen or block out the sun's burning rays. It is a common mistake to assume that the duration of effectiveness of a sunscreen can be calculated simply by multiplying the SPF by the length of time it takes for him or her to suffer a burn without sunscreen, because the amount of sun exposure a person receives is dependent upon more than just the length of time spent in the sun. The amount of sun exposure depends upon a number of factors including the length of exposure, time of day, geographic location, and weather conditions (COLIPA, 2006).

Materials and Methods

Collection and preparation of samples

The samples were collected from Magway Township, Magway Region and the plant sample was identified at Department of Botany, University of Yangon. The cleaned and dried plant materials were made into powder and stored separately in air-tight containers.

Preparation of crude extracts

Each dried powdered sample (200g) was percolated with 70% EtOH (1000mL), MeOH (1000mL) and acetone (1000mL) for crude extracts.

Determination of antioxidant activity on some crude extracts by DPPH assay

Materials

EtOH, MeOH and acetone extracts, 2, 2-diphenyl-1-picrylhydrazyl (DPPH), ascorbic acid and distilled water; Syringes (5mL, 3mL), brown bottles, electric balance, shaker and UV-spectrophotometer (SHIMADZU UV-Vis Spectrophotometer)

Preparation of solutions

(a) Preparation of 0.002% (w/v) DPPH solution

0.002% DPPH solution was prepared in the brown colored bottle by dissolving (2 mg) of DPPH powder in the 100 mL of ethanol. It must be stored in the refrigerator for no longer than 24 h.

(b) Preparation of test sample solutions

The stock solution (400 μg/mL) of the crude extract was prepared by dissolving (4 mg) of respective crude extract in 10 mL of ethanol. This stock solution was two-fold serially diluted with ethanol to get the sample solution with the concentrations of 400, 200, 100, 50, 25, 12.5, 6.25 and 3.125 μg/mL.

(c) Preparation of blank solution

Blank solution was prepared by mixing the sample solution 1.5 mL with ethanol (1.5 mL).

Procedure

DPPH radical scavenging activity was determined by using UV-visible spectrophotometer (SHIMADZU UV-Vis Spectrophotometer, 2011).

The control solution was prepared by mixing 1.5 mL 0f 0.002% DPPH solution and 1.5 mL of ethanol in the brown bottle. The sample solution was also prepared by mixing 1.5 mL of 0.002% DPPH solution and 1.5 mL of test sample solution. These bottles were incubated at room temperature and were shaken on shaker for 30 min. After 30 min, the absorbance values of these solutions were measured at 517 nm and the percentage of radical scavenging activity (% RSA) was calculated by the following equation.

$$\% \text{ RSA} = [A_{control} - (A_{Sample} - A_{Blank}) / A_{control}] \times 100$$

Where, % RSA = % radical scavenging activity of test sample

$A_{Control}$ = absorbance of DPPH in EtOH solution

A_{Sample} = absorbance of sample + DPPH solution

A_{Blank} = absorbance of sample + EtOH solution

The antioxidant power (IC_{50}) is expressed as the test substances concentration (μg/mL) that result in a 50% reduction of initial absorbance

of DPPH solution and that allows to determine the concentration. IC_{50} (50% inhibitory concentration) values were calculated by linear regressive excel program. The standard deviation was also calculated by the following equation.

$$\text{Standard Deviation (SD)} = \sqrt{\frac{(\overline{x} - x_1)^2 + (\overline{x} - x_2)^2 + \ldots (\overline{x} - x_n)^2}{(n-1)}}$$

Determination of sun protection factor (SPF) and skin irritation test of formulated sunscreen lotions

(a) Formulation of sunscreen lotions

Accurate quantities of cetyl alcohol, zinc oxide, stearic acid, glycerin, and hydroxyl propyl cellulose (HPC) were weighed as described in Table 1. Accurate quantity of water was measured and taken in a 250 mL beaker. 1.0g of triethanolamine was added to water and stirred. The water solution was heated to a temperature of 80°C to 85°C. After the water solution has reached the required temperature, melted cetyl alcohol, zinc oxide, stearic acid, glycerin, hydroxyl propyl cellulose mixture and propyl paraben were slowly poured into the water solution a little at a time, stirring constantly. Stirring was continued until a smooth and uniform paste was obtained. The prepared sunscreen lotion was set aside to cool. Then weighed quantity of aloe gel, ethanol roots extract (ER), ethanol shells extract (ES), olive oil, rose water and vitamin E were added and stirred well until all the ingredients mixed uniformly. Finally rose oil was added as flavoring agent.

(b) *In vitro* determination of sun protection factor (SPF)

Sun protection factor (SPF) was determined by using UV Visible spectrophotometer. 0.10 % solution (w/v) each of the two formulated sunscreen lotions in ethanol was prepared by dissolving 0.05g of the sunscreen lotion in 50.0 ml of ethanol. The prepared aliquots of each formulation were scanned between 290 and 320 nm, with 5 nm interval. SPF was calculated by using the equation derived

Table 1. Composition in Sunscreen Lotions

Sr No.	Ingredients	F-1 (%)	F-2 (%)
1	Aloe gel	5.0	5.0
2	ES	6.0	-
3	ER	-	6.0
4	Olive oil	2.0	2.0
5	Rose oil	1.0	1.0
6	Rose water	3.0	3.0
7	Cetyl alcohol	2.0	2.0
8	Zinc oxide	12.0	12.0
9	Stearic acid	4.0	4.0
10	Glycerin	2.0	2.0
11	Vitamin E	1.0	1.0
12	Triethanolamine	1.0	1.0
13	Hydroxyl propyl cellulose	10.0	10.0
14	Propyl paraben	0.5	0.5
15	Distilled water	50.5	50.5

by Mansaur (Mansaur 1986; Santo et al., 1999). EE (λ) x I (λ) values determined by Sayre (Sayre et al. 2003) was used in below Equation.

$$SPF_{spectrophotometric} = CF \sum_{290}^{320} EE(\lambda) \times I(\lambda) \times A(\lambda)$$

Where, correction factor, CF=10, EE (λ) = erythemogenic effect of radiation of wavelength λ, I (λ) = intensity of solar light of wavelength λ, A (λ) = spectrophotometric absorbance values at wavelength λ.

The values of EE (λ) x I (λ) are constants. They were determined by Sayre *et al*., (2003), and are showed in Table 2.

(c) Skin irritation test

The skin irritation test was performed on albino rats of both sexes weighing about 150–200 g. The animals were maintained in an air-conditioned room. Hair was shaved from the back of rats and an area of 2 cm^2 on both sides.

Table 2. Normalized Product Function Used in the Calculation of SPF

Wavelength (λ nm)	EE x I (normalized)
290	0.0150
295	0.0817
300	0.2874
305	0.3278
310	0.1864
315	0.0839
320	0.0180
Total	1

Figure 1 shows that the back of albino rats' hair was shaved. One group served for ES (F-1 formulation) and the second group for ER (F-2 formulation). Lotions were applied twice a day for two weeks and the sites were observed for any sensitivity, edema and erythema (Rasheed., *et al*, 2012).

Figure 1. Shaving hair of rat's back

Results and Discussion

Antioxidant activity of EtOH, MeOH and acetone extracts of shells and roots was determined by DPPH radical scavenging assay using UV spectrophotometer. The procedure for the determination of the antioxidant activity has been mentioned above.

The DPPH (2, 2-diphenyl-1-picrylhydrazyl) assay is widely used to investigate the scavenging activities of several natural compounds such as crude extracts of plants. DPPH radical is scavenged by antioxidant through the donation of electron forming the reduced DPPH. Sample's color changed from purple to pale yellow which can be quantified by its decrease of absorbance at wavelength 517 nm. The radical scavenging activity of some crude extracts of peanut shells and roots was expressed in terms of %RSA and IC_{50} (50% inhibitory concentration). The results are shown in Tables 3 and 4 and Figures 2.

The IC_{50} values of EtOH, MeOH and acetone extracts of the two samples were observed to be 41.19 μg/mL, 12.32 μg/mL, 11.01 μg/mL, and 133.59 μg/mL, 70.94 μg/mL, 28.88 μg/mL respectively (Table 3). The lower the value of IC_{50}, the higher the antioxidant activity.

From this investigation, it was found that MeOH and acetone extracts of shells were more antioxidant power than EtOH extracts of shells. In roots extracts, acetone extract was the highest antioxidant activity. By the comparison of shells and roots of peanut, it was suggested that MeOH (IC_{50}= 12.32 μg/mL) and acetone extracts of shells (IC_{50}= 11.01 μg/mL) were potent antioxidant power than that of roots in DPPH radical scavenging activity.

Table 3. Radical Scavenging Activity of Crude Extract of Shells and Roots of Peanut (*Arachis hypogaea* L.)

Sample	% RSA±SD at Different Concentration (μg/mL)							
	3.125	**6.25**	**12.5**	**25**	**50**	**100**	**200**	**400**
EtOH (S)	3.02 ±1.82	16.86 ±0.75	21.19 ±1.13	33.64 ±2.40	58.93 ±3.80	83.60 ±2.54	89.02 ±0.67	89.10 ±0.80
MeOH (S)	15.17 ±0.96	25.58 ±1.15	50.72 ±3.19	77.08 ±1.15	80.95 ±3.38	83.61 ±3.96	84.94 ±2.38	86.49 ±2.19

Sample	% RSA±SD at Different Concentration (µg/mL)							
	3.125	**6.25**	**12.5**	**25**	**50**	**100**	**200**	**400**
AC (S)	19.92 ±1.62	29.85 ±2.08	56.29 ±1.51	86.53 ±2.99	90.20 ±3.55	89.82 ±3.44	89.25 ±4.11	89.25 ±1.42
EtOH (R)	0.92 ±1.59	17.58 ±2.13	13.30 ±3.11	16.44 ±2.12	32.72 ±3.93	40.29 ±0.93	69.19 ±2.12	85.55 ±1.58
MeOH (R)	16.18 ±2.46	21.18 ±1.88	15.73 ±1.29	27.82 ±2.36	38.11 ±1.39	66.59 ±3.29	87.17 ±1.26	91.28 ±2.39
AC (R)	1.98 ± 4.12	12.34 ±2.57	23.10 ±4.11	44.03 ±2.52	82.51 ±1.49	89.31 ±3.69	89.97 ±2.46	89.57 ±4.12

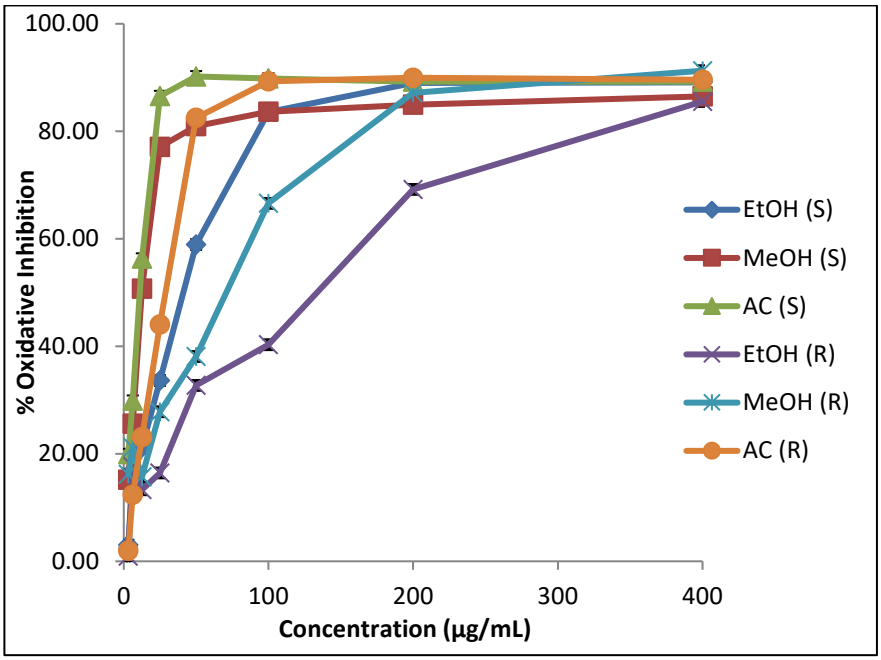

Figure 2. % RSA of crude extract of shells and roots of peanut (*Arachis hypogaea* L.)

Table 4. % RSA of Crude Extract of Shells and Roots of Peanut (*Arachis hypogaea* L.)

No.	Sample	IC_{50} (µg/mL)
1	EtOH (S)	41.19
2	MeOH (S)	12.32
3	AC (S)	11.01
4	EtOH (R)	133.59
5	MeOH (R)	70.94
6	AC (R)	28.88

The selected samples were potent antioxidant power. It can assume that the samples may have the power against UV radiation. Although acetone extract was most potent antioxidant power, ethanol extract was applied to formulate sunscreen lotions since it was commonly used to ethanol in UV spectrophotometer. After formulating the sunscreen lotions containing ethanol extracts of shells and roots of peanuts, *in vitro* sun protection factor was evaluated. The absorbance values at various wavelengths from 290 to 320 nm with 5 nm interval of both formulated sunscreen lotions are given in Table 5.

Table 5. Absorbance Values of the Formulated and Marketed Sunscreen Lotions

Wavelength (nm)	**F-1**	**F-2**	**SPF22(NIVEA)**
290	0.331	0.245	3.018
295	0.299	0.204	3.016
300	0.293	0.202	3.011
305	0.291	0.204	3.005
310	0.289	0.206	3.001
315	0.282	0.203	2.749
320	0.273	0.197	2.621

F-1 and F-2= Formulated sunscreen lotion containing ethanol extract of peanut shells and roots.

The SPF values of formulation F-1, F-2 and the marketed sunscreen lotion were calculated and presented in Table 6. As the formulations with ethanol extracts were found to possess SPF in the range of 5 to 10, they can be used for normal skin to prevent sun burns, medium skin and dark skin rely on the length of prevention time to protect suntans and sunburns.

Table 6. SPF of the Formulated Sunscreen Lotions

Sr No.	Sunscreen Lotions	SPF
1	F-1	8.1
2	F-2	6.5
3	Marketed lotion NIVEA with SPF 22	21.8

Table 7. Skin Irritation Test on Albino Rats

Sunscreen lotions	Sensitivity	Edema	Erythema
F-1	no	no irritation	no irritation
F-2	no	no irritation	no irritation

The skin irritation test of sunscreen lotions containing ethanol extracts of the two samples was performed on albino rats. It was shown no sign of sensitivity, erythema and edema and is described in Table 7 and Figure 3. Therefore, the prepared formulations may be considered to be safe. The formulated sunscreen lotions may be capable to block the UV-radiation and protect the skin from sunburn.

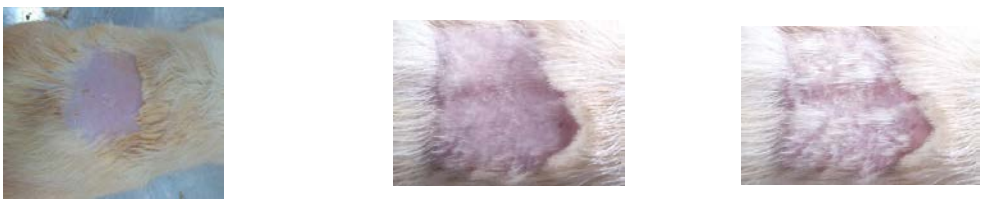

Before applying | After one week | After two weeks

Figure 3. The skin irritation test performed on albino rats

Conclusions

From this study on chemicals and bioactivity investigation of shells and roots of peanut, the following inferences can be concluded.

Antioxidant activity of the peanut shells was more activity than the peanut roots. Due to the available natural antioxidants, they were used for relieving coughs, decreasing blood pressure and preventing carcinogen. And then they were used for ingredients in cosmetics and in skin problems like disease, aging, damage and disorders. In the preparation of formulations F-1 and F-2 and evaluation for SPF, this study reveals that using UV Spectrophotometer is the rapid, acceptable and reproducible method for the evaluation of efficacy of sunscreen lotions. The skin irritation test of the formulations F-1 and F-2 showed good handling and

glow of the skin. It can be concluded that the present research might hopefully apply in the treatment of sun burns causing effects of UV rays.

Acknowledgements

I would like to express my gratitude to Dr Ni Ni Than, Professor and Head, Department of Chemistry, University of Yangon for giving the permission to submit this research paper and Dr Khin Thida Nyo, Associate Professor, Department of Chemistry, Mawlamyine University for her encouragement and good advice.

References

COLIPA. (2006). *COLIPA Guidelines*. International Sun Protection Factor (SPF) Test Method

Mansaur, J. S., M. N. Breder, M. C. Mansur and R. D. Azulay. (1986). "Determination of Sun Protection Factor by Spectrophotometry". *Anal Bras Dermatol*, **61**, 121–124

Mishra, A. K., A. Mishra and P. Chattopadhyay. (2011). "Herbal Cosmeceuticals for Photo Protection from Ultraviolet B Radiation: A Review". *Trop J. Pharm Res*. **10**(3), 351-360

Rasheed, A., S. N. Shama, S. Mohanalakshmi and V. Ravichandran. (2012). "Formulation, Characterization and *in vitro* Evaluation of Herbal Sunscreen Lotion". *Orient Pharm Exp Med*, **12**, 241-246

Santo, E. P., Z. M. Freitas, K. Z. Souza and S. Garcia. (1999). "*In vitro* and *in vivo* Determinations of Sun Protection Factors of Sunscreen Lotions with Octyl Methoxycinnamate". *Int. J. Cos. Sci.*, **21**, 1–5

Sayre, M. R., J. Stanfield, D. L. Lott and J. C. Dowdy. (2003). "Simplified Method to Substantiate SPF Labelling for Sunscreen Products". *Photodermatol Photoimmunol Photomed*, **19**, 254–260

Sim, E. W. (2011). *Isolation and Determination of Anti-Nutritional Compounds from Root and Shells of Peanut (Arachis Hypogaea)*. Malaysia, A project of Bachelor of Science (Hons) Biochemistry, Department of Chemical Science, University of Tunku Abdul Rahman, 8-12

Singh, S. and N. Sharma. (2017). "Herbal Sunscreens and Photo Protection Compositions: A Patent Review". ISSN: 2574-7797. *J Pharm Res*. **1**(8), 1-4

Wilkinson, J. B. and R. J. Moore. (1982). *Sunscreen, Suntan and Anti-sunburn Products*, Harry's Cosmeticology, Chemical Publishing New York, 7th ed., 222-263

Value Added Bioplastics from Biomass Waste

Hnin Yu Wai[1], Yamin Ko[2] & Cho Cho[3]

Abstract

The present work is concerned with the preparation and characterization of bioplastics. Jackfruit seeds were collected from Hledan Market, Kamayut Township, Yangon Region, Myanmar. Jackfruit seeds were washed with distilled water and peeled the thin brown seed coats. Then, they were cut into small pieces and dried in oven at 80 °C for 2 h. They were grained and screened to get the dried jackfruit seed powder (JS). The physicochemical properties (such as moisture content, ash content, bulk density, and pH) of prepared samples were determined by conventional methods and these samples were characterized by modern techniques such as FT IR, SEM and TG DTA analyses. The starch content in jackfruit seed powder was detected by conventional method. The yield percent of the starch from jackfruit seed powder is 58 %. Bioplastics were prepared from various proportions of jackfruit seed starch using 0.5 mL of sorbitol as plasticizer. The most favorable conditions for preparing bioplastic namely (JSB 5) was found to be 4 g of jackfruit seed powder starch with 0.5 ml of sorbitol and 2 ml of acetic acid, was the most suitable for preparing bioplastic. It was found that the bioplastic (JSB 5) possesses tensile strength (3.50 MPa), elongation at break (45.30 %) and tear strength (48.54 kNm^{-1}). The preparaed bioplastic JSB 5 was characterized by FT IR, SEM and TG DTA analyses. All prepared bioplastics showed plain, clear, smooth surface, flexible, highly transparent and light white colour. The prepared bioplastics can be used in making utensils.

Keyword: starch, bioplastic, physicochemical, sorbitol

Introduction

In daily life, plastics are used almost everywhere in the world for various purposes because plastics are inexpensive, readily available, durable and versatile. However, the main raw material in producing plastics derived from petroleum is declining and non-renewable. In addition, the plastics

[1] Lecturer, Department of Chemistry, University of Yangon

[2] MSc Student, Department of Chemistry, University of Yangon

[3] Professor, Dr.,Department of Chemistry, University of Yangon

cannot be destroyed quickly and naturally by destructive microbes in the soil, this causes the accumulation of waste, pollution and environmentally damage. The environmental, economic and safety challenges have prompted many scientists to replace part of a petrochemical-based polymer with another biodegradable type called bioplastics (Lubis *et al*., 2018).

Bioplastics can be made from many different sources and materials such as plant oil, cellulose, starch sugarcane, weeds hemp etc. Bioplastics are a form of plastic made from renewable biomass, instead of the conventional plastic that derived from petroleum. It can be divided into two groups which are biodegradable plastic or bio-based. Biodegradable plastic is made up of fossil materials while bio-based plastic is synthesized from biomass or renewable resources. An alternative for a low cost and a renewable substrate has been proposed by using agriculture waste. Bioplastic is very important to use because it is able to maintain a sustainable environment and to prevent the disposal synthetic plastic waste that damaging the ecology included the lands, waterways, and air pollution from plastic combustion (Richard *et al*., 2011).

Starch is used in its raw state or further processed by bacterial fermentation to produce bio-based monomers, which are polymerized into bioplastics. Food packaging has especially been one of the most quickly developed markets for starch-based bioplastics. Today, starch-based bioplastics can be found in packaging, food services, agriculture, automotive and consumer goods, and this range is only increasing. In the production of starch-based bioplastics, the different proportions and additives were tested to observe and compare the durability, flexibility and resistance to humid of the outcome products (Mohapatra *et al*., 2014). Starch use is extended also in non-food industries: it is used for adhesives and rubbers production, as a cement additive to reduce the stabilization time; in paper and textile industry as filling agent and to improve the ink adhesion; it is used also as a bulking agent, humectant and thickening agent in the formulation of cosmetic and pharmaceutical products. Not least is its use in the production of plastic products and for food packaging, food containers and cutlery and agriculture (Mathew *et al*., 2008).

Jackfruit (*Artocarpus heterophyllus* Lam) is popular fruit crop that is widely grown in Thailand and other tropical areas. The ripe fruit contains well flavored yellow sweet bulbs and seeds (embedded in the bulb). The edible bulbs of ripe jackfruit are consumed fresh or processed into canned

products. Many products develop from jackfruit that are candy, finger chips, fruit bars, fruit leather, halvah, papad, ready to serve beverages, toffee and ice-cream (Bobbio *et al.,* 1978). Jackfruit (*Artocarpus heterophyllus* Lam) is the largest borne tree fruit in the world. The name derives from the Greek words ‘artos’ means bread and ‘karpos’ means fruit, this fruit are commonly called breadfruit. The family of jackfruit is Moraceae, is native from India, but it is National fruit of Bangladesh.

Jackfruit is indigenous food crop, it contains some vitamins like vitamin A, vitamin C, thiamine, riboflavin also some minerals like calcium, potassium, iron, sodium, zinc and niacin also many other nutrients. Jackfruit has a very low calories content that is 100 g of jackfruit contains only 94 calories (Baliga *et al*., 2011). Jack fruit is a highly nutritious seasonal food. Edible bulb of jack fruit after fully ripening is rich in carbohydrate, protein, fiber, calcium, phosphorus, besides fructose, glucose and sucrose are the major sugars present in jack fruit. Some major fatty acids found in jackfruit are palmitic, oleic, stearic, linoleic, lauric, arachidic. Jackfruit contains phytonutrients like lignans, isoflavones, and saponins that shows some health benefits that are wide ranging from antiulcer, antibacterial, antioxidant, anti-inflammatory and antihypertensive. The unripe and ripe edible parts of jackfruits have good amount of phenolic acids and this have importance in human health (Singh *et al*., 2015).

Jackfruit seed has an oval or rounded shape, the length is 2-3 cm and diameter is1-1.5 cm, 500 to 550 seeds found in each jackfruit. It contains starch, dietary fiber, protein, carbohydrate, iron, potassium, sodium, copper and manganese. It is treated by diarrhea and dysentery, good for hair growth and healthy blood circulations and healthy digestion. Jackfruit seeds have some pasting, antioxidant properties. Jackfruit seeds mostly do not used as vegetable. It is eaten whole by boiling or roasting. Also, it contains same composition as like grains. The two lectins found in jackfruit seeds which have been proved to evaluation of immune status (Abraham *et al*., 2014).

Materials and Methods

The chemicals used in the experimental work were from British Drug House Chemical Ltd., England. In all the investigations, the recommended and standard procedures of both conventional and modern techniques were employed. The experiment was carried out in the Physical Chemistry Research Laboratory of the Department of Chemistry, and FT IR

spectra was measured at the Department of Chemistry, University of Yangon and SEM micrograph and TG DTA as at Universities Research Center. The apparatus consists of conventional laboratory glass ware and modern equipment. Some of the instruments used in the experiments are Balance (Precision Balance, AWS, PN-2100A, China), Magnetic Stirrer Oven (Universal Oven, Memmert, UFB-400, Germany), Furnace (Thermo scientific, USA), melamine plate, FT IR (Fourier Transform Infrared Spectrophotometer, Shimadzu, IR Prestige-21, Japan), SEM (Scanning Electron Microscope, Evo-18, Brandi cars ZEISS, Germany) and DTA-60H (Hi-TGA 2950) thermal analyzer .

Collection of Samples

In the experiments, Jackfruit seeds were collected from Hledan Market, Kamayut Township, Yangon Region, Myanmar.

Preparation of Jackfruit Seed Powder

Jackfruit seeds were washed with distilled water and peeled the thin brown seed coats. Then, they were cut into small pieces. The cut pieces were washed thoroughly with distilled water to remove dust and impurities. After cleaning the sample; it was dried at room temperature. The dried sample was then ground in a mechanical grinder and screened through a sieve to obtain fine power of uniform particle size. The sieved material was then stored in an airtight plastic bottle for further experiment.

Physicochemical Properties of Jackfruit Seed Powder

The physicochemical properties (moisture content, ash content, bulk density, and pH) of prepared samples were determined by conventional methods (Table 1).

FT IR analysis

FT IR analysis was performed in order to characterize the functional groups of samples. A Perkin-Elmer Spectrum GX, USA was used for FT IR analysis. The FT IR spectrum of jackfruit seed powder (Figure 1) and the description data (Table 2) were given.

SEM analysis

The morphology of prepared jackfruit seed powder was studied by using Scanning Electron Microscope (JSM-5160, JEOL Ltd., Japan) for analysing micro and macro pores present on the surface of the samples. The scanning electron micrographs of jack fruit seed powder (Figure 2) were presented.

TG DTA Analysis

Thermal analysis of jack fruit seed powder was determined by a DTA-60H (Hi-TGA 2950) thermal analyzer. TG DTA thermogram (Figure 3) and the description data (Table 3) are presented.

Preparation of Starch

The jackfruit seed powder (5 g) was mixed with 100 mL distilled water, soaked and stirred until 3 h to 4 h. The resulting slurry was filtered on a clean cloth, the sediment washed with distilled water for 3 times. They were combined and precipitated at overnight. The crude starch was obtained; they were cleaned with distilled water and filtered with filter paper. And then, 2-3 days dried in the room temperature, was obtained the starch. The starch content in jackfruit seed powder was prepared by conventional method. The yield percent of the starch from jackfruit seed powder was 58 %.

Preparation of Bioplastics

In this research, all of bioplastics were prepared by blending casting method.

On the Aspect of the Preparation of Bioplastics (JSB)

Various weights (2, 2.5, 3, 3.5, 4, 4.5 g) of jackfruit seed powder starch was dissolved in each 50 mL of hot distilled water. They were obtained the starch solution, added 0.5 mL of sorbitol as plasticizer and 2 mL of acetic acid. The solution was stirred on the magnetic stirrer at 70 °C for 15 min. The solution was casted onto cleaned and dried melamine plate at room temperature. And then, allowed to air dry for 3 days.

Determination of the Physicomechanical Properties of Bioplastics (JSB)

The physicochemical and physicomechanical properties (thickness, tensile strength, elongation at break, and tear strength) of the prepared bioplastics were determined by the conventional method and modern techniques. The description data (Table 4 and Figures 4, 5 and 6) are presented.

Determination of the Water Uptake Properties of Bioplastics (JSB)

The water uptake of the prepared bioplastics (Figure 7) and the description data (Table 5) are presented.

Determination of the Degree of Swelling Properties of Bioplastics (JSB)

The degree of swelling of the prepared bioplastics (Figure 8) and the description data (Table 6) are presented.

Characterization of the JSB 5 Bioplastic

FT IR analysis

The FT IR spectrum of JSB 5 bioplastic (Figure 9) and the description data (Table 7) were given.

SEM analysis

The scanning electron micrograph of JSB 5 bioplastic was presented in Figure 10.

TG DTA Analysis

Thermal analysis of JSB 5 bioplastic was determined by a DTA-60H (Hi-TGA 2950) thermal analyzer. TG DTA thermogram (Figure 11) and the description data (Table 8) are presented.

Determination of Biodegradation

Soil Burial Test

Biodegradation of prepared bioplastic was determined by soil burial test examining the morphology changes. Sample geometry on degradation was also recorded by photo (Figure 12).

Results and Discussion

Table 1 show that the physicochemical properties (moisture content, ash content, bulk density, and pH) of the jack fruit seed powder determined by the conventional methods. It can be observed that moisture content of the jack fruit seed powder f is 8.53 %, ash content is 1.70 %, solid content is 91.47 %, bulk density is 0.83 g mL^{-1} and pH is 6.86.

Table1. Physicochemical Properties of Jack Fruit Seed Powder

No.	Physicochemical properties	Quantity
1.	Moisture content (%)	8.53
2.	Ash content (%)	1.70
3.	Solid content (%)	91.47
4.	Bulk density (g mL^{-1})	0.83
5.	pH	6.86

Characterization of Jack Fruit Seed powder

FT IR analysis

The major constituent of the Jack fruit seed powder is starch. Starch content was also analysed by FT IR. FT IR spectrum of jack fruit seed powder (JS) (Figure 1) and the interpretation (Table 2) are given. The peaks were observed in the regions below 800 cm^{-1}, 800 to 1,500 cm^{-1} (the fingerprint region), the region 2973 cm^{-1} (C-H stretch region), and finally the region between 3277 cm^{-1}(O-H stretch region). The infrared spectrum of Polysaccharides was shown to be important in the structural elucidation of small molecules and also in polymer analysis where they represent structural units. The most frequently used IR spectral range in carbohydrate analysis was the anomeric region at 1000 cm^{-1}. Determination of the esterification degree of carbonyl groups of pectin by means of infrared spectroscopy was carried out at 1633 cm^{-1} for ester vs. carboxylate regions respectively.

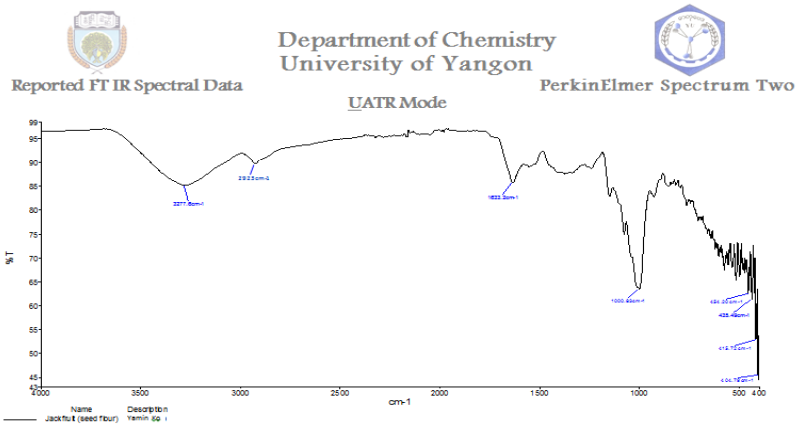

Figure1. FT IR spectrum of jack seed powder

Table 2. FT IR Band Assignment of Jack Seed Powder

Observed wavenumber (cm^{-1})	Literature wavenumber (cm^{-1})	Band assignment
3277	3100-3700	O-H (stretching)
2973	2850-2940	C-H (stretching)
1633	1550-1650	C=C (stretching)
	1600-1950	C=O (asymmetric stretching)
1000	1000-1300	C-O –C and C-OH (bending of ether, alcohols, sugars

*(Silverstein *et al*., 2003)

SEM analysis

Surface morphology of jack fruit seed powder was examined by SEM (Figure 2). It is obviously seen that bead like nature of JS is not similar in size.

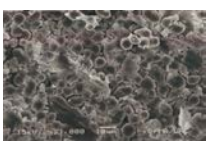

Figure 2. SEM photomicrograph of jack fruit seed powder

TG DTA analysis

Thermal stability of jack fruit seed powder (JS) (Figure 3) and the interpretation (Table 3) are given. Data showed four distinct weight losses: the first one corresponded to dehydration, the second to the thermal decomposition of organic compound of starch, the third to the degradation of organic compound of starch and the fourth to the carbonization.

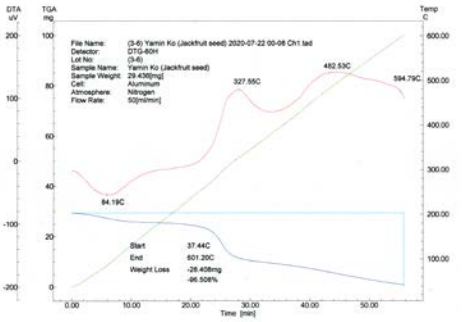

Figure 3. TG DTA thermogram of jack fruit seed powder (JS)

Table 3. Thermal Analysis Data of Jack Fruit Seed Powder

Sample	TG		DTA		Remarks
	Temperature range (ºC)	Weight loss (%)	Peak temperature (ºC)	Nature of peak	
JS	37-100	9.24	84.19	endothermic	Dehydration due to surface water
	100-340	55.65	327. 5 5	exothermic	Thermal decomposition of organic compound of jack fruit seed powder
	340-500	18.55	482.53	exothermic	Degradation of organic compound
	500-600	13.04	594.79	exothermic	Carbonization

On the Aspect of the Preparation of JSB Bioplastics
Determination of the Physicomechanical Properties of JSB Bioplastics

For all of the prepared bioplastics, physicomechanical parameters were determined. Among these parameters, tensile strength is more specific than other for determining bioplastics quality.

JSB 1, JSB 2, JSB 3, JSB 4, JSB 5 and JSB 6 bioplastics were prepared. The results of the physicochemical and physicomechanical properties of JSB 1, JSB 2, JSB 3, JSB 4, JSB 5 and JSB 6 bioplastics were presented (Table 4 and Figures 4, 5 and 6). The most favorable conditions for preparing bioplastic namely (JSB 5) was found to be with 4 g of jack fruit seed starch, 0.5 mL of sorbitol and 2 mL of acetic acid was the most suitable for preparing bioplastics .It was found that (JSB 5) has the highest tensile strength among them. Moreover, the water uptake tests of the bioplastics are also found to be satisfactory. The bioplastic JSB 5 has the equilibrium water uptake percentage among them (Table 4). Therefore, bioplastic JSB 5 was chosen to make the most suitable bioplastic.

Table 4. Physicomechanical Properties of JSB Bioplastics with Various Proportions of Jack Fruit Seed Powder Starch

Properties	**Jack Fruit Seed Starch Bioplastics**					
	JSB1	**JSB 2**	**JSB 3**	**JSB 4**	**JSB 5**	**JSB 6**
Thickness (mm)	0.15	0.20	0.23	0.25	0.27	0.30
Tensile strength (MPa)	1.30	1.80	2.40	2.70	3.50	3.20
Elongation at break (%)	13.20	20.40	26.10	34.60	45.30	42.70
Tear strength (kN/m)	14.50	21.80	30.67	42.37	48.54	43.35

JSB 1 = (2 g) JS + (50 mL) H_2O + (0.5 mL) sorbitol + 2 mL of acetic acid
JSB 2 = (2.5 g) JS + (50 mL) H_2O + (0.5 mL) sorbitol + 2 mL of acetic acid

JSB 3 = (3 g) JS + (50 mL) H_2O + (0.5 mL) sorbitol + 2 mL of acetic acid
JSB 4 = (3.5 g) JS + (50 mL) H_2O + (0.5 mL) sorbitol + 2 mL of acetic acid
JSB 5 = (4 g) JS + (50 mL) H_2O + (0.5 mL) sorbitol + 2 mL of acetic acid
JSB 6 = (4.5 g) JS + (50 mL) H_2O + (0.5 mL) sorbitol + 2 mL of acetic acid

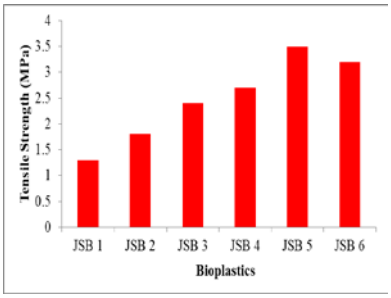

Figure 4. Tensile strength of JSB bioplastics

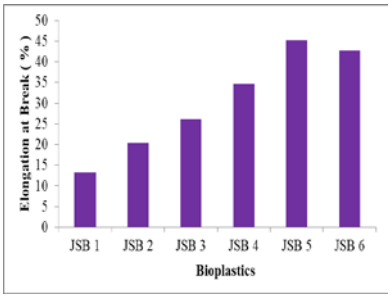

Figure 5. Elongation at break of JSB bioplastics

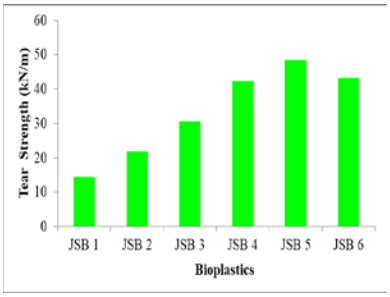

Figure 6. Tear strength of JSB bioplastics

Determination of Water Uptake Properties of JSB Bioplastics

The degree of water uptake was investigated with increasing immersion time. The water uptake was one of the most significant parameter when a bioplastic to be used as making utensils. The water uptake was the amount of water entrapped in the matrix including bound

water. The water absorption properties of JSB bioplastics were studied for varying time intervals such as 5 min, 10 min, 15 min, 20 min, 25 min and 30 min. The water uptakes as a function of time for JSB bioplastics were shown in Table 5 and Figure 7.

Table 5. Water Uptake of JSB Bioplastics

Bioplastics / Time (min)	Water uptake (%)					
	5	10	15	20	25	30
JSB 1	15.21	16.83	20.72	23.65	25.46	28.9
JSB 2	15.78	18.65	21.53	26.47	32.30	34.6
JSB 3	17.36	20.49	22.61	27.81	34.65	39.4
JSB 4	20.83	24.70	28.37	30.54	37.49	42.6
JSB 5	18.87	22.30	26.44	29.23	33.72	38.2
JSB 6	21.24	28.51	31.60	33.49	38.56	43.2

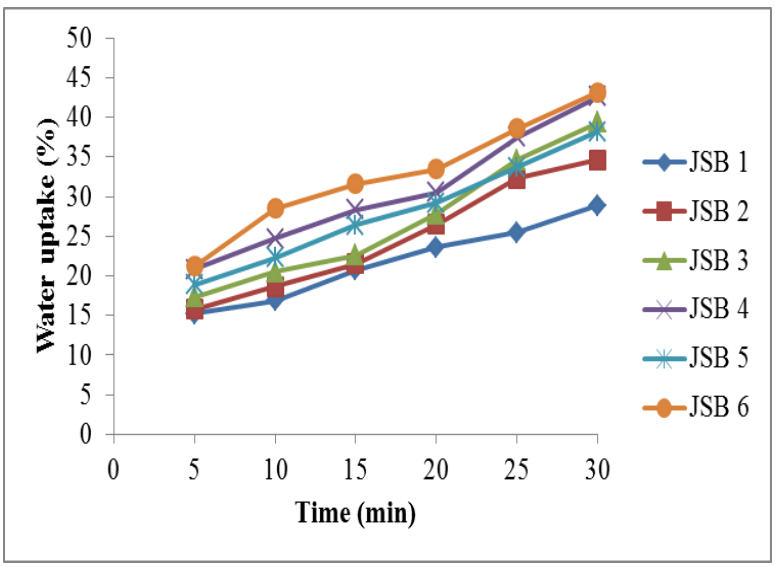

Figure 7. Water uptake of JSB bioplastic as a function of contact time

Determination of Degree of Swelling Properties of JSB Bioplastics

The degree of swelling of JSB bioplastic with different compositions was shown in Table 6 and Figure 8 as a function of immersion time in distilled water at room temperature. For a given blend composition time,

mostly the degree of swelling increased with increasing immersion time. The uptake of water from 5 min to 30 min was slightly difference for all prepared bioplastics.

Table 6. Degree of Swelling of JSB Bioplastics

Bioplastics / Time (min)	Degree of swelling (%)					
	5	10	15	20	25	30
JSB 1	12.2	12.8	15.7	17.6	20.4	26.9
JSB 2	15.5	18.6	20.5	22.4	26.0	28.6
JSB 3	19.3	22.4	25.6	27.3	24.2	32.4
JSB 4	22.1	24.7	27.3	29.5	32.4	34.6
JSB 5	21.4	23.0	26.5	28.6	30.8	33.2
JSB 6	25.4	28.0	31.5	33.6	37.8	40.2

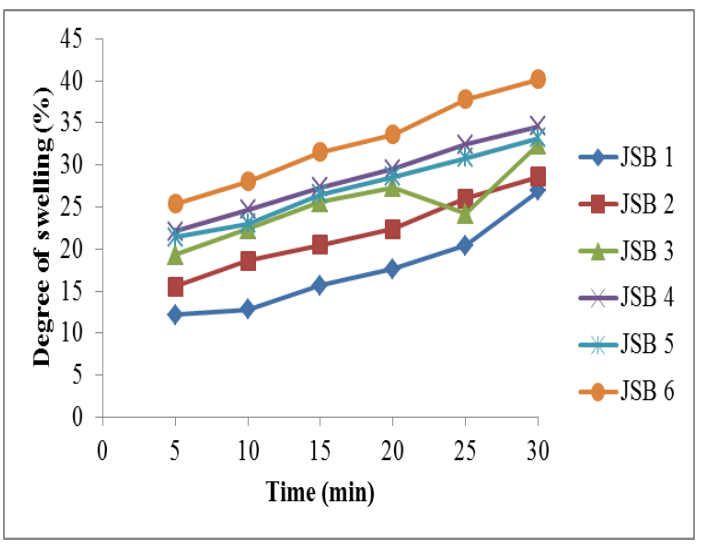

Figure 8. Degree of swelling of JSB bioplastic as a function of contact time

Characterization of JSB 5 Bioplastic

FT IR analysis

Figure 9 shows that the bands at 3271 $cm^{-1,}$ 2934 cm^{-1}, 1644 cm^{-1} may be due to O-H stretching, C-H stretching frequency of saturated hydrocarbon, C=O stretching, respectively. The characteristic peaks 1076

cm^{-1} and 1002 cm^{-1} indicate the C-O bond stretching of C-O-H group in the blends which means that the OH group of starch was involved in the hydrogen bond formation. This lead to conclude that the FT IR test for composition showed that sorbitol could form a more stable hydrogen bond. The interaction of polymer blends could be identified with FT IR spectrum.

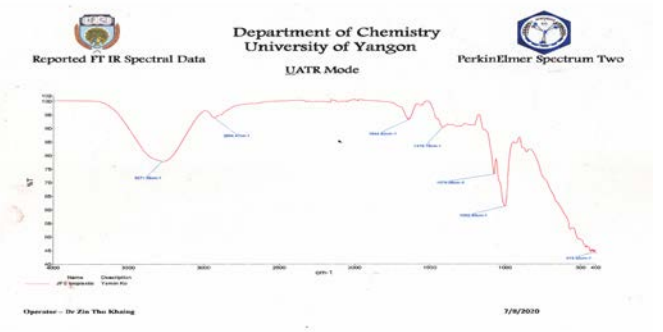

Figure 9. FT IR spectrum of JSB 5 bioplastic

Table 7. FT IR Band Assignment of JSB 5 bioplastic

Observed wavenumber (cm^{-1})	**Literature wavenumber (cm^{-1})**	**Band assignment**
3271	3200-3600	O-H (stretching)
2934	2850-2940	C-H (stretching)
1644	1600-1950	C=O (stretching)
1418	1260-1440	C-H (bending of CH)
1090,1024	1000-1125	C-O (stretching of C-OH)

* Silverstein *et al*., (2003)

SEM analysis

Surface morphology of JSB 5 bioplastic was examined by SEM (Figure 10). It illustrates that the JSB 5 bioplastic has an amorphous homogeneous matrix surrounds with predominant granular domains.

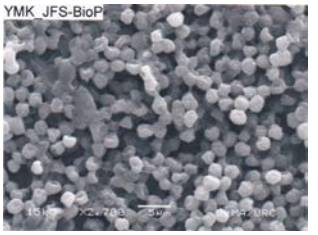

Figure 10. SEM photomicrograph of JSB 5 bioplastic

TG DTA analysis

Thermal stability of JSB 5 bioplastic (Figure 11) and the interpretation (Table 8) are given. Data showed three distinct weight losses: the first one corresponded to loss of volatiles (water and sorbitol), the second to the pyrolysis of starch and the third to the carbonization.

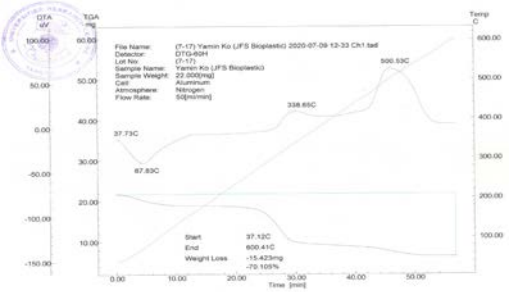

Figure 11. TG DTA thermogram of JSB 5 bioplastic

Table 8. Thermal Analysis Data of JSB 5 Bioplastic

Sample	TG		DTA		Remarks
	Temperature range (ºC)	Weight loss (%)	Peak temperature (ºC)	Nature of peak	
JSB 5	37-80	9.09	67.83	endothermic	Loss of volatiles (water and sorbitol)
	80-400	49.09	338.65	exothermic	Pyrolysis of starch
	400-540	12.72	500.53	exothermic	Carbonization

On the Aspect of Biodegradation

The environment friendly degradable plastic has been developed by using the jack fruit seed starch with the sorbitol as plasticizer. One of the objectives of development of JSB 5 bioplastic is to make easy throw away materials from degradable plastic to alleviate waste disposal problems by means of environmental degradation. In this work, biodegradation of bioplastics were tested by soil burial method actual condition of waste disposal. Uniformly sized samples were buried in the soil from waste disposal. The physical appearance of bioplastics buried in the soil is shown in Figure 12. Figure shows biodegradation nature of JSB 5 bioplastic for 2 days interval. These figures clearly showed significant deformation of bioplastics observed at bioplastics at each investigation period.

(a) (b) (c) (d) (e)

Figure 12. The physical appearances of JSB 5 bioplastic
(a) Before burial test (b) After two days (e) After four days
(c) After six days (d) After eight days

Some Possible Application of Prepared JSB Bioplastic

The prepared JSB bioplastics will be widely used in making utensils and packaging materials. The photographs of JSB bioplastic film are presented (Figure 13) and the photograph of the bioplastic product is shown (Figure 14).

Figure 13. JSB bioplastic

Figure 14. Bioplastic product

Conclusion

JSB bioplastics were prepared by blending, casting technique. According to the physicomechanical properties, 4 g of starch was found to have optimal composition. Bioplastics prepared 4 g of jack fruit seed starch (namely JSB 5) bioplastic possess 3.50 MPa of tensile strength, 45.30 % of elongation at break and 48.54 kNm^{-1} of tear strength. All prepared JSB bioplastics showed plain, clear, smooth surface, flexible, highly transparent and light white colour. The prepared JSB bioplastics will be widely used in making utensils.

Acknowledgements

The authors would like to thank the Department of Higher Education (Lower Myanmar), Ministry of Education, Yangon, Myanmar, for the permission of doing this research and University of Research Journal for allowing the writing of this paper. I would like to express my sincere thanks to Dr. Ni Ni Than (Professor and Head), Department of Chemistry, University of Yangon, for her kind advice, guidance and permission to allow this research work. Thanks, are also due to the Rubber Research and Development Centre for the necessary research testing and Universities' Research Center (URC) for FT IR, SEM and TG DTA.

References

Abraham, A. and J. Jayamuthunagai.(2014). "An Analytical Study on Jackfruit Seed Flour and Its Incorporation in Pasta". *J. Pharm., Biol. and Chem. Sci*, vol. **4**, pp 3-15

Bobbio, F. O., A. A. Dash and L. R. Rodrigues. (1978). "Isolation and Characterization of Physicochemical Properties of the Starch of Jackfruit Seed (*Artocarpus heterophyllus*)". *J. Cereal Chem.*, vol. **55**, pp 45-60

Baliga, M. S., A. R. Shivashankara, R. Haniadka, J. Dsouza and H. P. Bhat. (2011). "Phytochemistry, Nutrition and Pharmacological Properties of *Artocarpus heterophyllus* Lam (Jackfruit): A Review". *Inter. Res. J. Food*, vol. **44**, pp18-48

Lubis, M., A. Gana, S. Maysarah, M. H. S. Ginting and M. B. Harahap. (2018). "Production of Bioplastic from Jackfruit Seed Starch (*Artocarpus heterophyllus*) Reinforced with Microcrystalline Cellulose from Cocoa Pod Husk (*Theobroma cacao* L.) Using Glycerol as Plasticizer". *Inter. J. Mater. Sci. and Eng.*, vol. **9**, pp 1-21

Mathew, S. and T. E. Abraham. (2008). "Characterization of Ferulic Acid Incorporated Starch-Chitosan Blended Films". *J. Food Hydrocoll*, vol. **22**, pp 20-28

Mohapatra, A., S. Prasad and H. Sharma. (2014). "Utilization of Mango Seed Starch in Manufacture of Bioplastic Reinforced with Microparticle Clay Using Glycerol as Plasticizer". *J. Mater. Sci. and Eng.*, vol.**13**, pp 10-22

Richard, C., K. Martin and S. Jim. (2011). "Bioplastics: Environmentally Applied Packaging Technology". *Inter. J. Appl. Sci*, vol. **11**, pp 10-20

Silverstein, R. M., F. X. Webster and D. J. Kiemle. (2003). "Spectrometric Identification of Organic Compounds". *J. Environ. Sci.*,vol. **20**, pp 15-42

Singh, A., S. Maurya, M. Singh and U. P. Singh. (2015). "Studies on the Phenolic Acid Contents in Different Parts of Raw and Ripe Jackfruit and Their Importance in Human Health". *Inter. J. Appl. Sci.*, vol. **3**, pp 2-15

Enzymic Studies on Polyphenol Oxidase from *Ipomoea batatas* (L.) Lamk (Sweet Potato)

Thida Maw[1], Hein Htet Oo[2] & Ye Myint Aung[3]

Abstract

The enzymic studies on polyphenol oxidase (PPO) were conducted to isolate from browning potent *Ipomoea batatas* (L.) Lamk (Sweet Potato). The sweet potato sample was collected from Pathein Myoma market, Ayeyarwady Region. PPO was extracted from sweet potato by extraction with phosphate buffer at pH 6.8. Crude PPO extracted solution (75 mL) was obtained from 100 g of sweet potato sample. In this work, catechol was used as substrate and a spectrophotometric assay method was applied for the determination of PPO activity by measuring the absorbance at 420 nm. The parameters such as pH, temperature, pH stability, and thermostability for enzyme-catalyzed reaction were necessarily studied by measuring the product *o*-quinone concentration. The optimum pH and optimum temperature of the PPO enzyme were 6.5 and 37 °C, respectively. The pH stability and thermostability of the PPO enzyme were studied at different pH and temperatures. In this research, the crude PPO enzyme was applied for dye removal activity from wastewater of the local textile service.

Keywords: sweet potato, polyphenol oxidase, thermostability, temperature

Introduction

Ipomoea batatas (L.) Lamk, commonly known as sweet potato belonging to the family Convolvulaceae, is an important root vegetable that is large, starchy, and sweet-tasting (Ray and Ravi, 2005). *I. batatas* have played an important role as an energy and phytochemical source in human nutrition and animal feeding. Sweet potato, which originated in Central America, is now widely cultivated and consumed throughout the world. Among the root and tuber crops grown in the world, sweet potato ranks second after cassava. The storage roots are the commercial part of the sweet potato plant.

[1] Associate Professor, Dr, Department of Chemistry, Pathein University
[2] MSc Student, Department of Chemistry, Pathein University
[3] Professor and Head, Dr, Department of Chemistry, Pathein University

The plant has significant medicinal importance and various parts of the plant are used in traditional medicine. The leaves are simple and spirally arranged alternatively on the stem (Remya and Subha, 2009). Their color can be green, yellowish-green, or can have purple pigmentation in part or all of the leaf blades.

Classification of Sweet Potato (Yellow)

Scientific name	: *Ipomoea batatas* (L.) Lamk
Myanmar name	: Kazun-u
English name	: Sweet potato
Family	: Convolvulaceae
Part used	: Tuber

Figure 1. Sweet potato plant

Figure 2. Sweet potato tuber

Nutritional Value and Medicinal Potentials

Sweet potato is high in nutritional value, with the exception of protein and niacin (vitamin B_3) (Remya and Subha, 2009). Roots are a valuable source of carbohydrates, vitamins, and minerals. It has a superior ability to raise blood levels of vitamin A. This benefit may be particularly true for children.

In traditional medicine, sweet potato has been used to treat many diseases such as oral infections, and inflammatory diseases and also in the

management of diabetic conditions (Anbuselvi and Balamurugan, 2014). Sweet potato has the potential of lowering blood glucose levels. In some animal and human studies, different forms of sweet potato have been reported to help in maintaining blood sugar levels and lowering insulin resistance.

Enzyme

Enzymes are complex protein molecules, often called biocatalysts, which are produced by living cells (Berg *et al*., 2002). They are highly specific both in the reactions that they catalyze and in their choice of reactants, which are known as substrates.

Enzymes typically have common names (often called 'trivial names') which refer to the reaction that they catalyze, with the suffix -ase (e.g., oxidase, dehydrogenase, carboxylase), although individual proteolytic enzymes generally have the suffix -in (e.g. trypsin, chymotrypsin, papain) (Robinson, 2015).

Enzymatic activity depends on a number of factors (Chandra *et al*., 2014). The most important factors that affect enzyme activity are enzyme concentration, the amount of specific enzyme-substrate, pH of the reaction medium, temperature, and the presence of activators and inhibitors.

All enzymes are described by a four-part Enzyme Commission (EC) number. The first part of the EC number refers to the reaction that the enzyme catalyzes. The remaining digits have different meanings according to the nature of the reaction identified by the first digit.

Polyphenol Oxidase Enzyme

Polyphenol oxidase, PPO (EC 1.10.3.1) is a Cu-containing enzyme that is also known as tyrosinase, diphenol oxidase, *o*-diphenolase, and catechol oxidase, catecholase, phenolase (Martinez and Whitaker, 1995).

Polyphenol oxidase catalyzed the oxidation of several phenols to *o*-quinones (Oliveira *et al*., 2011). In turn, *o*-quinones are highly reactive molecules that can undergo non-enzymatic secondary reactions to form brown complex polymers known as melanin and cross-linked polymers with protein functional groups.

Application of Polyphenol Oxidase

Polyphenol oxidase enzymes have different applications in many areas such as food, medicine, and industry (Motoda, 1979).

In food processes, polyphenol oxidases have been mainly used to the enhancement of the flavor of tea, coffee, and cocoa. Browning of the edible part is due to the presence of PPO in fruits and vegetables, which is undesirable and can lead to unpleasant sensory qualities and losses in nutrient quality (Umesh *et al*., 2011). PPO also plays an important role as an efficient reagent for the cleaning of wastewater-containing polyphenols.

In medicine, polyphenol oxidases are used for the prevention of bacterial adhesion, treatment of Parkinson's disease, and control of melanin synthesis.

In industrial applications, polyphenol oxidases are mainly used for the elimination of toxic wastes (Edward *et al*., 1998).

Materials and Methods

Polyphenol oxidase (PPO) was extracted from sweet potatoes by using sodium chloride and sodium phosphate buffer (pH 6.5) solutions, centrifugation method, and stored at 4 °C. The polyphenol oxidase catalyzed the oxidation of catechol and gives *o*-quinones as products. Therefore, the activity of the polyphenol oxidase enzyme was followed by measuring the absorbance at 420 nm related to *o*-quinones. The enzymic properties such as pH, pH stability, temperature, and thermostability of PPO were studied by using the spectrophotometric method. From the pH stability and thermostability studies, PPO activities were determined for the different incubation periods. The application of crude PPO enzyme was carried in the local textile service.

Results and Discussion

Extraction of Crude PPO Enzyme from Sweet Potato

In the presence of atmospheric oxygen and polyphenol oxidase (PPO, EC-1.10.3.1), monophenol is hydroxylated to *o*-diphenol (monophenol oxidase activity) and diphenol can be oxidized to *o*-quinones (diphenol oxidase activity), which then undergoes polymerization to yield dark brown polymers (Fang, 2007).

In this research, crude PPO was extracted from sweet potato samples obtained from Pathein Myoma Market, Ayeyarwady Region. The extracted PPO (75 mL) was obtained from 100 g of sweet potato samples and this crude enzyme solution was stored at 4°C for the determination of enzymic properties. And then PPO activity was determined by the spectrophotometric method.

Optimum pH for Crude PPO-Catalyzed Reaction

Enzymes are extremely sensitive to pH fluctuations, and each enzyme performs optimally within a narrow range known as its optimum (Robinson, 2015). Enzyme stability and catalytic efficiency are pH-dependent parameters of polyphenol oxidase that attract the greatest attention. In all enzymatic investigations, control the pH by the addition of a suitable buffer, although the type of buffer may influence the optimum pH. The buffer system used will often affect the overall activity of an enzyme and may alter pH optimum. Most enzymes have a characteristic optimum pH at which the velocity of the catalyzed reaction is maximal and above and below which the velocity declines. The pH profile is dependent on a number of factors.

The effect of pH on polyphenol oxidase activity was studied in the range of pH from 5.0 to 8.0 (Table 1 and Figure 3). The figure showed the optimum pH found at pH 6.5 for the PPO enzyme. It was found that at pH 6.0 and 7.0, the activity of the PPO enzyme from sweet potato decreased to 38.3 % and 24.5 %, respectively.

Table 1. Relationship between Crude PPO Activity and pH of the Solution

pH	Absorbance at 420 nm	PPO activity × 10^2 (μ mol min^{-1} mL^{-1})
5.0	0.252	1.260
5.5	0.336	1.680
6.0	0.469	2.345
6.5	0.760	3.800
7.0	0.574	2.870
7.5	0.268	1.340
8.0	0.180	0.900

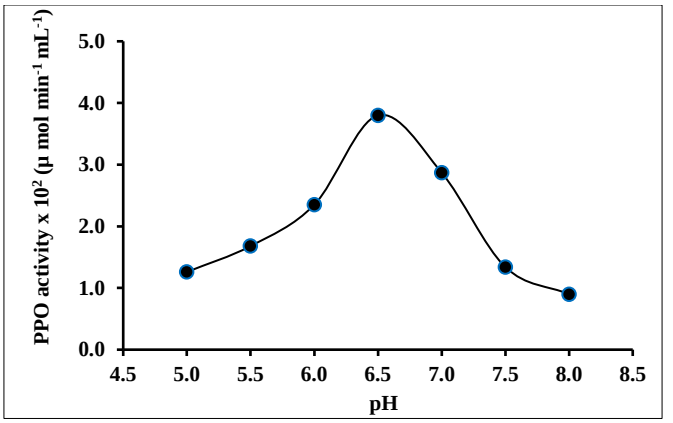

Figure 3. Plot of crude PPO activity as a function of pH of the solution

pH Stability of Crude PPO Enzyme at Different pH Values

The pH stability is determined by pre incubating the enzyme at various pH values for a fixed time (Sawhney and Singh, 2000). The pH stability curves are applied to distinguish reversible pH-dependent processes. Enzyme activity exhibits a significant dependence on the pH value of the medium.

The pH stability of PPO activity was studied by pre-incubating the crude enzyme in sodium phosphate buffer solutions with various pH values (6.0, 6.5, and 7.0) at various incubation times of 0, 30, 60, 90, 120, 150, and 180 min (Figure 4). It was found that the polyphenol oxidase activity at pH 6.5 was relatively stable, whereas, at pH 6.0 and 7.0, PPO activity decreased about 44.7% and 65.2% of original activity for 180 min incubation.

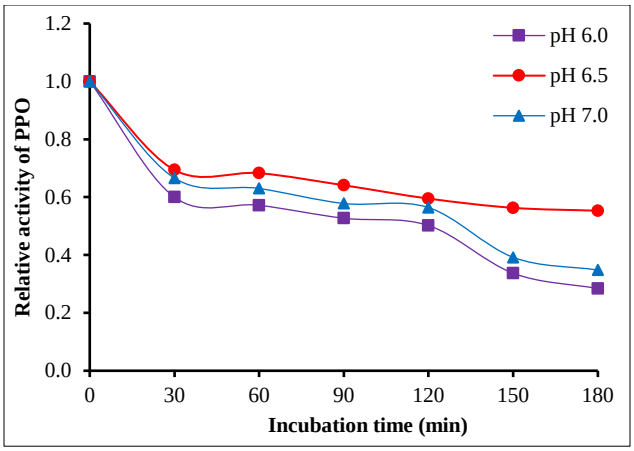

Figure 4. Plot of the relative activity of crude PPO as a function of incubation time at different pH values

Optimum Temperature for Crude PPO-Catalyzed Reaction

Enzyme-catalyzed reactions are influenced by temperature (Charles *et al.*, 2007). The rate of an enzyme-catalyzed reaction increases as the temperature of the reaction medium increases, but only up to a point. For every enzyme, there is one temperature at which the reaction rate will be at a maximum and that temperature is called the optimum temperature for that enzyme.

The effect of the temperature on the PPO activity was investigated at a temperature ranging from 17-77°C. The optimum temperature for the PPO enzyme was found to be 37°C. It was found that the activity of the PPO enzyme increased from 17-37°C and then decreased from 47-77°C (Table 2 and Figure 5).

Thermostability of Crude PPO Enzyme at Different Temperatures

Thermal denaturation is time-dependent and for an enzyme, the term optimum temperature has little real meaning unless the duration of exposure to that temperature is recorded (Robinson, 2015). The thermal stability of an enzyme can be determined by first exposing the protein to a range of temperatures for a fixed period of time and subsequently measuring its activity at one favourable temperature. At high temperatures, the enzyme is less stable.

Thermostability of PPO activity was studied using a particular pH of 6.5 at different temperatures 27, 37, and 47℃ for various incubation times of 0, 30, 60, 90, 120, 150, and 180 min (Figure 6). And then the residual activity of the PPO enzyme was measured. 37 °C, the PPO activity was retained about 57.7 % of its original activity. At 27 °C and 47 °C, the PPO activities were decreased by 68.3 % and 79.0 % for 180 min incubation.

Table 2. Relationship between Crude PPO Activity and Temperature of the Solution at pH 6.5

Temperature (°C)	**Absorbance at 420 nm**	**PPO activity × 10^2 (μ mol min^{-1} mL^{-1})**
17	0.225	1.010
27	0.292	1.660
37	0.385	2.050
47	0.268	1.48.5
57	0.221	0.555
67	0.097	0.410
77	0.080	0.150

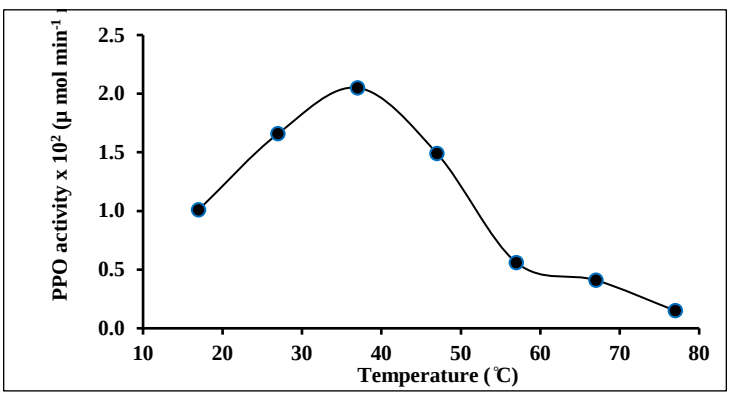

Figure 5. Plot of crude PPO activity as a function of the temperature of the solution

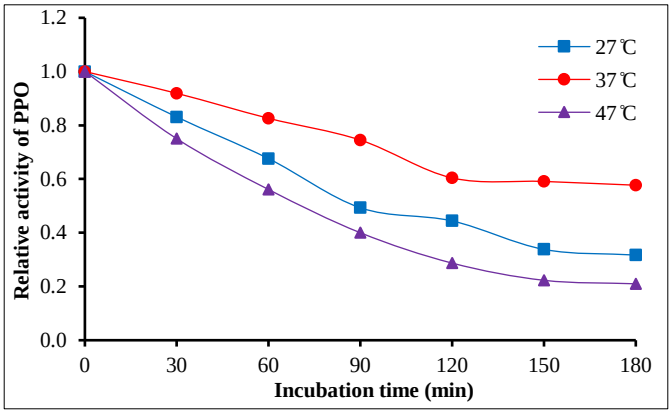

Figure 6. Plot of the relative activity of crude PPO as a function of incubation time at different temperatures

Application of Crude PPO for the Treatment of Textile Wastewater

The superior biological technique to remove phenols from industrial effluent is to use enzymes (Klibanov *et al*., 1980). The use of oxidoreductive enzymes to treat aqueous phenols is a cost-effective and efficient procedure. Peroxidases, or PPO, they claim, can be more effectively used to remove phenolic pollutants.

In this research, a crude PPO enzyme was used to remove the phenols and related organic compounds in wastewater from the local textile service. After treatment, the absorbance of wastewater was measured at 262 nm (Table 3 and Figure 7). It was found that the changes in absorbance with incubation time for wastewater treatment. The absorbance was directly related to the concentration of dissolved phenols and related organic compounds in wastewater. A decrease of absorbance indicated the degradation of phenols and related organic compounds. Therefore, treatment with crude PPO can be decreased the dissolved phenols and related organic compounds in wastewater.

Table 3. Relationship between Decrease of Absorbance and Incubation Time

Incubation time(hour)	Absorbance at 262 nm
0	2.463
1	1.774
2	1.760
3	1.744
4	1.501
5	1.376
6	1.105

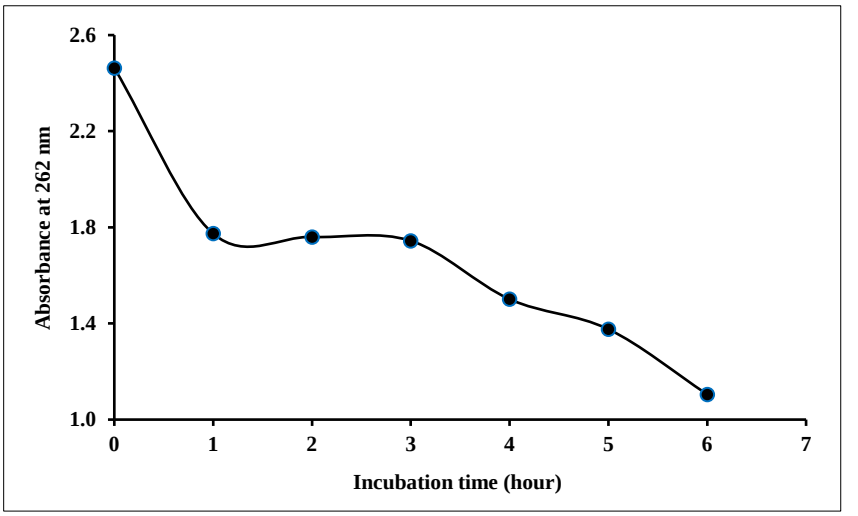

Figure 7. Plot of absorbance at 262 nm as a function of incubation time

Conclusion

PPO was isolated from a sweet potato sample with sodium phosphate buffer solution at pH 6.8. PPO catalyzed the oxidation of catechol and gives *o*-quinones as products. Therefore, PPO activity was followed by measuring the absorbance at 420 nm related to *o*-quinones.

Enzymic studies such as optimum pH, pH stability, optimum temperature, and thermostability were determined by using the spectrophotometric assay method. The optimum pH of crude PPO enzyme was found at pH 6.5 and pH stability of crude PPO enzyme was studied at various pH values. The enzyme activity was retained by 46.4 %, 53.6 %, and 40.6 % of its original activity at pH 6.0, 6.5, and 7.0, respectively for 180 min incubation time.

The optimum temperature of crude PPO enzyme was found to be 37 °C and the thermostability of crude PPO enzyme was studied at different temperatures. It was found that the crude PPO activity was decreased by 77.3 %, 68.0 %, and 90.0 % of its original activity at 27, 37, and 47 °C, respectively for 180 min incubation time.

Treatment of textile wastewater requires enormous cost and continuous input of chemicals which becomes uneconomical and causes further environmental damage. Hence, economical and eco-friendly techniques by using various parts of the plant extracts can be applied for fine turning of wastewater treatment. Thus, extracted PPO enzyme from sweet potato samples should penetrate the industrial market as it is environmentally friendly and cost-effective.

Acknowledgment

The authors would like to express their gratitude to Pathein University's Rector, Professor Dr Si Si Hla Bu, and Pro-rector, Dr Than Htun, for allowing them to use their research facilities.

References

Anbuselvi, S., and T. Balamurugan. (2014). "Phytochemical and Antinutrient Constituents of Cassava and Sweet Potato", *World J. Pharm. Sci.*, **3**, 1440-1449

Berg, J. M., J. L. Tymoczkoand L. Stryer.(2002). “Biochemistry”, 5thed^{n}. W H Freeman and Co., New York, 5-10

Chandra, M., D. L. Kevinand M. Manpreet, (2014). "*An Introduction to Inhibitors and their Biological Application*", 1sted^{n}. EMD Millipore, Merck KGaA Co., Darmstadt, Germany, 8-12

Charles, H. H., C. B. Larryand W. H. Norman, (2007). "*A Laboratory for General, Organic and Biochemistry*", McGraw-Hill Co., New York, 357-378

Edward, W., R. Bownes,W. D. Leukes, E. P. Jacobs, R. Sanderson, P. D. Roseand S. G. Burton. (1998). "A Capillary Membrane Bioreactor Using Immobilized Polyphenol Oxidase for the Removal of Phenols Industrial Effluents", *Journal of Enzyme and Microbial Technology*, **24**, 209-217

Fang, C., (2007). "*Characterization of Polyphenol Oxidase and Antioxidants from Pawpaw Fruits*", Master Thesis, Kentucky University, United Kingdom, 477-484

Klibanov, A. M., B. N. Alberti,E. D. Morrisand L. M. Felshin.(1980). "Enzymatic Removal of Toxic Phenols and Anilines from Wastewaters", *J. Applied Biochem.*, **2**, 414-421

Korte, F., (1974)."*Analytical Methods*", Academic Press Inc., New York, **1**, 1082-1085

Martinez, M. V., and J. R. Whitaker, (1995)."The Biochemistry and Control of Enzymatic Browning", *Journal of Trends in Food Science and Technology*, **6** (6), 195-200

Motoda, S. (1979). "Formation of Aldehydes from Amino Acids by Polyphenol Oxidase", *Journal of Fermentation Technology*, **57**, 395-399

Oliveira, C. M., A. C. S. Ferreira, V. Freitas and A. M. Silva, (2011). "Oxidation Mechanisms Occurring in Wines", *J. Food Res. Int.*, **44**, 1115–1126

Ray, R. C., and V. Ravi. (2005). "Post-Harvest Spoilage of Sweet Potato and its Control Measures" *Critical Review Journal of Food Science and Nutrition*, **35**, 623-644

Remya, M., and S. Subha. (2009). "Sweet Potato-A Valuable Medicinal Food: A Review". *Journal of Medicinal Food*, **17** (7), 733-741

Robinson, P. K. (2015)." Enzymes: Principles and Biotechnological Applications" *Journal of Biochem.*, **59**, 1-41

Sawhney, S. K., and R. Singh, (2000). "*Introductory Practical Biochemistry*", Narosa Publishing House, New Delhi, 88-100

Umesh, J. U., D. V. Vishal, J. U. Mitaland G. P. Sanjay. (2011). "Decolorization of the Textile Dyes Using Purified Banana Pulp Polyphenol Oxidase", *International Journal of Phytoremediation*, **13** (40), 357-372

Synthesis and Characterization of Gold Nanoparticle-Quercetin Complex by Citrate Reduction Method

Zin Thu Khaing[1], Ei Pwint Phyu[2] & Myint Myint Khine[3]

Abstract

Quercetin is a flavonoid having cancer-fighting, anti-inflammatory, and antioxidant effects. The goal of this research is to create and characterize a gold nanoparticle-quercetin complex. In this experimental work two processes were carried out. The first process was the preparation of gold nanoparticles. The second process was the synthesis of gold nanoparticles–quercetin complex. Trisodium citrate was used as a reducing agent in the synthesis of gold nanoparticles. By citrate reduction of tetrachloroauric acid, quercetin was coupled with gold nanoparticles during particle production. The color of gold nanoparticles at room temperature, UV-visible spectroscopy, SEM, Zeta sizer, and XRD were used to characterize gold nanoparticles. The volume of trisodium citrate was altered and optimized for this purpose. In the present work optimal gold salt concentration, trisodium citrate concentration, pH, and temperature were found to be 20 ppm, 40 mL, 9, and 90 °C, respectively. These optimize ratio was used for gold nanoparticle-quercetin complex. UV-visible spectroscopy, SEM, and Zeta sizer were used to identify the gold nanoparticle-quercetin complex. The maximum absorbtion of the gold nanoparticle quercetin complex are 205 nm and 321 nm, respectively. the zeta potential of QGNPs was less than − 40 mV, they were exceedingly stable in solution and the colloidal particle size less than 100 nanometers.

Keywords: gold nanoparticles, quercetin, trisodium citrate, tetrachloroauric acid, Zeta sizer

Introduction

In recent years, considerable attention has been paid to the synthesis and characterization of gold nanoparticles; because they can be used in different chemical science and technologies. Gold nanoparticles(GNPs) are biologically inert and cause no serious side effects in biological systems. Many forms of GNPs, including spheres, rods, stars, pyramids, and worms, have been employed as drug delivery systems (Kumar *et al*.,2013). Flavonoids are ubiquitously present in common plant-based food items and

[1] Lecturer, Dr., Department of Chemistry, University of Yangon
[2] MSc candidate, Department of Chemistry, University of Yangon
[3] Professor, Dr., Department of Chemistry, University of Yangon

beverages and they are known to have antioxidant properties that can protect against cardiovascular diseases, certain kinds of cancers, cell apoptosis, etc. (Block, 1992). Since diabetes mellitus is considered a free radical-mediated disease, there has been renewed interest in the use of flavonoids in diabetes research. Quercetin, an important flavonoid, has been reported to have an ameliorative effect on diabetes mellitus (Vijayababu *et al*., 2006). To enhance the efficacy of a therapeutic agent, the use of nanoparticle-based drug formulation is an important aspect of nanomedicine, for which the first step is the preparation of a stable nanoparticle-drug complex (Wang *et al.,* 2007) have reported detection of flavonoids namely quercetin, daizeol and querarin and an assay of their antioxidant activities by using gold nanoparticles. The present study synthesizes gold nanoparticle-quercetin formulation and characterizes the composite for further study of its antioxidant and antidiabetic effects. Quercetin is derived from medicinal herbs and is an important bio-flavonoid with anti-cancer, anti-inflammatory, and anti-oxidant properties (Russo *et al*., 2014).

The proposed research looks at the manufacture of gold nanoparticles using a reduction process between tetrachloroauric acid, the precursor solution, and trisodium citrate, the reducing agent. By varying the volume of trisodium citrate, the dependence of nanoparticle size and size distribution was investigated. UV, SEM, and XRD were used to characterize the nanoparticles.

Materials and Methods

Materials

The chemicals used in this study were prepared according to requirements. The tetrachloroauric acid, trisodium citrate, sodium carbonate from BDH (England), and Distilled water were used.

Tetrachloroauric acid ($HAuCl_4$) solution

In this part of the study, a 1000 ppm tetrachloroauric acid solution was mixed with distilled water (pH 7.2) to get a 50 ppm solution.

Trisodium citrate solution

1.613 g of trisodium citrate was dissolved in distilled water and the volume made up to 1 L in a beaker to obtain 6.25 mM trisodium citrate

solution. The effect of trisodium citrate, which was used as a reducing agent on the nanoparticle size, was investigated in this part of the study. Trisodium citrate concentration was changed from 10 to 40 mL.

Sodium carbonate solution

10.6 g of sodium carbonate was dissolved in distilled water and the volume was made up to 1L in a beaker to obtain a 0.1M sodium carbonate solution.

Synthesis of gold nanoparticles

Synthesis of gold nanoparticles was done with the citrate reduction method (Turkevich, 1951 and Frens, 1973). 20 mL of tetrachloroauric acid ($HAuCl_4$) (50 ppm) solution in beaker was boiled until the temperature reach 90 ˚C on hot plate with magnetic stirrer. To this boiling solution 10 mL of trisodium citrate (6.25mM) and 10 mL of sodium carbonate (0.1 M) were added in continuous mode quickly with simultaneous stirring (90 rpm). After addition of trisodium citrate and sodium carbonate, stirring and heating continued until one hour (Turkevich *et al*., 1951). This solution was recorded as GNP-1. Similarly, the same procedure was used for various volumes of trisodium citrate solutions such as 20, 30, and 40 mL respectively. The resulting colour of solutions was recorded as GNP-2, GNP-3, and GNP-4. Moreover, the preparation of gold nanoparticles with 30 mL of trisodium citrate only was also made as the same procedure without sodium carbonate and noted as GNP-5. The influence of nanoparticle size and size distribution was explored in this section of the study. The volume of trisodium citrate was altered and optimized for this purpose. Other variables such as gold salt concentration, temperature, and sodium carbonate concentration were kept constant.

Preparation of gold nanoparticle- quercetin complex by using GNP-4

20 mg of quercetin was inserted into the beaker and 100 mL of ethanol was added to make the gold nanoparticle-quercetin complex (GNPQ). To make the gold nanoparticle-quercetin complex solution, the gold nanoparticles (GNP-4) and quercetin solutions (2:1 v/v) ratios were mixed.

Characterization of gold nanoparticles and gold nanoparticle – quercetin complex

The characterizations of gold nanoparticles such as a scanning electron microscope, SEM (Type: JEOL15 kV), UV-visible spectrophotometer (UV Mini 1240, Shimadzu, Kyoto, Japan), and X-ray diffractometer (XRD) to characterize the morphology, size, and shape of synthesized gold nanoparticles and gold nanoparticle-quercetin complexes were measured at the University Research Center, University of Yangon.

The characterizations of gold nanoparticle-quercetin complex such as a scanning electron microscope, SEM (Type: JEOL15 kV), UV-visible spectrophotometer (UV Mini 1240, Shimadzu, Kyoto, Japan), were measured at the University Research Center, University of Yangon. The diameters of gold nanoparticle-quercetin complexes were measured using the Zeta Sizer Nano – ZS at Osaka University, Japan, and the surface charges were calculated using the Zeta potential (Malven instrument, Japan).

Results and Discussion

Preparation and Characterization of gold nanoparticles and gold nanoparticle – quercetin complex

Trisodium citrate was used as a reducing agent to reduce tetrachloroauric acid ($HAuCl_4$) in colloidal gold particles. Gold nanoparticles (GNP-1, 2, 3, 4 and 5) were found to be grey, pale cherry red, pale cherry red, and cherry red in various quantities of trisodium citrate solutions, such as 10, 20, 30, and 40 mL. According to results the optimal gold salt concentration, trisodium citrate concentration, pH, and temperature were found to be 20 ppm, 40 mL, 9, and 90 °C, respectively. So gold nanoparticles (GNP-4) was regarded as homogenous gold nanoparticles with small sizes. The results are shown in Figure 1 and Table 1.

GNP-1	GNP-2	GNP-3	GNP-4	GNP-5

Figure 1. Colour variation of gold nanoparticles of different sizes

Table 1. Reduction of Standard Tetrachloroauric acid by Trisodium Citrate

Sample	50ppm tetrachloroauric acid (mL)	6.25M trisodium citrate(mL)	0.1 M sodium carbonate(mL)	Color	pH	λ_{max} (nm)
GNP-1	20	10	10	grey	9	530
GNP-2	20	20	10	pale cherry red	9	526
GNP-3	20	30	10	Pale cherry red	8	526
GNP-4	20	40	10	Cherry red	9	522
GNP-5	20	30	-	Dark Grey	4	530

GNP = Gold nanoparticles

To make the gold nanoparticles-quercetin complex, gold nanoparticles (GNP-4) were coupled with quercetin since cherry red colour GNP-4 was regarded as homogenous gold nanoparticles with small sizes. Figures 2 depict these finding.

UV Figure 2. Gold nanoparticle-quercetin complex

Another significant aspect of gold nanoparticle characterization is spectroscopy. The absorption peak shifts to longer wavelengths as particle size increases and the width of absorption spectra is linked to the size distribution range. Because of surface Plasmon resonance, gold nanospheres have a single absorption peak in the visible range between 510-550 nm and

show strong absorption of visible light at 520 nm (Kwon, 2006). Gold Nanoparticles (GNP) have a vivid red color that varies depending on their size. The absorption peaks of gold nanoparticles GNP-1, 2, 3, and 4 at different pH levels are 530, 526, 526, and 522 nm, respectively, in this work. Due to a decrease in particle size, a red shift from 532 nm to 522 nm developed as the volume of trisodium citrate was increased. At 522 nm, colloidal gold generated in the experiment showed strong absorption. Figures 3 and Tables 1 depict these findings. GNP only had one peak at 522 nm, which is consistent with earlier observations (Storhoff *et al*., 2000).

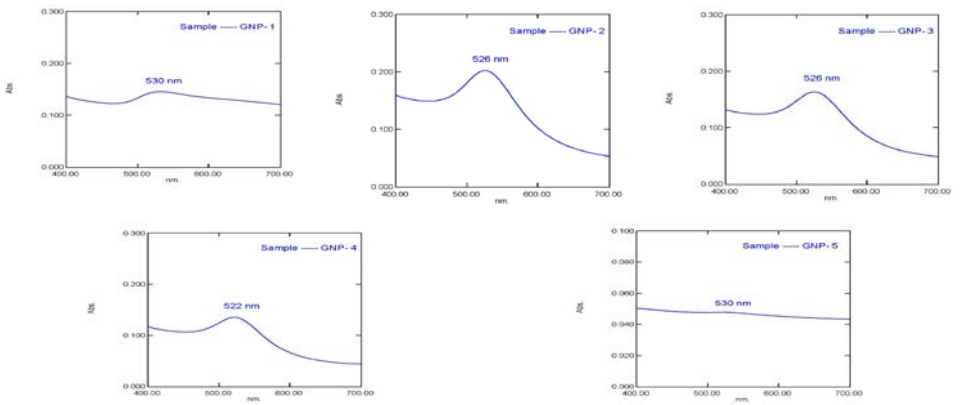

Figure 3. UV-visible spectrum of gold nanoparticles

XRD analysis

The crystalline phase existing in a substance is identified by XRD analysis, which reveals chemical composition information. Crystalline nanoparticles represented by four peaks corresponding to standard Bragg reflections (111), (200), (220), and (311) of face centers cubic lattice. The high crystallinity of nanoparticles is evident from the peaks in the XRD pattern. The peaks in XRD pattern showed uniform gold nanoparticles in aqueous solutions via chemical reduction method. Figure 8 depicts the X-ray diffraction patterns of gold nanoparticles.

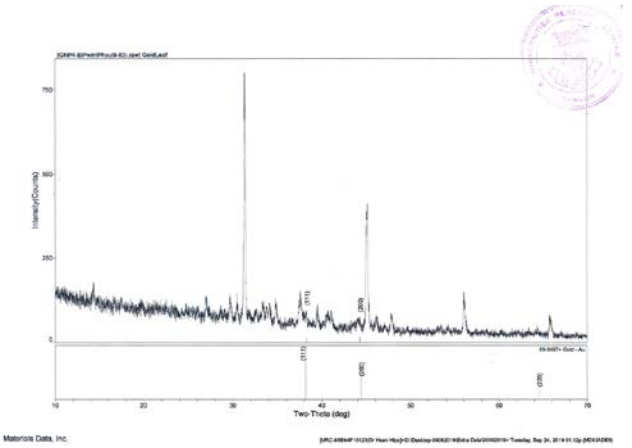

Figure 8. XRD spectrum of gold nanoparticles (GNP-4)

UV- visible spectroscopy of gold nanoparticle-quercetin complex

The maximum shifts to lower wavelengths of 205 and 321 nm in the UV-visible spectra of the gold nanoparticle-quercetin complex (QGNP). These maximum values were shorter than the 522 nm wavelength of gold nanoparticles. Figures 4 as well as Table 2 depict these findings.

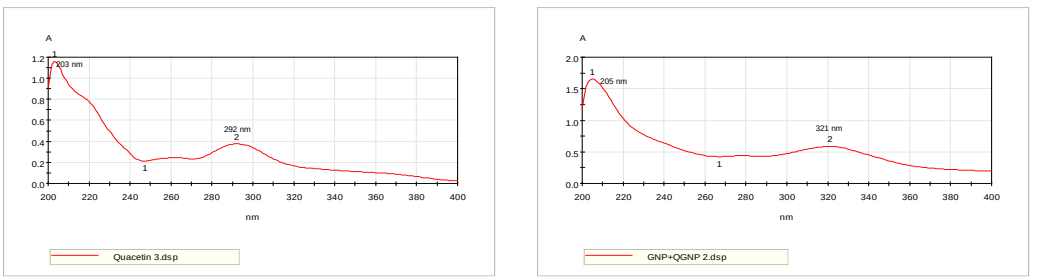

Figure 4. UV-visible spectrum of quercetin and gold nanoparticle-quercetin complex

Table 2. UV-visible Spectra Data of Quercetin and Gold Nanoparticle-Quercetin Complex

Sample	Observed λ_{max} (nm)
Quercetin	203, 292
QGNP	205, 321

SEM analysis

SEM analysis was used to investigate the surface morphology of gold nanoparticles, gold nanoparticle-quercetin complex and quercetin. According to the SEM image, the shape of gold nanoparticles, gold nanoparticles-quercetin complex and quercetin were all different morphologies. The gold nanoparticles samples were examined with SEM to confirm the presence of GNPs as shown in Figure 5. The form of gold nanoparticles can plainly be observed to be rod shapes. Quercetin granules kept its own structure properties which is confirmed by Figure 6 that the strip-like quercetin structure. Figure 7 shows SEM microphotograph of gold nanoparticle-quercetin complex which was smoother and with the absence of the strip-like quercetin structure. The SEM image shows that the gold nanoparticles- quercetin complex has porous.

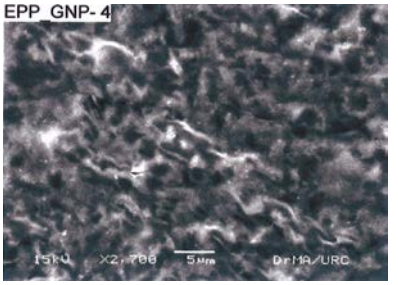

Figure 5. SEM micrograph of gold nanoparticles

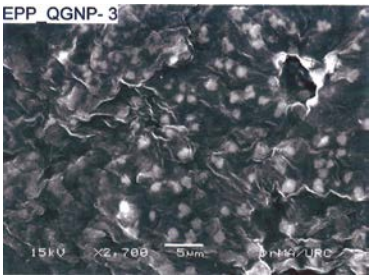

Figure 7. SEM micrograph of gold nanoparticle-quercetin complex

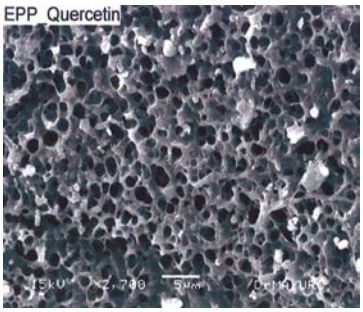

Figure 6. SEM micrograph of quercetin

Zeta size and zeta potential distribution of gold nanoparticle- quercetin complex

The zeta investigation was carried out to determine the particle size, and zeta potential of both bare gold nanoparticles and antibody conjugated gold nanoparticles. Peak number and peak area are critical factors in determining the zeta potential distribution. The average of the 510-550 nm counts was taken after three cycles of varied counts. The peak mean calculates the particle's mean diameter, while the peak area calculates the percentage of the mean diameter based on intensity. As illustrated in Figure 9, the graphs were constructed using the means of all peaks mean diameter, and peak area intensity. The average zeta of peak 1 in a 50 ppm centrifuged sample was found to be 699.5 nm with a 68.4 percent intensity in the current study. Peak 2 has a value of 30.8 percent at 172 nm, while peak 3 has a value of 0.8 percent at 48 nm. Table 3 summarizes the findings. In addition to size distribution, zeta potential measurement is critical for characterization. The magnitude of the Zeta Potential provides information about particle stability, with higher magnitude potentials exhibiting increased electrostatic repulsion and therefore increased stability. Another key measure for particle size is the negative charge on nanoparticles caused by citrate ions (Amir, *et al*., 2009). Because the zeta potential of QGNPs was less than − 40 mV, they were exceedingly stable in solution (Jung *et al*., 2014). The negative charge denotes a particle size of less than 100 nanometers. Figure 10 depicts the results.

Table 3. Zeta Size Distribution of Gold Nanoparticle- Quercetin Complex

Record	Peak	Samples	Size (nm)	% Intensity
38	peak 1	QGNPs	699.50	68.4
39	peak 2	QGNPs	172.00	30.8
40	peak 3	QGNPs	48.01	0.8

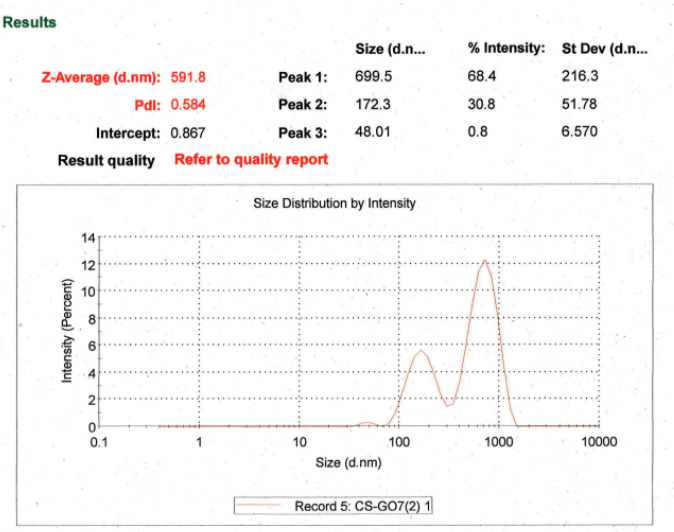

Figure 9. Ziter size distribution of gold nanoparticle- quercetin complex

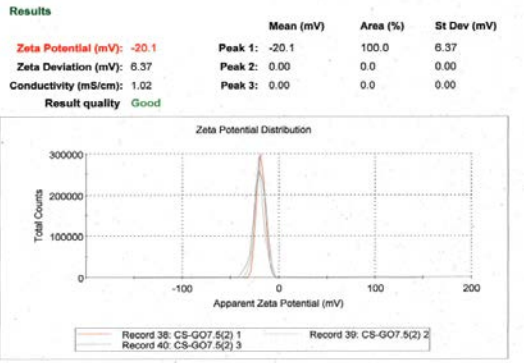

Figure 10. Ziter potential distribution of gold nanoparticle- quercetin complex

Conclusion

The goal of this study was to look into the synthesis and characterization of a gold nanoparticle-quercetin complex as well as the effect of various experimental parameters on its size and size distribution temperature, gold salt concentration, trisodium citrate concentrations, and pH. The citrate reduction process can be used to make homogenous gold nanoparticles with small sizes from a high concentration of tetrachloroauric acid precursor. The ideal gold salt concentration, trisodium citrate concentration, pH, and temperature were found to be 20 ppm, 40 mL, 9, and 90 °C, respectively. SEM, zeta sizer, and UV-vis spectrophoscopy were used to examine the morphology, size, and shape of the produced gold nanoparticle-quercetin complex. In the study colloidal particle size of less than 100 nanometers gold nanoparticle-quercetin complex was obtained. All of these findings point to the creation of a stable gold nanoparticle-quercetin complex, which will be worth investigating in biological systems for therapeutic efficacy.

Acknowledgments

The authors express their gratitude to the Ministry of Education, Department of Higher Education (Yangon), Osaka University, to measure Zeta sizer, Professor Dr Phoe Kaung, Rector, University of Yangon, and Professor Dr Ni Ni Than, Professor and Head, Department of Chemistry, University of Yangon, for allowing us to conduct this research and providing research facilities.

References

Amir, T., A. Fatma, and A. Hakan. (2009).“Gold Nanoparticle Synthesis and Characterization .” *Hacettepe J. Bol. & Chem.* **37(3),** 217-226

Block, G. (1992) “Fruit, Vegetables, and Cancer Prevention: A Review of the Epidemiological Evidence”. *Nutr. Rev.*, **50,** 207 – 213

Frens, G. (1973). “Controlled Nucleation for the Regulation of the Particle Size in Monodisperse Gold Suspensions”. *Nat. Phys. Sci.*, **241,** 20-22

Karthic, K., K.S. Kirthiram, S. Sadasivam, and B. Thayumanavan. (2008). “Identification of α - amylase Inhibitors from *Syzygium cumini* Linn Seeds”. *Indian J. Exp. Biol*., **6**, 677- 680

Kumar, A., X. Zhang and X.J. Liang. (2013). "Gold Nanoparticles: Emerging Paradigm for Targeted Drug Delivery System." *Biotechnol. Adv*. **31,** 593–606

Russo, G.L., M. Russo, C. Spagnuolo, I. Tedesco, S. Bilotto, R. Iannitti, and R. Palumbo. (2014)." Quercetin: A Pleiotropic Kinase Inhibitor Against Cancer". *Cancer Treat Res.* **159,** 185–205

Storhoff, J. J., A. A. Lazarides, R.C. Mucic, C.A. Mirkin, R.L. Letsinger, and G.C. Schatz. (2000). "What Controls the Optical Properties of DNA-Linked Gold Nanoparticle Assemblies?". *J. Am. Chem. Soc***.,** **122,** 4640 – 4650

Turkevich, J., P.C. Stevenson, and J. Hillier, (1951). "A Study of the Nucleation and Growth Processes in the Synthesis of Colloidal Gold". *Discuss Faraday Soc.*, **11**, 55-75

Vijayababu, M.R., P. Kanagaraj, A. Arunkumar, R. Ilangovan, and J. Dharmarajan. (2006). "Effects of Quercetin on Insulin-like Growth Factors (IGFs) and Their Binding Protein-3 (IGFBP-3) Secretion and Induction of Apoptosis in Human Prostate Cancer Cells". *Arunkumaran Oncol. Res.*, **16**, 67 – 74

Wang, J., N.D. Zhou, Z.Q. Zhu, J.Y. Huang, and G.X. Li. (2007). "Detection of Flavonoids and Assay for Their Antioxidant Activity Based on Enlargement of Gold Nanoparticles". *Anal. Bioanal. Chem.*, **388,** 199–1205

Identification of Diterpene Alkaloid Compound and Investigation of Antitumour Activity from the Leaf of *Taxus baccata* L. (Yew Tree)

Myint Myint Khine[1], Moh Moh Myint[2] & Maw Maw Lwin[3]

Abstract

The *Taxus baccata* tree is a highly toxic plant that has occasionally been used medicinally. It is well-known medicinal plant employed to cure various diseases in the Ayurvedic system of medicine. This paper presents the identification of diterpene alkaloid and antitumor activity of this medicinal plant. Identification of taxin-B from the leaf of *Taxus baccata* L. (Yew Tree) by using ^{1}H NMR, ^{13}C NMR, 2D NMR (HSQC, HMBC and COSY). The antitumor activity of ethanolic extract from the leaf of *Taxus baccata* L. (Yew Tree) was determined by using potato crown gall test or potato disc assay method. An ethanolic extract of this plant showed active antitumor activity.

Keywords: *Taxaceae*, Taxin-B, ^{2D}NMR, antitumor activity

Introduction

Taxus baccata L. originally known as Yew is an evergreen and widely spread shrub commonly used for the ornamental landscaping. However, with the exception of the arrillus part which is enveloping the seeds, all plants parts contain toxic taxine alkaloids (Wilson *et al*., 2001) and have been implicated in many human and animal poisonings. It contains toxoids, flavonoids, steroids and sugar derivatives (Wen, 2006). It is a conifer native to western, central and southern Europe and northern west Asia (Sharma, 2014).

[1] Professor, Dr. Department of Chemistry, University of Yangon
[2] Lecturer, Dr., Department of Chemistry, West Yangon University
[3] Associate Professor (retired), Dr., Department of Chemistry, Pyay University

Materials and Methods

Plant Material

The leaf of *Taxus baccata* L. (Figure 1) was collected from Pyin Oo Lwin (Botanical Garden), Shan State. The sample was authenticated by botanist of Department of Botany, University of Yangon.

Figure 1. Photographs of the *Taxus baccata* L. (Yew Tree)

Extraction and Isolation of Diterpene Alkaloid

The air-dried powder sample of *Taxus baccata* L. (500 g) was macerated with ethyl acetate (3 x 1 L) at room temperature for about two weeks by percolation method. It was repeated for three times. The ethyl acetate extract (20 g) was subjected to column chromatography over silica gel eluted with Pet-ether (60-80 ºC and ethyl acetate increasing polarity and finally with MeOH which yielded a total of four fractions (F-I, F-II, F-III and F-IV). Based on thin layer chromatography (TLC) analysis, F-II (1 g) was subjected to second column separation eluted with solvent system PE: $CHCl_3$:MeOH (1:1:0.02) to give four fractions. Among these four fractions, fraction III was subjected to the third column chromatography eluting with PE:$CHCl_3$:MeOH (9:1:0.02; 9:1:0.04; 9:1:0.05 and 9:1:0.05) to obtain four fractions. The fraction obtained from the solvent system PE:$CHCl_3$:MeOH (9:1:0.05) yielded isolated compound.

General Experimental Procedure

The FT IR spectra of alkaloid compound was taken with KBr pellets and recorded on Shimadzu FT IR 8400 Fourier Transform Infrared Spectrometer. The ^{1}H NMR spectra of this compound was determined in

$CDCl_3$, CD_3OD and acetone using TMS as internal standard and recorded on INOVA-600 (600 MHz for proton). The ^{13}C NMR spectra of this compound were determined in CD_3OD using TMS as internal standard and recorded on INOVA 500 (125 MHz for carbon). COSY, HMBC and HSQC spectra were determined in CD_3OD recorded on INOVA 600 (600 MHz for proton and 125 MHz for carbon).

Antitumour Activity by using Potato Assay Method

Fresh, disease free potato tubers (*Solanum tuberosum* L. Solanaceae) were collected from local market. Moderate sizes of potatoes were sterlized with 50 % sodium hypochlorite (Clorox) for 20 min. Sliced potato discs (0.5 cm thick) were placed on 1.5 % agar plates (1.5 g of Difco agar was dissolved in 100 mL of distilled water, autoclaved and 20 mL was poured into each petri dish). Each plate contained five discs. This procedure was done in the clean bench in the sterilized room.

Ethanol extract of *Taxus baccata* L. (Yew tree) was made to give the serial dilutions of 1 mg/mL and 0.25 mg/mL in volume 1 mL of DMSO as stock solutions and this solution was filtered through millipore filters (0.22 μm) into a sterile tube. 0.5 mL of each solution was added to 1.5 mL of sterile distilled water and 2 mL of broth culture of *A. tumefaciens* strain (48 h culture containing 5 x 10^9 cell/mL) were added aseptically. Each disc was overloaded with 50 μL of appropriate mixture. Petridishes were sealed by parafilm and incubated at room temperature (25-30 ºC) for one month. After one month, discs were stained with Lugol's iodine solution for 30 min and tumours were observed visually.

Results and Discussions

Identification of Diterpene Alkaloid Compound

Diterpene alkaloid compound was isolated as a white crystal from the ethyl acetate extract of the leaf of *Taxus baccata* L. and appeared on Thin Layer Chromatography, TLC using solvent system, $CHCl_3$: MeOH (20:1) as cherry red spot by spraying with vanillin. Its R_f value was at 0.53 on precoated silica gel GF_{254} aluminum TLC plate.

Infrared spectrum (Figure 2) shows the absorption bands at 3444, 2922 and 2850 cm^{-1} indicating the OH stretching and aliphatic C-H

stretching in CH_2 and CH_3 groups. A strong peak at 1737 cm^{-1} attributed to C=O group, while weak peak at 1629 cm^{-1} was signal of C=C group and peak at 1158 cm^{-1} and 1122 cm^{-1} indicated C-O group, and peak at 1446 and 1371 cm^{-1} is due to aliphatic C-H bending respectively.

In the ^{13}C NMR spectrum (Figure 3), the signals of four olefinic carbons appeared at δ 130.3, 140.1, 124.2 and 139.6 (C-3, C-4, C-10 and C-11). The signal at δ 208 ppm indicated the carbonyl group (C-1) in this compound. The signals at δ 79.6, 69.8, 72.5, 69.0 ppm showed the presence of five oxygenated methine carbons. C-10/C-11 double bond might be endocyclic instead of exocyclic which is found in many natural taxanes. This conclusion was confirmed by the lack of any signal at δ 2.8 to 4.2 ppm in the ^1H NMR spectrum characteristics of proton H-4 in most taxanes and also by the presence of an isolated spin system of doublets at δ 2.60 and 2.00 ppm with the coupling constant J = 15.7 Hz, which will assignable to H-12. Thus, the skeleton of it was elucidated as consisting of 6/10/6 membered rings with a C-10/ C-11 endocyclic double bond. The C-H signal moved to upfield region δ 4.40 ppm due to the attachment of free hydroxyl group (OH) at C-16. The observed ^{13}C NMR data agree with the literature data (Yue *et al*., 1995).

^1H NMRpectrum (Figure 4) shows the presence of one olefinic proton, five oxygenated methine protons, two aliphatic methylene protons, the four taxane methyl groups and the four acetate methyl groups. The olefinic proton showed the signal at δ 5.80 ppm. Five oxygenated protons appeared at δ 6.35, 5.35, 5.80, 5.25 and 4.40 ppm. The four signals appeared at δ 1.24, 1.30, 1.13 and 1.90 (H-17, H-18, H-19 and H-20) due to the presence of four taxane methyl groups. The other four singlets at δ 1.96, 2.00, 2.10 and 2.14 (H-2, H-5, H-9 and H-14) also showed the presence of four acetate methyl groups. The correlation of four acetate groups can be seen in the HSQC and HMBC spectra (Figure 5 and Figure 6). The ^1H NMR spectral data of this compound agree with the reported proton spectral data of Taxin B (Yue *et al*., 1995).

The ^1H-^1H COSY spectrum (Figure 7) shows the correlations of adjacent protons. COSY spectrum indicated the correlation of H-12/H-14, H-5/H-6; H-14/H-15; H-9/H-7 and H-16/ H-17 respectively. The ^1H-^{13}C HMBC spectrum shows the long range correlations. The signal at δ 124.2 ppm was only correlated with the one proton broad doublet at δ 5.80 ppm in ^1H-^{13}C HMBC. The correlation of two singlet signals at δ 1.30 and 1.13

ppm and the carbon signal at δ 38.6 ppm in HMBC spectrum showed the direct attachment of C-18 and C-19 at C-8.

The EI-MS spectrum (Figure 8) showed $[M]^+$ at *m/z* 534 ($C_{28}H_{38}O_{10}$), $[C_{20}H_{23}O_2]^+$ at *m/z* 295, $[M\text{-}CH_3CO]^+$ at *m/z* 239 ($C_{12}H_{15}O_5$), $[C_{11}H_{15}O_4]^+$ at m/z 211 and $[C_9H_{12}O_3]^+$ at *m/z* 169. All the observed ^{13}C NMR data agree with the literature data (Yue *et al*., 1995). Therefore this diterpene alkaloid compound must be taxin B (Figure 9).

Investigation of Antitumor Activity

The ethanol extract tested in this study, inhibited tumor information in the Potato Disc Tumor Assay. Ethanol extract of *Taxus baccata* L. (Yew Tree) was good in preventing the tumour information at a dose of 1.56 μg/mL, 3.13 μg/mL and 6.25 μg/mL (Figure 10 and Table 1).

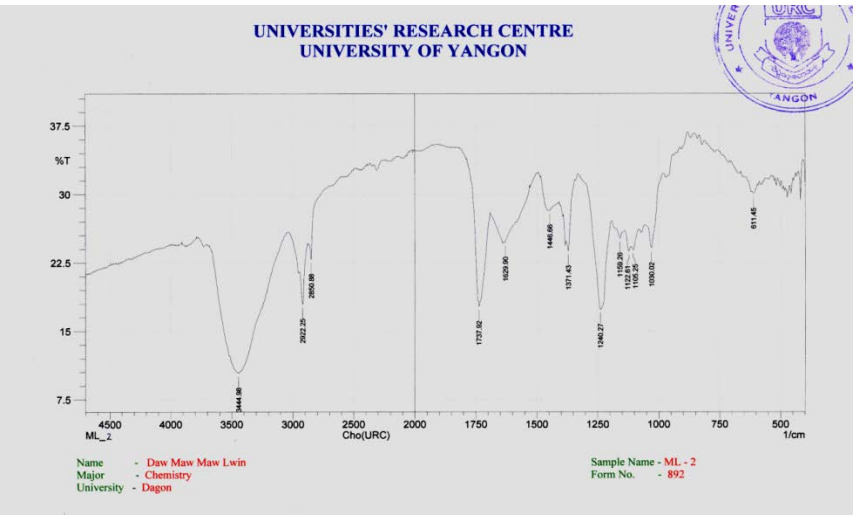

Figure 2. FT IR spectrum of taxin B (CD_3OD, 125 Hz)

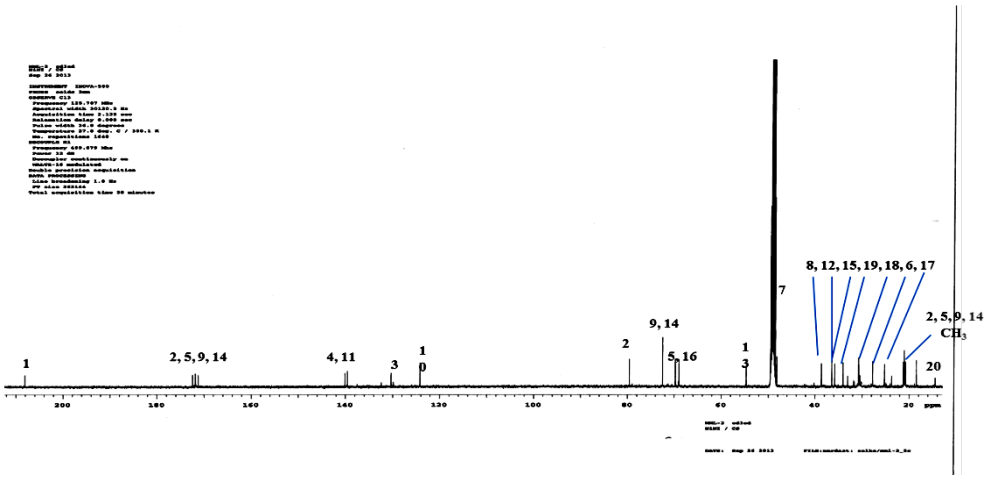

Figure 3. ^{13}C NMR spectrum of taxin B (CD_3OD, 125 Hz)

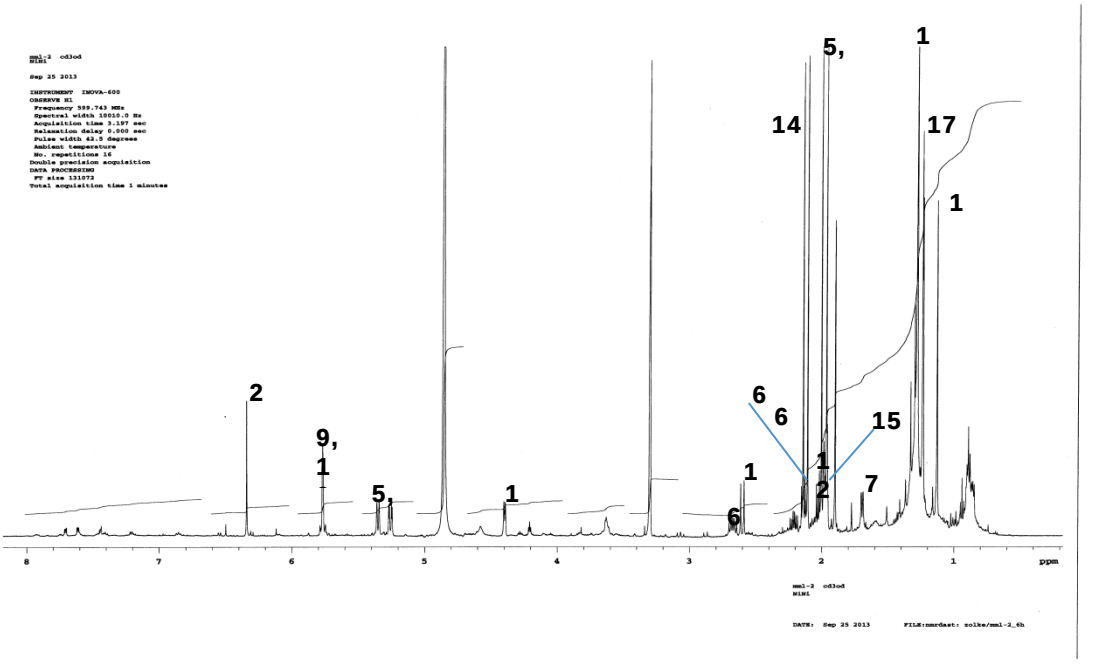

Figure 4. ^{1}H NMR spectrum of taxin B (CD_3OD, 600 Hz)

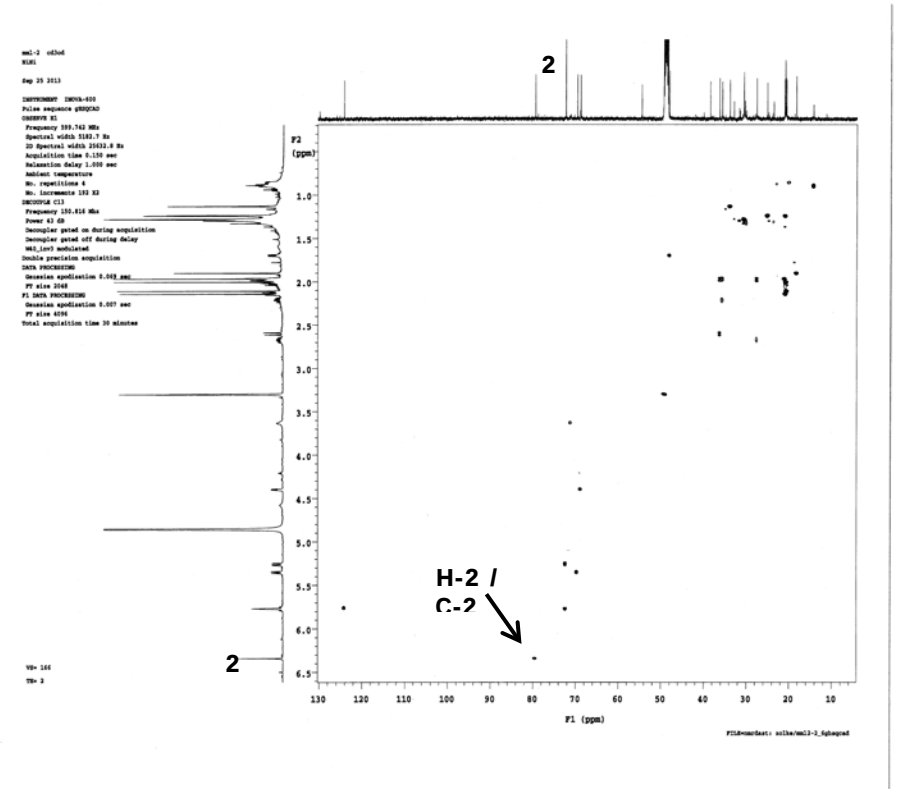

Figure 5. HSQC spectrum of taxin B (CD_3OD, 600 MHz)

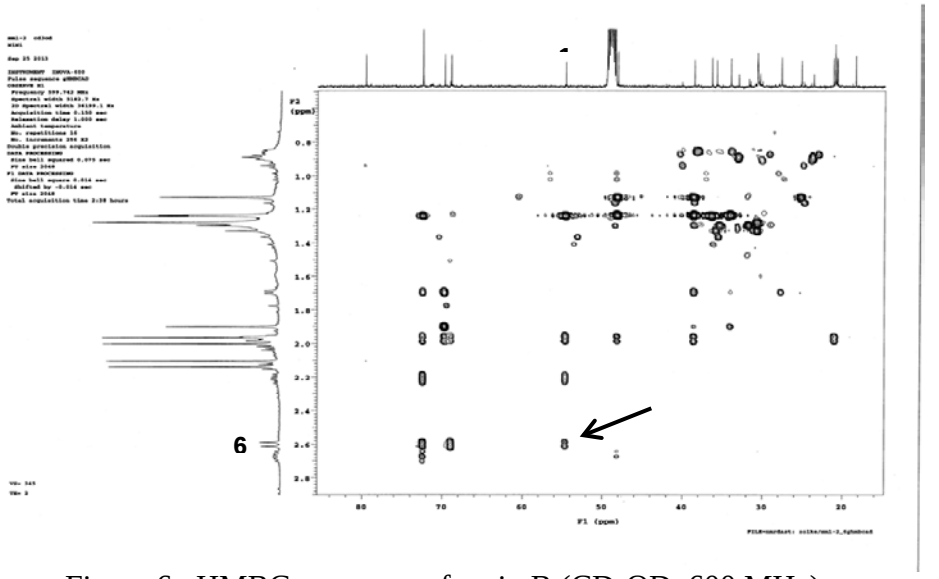

Figure 6. HMBC spectrum of taxin B (CD_3OD, 600 MHz)

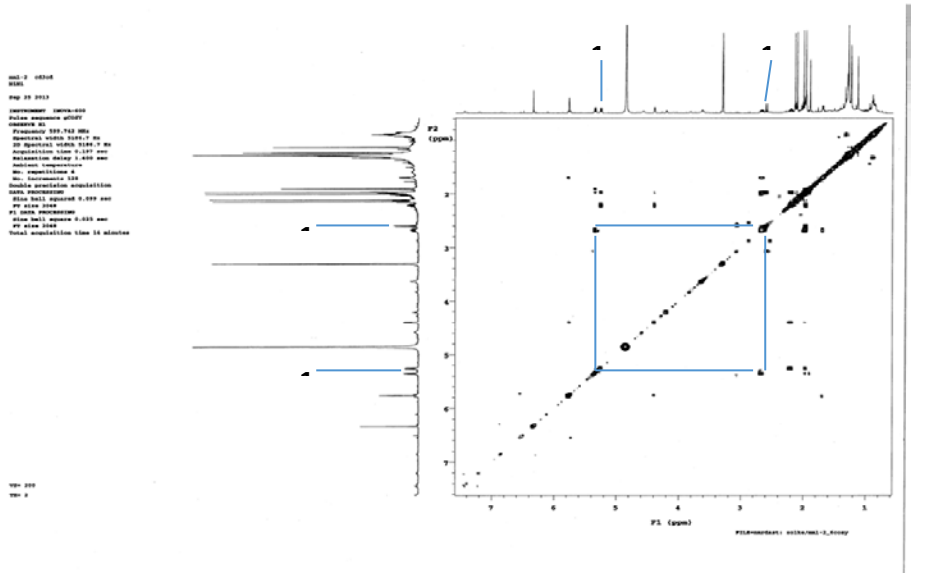

Figure 7. COSY spectrum of taxin B (CD_3OD, 600 MHz)

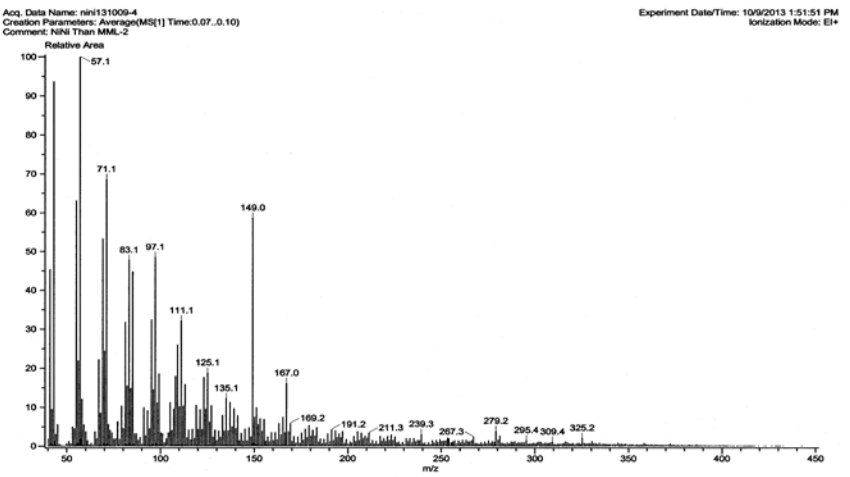

Figure 8. EI-MS spectrum of taxin B (CD_3OD, 600 MHz)

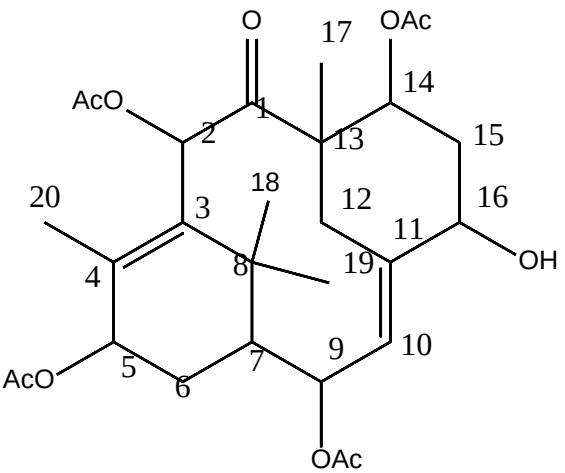

Figure 9. Structure of diterpene alkaloid (Taxin B)

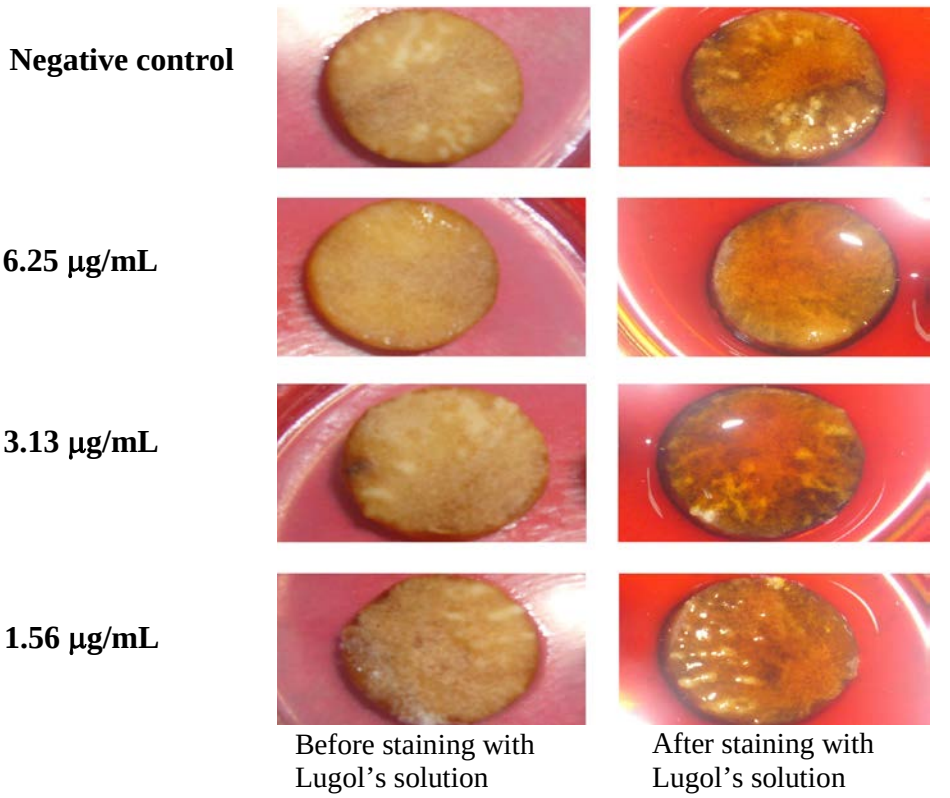

Figure 10. Photographs showing tumour inhibition by the ethanol extract of *Taxus baccta* L. leaf on potato dics at 6.25 µg/mL

Table 1. Antitumor Activity of *Taxus baccata* L. (Yew Tree) by PCG Test

No.	Test Sample	Concentration/dics (µg/mL)	Tumor Inhibition
1.	Control DMSO	-	-
2.	Ethanol extract	6.25	+
3.	Ethanol extract	3.13	+
4.	Ethanol extract	1.56	+

(+) no tumour appeared, (-) tumor appeared

Conclusion

In the chemical investigation, diterpene alkaloid (Taxin B) was isolated from the ethyl acetate extract of leaf of *Taxus baccata* L. By using a column chromatographic method, it was identified by using modern spectroscopic techniques such as FT IR, ^{1}H NMR, ^{13}C NMR, COSY, HSQC, HMBC,and EI-MS

The antitumor activity of ethanolic extract of the leaf of *Taxus baccata* L. (Yew tree) was screened by using the Potato Crown Gall (PCG) test. It was found that ethanol extract of the leaf of *Taxus baccata* L. has to be good preventing tumour activity. According to overall findings, present study shows that the leaf of *Taxus baccata* L. (Yew tree) will be used in antitumor activity.

Acknowledgements

The authors wish to thank Professor and Head Dr Ni Ni Than, Department of Chemistry University of Yangon for her providing the research facilities and giving the opportunity to submit this research paper. The authors wish to thank Retired Professor Dr Saw Hla Myint, Department of Chemistry University of Yangon for his kind guidance, and invaluable suggestions of this research paper. We are grateful to Department of Botany, University of Yangon for identification of the plant species. We would like to express our sincere thanks to Mrs Carola Zolke, NMR Department, Georg August University, Goettingen, Germany for measuring spectra.

References

Sharma, A. K., D. Srishti and K. G. Deep.(2014). "*Taxus baccata* Linn.: A Mystical Herb". *J. Pharmaceutical and Biological Sciences*, **2**(2), 68–70.

Wen, M., C. Buschhaus and R. Jetter.(2006). "Nanotubules on Plant Surfaces: Chemical Composition of Crystals on Needles of *Taxus baccata* Linn". *J. Planta Med.*, **67**(16), 1808–1817.

Wilson, C.W., J. M. Sauer and S. Hooser.(2001). "Taxines: A Review of the Mechanism and Toxicity of Yew (*Taxus* spp.) Alkaloids Toxicon". *J. Planta Med.*, **39**, 175–185.

Yue, Q., Fang, O., X. Liang, C. He and X. Jing.(1995). "Rearranged Taxoids from *Taxus yunnanensis*". *J. Planta Med.*, **61**, 375–377.

Structural Elucidation of Isoflavonoid Compound Isolated from Root Bark of *lagerstroemia tomentosa* Presl. (Pyinma-byu)

Khin Kay Thi Soe[1] & Myint Myint Sein[2]

Abstract

In this paper, *Lagerstroemia tomentosa* Prel. (Pyinma-byu) which is one of the Myanmar Medicinal Plants was selected for chemical analysis. The root bark of this plant was carried out for phytochemical screening which giving rise to alkaloids, flavonoids, glycosides, phenols, polyphenols, reducing sugars, saponins, steroids and terpenes respectively. By using Agar-well diffusion method on six selected organisms, the antimicrobial activity of various solvent extracts of sample was tested. The medium antimicrobial activity on *Bacillus subtilis, Staphylococcus aureus, Pseudomonous aeruginosa,* and *Mycobacterium* organism species were found to be in ethyl acetate and ethanol crude extracts of sample. Advanced separation methods, Thin Layer and Column Chromatograms were used to isolate the pure organic compound, pale yellow needle shape crystal form compound (0.0173 g) from the root bark of Pyinma-byu. This pure compound was reconfirmed by phytochemical test which gives rise to positive for flavonoid and polyphenol tests. This pure compound was rechecked by antimicrobial activity test which gives medium activity on four tested organisms, *Bacillus subtilis, Staphylococcus aureus, Pseudomonous aeruginosa,* and *Escherichia coli*. Some spectroscopic techniques, FT-IR, ^{1}H NMR (500MHz), ^{13}C NMR (125 MHz), DEPT, HMQC and EI mass spectral data were used to determine the molecular formula of this pure compound as $C_{16}H_{12}O_5$. By applying DQF- COSY, ^{1}H NMR, splitting patterns, coupling constants (J values) and HMBC spectroscopic studies, the complete structure of this pure compound could be elucidated.

Keywords : Isoflavonoid , FT-IR, ^{1}H NMR,^{13}C NMR, DEPT, HMQC, EI-mass, DQF- COSY

[1] Associate Professor, Dr, Department of Chemistry, Taunggyi University
[2] Professor and Head (Retired), Dr, Department of Chemistry, Mandalay University

Introduction

Medicinal plants are the sources for drug formation compounds and they have always played a pivotal role. The presence of phytochemical constituents of medicinal plants have been used for curing human diseases. The wonderful chemical compounds of these medicinal plants can be extracted and are able to cure several diseases and very much popular in medicinal world. The traditional medicines are not only affordable and accessible to the people but also effective, safe and reliable for both rural folks and urbanites. Varying degrees of chemicals (or antibiotics) of medicinal plants have a direct impact on physiological activity.

Most common plants have valuable medicinal properties in Myanmar. Aromatic compounds, phenol are used as a medicinal compound from these plants. All plants produce chemical compounds as part of their metabolic activities. Research activities have also been conducted to produce the modern and palatable traditional medicine using modern technique (Gangola, *et al*., 2017). Flavonoid is organic compound, any member of a class of biological pigments containing no nitrogen that are found in many plants.

In this research paper, pure compound of the root bark of *Lagerstroemia tomentosa,* locally known as Pyinma-byu was isolated and chemically analyzed for new source of compound in this field. A pure bioactive organic compound was isolated from this sample by applying Thin-Layer and Column Chromatographic methods. The antimicrobial activity of isolated compound were measured by Agar-well diffusion method. The molecular formula (C_{16} H_{12} O_5) and structure of this isolated compound could be determined by using some spectroscopic methods, such as FT - IR, ^{1}H NMR (500 MHz), ^{13}C NMR (250 MHz), DEPT, HMQC, HMBC, DQF-COSY and EI mass spectra data respectively.

Aim of the Research Work

The aim of this research work is to isolate and elucidate the structure of the bioactive compound from the root bark of *Lagerstroemia tomentosa* Presl (Pyinma-byu).

Botanical Description

Family name - Lythraceae

Botanical name - *Lagerstroemia tomentosa* Presl.

Local name - Pyinma-byu

Habit - Trees

Parts used - Root bark

Figure 1. The plant and flowers of pyinma- byu

Materials and Methods

Commercial grade reagents, solvents and analytical grade reagents were used for chemical analysis in this research. Analytical preparative Thin-Layer Chromatography was performed by using aluminium precoated sheets silica gel (Merk. Co. Inc Kiesel gel 60 F_{254}). Silica gel (Merk. Co. Inc Kiesel gel 70 -230 mesh ASTM) was used for Column Chromatography.

Sampling

Pyinma-byu was collected from Patheingyi Township, Mandalay Region. The root barks of this plant were used for analysis. After cleaning, the samples were cut into small pieces and allowed to air dry. The dried pieces were stored in a well-stoppered bottle and used throughout the experiments.

Phytochemical Screening on Root Bark Extract of Pyinma-byu

Different types of chemical constituents present in the selected sample were determined by preliminary phytochemical analysis (Harbone, 1993).

Antimicrobial Activity of Root Bark Extract of Pyinma-byu

Crude extract of Pyinma-byu was used to determine the antimicrobial activity by Agar well diffusion method in various solvents on six selected organisms, such as *Bacillus subtilis, Staphylococcus aureus, Pseudomonas aeruginosa, Bacillus Pumalis, Candida albican* and. *Mycobacterium* species.

Extraction and Isolation of Pure compound

800 g of air dried sample was percolated with 2 L of EtOH for two months. The ethanol extract was filtered and concentrated. It was extracted with 300 mL of ethyl acetate and evaporated. 2.58 g of ethyl acetate crude sample was obtained and chromatographed by column using silica gel (70-230) mesh as adsorbent and n-hexane, ethyl acetate as eluent with various ratios from non- polar to polar. After the column separation, totally (142) fractions were collected. Each fraction was checked by TLC, and combined the same R_f value fractions. After that, six combined fractions were obtained. Pale yellow solid fraction was checked by TLC for purity and amount. It gives one spot on TLC in R_f 0.43 with n-hexane: EtOAc (3 : 2 v/v) and UV active. It was recrystallized in n-hexane: EtOAc (9 : 1 v/v) for two times. Pale yellow needle shape crystal (0.0173 g) was obtained. The yield percent of pure compound was found to be (0.67 %) based upon the EtOAc crude extract.

Phytochemical Test of Pure Compound

The resulting pure compound of this sample was checked by flavonoid and polyphenol tests.

Antimicrobial Activity Screening of Pure Compound

The antimicrobial activities of pure compound isolated from Pyinma-byu were tested by using Agar well diffusion method on six selected organisms in DCPT, Insein, Yangon.

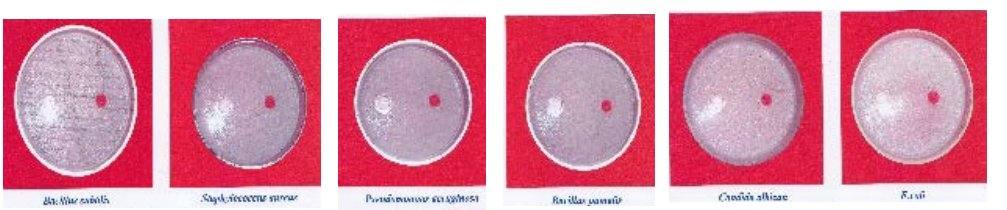

Figure 2. Antimicrobial activity of pure compound

Spectroscopic Studies of the Pure Compound

The pure compound was subjected to analyze by infrared spectrophotometer (hyper-IR-SHIMADZU) at the Department of Chemistry, University of Mandalay. Mass spectroscopy, Single Proton Nuclear Magnetic Resonance (^{1}H NMR), Carbon-13 Nuclear Magnetic

Resonance (^{13}C NMR) , Distortionless Enhancement by Polarization Transfer (DEPT), Double Quantum Filtered Correlation Spectroscopy (DQF-COSY) , Heteronuclear Multiple Quantum Coherence (HMQC) and Heteronuclear Multiple Bond Coherence (HMBC) spectral data were measured at Department of Natural Resource Chemistry, Faculty of Pharmacy, Mejio University, Japan.

Results and Discussion

Assignment of molecular formula, elucidation of pure compound and confirmation of this structure by fragmentation behaviour in EI mass spectra of selected sample were performed in this discussion.

Molecular Formula Determination of Pure Compound

FT-IR, ^{1}H NMR (500 MHz), ^{13}C NMR (125 MHz), DEPT and EI mass spectral data were used to determine the molecular formula of pure compound.

FT-IR Spectrum of Pure Compound

The FT-IR spectrum of compound, figure 5 represents the prominent functional groups of a pure compound. In this spectrum, the band which appears at 3394.5 cm^{-1} represents the O-H stretching vibration of alcohol group. The band at 3078.2 cm^{-1} shows the C-H stretching vibration of sp^2 hydrocarbons. The bands at 2923.9 cm^{-1} and 2846.7 cm^{-1} show the C-H stretching vibration of sp^3 hydrocarbons. The characteristic absorption at 1681.8 cm^{-1} indicates the presence of carbonyl group C=O in this pure compound. The band which occurs at 1596.9 cm^{-1} should be C = C ring skeletal stretching vibration of aromatic benzene ring. Moreover, the O-H group could also be confirmed by the occurrence of C-C-O stretching vibration bands at 1242.1 cm^{-1}. The C-O-C stretching vibration band of ether group is found at 1164.9 $cm^{-1}$and 1103.2 cm^{-1}. In addition, the existence of C-H out of plane bending vibration of trans or E and cis or Z alkenic groups could be detected at 933.5 cm^{-1} and 848.6 cm^{-1} (Silverstein, *et al*., 2005).

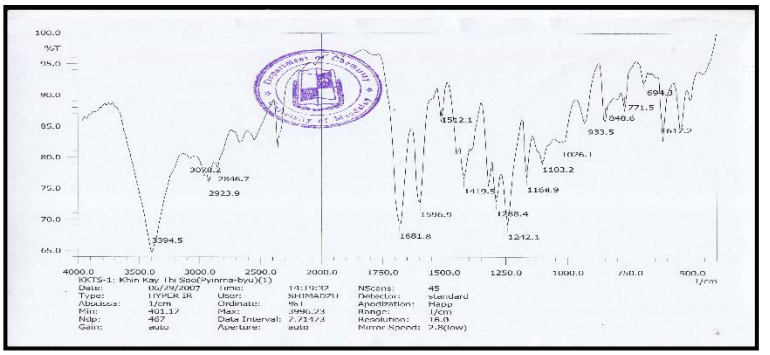

Figure 3. FT-IR spectrum of pure compound

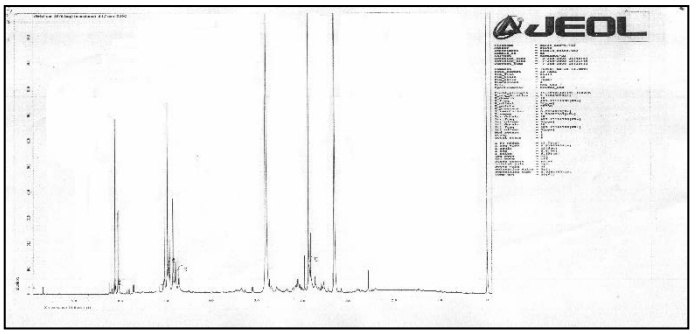

Figure 4. ^{1}H NMR spectrum of pure compound

Spectra Assignments of Pure Compound

^{1}H NMR (500 MHz) spectrum, figure 6 showed 10 protons that represents the chemical shifts, splitting patterns and coupling constants (J values) of protons. (Breitmaier, 2002) (Silverstein, *et al*., 2005)

The ^{13}C NMR (125 MHz) spectrum, figure 7 described the 16 total carbons in pure compound. DEPT spectrum, figure 8 presented that one methoxy methyl carbon, seven sp^2 methine carbons, seven sp^2 quaternary carbons and one carbonyl carbon, totally (16) carbons in this compound. HMQC spectrum of pure compound, figure 9 gave the direct correlation of proton and carbon. The chemical shift values of protons and their related carbons could be observed in this spectrum. (Silverstein, *et al*., 2005) (Crews, *et al*.,1998)

The partial molecular formula of this pure compound could be assigned as C_{16} H_{10} by using the data of ^{1}H NMR and ^{13}C NMR spectra. Thus, the partial molecular mass is 202. According to FT-IR spectrum, this compound should consist of at least one - OH (hydroxy), one C=O group and one ether functional group. Therefore, the extended partial molecular formula of this compound becomes C_{16} H_{11} O_3 and the partial molecular mass is 251. The molecular ion peak at m/z 284 which represents its molecular mass of this compound was obtained from EI mass spectrum of this compound, figure 10. Thus, the remaining partial molecular mass is [284 -251 = 33]. It should be one hydroxyl group and one ether oxygen atom. Therefore, the real molecular formula of compound could be assigned as C_{16} H_{12} O_5.

$$\text{Hydrogen deficiency index (HDI)} = C - \frac{H}{2} + 1 = 16 - \frac{12}{2} + 1 = 11$$

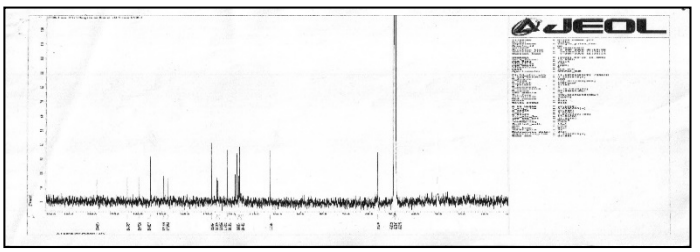

Figure 5. ^{13}C NMR spectrum of pure compound

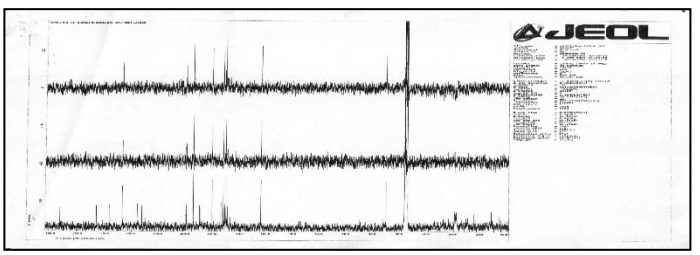

Figure 6. DEPT spectrum of pure compound

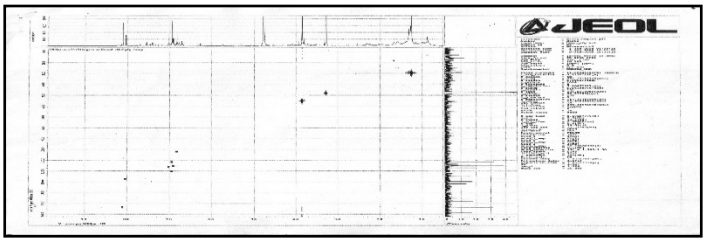

Figure 7. HMQC spectrum of pure compound

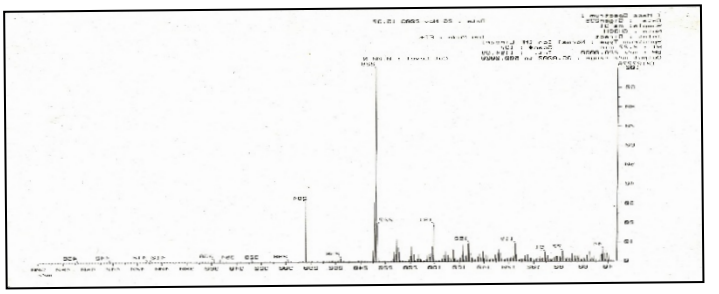

Figure 8. EI mass spectrum of pure compound

Confirmation of Molecular Formula of Pure Organic Compound

DEPT spectrum and FT-IR spectrum which represents the number and kind of carbon, proton, oxygen in this compound were used to confirm the molecular formula of pure compound. Eight sp^2 quaternary carbons, seven sp^2 methine carbons and one methoxy methyl group were presented in DEPT spectrum. FT-IR spectrum showed that the presence of one hydroxyl group, one carbonyl group and one ether oxygen group. Totally 16 carbons, 1 hydrogen and 4 oxygens were observed in this pure compound.

Therefore, the partial molecular formula of this compound = $C_{16}H_{11}O_4$.

The partial molecular mass = 267

EI mass spectrum gave the molecular ion peak at m/z 284 which indicates the molecular mass of compound .

Therefore, the remaining partial molecular mass = 284 – 267 = 17

Thus, the remaining group should be one -OH group. .

Hence, the real molecular formula of pure compound must be $C_{16}H_{12}O_5$

Structural Elucidation of Pure Compound

The structure of a pure compound was elucidated by applying DQF-COSY, HMBC, HMQC spectral data, ^{1}HNMR splitting pattern and coupling constant (J value). From these observations, the following fragments could be assigned.

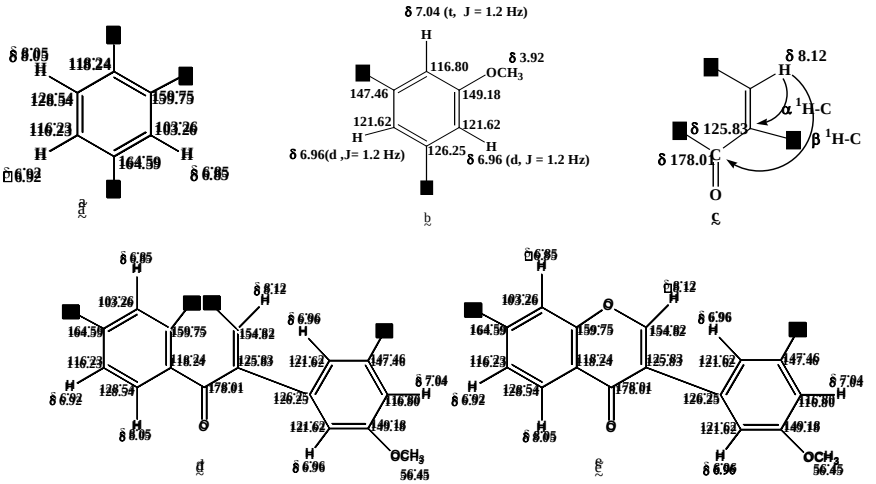

The elucidated structure of pure isoflavonoid compound could be described. The complete structure of this compund is

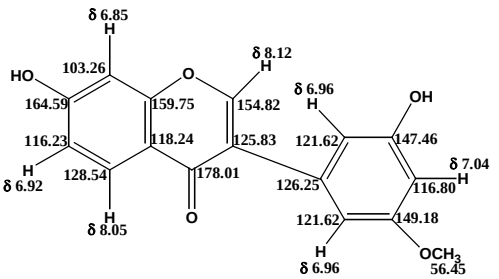

EI mass Fragmentation Behaviour of Pure Compound

The elucidated structure of pure compound could be confirmed by EI mass fragmentation behaviour of this compound (Poster and Baldas, 1971).

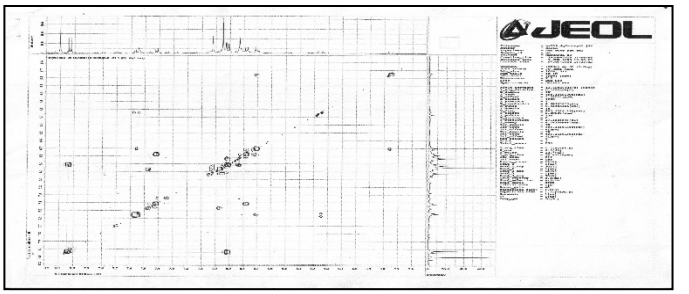

Figure 9. DQF-COSY spectrum of pure compound

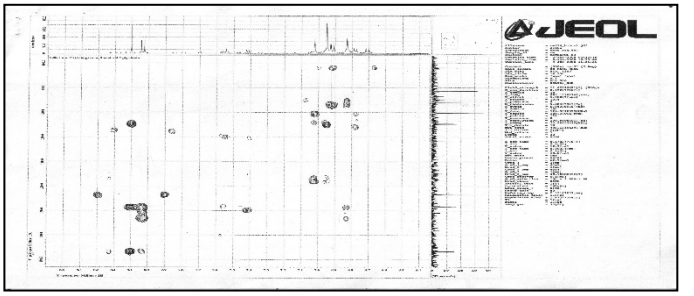

Figure 10. HMBC spectrum of pure compound

Conclusion

In this analysis, the presence of alkaloids, flavonoids, glycosides, phenols, polyphenols, reducing sugars, saponins, steroids and terpenes of root bark of Pyinma-byu were determined by the phytochemical screening of this sample. Ethyl acetate crude extract of sample showed that the medium antimicrobial activities on four tested organisms. By applying Thin-Layer and Column Chromatographic methods, a pure compound was isolated from this crude extract. A pure compound which is pale yellow needle shaped crystal form (0.0173 g, 0.67 %) was found to be in sample by column separation. The pure compound must be flavonoid compound due to the result of positive nature of flavonoid and polyphenol tests. Antimicrobial activity test was used to recheck this pure compound which gave medium activities on four tested organisms, such as *Bacillus subtilis, Staphylococcus aureus, Pseudomonas aeruginosa* and *Escherichia coli.*

The molecular formula of this pure compound was determined as C_{16} H_{12} O_5 by applying some modern spectroscopic technique, such as FT-IR, ^{1}H NMR (500 MHz), ^{13}C NMR (125MHz), DEPT , HMQC and EI-mass spectral data, respectively. DQF-COSY, ^{1}H NMR, splitting pattern, coupling constants (J values) and HMBC spectroscopic studies were used to elucidate the complete structure of this isolated compound which gave rise to the following isoflavonoid compound structure.

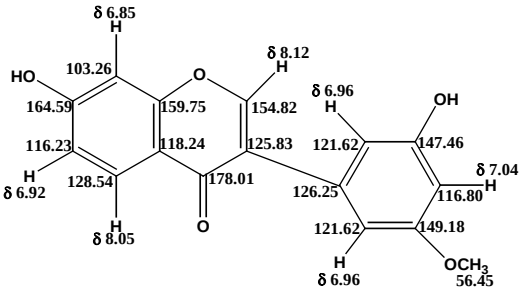

The IUPAC name of this isolated compound is 7-hydroxy-3-(3-hydroxy-5-methoxyphenyl)-4H-chromen-4-one.

It is noted that the elucidated structure of pure compound which was isolated from Pyinma-byu could be confirmed by naturally occurring isoflavonoid compound. This plant may be one of its mode of action in traditional medicine.

Acknowledgement

I am thankful to Dr Kay Thi Thin, Rector of Taunggyi University, for her permission and invitation for URJ. I owe great gratitude to Dr Ni Ni Than, Professor and Head, Department of Chemistry, University of Yangon for her invaluable guidance and permission to prepare this paper.

References

Breitmaier, E. (2002). *Structure Elucidation by NMR in Organic Chemistry, A Practical Guide*, Germany, John Wiley & Sons, Inc., 3rd edn, 48-64

Crews, P., J. Rodriguez and M. Jaspars. (1998). *Organic Structure Analysis*, New York, University of California, Santa Cruz, Oxford University.

Gangola, S., P. Khati, P. Phatt and A. Sharma. (2017). "India as the Heritage of Medicinal Plant and Their Uses". *Current Trends in Biomedical Engineering & Biosciences.*, **4** (4), 1-2

Harbone, J. B. (1993). *Phytochemical Dictionary, A Handbook Bioactive Compounds from plants*. London, Taylor and Francis, 2nd edn, 120-128

Mohan, J. (2000). *Organic Spectroscopy*. India, Department of Chemistry, Maharshi Dayanand University

Poster, Q. N. and J. Baldas. (1971). *Mass Spectrometry of Heterocyclic Compounds*. New York, Wiley-Inter Science, a Division of John Wiley & Sons, Inc., 120-134

Silverstein, R. M., X.W., Francis, J. K., David and L.B., David. (2005). *Spectrometric Identification of Organic Compounds*, USA, John Wiley& Sons, Inc. 7th edn, 320-350

Characteristics of Solid State, Nuclear Track Detectors (SSNTDs) for Detection of Neutron and Gamma Radiations

Mar Mar Khine[1], Hnin Hnin Than[2], Naw Aye Aye Thein[3]
& Hnin Wut Yi Kyaw[4]

Abstract

Solid state nuclear track detectors (SSNTDs) are widely used to measure the various types of ionizing radiation. In this work, the interaction between SSNTDs (mica, film and glass) and two types of radiations (neutron and gamma) were studied. For this purpose, neutron radiation and gamma ray were exposed to mica, film and glass detectors. And then, these all detectors were chemically etched with respective etchant solutions to detect the fission track by using the optical microscope. In the investigation of track formation on irradiated SSNTDs, non-irradiated SSNTDs images were always comparatively studied. Besides, the net track densities of SSNTDs were studied. Finally, the characterization of mica, film and glass detectors (before and after the gamma irradiation) was also made by using SEM (Scanning Electron Microscope) analysis.

Keywords*:* mica, film, glass, radiation, SSNTDs

Introduction

Solid State Nuclear Track Detectors (SSNTDs) are insulating solids both naturally occurring and man-made. SSNTDs are also known as etched track detectors. These materials are light weight, small volume, free of electronics, easy to process and very cheap comparing to any active detectors. These detectors are used to measure the radon concentration in the environmental samples (Yousef, 2017).

There are several types of these detectors including inorganic crystals (e.g., apatite, zircon, quartz, mica, etc), glasses (e.g., phosphate, soda lime, silica, flint, etc.) and plastics (e.g., cellulose acetate, cellulose nitrate and Columbia Resin (CR-39) plastics, etc.) (Sultan,2019). Plastics, the most sensitive group, have been widely used in the study of heavy ions, cosmic rays, neutron dosimetry and radon dosimetry etc. (Kumar, 1993).

[1] Lecturer, Dr, Department of Chemistry, Dawei University
[2] Professor and head, Dr, Department of Chemistry, Mubin University
[3] Lecturer, Dr, Department of Chemistry, University of Yangon
[4] MSc, Department of Chemistry, University of Yangon

Mica, any of a group of hydrous potassium, is aluminum silicate minerals. It is a type of phyllosilicate, exhibiting a two-dimensional sheet or layer structure. Due to its ability to cleave into thin, nearly transparent sheets of considerable size, low coefficient of friction between individual sheets, a low coefficient of thermal expansion, thermal resistance, general inertness, and excellent electrical- and heat-insulating properties, muscovite has many industrial and scientific uses (Dietrich, 2013).

The photographic film is one of the first used in radiation natural detection, due to traceable effect produced on photographic film. A commonly used detector is the cellulose nitrate films, which are sensitive in the detection of alpha and heavy ion rays (Scarlat, 2008).

The glass track recorders have a special place among the SSNTDs due to their better homogeneity, transparency, and relatively high threshold for registration of nuclear charged particles. They are more stable under a variety of environmental conditions and rather insensitive to lightly ionizing radiations. Glass detectors have played an important role in dosimetry (Fowler, 1982)

The areas of potential applications of solid state nuclear track detectors are growing rapidly. They have been employed in various fields and in particular to nuclear science and technology. The disciplines where track detectors are regularly employed in nuclear physics, nuclear imaging, nuclear technology, space physics, microanalysis, mine safety, environmental research, uranium prospecting, biomedical sciences, material sciences, and geological sciences (Kalsi, 2005).

Materials and Methods

Sample Collection

Mica (natural muscovite mineral) ($KAl_3Si_3O_{10}(OH)_2$) was collected from Department of Geology, Dawei University. Photographic film ($C_{18}H_{21}N_{11}O_{38}$) Kodak Colorplus and glass were purchased from the local market.

Sample Preparation

Film and mica samples were cut into small pieces of 1 x 1 cm^2. Glass was cut into small pieces of 1 x 1 $inch^2$.

Chemicals and Apparatus

40% potassium hydroxide solution (v/v), 40 % hydrofluoric acid solution (v/v), volumetric flasks (50 mL), glass rod, glass tube, analytical balance, water bath, beaker (50 mL)

Procedure

In this research, mica, film and glass were used as SSNTDs. These three types of sample were irradiated with neutron from Am (Be) source with the flux 10^4 $ncm^{-2}s^{-1}$ at 3.5 cm distance from source target for 30 days in Nuclear Chemistry Laboratory, University of Yangon. At the same time, these three types of other detectors were irradiated with 50 kGy and 100 kGy gamma radiation from Co-60 source (dose rate 1.00 k Gy/h) for 50 and 100 hrs at Department of Atomic Energy, Ministry of Education. After an exposure time, all mica and film detectors were etched in 40 % KOH solution at 60 °C for 30 minutes in a temperature controller water bath. Besides, all glass detectors were etched in 40 % HF solution at room temperature for 60 seconds. Then, these detectors were washed with distilled water, dried and scanned under a microscope with 400 × magnification. After that, these etched detectors were characterized by SEM technique.

Results and Discussions

In this work, non-irradiated SSNTDs are always compared with the irradiated SSNTDs. In the study of the neutron irradiation process, formation of hole tracks on mica, film and glass were observed due to the interaction of neutron. It can be clearly seen in Figure 1(b), Figure 2 (b) and Figure 3(b).And then, the photomicrographs of non-irradiated mica, film and glass are shown in Figure 1 (a), Figure 2(a) and Figure 3(a) respectively. Therefore, it may be suggested that these are the good SSNTDs for detection of neutron with low flux (10^4 $ncm^{-2}s^{-1}$). It can be found that mica, film and glass detectors had detected neutron from Am

(Be) neutron source. These formations of tracks agreed well with the literature (Spohr, 1990).

The resulting photomicrographs of irradiated mica, film and glass with different doses of gamma radiation (50 kGy and 100 kGy) are seen in Figure 4, Figure 6 and Figure 8. Comparison with the ordinary detectors such as mica, film and glass are also shown in all of these figures respectively. The black spots formed by different gamma doses were observed on all of these detectors but the track densities of these detectors were different. According to the results, it was found that the higher the gamma doses, the greater the track densities of the detectors. The calculated track densities are reported in Table 1 (mica), Table 2 (film) and Table 3(glass). Besides, these obtained data can be clearly seen in Figures 5, 7 and 9. The calculations of track density of these detectors were carried out by using the following formula (Spohr, 1990).

$$\text{Track density} = \frac{\textit{Number of tracks}}{\textit{Microscopic} \text{ view area}}$$

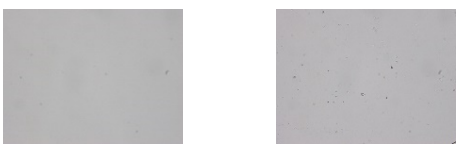

a b

Figure 1. (a) Photomicrograph of non-irradiated mica
(b) Photomicrograph of irradiated mica with neutron from Am (Be) source (×400)

a b

Figure 2. (a) Photomicrograph of non-irradiated film
(b) Photomicrograph of irradiated film with neutron from Am (Be) source (×400)

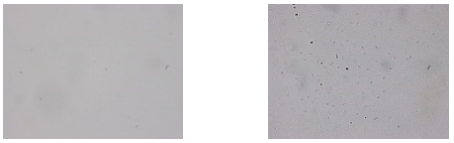

a b

Figure 3. (a) Photomicrograph of non-irradiated glass
(b) Photomicrograph of irradiated glass with neutron from Am (Be) source (×400)

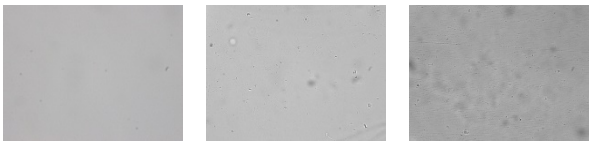

a b c

Figure 4. Photomicrographs of mica detector
(a) non-irradiated
(b) 50 kGy of gamma irradiated
(c) 100 kGy of gamma irradiated

Table 1. Net Track Density on Mica with Different Gamma Doses

Gamma dose (kGy)	**Net track density (10^4) (tracks/cm^2)**
50	1.0694
100	1.2731

Microscopic view area = 19.6375×10^{-4} cm^2 (×400)

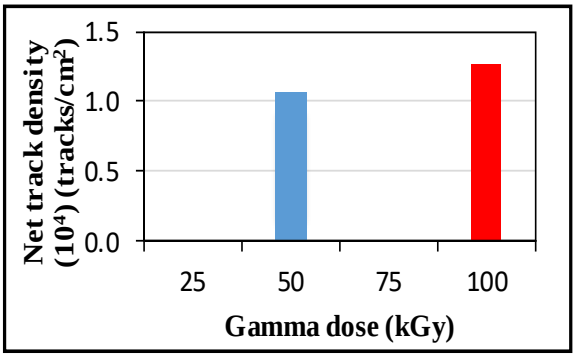

Figure 5. Relation between different gamma doses and the net track density etched with 40 % KOH for 30 min (mica)

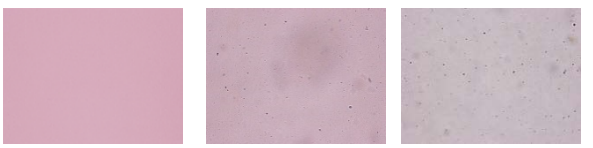

a b c

Figure 6. Photomicrographs of film detector
(a) non-irradiated
(b) 50 kGy of gamma irradiated
(c) 100 kGy of gamma irradiated

Table 2. Net Track Density on Film with Different Gamma Doses

Gamma Dose (kGy)	**Net Track Density (10^4) (tracks/cm^2)**
50	1.5786
100	2.0878

Microscopic view area = 19.6375×10^{-4} cm^2 (×400)

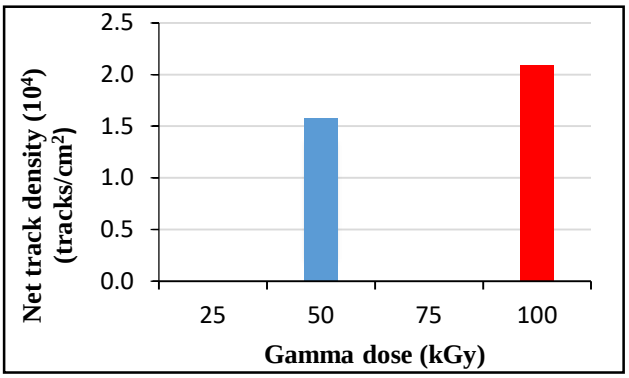

Figure 7. Relation between different gamma doses and the net track density etched with 40 % KOH for 30 min (film)

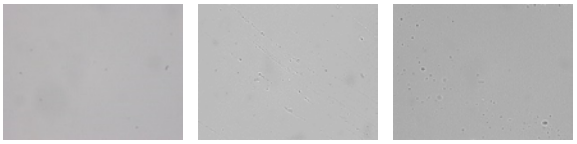

a b c

Figure 8. Photomicrographs of glass detector
(a) non-irradiated
(b) 50 kGy of gamma irradiated
(c) 100 kGy of gamma irradiated

Table 3. Net Track Density on Glass with Different Gamma Doses

Gamma Dose (kGy)	**Net Track Density (10^4) (tracks/cm^2)**
50	0.6619
100	1.3239

Microscopic view area = 19.6375×10^{-4} cm^2 (×400)

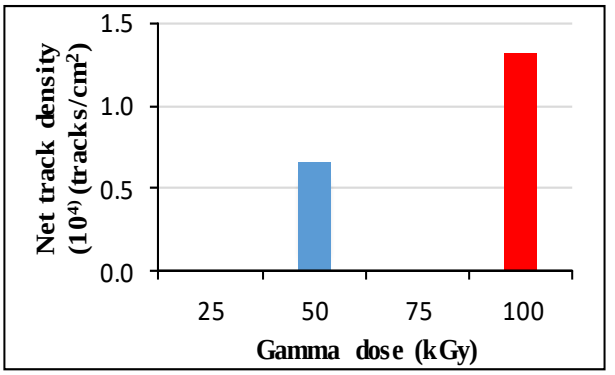

Figure 9. Relation between different gamma doses and the net track density etched with 40 % HF for 60 s (glass)

In this research work, SEM method was used to investigate the surface morphology on various SSNTDs such as mica, film and glass. SEM photomicrographs of gamma irradiated mica detectors are shown in Figures 10(b) and (c). SEM photomicrographs of gamma irradiated film detectors are reported in Figures 11 (b) and (c). Figures 12 (b) and (c) show the SEM photomicrographs of gamma irradiated glass detectors. Studying from these figures, it was found that all of these gamma exposed detectors were different from non-irradiated detectors. The surface morphology of irradiated detectors were changed into different surface textures.

a b c

Figure 10. SEM photomicrographs of mica detector
(a) non-irradiated
(b) gamma irradiated (50 kGy)
(c) gamma irradiated (100 kGy)

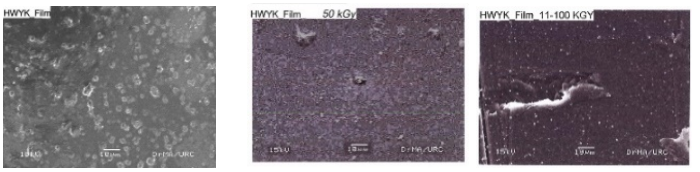

a b c

Figure 11. SEM photomicrographs of film detector
(a) non-irradiated
(b) gamma irradiated (50 kGy)
(c) gamma irradiated (100 kGy)

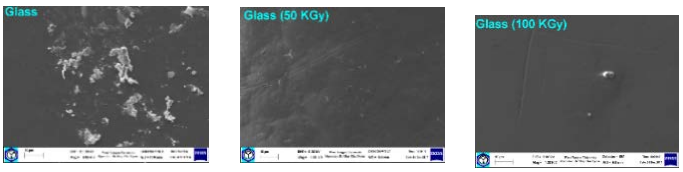

a b c

Figure 12. SEM photomicrographs of glass detector
(a) non-irradiated
(b) gamma irradiated (50 kGy)
(c) gamma irradiated (100 kGy)

Conclusion

The present work deals with the study of the solid state nuclear track detectors (mica, film and glass) irradiated with neutron and gamma radiations. In this investigation, it was observed that the greater the energy of gamma ray, the higher the track density in each detector. From the SEM analysis, it was clearly seen that the surface morphology of irradiated detectors had changed into different surface textures. Therefore, SEM was recommended as one of the most appropriate techniques for solid state nuclear track detectors research field. According to overall results, it was clearly found that neutron and gamma radiation can be detected by using solid state nuclear track detectors.

Acknowledgements

I would like to express my deep appreciation to professor and head Dr Daw Khin Aye May, Department of Chemistry, Dawei University, for her kind provision of this research paper. I also wish to express my profound gratitude to all Associate Professors, teachers and staff in my Department for their helps, kindness and comments offered to me during the course of this research work.

References

Dietrich, R. V. (2013). *Mica Mineral*. U.S.A: Central Michigan University, 1-4

Fowler, P. H. and V. M. Clapham. (1982). *On the Improved Energy Resolution of Glass Track Recorders in Solid State Nuclear Track Detectors.* UK: Pergamon Press, 321-322

Kalsi, P. C., A. Ramaswami, and V. K. Mnachanda. (2005). *Solid State Nuclear Track Detector and Their Applications*. India: Gurau Nanak Dev University, 15-18

Kumar, A. (1993). *Study of Characteristics of Heavy Ions in Plastics and Applications.* India: Department of Applied Physics, Z. H. College of Engineering and Technology, Aligarh Muslim University, 42-48

Scarlat, F., A. Scarisoreanu, M. Oane, E. Mitru, and E. Badita. (2008). "Determination of Absorbed Dose Using Dosimetric Film". *Radiation Physics & Protection Conference*, **9**, 313-314

Spohr, R. (1990). *Ion Tracks and Microtechnology: Principles and Applications.* Germany: Bertelsmann Publishing, 155-156

Sultan, M. F. (2009). "Relationship between the Energy of Alpha Particle and the Geometrical Parameters of Alpha Particle Track on Cr-39 Nuclear Track Detector". *Iraqi Academic Scientific Journals*, **20(**3), 83-84

Yousef, H. A. (2017). "Effect of Gamma Rays on the Bulk Etching Rate of LR-115 Detector", *Journal of Applied Physics*, **9**(2), 14-15

Study on Extraction, Characterization and Colour Fastness Properties of Red Onion Dye

Zue Zue Win Myint[1], Nay Mar Soe[2] & Moe Win[3]

Abstract

Onion's outer skin waste is found all over the world. It is very useful for the domestic and industrial products. This study was focused on extraction of natural dye from red onion skin and also study colour fastness properties of extracted dye. Red onion dye was prepared by two methods such as aqueous extraction and solvent extraction. Yield percentages of extracted dyes were found to be 6.6 % from aqueous extraction and 3.2% from solvent extraction. Extracted red onion dye was characterized by pH measurement, UV-visible and FT IR spectroscopy. From pH data observation, aqueous dye was 4 and solvent dye was 5. According to UV-visible spectral data, π-π^* transition was found in two extracted red onion dyes. In the FT IR spectrum results, aqueous dye and solvent dye were consistent with reported value. Cotton fabric was dyed with two extracted dyes by three methods such as without mordanting, pre-mordanting and post-mordanting. In this dyeing process, mordant copper (II) sulphate and mordant alum were used. Then, colour fastness properties of dyed cotton fabric were tested by washing fastness properties and rubbing fastness properties. According to these results, use of mordant copper (II) sulphate with onion dye was of better quality than that of mordant alum in textile dyeing.

Keywords: Red onion skin waste, onion dye, colour fastness properties

Introduction

Natural dye was derived from plants, invertebrates or minerals. Nowadays, natural dyes are commonly used in the cosmetic industry due to no side effects, UV protection and anti-aging properties. These are safe, eco-friendly, easier to use, unique, used as antioxidants, clothes dyed with natural dyes yield higher profits to the dyers and manufactures, variety of shades produced and used in cosmetics. (Islam *et al.*, 2013). Recycling is the process of converting waste materials into new materials and objects.

[1] MSc. Student, Department of Chemistry, Taungoo University

[2] Professor, Department of Chemistry, Yangon University of Education

[3] Lecturer, Department of Chemistry, Taungoo University

The onion waste includes the dry skin, outer layers, roots and stalks are not big enough for commercial use and they are damaged. In this study, natural dye was recycled from red onion waste with chemical processing. In addition, extracted onion dye was characterized and also determined colour development on cotton fabric. Finally, it was also studied the application of natural dye in textile.

Red Onion Skin

Red onion skin is a natural by-product waste from food industry. (Waldron, 2001). Large amount of onion wastes are produced by consumption of onion both domestically and industrially, making it necessary to search for their utilization. These wastes get decayed and add themselves to the soil causing odor and in some cases causing harm to the environment (Benitez, 2011).It gives bright reddish brown colour in textile colouration. Previous studies on red onion skin investigated large amounts of flavonoids, flavones and anthocyanin (natural dyes) (Oance, 2013). Pelargonidin is an anthocyanin, a type of plant pigment used in food and industrial dyes. The skin of onion is inedible however it contains a dyestuff called “Pelargonidin” (3, 5, 7, 4'tetra hydroxyl antocyanidol) (Mishra and Patni, 2011).

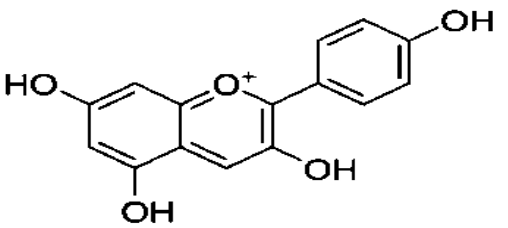

Figure 1. Structure of Pelargonidin (3,5,7,4'tetrahydroxyantocyanidol)

Materials and Methods

Red onion skin waste samples were collected in Nyaung Pin Lay Market, Taungoo Township, Bago Region, and Myanmar. The collected samples were dried at room temperature, away from direct sunlight. The dried samples were made into powder by using grinding machine. The powdered samples were stored in air-tight container to store for further analysis.

Extraction of Red Onion Dye

Red Onion dyes were extracted by aqueous extraction and solvent extraction methods. Aqueous extraction method was traditionally used to extract dyes from plants and other materials. In solvent extraction, natural dye was extracted from onion skin wastes by using ethanol. Acid or alkali can be added to alcoholic solvents to facilitate hydrolysis or glycosides and release of colouring matter. (Gawish *et al.,* 2016)

Characterization of Extracted Red Onion Dye

The extracted red onion dye was characterized by pH, UV-visible and FT IR spectroscopy. The pH of extracted red onion dye solution was determined using pH paper. Extracted dye was identified by modern spectroscopic techniques such as UV-visible and FT IR spectroscopy.

Dyeing of Cotton Fabric with Extracted Dye

Cotton fabric was dyed by three kinds of methods. These are (1) without mordanting method (2) pre-mordanting method and (3) post-mordanting method. After dying, the amount of dye uptake on cotton fabric and colour development on dyed cotton fabric was determined.

Testing the Colour Fastness Properties of Dyed Cotton Fabrics

In general, clothing should be tested for colour **fastness** before using bleach or other cleaning products. The colour fastness properties of dyed cotton fabrics were tested at Paleik Textile Factory. In washing fastness properties, the colour change of the material was assessed by comparing with the original dyed cotton fabric. The rubbing fastness properties of dyed cotton fabric was determined by Rubbing Tester machine (Crock Meter M/C Germany CM/I MFL-014).

Results and Discussion

Yield Percent of Dye Extraction

Red onion dye was extracted by aqueous extraction and solvent extraction. According to this observation, yield percent of aqueous extraction (6.6%) was more than that of solvent extraction (3.2%).

Determination of pH

pH of extracted red onion dye were tested by pH paper. In this study, it was found that aqueous dye was 4 and solvent dye was 5. The reported pH value was 4 to 8 (Gawish et al., 2016). The observed pH data was consistent with reported value and it was found that two extracted dyes were acidic dyes.

Study on UV-visible spectroscopy

According to literature survey, the absorbance of red onion colorant extract has two peaks at 290 nm and 363 nm in UV region. From UV-visible spectral data, extracted aqueous dye in observed values were 290 nm and 330 nm. Extracted solvent dyes in observed value were 296 nm and 369 nm. So, it was observed that π-π* transition was found in two extracted dyes and these were consistent with reported data.

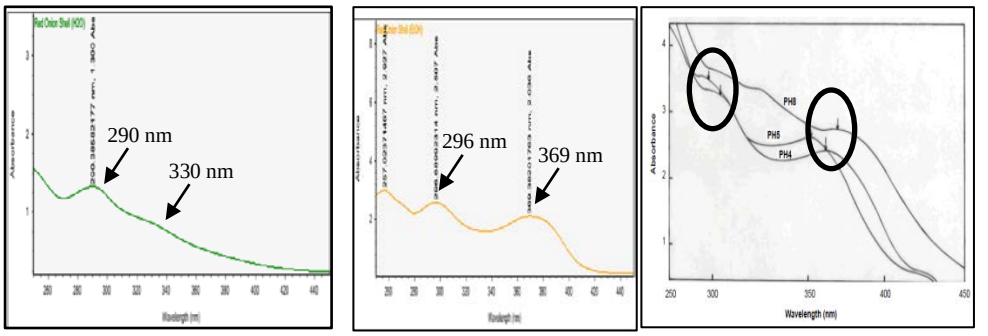

(a) Aqueous dye (b) Solvent dye (c) Reported data

Figure 2. UV-visible spectral data of two extracted dyes and reported data

Table 1. UV-visible Spectral Data of Two Extracted Dyes

	λ_{max}(nm)		Type of transition	Remark
	Observed value	Reported value		
Aqueous Dye	290	290-320	π-π*	Colourant absorbance radiation were observed
	330	320-400	π-π*	
Solvent Dye	296	290-320	π-π*	
	369	320-400	π-π*	

*(Gawish et al., 2016)

Study on FT IR spectroscopy

FT IR spectrum of two extracted dyes and reported onion dye were shown in Figure 3. The observed FT IR spectral data of two extracted dyes were consistent with reported value (Geetha, 2013). Pelargonidin is polyphenol which is found in plants as red pigments. According to this data, extracted dyes contained phenol group and there are in accordance with the reported data. These spectral data were indicated in Table 2.

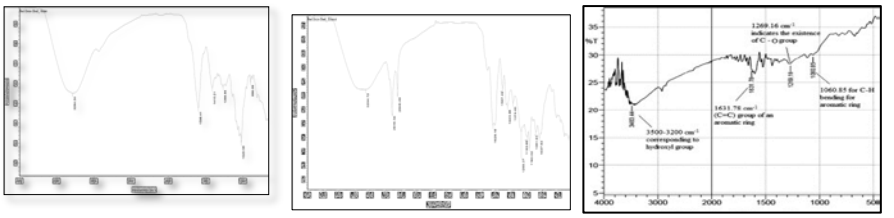

Aqueous dye Solvent dye Reported dye

Figure 3. FT IR spectrum of two extracted dyes and reported dye

Table 2. FT IR Spectral Data of Two Extracted Onion Dyes

Wave number (cm^{-1})			Mode of Vibration
Observed value		Reported value*	
Aqueous dye	Solvent dye		
3284	3254	3483	Phenolic O-H stretching
3000	3050	3100-3000	-C=C-H stretching
1598	1629	1631	Aromatic C=C stretching (benzene ring)
1266	1269	1269	C-O stretching
1020	1081	1060	Aromatic C-H bending

* (Geetha, 2013)

Dyeing of Cotton Fabric with Extracted Onion Dye

Colour of dyed cotton fabric without mordant, with pre-mordant and post-mordant were shown in Figure 4. Dying quality of three methods was similar quality. However, visible colour of pre-mordanting cotton fabric was brighter than other two.

(a) without mordant (b) Pre-mordant (c) Post- mordant

Figure 4. Colour of dyed cotton fabrics

Colour Fastness Properties of Onion Dyed Cotton Fabric

(a) Washing fastness properties of onion dyed cotton fabric

Washing fastness properties of dyed cotton fabric using pre-mordant and post- mordant were studied. Pre-mordant and Post-mordant using alum and two extracted dyes were showed in Figure 5. Similarly, pre-mordant and post-mordant of Copper (II) sulphate and two extracted dyes were showed in Figure 6.Mordant copper (II) sulphate used cotton fabric was found between 4 to 5 grade of colour changing and colour staining properties. Mordant alum used cotton fabric was found between 3-4 grade of colour changing and between 4-5 grade of colour staining properties. (Table 3) From these observations, mordant copper (II) sulphate used in cotton fabric was better quality of washing fastness properties than mordant alum used.

Table 3. Results of Washing Fastness Properties of Onion Dyed Cotton Fabric

Fabric Type	Mordant	Method of Mordanting	Dyed Cotton Fabric			
			Solvent dye		Aqueous dye	
			Colour ChangingGrade	Colour Staining Grade	Colour Changing Grade	Colour Staining Grade
Cotton	Alum	Pre-mordanting	3-4	4-5	4	4
		Post-mordanting	3-4	4-5	4-5	4-5
	Copper (II) sulphate	Pre-mordanting	4	4	4-5	4
		Post-mordanting	4	4-5	4-5	4-5

5 = excellent, 4 = good, 3 = fair, 2 = poor, 1 = very poor

(a) Pre-mordant using Alum

(b) Post-mordant using Alum

Figure 5. Washing fastness properties of dyed cotton fabric using mordant alum

(a) Pre-mordant using Copper (II) sulphate

(b) Post-mordant using Copper (II) sulphate

Figure 6. Washing fastness properties of dyed cotton fabric using mordant Copper (II) sulphate

(b) Rubbing fastness properties of onion dyed cotton fabric

Rubbing fastness properties of dyed cotton fabric using pre-mordant and post-mordant using alum and extracted dyes were shown in Figure 7.

Using post-mordant Copper (II) sulphate and two extracted dyes of rubbing fastness properties were indicated in Figure 8. The results of rubbing fastness properties of dyed cotton fabric were shown in Table 5. From these results, mordant copper (II) sulphate and mordant alum are similar quality in rubbing fastness properties.

Figure 7. Rubbing fastness properties of dyed cotton fabric using pre and post mordant Alum

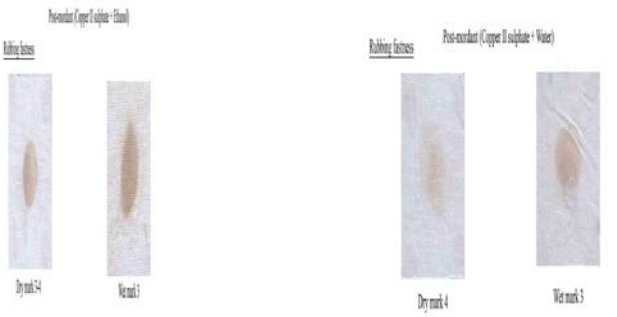

Figure 8. Rubbing fastness properties of dyed cotton fabric using pre and post mordant Copper (II) sulphate

Table 5. Results of Rubbing Fastness Properties of Onion Dyed Cotton Fabric

Fabric Type	Mordant	Method of Mordanting	Dyed Cotton Fabric			
			Solvent dye		Aqueous dye	
			Dry Rub	Wet Rub	Dry Rub	Wet Rub
Cotton	Alum	Pre	3	3	4	3
		Post	4	3	4	3
	Copper (II) sulphate	Pre	4	3	4	3
		Post	3-4	3	4	3

Conclusion

Red onion dye was extracted by two methods such as aqueous extraction and solvent extraction. The yield percentage of aqueous extraction was 6.6 % and that of solvent extraction is 3.2 %. From the pH data observation, aqueous dye was 4 and solvent dye was 5. Therefore, two extracted dyes were acidic dye. According to UV-visible spectral data, π-π^* transition was found in two extracted dyes. FT IR spectral data of two extracted dyes showed that the presence of O-H stretching, C=C stretching, C-O stretching and aromatic C-H bending. From these results, extracted dyes were in accordance with the reported dye data. Cotton fabrics were dyed with two extracted dyes by three methods. Then, colour fastness properties of washing fastness properties and rubbing fastness properties were tested. From these results, mordant copper (II) sulphate was better quality of washing fastness properties than mordant alum. However, mordant copper (II) sulphate and mordant alum were using in rubbing fastness properties which are similar quality. According to this observation, onion dye can be extracted easily and it is also cost effective. Moreover, it has been used better quality due to its colour fastness properties. Therefore, Onion dye can be used as a substitute for commercial dyes in textile industry.

Acknowledgements

The author acknowledges the Ministry of Education, Department of Higher Education, Pro-Rector Professor Dr Pyone Pyone Aung and Pro-Rector Professor Dr Kay Thwe Hlaing, Yangon University of Education. I also thank extend to Professor and Head (retired) Dr Mi Mi Kyaing, Department of Chemistry, Taungoo University for allowing to carry out this research.

References

Benitez,Y., E., M. A Molla. Y.Martin-Cabrejas, F. J Aguilera. K.Lopez-Andreu. L. A.Cools. Terry and R. M. Esteban. (2011). "Characterization of industrial onion wastes (Allium cepa L.): Dietary fiber and bioactive compounds". *Plant Foods for Human Nutrition*, **66.** 48-57

Gawish, S.M., H.M. Holmy. A.N. Ramadan. R. Farcuk and H.M. Mashaly. (2016)." UV Protection Properties of Cotton, Wool, Silk and Nylon Fabrics Dyed with Red Onion Peel, Madder and Chamomile Extracts". *Journal of Textile Science & Engineering*, **6**(4), 1-13

Geetha, B., and V. Judia Harriet Sumathy. (2013). "Extraction of Natural Dyes from Plants". *International Journal of Chemistry and Pharmaceutical Sciences*, **1** (8), 502-509

Islam, U.I, S. et al. (2013)." Perspective for natural product-based agents derived from industrial plants in textile application- a review". *Journal of Cleaner Production*, 1-17

Mishra, P. and V. Patni. (2011). "Extraction and application of dye extracted from eriophyid leaf galls of *Quercusleucotrichophora* – A Himalayan blue jack oak", *African Journal of Biochemistry Research* **3** (5), 90-94

Oancea S. and O. Draghici.(2013). "pH and thermal stability of anthocyanin-based optimized extracts of Romanian red onion cultivars", *Czech J Food Sci* **31**, 283-291

Waldron, K. W. (2001). "Useful ingredients from onion waste". *Food SciTechnol*, **15**(2), 38-41

Investigation on some Chemical Constituents in Essential Oil and Antibacterial Activity of *Cinnamomum obtusifolium* Roxb. (Na-lin-gyaw) Roots

Tet Tun*

Abstract

Myanmar medicinal plant namely *Cinnamomum obtusifolium* Roxb. (Na-lin-gyaw, NLG) possessing Lauraceae family has been chosen to investigate some chemical constituents in essential oil and the antibacterial activity of its roots. The preliminary phytochemical investigation reveals the presence of alkaloids, α-amino acids, carbohydrates, flavonoids, glycosides, organic acids, phenolic compounds, reducing sugars, starch, steroids, tannins and terpenoids. Based on the steam distillation method, the essential oil (0.04 % yield) was extracted from the roots of NLG. In accord with GC-MS spectral results, five organic constituents namely 2,4-di-tert-butylphenol, Asarone, 1,2,3-trimethoxy-5-[(E)-prop-1-enyl]benzene, Curcumenol and Dehydrocostus lactone were detected from essential oil of roots of NLG. By agar well diffusion method, the antibacterial activity of PE extract (inhibition zone diameter range = 11 ~ 12 mm), EtOAc extract (inhibition zone diameter range = 11 ~ 13 mm), EtOH extract (inhibition zone diameter range = 14 ~ 17 mm), MeOH extract (inhibition zone diameter range = 15 ~ 18 mm) and H_2O extract (inhibition zone diameter = 11 mm) were screened against five species of bacteria namely *Bacillus subtilis*, *Staphylococcus aureus*, *Pseudomonas aeruginosa*, *Bacillus pumilus* and *Escherichia coli*. In addition, the minimum inhibitory concentrations (MIC) of ethanol (3.125 mg/mL) and methanol (0.012 mg/mL) extracts against *P.aeruginosa* and that of both extracts (1.9×10^{-4} mg/mL) against *B.pumilus* and *Escherichia coli* were also determined by using serial dilution method.

Keywords : *Cinnamomum obtusifolium* Roxb., Na-lin-gyaw, essential oil, antibacterial activity, MIC

* Professor (Head), Dr., Department of Chemistry, Sittway University

Introduction

Medicinal plants represent a rich source of antimicrobial agents. These plants possess potent medicinal value that is due to the presence of a variety of phytochemical constituents in the plant tissues which cast a definite physiological action on the human body (Thalwal *et al*., 2013). They are used medicinally in different countries as well a source of many potent and powerful drugs (Mahesh and Satish, 2008). The essential oils are plant-based volatile oils with strong aromatic components that are made up of different chemical compounds. Oils from hundreds of plant species are available commercially. Numerous studies have demonstrated the efficiency of essential oils in low doses in the fight against bacterial pathogens even against multi-resistant bacteria (Hesham *et al*., 2016)

Cinnamomum obtusifolium is ever green tree. Leaves quiteglabrous 8-12 in; very coriaceous, elliptic-oblong, obtuse-acute 3-nerved, nerves not impressed above, panicles very large at stout. Flowers small, 2-sexual or polygamous, in axillary and subterminal panicles, females usually largest, with often fewer parts – perianth-tube short, segments 6, subequal. Perfect stamen 9 or fewer, filaments of 1st and 2nd series glandular (Grieve, 1976). Flowering period is February to March and fruiting period is September to October (Choudhury *et al*., 2013). It is distributed in India, Bhutan, Nepal, Bangladesh, China, Myanmar, Thailand and Vietnam (Choudhury *et al*., 2013). Figure 1 shows the photographs of flowers, roots and plant of *Cinnamomum obtusifolium* Roxb. (Na-lin-gyaw). It has many pharmacological activities such as antihyperglycemic, antioxidant (Gogoi *et al*., 2014), antimicrobial, antibacterial, antifungal (Atiphasaworn *et al*., 2017) and anti-inflammatory (Miguel, 2010) activities. It is used for relieving aches and pains (Kyaw Tun and Pe Than, 2006). It is a medicinal plant applied as the treatment of cough, cold, toothache, liver complaints (Rao, 1979), diabetes, gall stone, as a mouth fresher (Gogoi *et al*., 2014).

(a)Flowers (b)Roots (c)Plant

Figure 1. Photographs of flowers, roots and plant of *Cinnamomum obtusifolium* Roxb. (Na-lin-gyaw)

The major constituents of the bark oils were 1,8-cineole, α-terpineol, linalool. The predominant components in the flower oils were α–pinene and β–pinene (Choudhury *et al*., 2013). Three new methyl derivatives flavan-3-ols namely 3′-O-methylate, 5,3′-di-O-methylate and 5,7,3′-tri-O-methylate were isolated from the bark of *Cinnamomum obtusifolium* (Morimoto *et al*., 1985).

Materials and Methods

Sample collection

The roots of *Cinnamomum obtusifolium* Roxb. (Na-lin-gyaw, NLG) were collected from Eaindu Village, Hpa-an Township, Kayin State. After washing with water, the collected samples were dried at room temperature. The dried samples were cut into small pieces and ground into powder with a grinding machine. These powdered samples were stored in air-tight containers.

Preliminary phytochemical analysis

The preliminary phytochemical investigations were carried out on roots of the selected medicinal plant in order to determine the presence of alkaloids, α-amino acids, carbohydrates, cyanogenic glycosides, flavonoids, glycosides, organic acids, phenolic compounds, reducing sugars, saponins, starch, steroids, tannins and terpenoids (Harborne, 1984; Marini- Bettolo *et*

al., 1981; Robinson, 1983; Shriner *et al.*, 1980; Tin Wa, 1972 ; Trease and Evans, 1980; Vogel, 1966).

Extraction of essential oil from roots of *Cinnamomum obtusifolium* Roxb. (Na-lin-gyaw)

The essential oil was extracted from the roots of NLG by using steam distillation method.

Screening of Antibacterial Activity

The antibacterial activity of the various crude extracts of roots of *Cinnamomum obtusifolium* Roxb. (Na-lin-gyaw) was screened against five species of bacteria such as *B.subtilis*, *S.aureus*, *P.aeruginosa*, *B.pumilus* and *E.coli* by using agar well diffusion method at the Pharmaceutical Research Department (PRD), Yangon.

Samples

PE, EtOH, EtOAc, MeOH and H_2O extracts of NLG

Chemicals

PE, 95% EtOH, EtOAc, MeOH, Trypticase soy agar, Trypticase soy broth

Apparatus

Petri dishes, test tubes, a hot plate compound stirrer, a constant temperature bath, an autoclave, a hot air sterilizer, an incubator, an electronic balance, a refrigerator, spirit burner, aluminium foil

Test Organisms

Bacillus subtilis, *Staphyococcus aureus*, *Pseudomonous aeruginosa*, *Bacillus pumilus*, *and E.coli* were used for antibacterial activity screening on crude extracts.

Procedure

The procedure for screening of antibacterial activity by agar well diffusion method (Crucksank, 1960) is as follows. In this method, PE, EtOH, EtOAc, MeOH, and H_2O extracts and isolated compounds were used as the samples. The sample (1g each) was introduced into sterile Petri dish and dissolved in 1 mL or with least amount of its respective solvent (PE or 95 % EtOH or EtOAc or MeOH or distilled

water) till it was dissolved. The organism suspension in trypticase soy agar was poured into Petri dish and immediately after hardening of the agar, wells were made on agar disk with a 10 mm sterile cork bore. After inoculum had been dried for 5 minutes, the agar disks were removed and the wells were filled with sample to be tested. And then the plates were incubated at 37°C. After overnight incubation at 37°C, the diameter of inhibition zone including 10 mm wells were measured. The agar well diffusion method was used to test antimicrobial action of the extracts on 24 hours broth culture of the organisms used.

Determination of minimum inhibitory concentration

(a) Samples

EtOH, MeOH and EtOAc extracts

(b) Chemicals

Ethanol, methanol and ethyl acetate

(c) Procedure

Minimum inhibitory concentration (MIC) values of three crude extracts was determined by agar well diffusion method. 0.1 mL of test sample solution from 100 mg per mL mixture was introduced into the agar well of first plate to obtain the concentration of 1×10^5 μg/mL. And then, 0.1 mL of test sample solution from 50 mg per 2 mL mixture was put into the agar well of second petridis to obtain the concentration of 50×10^3 μg/mL and then the agar well of third plate was filled with 0.1 mL of test sample solution from 25 mg/3mL mixture to obtain the concentration of 25×10^3 μg/mL. By this way, 0.1 mL of each test sample solution was introduced into the agar well of different plate to obtain the respective concentration (1×10^5 μg/mL ~ 0.00016×10^3 μg/mL). All the plates were incubated at 27°C for 24 hours. After incubation, the diameters of inhibition zones including 10 mm wells were measured. The amount of sample that showed the least inhibition zone diameter was determined as the corresponding MIC value. The microorganisms of *Pseudomonas aeruginosa*, *Bacillus pumilus* and *Escherichia coli* were tested.

Results and Discussion

Preliminary phytochemical investigations

From these experiments, alkaloids, α-amino acids, carbohydrates, flavonoids, glycosides, organic acids, phenolic compounds, reducing sugars, starch, steroids, tannins and terpenoids were observed in the selected medicinal plant.

Extraction of essential oil

The essential oil (0.04 % yield) was extracted from the roots of *Cinnamomum obtusifolium* Roxb. (Na-lin-gyaw) by using steam distillation method.

Investigation on some chemical constituents in essential oil of NLG

The essential oil extracted from NLG roots was detected by GC-MS spectrometer and the resultant GC-MS spectrum was shown in Figure2.

From the figure, it was found that five organic constituents namely 2,4-di-tert-butylphenol, Asarone, 1,2,3-trimethoxy-5-[(E)-prop-1-enyl]benzene, Curcumenol and Dehydrocostus lactone were detected from essential oil of roots of NLG. The results were shown in Table 1.

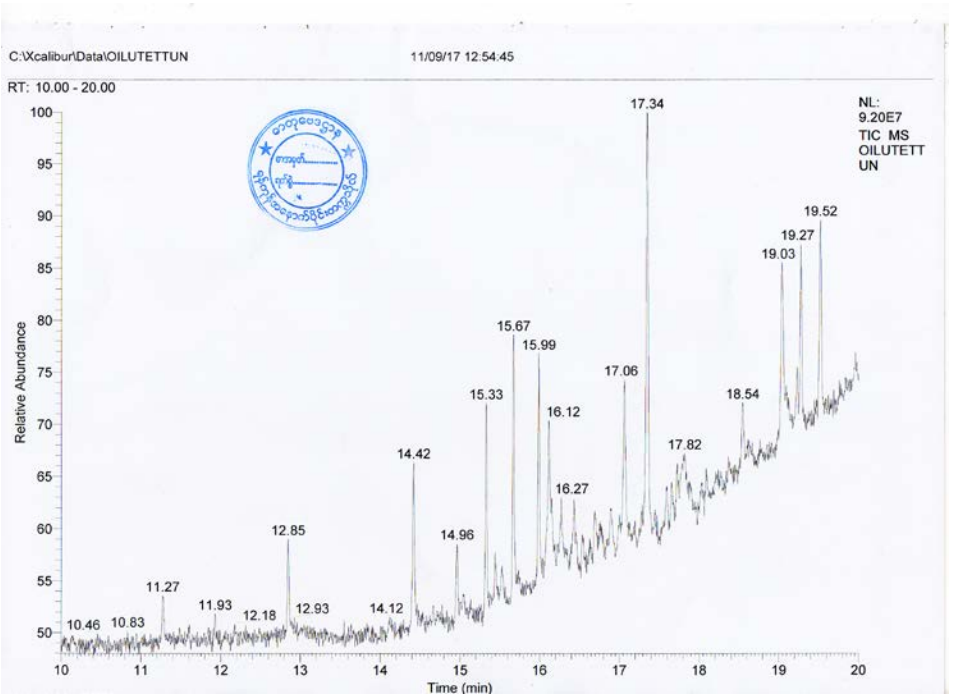

Figure 2. GC chromatogram of some chemical constituents in essential oil of roots of *Cinnamomum obtusifolium* Roxb. (Na-lin-gyaw)

Table 1. Chemical Constituents Present Essential Oil of NLG Detected by GC-MS Spectrometer

Constituents	Retention time (min)	Structure	M. wt & M. formula
2,4-di-tert-butylphenol	14.42	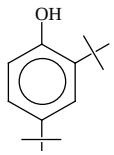	206 $C_{14}H_{22}O_3$
Asarone	15.67	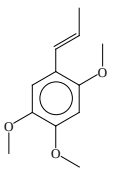	208 $C_{12}H_{16}O_3$

Constituents	Retention time (min)	Structure	M. wt & M. formula
(E)-1,2,3-trimethoxy-5(1-propenyl)-benzene	15.99	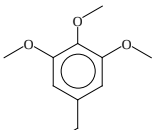	208 $C_{12}H_{16}O_3$
Curcumenol	17.34	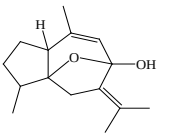	34 $_{22}O_2$
Dehydrocostuslactone	19.52	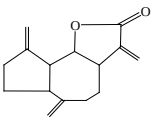	230 $C_{15}H_{18}O_2$

Investigation on Screening of Antibacterial Activity of Roots of *Cinnamomum obtusifolium* Roxb. (Na-lin-gyaw)

The results of antibacterial activity screening of five crude extracts (PE, EtOAc, 95 % EtOH, MeOH, H_2O) were recorded in Table 2 and Figure 3.

From the table and figure, it was found that all of the crude extracts except petroleum and water exhibited the significant antibacterial activity against five species of bacteria such as *B.subtilis*, *S.aureus*, *P.aeruginosa*, *B.pumilus* and *E.coli*. Of three extracts, methanol extract (inhibition zone diameter range = 15 ~ 18 mm) possessed stronger antibacterial activity than ethanol (inhibition zone diameter range = 14 ~ 17 mm) and ethylacetate (inhibition zone diameter range = 11 ~ 13 mm) extracts. Petroleum ether extract (inhibition zone diameter range = 11 ~ 12 mm) is positive on only four species of bacteria except *P.aeruginosa* whereas watery extract (inhibition zone diameter = 11 mm) showed positive only one bacteria namely *B.pumilus*.

Nevertheless, it could be deduced that all of the crude extracts exhibited the mild antibacterial activity against five species of bacteria tested.

Table 2. Inhibition Zone Diameters of Various Crude Extracts of Roots of *Cinnamomum obtusifolium* Roxb. (Na-lin-gyaw) against Five Species of Bacteria by Agar Well Diffusion Method

Organisms and Inhibition zone diameters (mm)					
Samples	*B. Subtilis*	*S. aureus*	*P. aeruginosa*	*B. pumilus*	*E. coli*
PE	12 (+)	11(+)	–	12(+)	11 (+)
EtOAc	12 (+)	11 (+)	12 (+)	13 (+)	13 (+)
EtOH	15 (++)	14 (+)	15 (++)	17 (++)	17 (++)
MeOH	16 (++)	15 (++)	17 (++)	15 (++)	18 (++)
H_2O	11 (+)	–	–	–	–

Agar Well – 10 mm
10 mm ~ 14 mm (+)
15 mm ~19 mm (++)
20 mm above (+++)

Organisms
(1) *Bacillus subtilis* (N.C.T.C-8236)
(2) *Staphylococcus aureus* (N.C.P.C-6371)
(3) *Pseudomonas aeruginosa* (6749)
(4) *Bacillus pumilus* (N.C.I.B- 8982)
(5) *Escherichia coli* (N.C.I.B-8134)

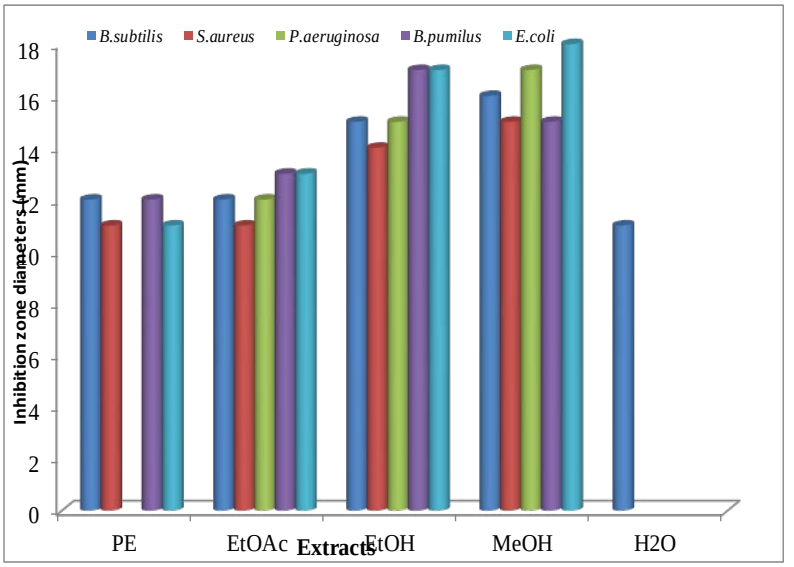

Figure 3. A bar graph of inhibition zone diameters for isolated compounds and various crude extracts of roots of NLG against five species of bacteria

Minimum inhibitory concentration (MIC) of ethanol, methanol and ethylacetate extracts from roots of *Cinnamomum obtusifolium* Roxb. (Na-lin-gyaw)

The MIC values of ethanol, methanol and ethylacetate extracts from roots of NLG were determined by agar well diffusion method. In this study, they were tested on three species of bacteria strains such as *Pseudomonas aeruginosa*, *Bacillus pumilus* and *Escherichia .coli*, with different concentration ranging from 100 mg/mL to 1.9 x 10^{-4} mg/mL.

From the results, it was found that the lowest MIC value of ethanol and methanol extracts were 3.125 mg/mL and 0.012 mg/mL against *Pseudomonas aeruginosa* and that were 1.9 x 10^{-4} mg/mL against *Bacillus pumilus* and *E.coli*. However, ethylacetate extract was no effective against these three species of bacteria by serial dilution and therefore the MIC values for ethylacetate extract were not measured within the concentration range described above. Therefore, it was deduced that methanol extract showed more effective antibacterial activity than ethanol and ethylacetate extracts against these three organisms.

Conclusion

From the overall assessment of this research work, it can be deduced that MeOH extract and EtOH extract of roots of NLG should be used as the antibacterial agents for the treatment of the diseases related to five species of bacteria described above. In addition, the essential oil of NLG roots should be useful in a wide variety of consumer goods such as detergents, soaps, toilet products, cosmetics and pharmaceuticals.

Acknowledgements

I would like to express my deep appreciation to the Rector Dr Win Naing and Pro-rector Dr Khin Maung Zaw, Sittway University, for allowing this paper to print in Universities Research Journal.

References

Atiphasaworn, P., S. Monggoot and P. Pripdeevech. (2017). "Chemical Composition, Antibacterial and Antifungal Activities of *Cinamomum bejolghota* Bark Oil from Thailand". *Journal of Applied Pharmaceutical Science*, **7** (04), 069-073

Choudhury, D., R. Biswas, P. Mandal and A.P. Das. (2013). "Diversity of *Cinnamomum schaeffer* (Lauraceae) in Terai and Duars Region of WestBengal,India". *Pleione* **7**(2), 441-448

Cruickshank. (1960). *Handbook of Bacteriology*. Edinburgh, E&S. Living Stone Ltd., 10thed^{n}, 256

Gogoi, B., B.B. Kakoti, S. Borah and N.S. Borah. (2014). "Antihyperglycemic and *In Vivo* Antioxidative Activity Evaluation of *Cinnamomum bejolghota* (Buch.Ham.) in *Streptozotocin* Induced Diabetic Rats: An Ethnomedicinal Plant in Assam". *Asian Pac J Tro Med*, **7** (Suppl 1), S427-S434

Grieve, MRS. M. (1975). *The Medicinal, Culinary, Cosmetic anmd Economic Properties, Cultivation and Folklore of Herbs, Grasses, Fungi, Shrubs andTrees with all their Modern Scientific Uses*. London, Jonathan Cape, Thirty Bedford Square, 169

Harborne, J.B. (1984). *Phytochemical Methods, A Guide to Modern Techniques of Plant Analysis*. London, 2nd ed^{n}, **37**, 101

Hesham, H.A., A.H. Nour and R.M. Yunus. (2016). "Techniques for Extraction of Essential Oil from Plants : A Review". *Australian Journal of Basic and Applied Sciences*, **10**(16), 117-127

M-Tin Wa. (1972). "Phytochemical Screening, Methods and Procedures". *Phytochemical Bulletin of Botanical Society of America*". **5**(3),4-10

Mahesh, B. and S. Satish. (2008). "Antimicrobial Activity of some Important Medicinal Plant against Plant and Human Pathogens". *World Journal of Agricultural Science*, **4**, 839-843

Marini- Bettolo, G.B., M. Nicole Hic and M. Palamia. (1981). "Plant Screening by Chemical and Chromatographic Procedure under Field Conditions". *J.Chromate*, **46**(2), 359-363

Miguel, M.G. (2010). "Antioxidant and Anti-inflammatory Activities of Essential Oils: A Short Review". *Molecules*, **15**, 9252-9287

Morimoto, S., G-I. Nonaka, I. Nishioka, N. Ezaki and N. Takizawa. (1985). "Tannins and Related compounds. XXIX : Seven New Methyl Derivatives of Flavan-3-ols and a 1,3-Diarylpropan-2-ol from *Cinnamomum cassia*, *C. obtusifolium* and *Lindera umbellata* var. *membranacea*". *Chem.Pharm.Bull.*, **33**(6), 2281- 2286

Rao, R. (1979). "Ethnobotanical Studies on the Flora of Meghalaya—some Interesting

Reports of Herbal Medicines". New Delhi, Oxford and IBH Publishing, Glimpses of Indian Ethnobotany, 2nd edn, 137-148

Robinson, T. (1983). *The Organic Constituents of Higher Plants*. North America, Cordus Press, 5th edn, 63-68

Shriner, R.L., R.C. Fuson, D.Y. Curtin and T.C. Morrill. (1980). *The Systematic Identification of Organic Compounds, A Laboratory Manual*. New York, John Wiley and Sons, 15-20

Thalwal, S.S., A. Gupta, N. Abhimanyu, S. Saini, K. Patel and L. Kapoor. (2013). "Antimicrobial Activity of Traditionally Used Herbs against Human Pathogens". *International Journal of Biomedical Research*, **4**(6), 236-240

Trease, G.E. and W.C. Evans. (1980). *Pharmacognosy*. London, Spottis Woode Ballantyne, 622

U Kyaw Tun and U Pe Than. (2006). "Medicinal Plants of Myanmar". https://www.tuninst.net/MMPD/... (Accessed 5 November 2017)

Vogel, A.I. (1966). *A Text Book of Practical Organic Chemistry*. London, Longmans, Green & Co. Ltd., 3rd edn, 112

Study of Ageing and Production of Wine from Rhizomes of Ginger (*Zingiber officinale*) by Anaerobic Fermentation Process

Aye Aye Myint*

Abstract

In the present study, an attempt has been made to produce wine by anaerobic fermentation process along with the assessment of the aging of wine. Ginger was chosen as a precursor of wine making. *Zingiber officinale* was used as raw material and the fermentation process was carried out with yeast (*Saccharomyces cerevisiae*), sugar, hot distilled water, different amounts of samples and different amounts of yeast. Primary and secondary fermentation of the ginger lasted from 3 days to 27 days respectively. During the experiment growth of yeast cell, total solid contents and aliquot samples analysis of pH, alcohol content, reducing sugar content, total dissolved solids and total suspended solid contents were carried out using standard procedures. The elemental contents of sample were analyzed by an Energy Dispersive X-Ray Fluorescence spectrophotometer (EDXRF). Ginger wine was produced using commercial yeast (*Saccharomyces cerevisiae),* during which at 6^{th} day, 12^{th} day, 18^{th} day and 24^{th} day, the antioxidant activity of all types of wines were measured by using the DPPH assay. When wine aging one month, the antimicrobial activity of the sample (ginger wine) was determined by Agar Well Diffusion method.

Keywords: Ginger, Wine, Aging, Elemental contents, Anaerobic fermentation process

Introduction

Fermentation biotechnology is an important industrial process for the production of alcoholic beverages including wine. However, the aging of wine is always an important issue during production. Wine is one of the functional fermented foods that have many health benefits. Commercially, wine is produced by yeast fermentation which involves the conversion of sugar to alcohol. Wine can act as a health supplement attributed to polyphenols, flavonoids, minerals, etc. extracted from fruits and vegetables during the process of fermentation (Sekiwa, *et al*., 2000; Wei, *et al*., 2005; Young, *et al*., 2005; Shukla and Singh, 2007). Wines made from fruits are

* Associate Professor, Dr., Department of Chemistry, Kyaing Tong University

often named after the fruits. Fruit wines are undistilled alcoholic beverages usually made from grapes as other fruits such as peaches, plums or apricots, bananas,s, etc. which are nutritive, more tasty and mild stimulants.). There are two types of wines namely Natural wines with 9-14% alcohol and Fortified (Dessert and appetizer) wines with 15 to 21% alcohol (Nduka, 2007). Ginger is an herbaceous perennial plant of the family Zingiberaceae which consists of 47 genera. Ginger is a rhizome plant, used for its medicinal and culinary properties. Ginger is rich in vitamins and minerals. It contains health-benefiting essential oils like gingerol and zingerones. Gingerols help improve intestinal motility and act as painkillers, nerve soothing as well as antibacterial properties. Ginger is traditionally known for its medicinal and culinary value. There is a need to exploit the medicinal properties of ginger in modern applications such as in medicine, supplement and cosmetics, aligned with consumer demands for safe, natural and sustainable, effective and economical products. (Ujang, *et al*., 2015). Ginger wine is a fortified wine made from a fermented blend of ground ginger root and raisins. Wine is produced using the yeast strain *Saccharomyces serevisiae*. Ginger wine can be drunk with ice as without ice and is frequently used as an ingredient along with whisky. Ginger wine can also be served mixed with other beverages such as lemonade, ginger ale, bitter lemon or diluted with water. Ginger wine is an alcoholic beverage made from a fermented blend of ginger fermenting by the yeast, *Saccharomyces cerevisiae*. It is a popular beverage in Europe. Ginger is usually used to flavor wine. It has many health benefits. Ginger wine can be consumed by blending with whisky, brandy or rum. The research work will be focused on the preparation of a good quality ginger wine by using commercial yeast. Especially change in aroma compounds of wine during aging process after fermentation.

Botanical Description

Family name	: Zingiberaceae
Scientific name	: *Zingiber officinale*
Local Name	: Gyin, Gyin Sein
English name	: Ginger
Medicinal uses	: treatment of headache, treatment of several gastrointestinal diseases, treatment of morning sickness, antioxidant activities, antimicrobial properties, insulin sensitivity

Figure 1. Rhizomes of ginger

Materials and Methods

Collection and Preparation of Samples

Ginger and sugar were obtained from Yadanarbon Market, Mandalay Region, Myanmar. Yeast were purchased from local market.The samples were washed with distilled water to remove unwanted materials. The fresh ginger was used in wine fermentation.

Determination of Elemental Contents from the Rhizomes of Ginger

Elemental analysis of the rhizomes of ginger (*Zingiber officinale*) was measured at Department of Chemistry, Monywa University by applying Energy Dispersive X-Ray Fluorescence (EDXRF) Spectroscopy method.

Wine Making Process (FugelsangandCharles,2007)

Ginger wines were prepared by using the same amount of sugar, yeast, hot distilled water and different amounts of sample (ginger). Moreover, different amounts of yeast and the same amount of others were used in wine making process.

Wine Making with Different Amount of Sample

Fifty plastic bottles were rinsed and sterilized. The 20 g of sugar, 300 mL of hot distilled water and 1 g of yeast were added into each plastic bottles. The mixture solutions were stirred until all sugar was dissolved. The 10 g of ginger was added into each ten plastic bottles. Similarly, 15 g of ginger in ten bottles, 20 g of ginger in ten bottles, 25 g of ginger in ten bottles and 30 g of ginger in ten bottles were prepared. After that, the fifty plastic bottles were covered and air locks on. The drip pipes were immersed into water. Fermentation process was studied in anaerobic condition.

Figure 2 .The fifty plastic bottles with different amounts of sample (ginger wine)

Wine Making with Different Amount of Commercial Yeast

Fifty plastic bottles were rinsed and sterilized. The 20 g of sugar, 20 g of ginger and 300 mL of hot distilled water were added to each plastic bottle. The mixture solutions were stirred until all sugar was dissolved. 0.5 g of yeast was added to every ten plastic bottles. Similarly, 1 g of yeast in ten bottles, 1.5 g of yeast in ten bottles, 2 g of yeast in ten bottles and 2.5 g of yeast in ten bottles were prepared. After that, the fifty plastic bottles were covered and air locks on. The drip pipes were immersed in water. The fermentation process was studied in anaerobic conditions.

Figure 3. The fifty plastic bottles with different amounts of commercial yeast (ginger wine)

Some physical and chemical parameters such as pH, alcohol content, sugar content, total dissolved solids, and total suspended solid of all types of wines were determined on the 3rd day, 6th day, 9th day, 12th day, 15th day, 18th day, 21st day, 24th day, and 27th day. Furthermore, the antioxidant activity of ginger wine was determined on the 6th day, 12th day, 18th day, and 24th day.

Determination of the physiochemical properties of ginger wine

Physicochemical parameters like acidity, temperature, and pH were determined by using the methods of A.O.A.C. (1990). pH was determined with a pH portable digital device. The probe of pH and temperature was immersed into a 50 mL prepared wine for 2 min (for stable reading). Recorded data were means of triplicate values. The alcohol content of wine was estimated by using the methods of A.O.A.C. (1990). The alcohol content of the prepared ginger wine was directly measured by using an alcohol meter.

Determination of Reducing Sugar Content (Browne, 1912)

To determine the sugar content of ginger wine, Iodometric Titration Method was used.

Determination of Total Dissolved Solid(TDS) (Howard, C.S., 1933)

To determine the TDS of ginger wine, the oven drying method was used.

Determination of Total Suspended Solid(TSS) (Degen, J., 1956)

The TSS content of the prepared ginger wine was directly measured by using filter paper. Firstly, the filter paper was weighed at the digital balance, until the constant weight. And then, the 50 mL of ginger wine was filtered. The filter paper with residue was dried at room temperature. The filter paper with residue was weighed until it reached a constant weight by using a digital balance.

Determination of Antioxidant Activity (Blois,M.S.,1958)

The antioxidant activity of ginger wine was evaluated spectrophotometrically by DPPH (1,1-Diphenyl-2-Picryl-Hydrazyl) Radical Scavenging Assay in the Department of Chemistry, University of Mandalay.

Determination of Antimicrobial Activity

The Agar Well Diffusion Method was used to test the antimicrobial activity of the wine after one month at the Department of Chemistry, Meikhtila University.

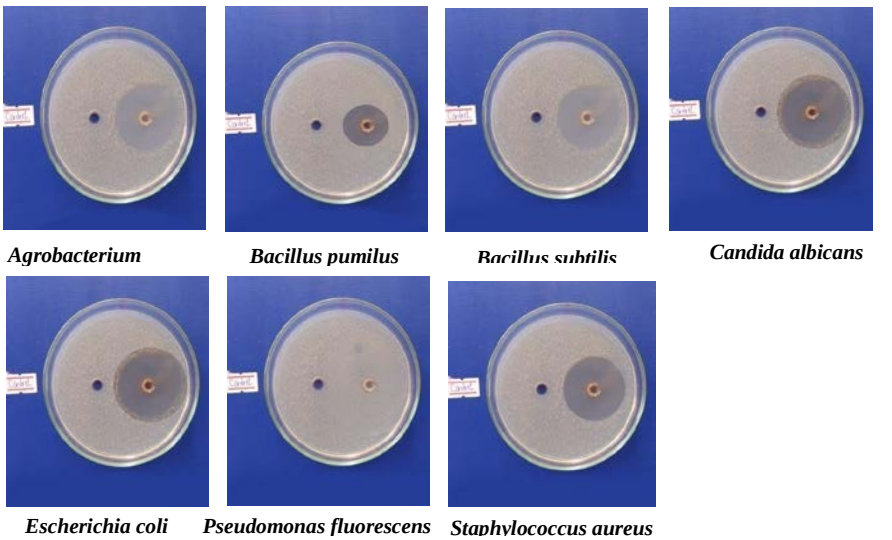

Figure 4. Antimicrobial activity of ginger wine

Results and Discussion

Elemental Contents of Rhizomes of Ginger

The elemental content of rhizomes of ginger were described in Table 1.

Table 1. Elemental Contents of Rhizomes of Ginger

Element	Symbol	Relative Abundance(%)	Element	Symbol	Relative Abundance(%)
Potassium	K	0.846	Manganese	Mn	0.016
Silicon	Si	0.408	Iron	Fe	0.004
Phosphorus	P	0.154	Copper	Cu	0.002
Sulphur	S	0.086	Zinc	Zn	0.001
Calcium	Ca	0.027			

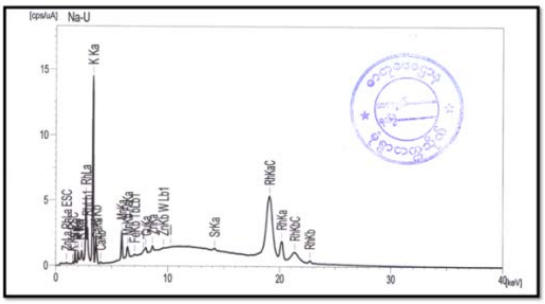

Figure 5. EDXRF spectrum of dried rhizomes of ginger

The elemental analysis of ginger indicated the presence of potassium, silicon, phosphorous, sulphur, calcium, manganese, iron, copper, and zinc respectively. Potassium is the highest amount (0.846 %) in the sample (ginger). A potassium-rich diet may reduce blood pressure and water retention, protect against strokes and help prevent osteoporosis and kidney stones.

pH Values of Wine with Different Amounts of Sample

The pH values of wine were determined by using pH meter. The data are shown in Table 2.

Table 2. pH Values of Wines with Different Amounts of Sample

Sample	pH									
	1st day	3rd day	6th day	9th day	12th day	15th day	18th day	21st day	24th day	27th day
10 g	4.07	3.93	3.88	3.75	3.61	3.53	3.51	3.34	3.31	3.24
15 g	4.74	4.03	3.99	3.87	3.73	3.72	3.69	3.64	3.42	3.33
20 g	4.05	4.02	3.78	3.77	3.61	3.56	3.51	3.49	3.39	3.20
25 g	4.57	4.01	3.97	3.96	3.86	3.71	3.64	3.60	3.57	3.38
30 g	4.18	4.15	4.14	4.09	4.00	3.76	3.53	3.19	3.12	3.01

According to these data, the pH values of wines with different amounts of sample are more acidic as long as fermentation time.

pH Values of Wine with Different Amounts of Commercial Yeast

The pH values of wine were also determined by using pH meter. The data are shown in Table 3.

Table 3. pH Values of Wines with Different Amount of Commercial Yeast

Yeast	pH									
	1st day	3rd day	6th day	9th day	12th day	15th day	18th day	21st day	24th day	27th day
0.5 g	4.57	4.01	3.92	3.88	3.84	3.84	3.78	3.71	3.61	3.56
1 g	4.05	4.02	3.78	3.77	3.61	3.56	3.51	3.49	3.39	3.20
1.5 g	4.19	4.18	4.06	3.99	3.91	3.90	3.80	3.79	3.73	3.73
2 g	4.15	4.11	4.00	3.90	3.88	3.79	3.76	3.75	3.74	3.48
2.5 g	4.17	4.12	4.00	3.97	3.95	3.92	3.89	3.82	3.80	3.72

According to these data, the pH values of wines with different amounts of commercial yeast are more acidic as long as fermentation time. According to the literature, the pH value of fermented wines falls around 3 to 4. pH determination points out 3.01 to 3.38 (different amounts of the sample), and different amounts of yeast fall in the wine pH range of 3.20 to 3.73.

The Alcohol Content of Wines was Determined by Using Alcohol Meter

The alcohol content of wines was determined by using an alcohol meter. The data were tabulated in Table 4.

Table 4. Alcohol Content of Wines with Different Amount of Sample

Sample	Alcohol content (%)								
	3rd day	6th day	9th day	12th day	15th day	18th day	21st day	24th day	27th day
10 g	1.0	1.0	1.5	1.5	1.7	1.8	1.8	2.0	2.0
15 g	1.0	1.5	1.5	1.5	1.8	1.8	2.0	2.0	2.5
20 g	1.5	1.7	2.0	2.0	2.2	2.3	2.5	2.5	3.0
25 g	1.5	1.7	1.8	2.0	2.2	2.4	2.6	2.8	3.0
30 g	1.0	1.0	1.2	1.4	1.5	1.7	1.9	2.0	2.0

According to experimental results, the alcohol content of wines with different amounts of samples increased as long as fermentation time.

Alcohol Content of Wines with Different amounts of Commercial Yeast

The alcohol content of wines was also determined by using an alcohol meter. The data were tabulated in Table 5.

Table 5. Alcohol Content of Wines with Different Amount of Commercial Yeast

Yeast	Alcohol content (%)								
	3rd day	6th day	9th day	12th day	15th day	18th day	21st day	24th day	27th day
0.5 g	1.5	1.7	1.9	2.0	2.0	2.2	2.4	2.5	2.5
1 g	1.5	1.7	2.0	2.0	2.2	2.3	2.5	2.5	3.0
1.5 g	2.0	2.2	2.4	2.6	2.8	2.8	2.9	3.0	3.0
2 g	2.2	2.6	2.8	2.8	2.9	3.0	3.0	3.0	3.0
2.5 g	2.4	2.8	2.9	2.9	2.9	3.0	3.0	3.0	3.0

According to experimental results, the alcohol content of wines with different amounts of commercial yeast increased as long as fermentation time. The alcohol content of ginger wines contained 1% to 3.5 % (different amounts of the sample) and 1.5 % to 3 % (different amounts of yeast).

Reducing Sugar Content of Wines with Different Amounts of Sample

The reducing sugar content of wines was determined by using iodometric titration method from initial day to last 27th day. The data were tabulated in the Table 6.

Table 6. Reducing Sugar Content of Wines with Different Amounts of Sample

Sample	Sugar content (mmol/mL)									
	1st day	3rd day	6th day	9th day	12th day	15th day	18th day	21st day	24th day	27th day
10 g	0.0600	0.0315	0.0175	0.0150	0.0150	0.0125	0.0125	0.0075	0.0075	0.0075
15 g	0.0825	0.0825	0.0825	0.0225	0.0200	0.0150	0.0150	0.0125	0.0125	0.0100
20 g	0.0725	0.0275	0.0225	0.0200	0.0200	0.0200	0.0175	0.0125	0.0125	0.0125
25 g	0.0800	0.0375	0.0275	0.0275	0.0225	0.0225	0.0220	0.0125	0.0100	0.0100
30 g	0.0850	0.0350	0.0275	0.0250	0.0200	0.0175	0.0150	0.0150	0.0125	0.0100

According to the experimental data, the reducing sugar content of wines with different amounts of sample decreased when their life increased.

Reducing Sugar Content of Wines with Different Amounts of Commercial Yeast

The reducing sugar content of wine sample was determined by using Iodometric titration method. The data were tabulated in the Table 7.

Table 7. Reducing Sugar Content of Wines with Different Amount of Commercial Yeast

Yeast	Sugar content (mmol/mL)									
	1st day	3rd day	6th day	9th day	12th day	15th day	18th day	21st day	24th day	27th day
0.5 g	0.0825	0.0275	0.0200	0.0200	0.0175	0.0150	0.0100	0.0075	0.0075	0.0075
1 g	0.0725	0.0275	0.0225	0.0225	0.0200	0.0200	0.0175	0.0125	0.0125	0.0125
1.5 g	0.0900	0.0250	0.0250	0.0250	0.0200	0.0175	0.0150	0.0150	0.0125	0.0125
2 g	0.0875	0.0500	0.0500	0.0400	0.0400	0.0250	0.0225	0.0175	0.0175	0.0175
2.5 g	0.0850	0.0350	0.0350	0.0275	0.0250	0.0175	0.0150	0.0150	0.0100	0.0100

According to the experimental data, the reducing sugar content of wines with different amounts of commercial yeast decreased when their life increased. The reducing sugar content in all types of wine remained 0.0125 to 0.0075 mmol/ mL.

Total Dissolved Solid of Wines with Different Amounts of Sample

The total dissolved solid of ginger wines was determined by using the oven drying method. These data are shown in Table 8.

Table 8. TDS Content of Wines with Different Amounts of Sample

Sample	Total Dissolved Solid (mg/mL)								
	3rd day	6th day	9th day	12th day	15th day	18th day	21st day	24th day	27th day
10 g	1.00	2.08	3.16	3.52	4.90	6.96	7.66	10.52	14.48
15 g	1.32	2.78	3.20	4.08	6.90	7.28	8.19	12.00	14.92
20 g	1.72	2.86	3.12	4.30	7.00	12.62	12.72	14.76	16.28
25 g	1.80	4.22	5.82	6.04	7.45	13.50	19.82	31.52	48.90
30 g	1.86	4.99	11.40	12.58	13.56	15.14	28.60	38.84	50.08

According to the experimental results, the total dissolved solid content of wines with different amounts of sample increased when their life increased.

Total Dissolved Solid of Wines with Different Amounts of Commercial Yeast

The TDS content in the wine sample was determined by using the oven drying method. These data are shown in Table 9.

Table 9. TDS Content of Wines with Different Amounts of Commercial Yeast

Yeast	Total Dissolved Solid (mg/mL)								
	3rd day	6th day	9th day	12th day	15th day	18th day	21st day	24th day	27th day
0.5 g	1.42	2.24	2.62	3.22	6.46	9.72	12.68	12.84	13.62
1 g	1.32	2.86	3.12	4.30	7.00	14.76	12.62	12.72	16.28
1.5 g	3.44	3.78	6.44	7.20	12.20	12.76	14.28	14.78	14.98
2 g	1.42	2.16	5.42	5.86	8.14	10.20	10.76	13.26	15.22
2.5 g	0.11	2.33	3.64	3.88	10.44	11.64	12.78	16.02	18.52

According to the experimental results, the total dissolved solid of wines with different amounts of commercial yeast increased when their life increased.

Total Suspended Solid of Wines with Different Amounts of Sample

The TSS content in the wine sample was determined by using filter paper. These data were tabulated in Table 10.

Table 10. TSS Content of Wines with Different Amounts of Sample

Sample	Total Suspended Solid (mg/mL)								
	3rd day	6th day	9th day	12th day	15th day	18th day	21st day	24th day	27th day
10 g	5.00	3.95	3.38	3.00	2.98	1.81	1.54	1.18	0.97
15 g	5.86	4.52	3.63	3.21	2.18	1.83	1.45	1.46	1.01
20 g	6.34	4.76	4.49	3.75	2.74	2.64	1.49	1.58	1.03
25 g	6.35	4.75	4.59	4.58	3.18	2.88	1.87	1.12	1.02
30 g	5.00	7.58	5.41	5.26	3.77	3.32	2.14	1.15	1.17

According to the experimental results, the total suspended solid of wines with different amounts of sample decreased when their life increased.

Total Suspended Solid of Wines with Different Amounts of Commercial Yeast

The TSS content in the wine sample was determined by using filter paper. These data were tabulated in the Table 11.

Table 11. TSS Content of Wines from Different Yeast

Yeast	Total Suspended Solid (mg/mL)								
	3rd day	6th day	9th day	12th day	15th day	18th day	21st day	24th day	27th day
0.5 g	5.02	2.92	2.86	2.72	2.12	1.59	1.18	1.10	1.05
1 g	6.34	4.76	4.49	3.75	2.74	2.64	1.49	1.68	1.03
1.5 g	6.10	5.60	3.94	3.88	3.64	1.48	1.19	1.18	0.41
2 g	5.60	5.39	4.46	3.79	3.61	1.47	1.28	1.26	1.22
2.5 g	6.11	5.95	5.74	3.83	2.45	1.43	1.30	1.26	1.24

According to the experimental results, the total suspended solids content of wines with different amounts of commercial yeast decreased when their life increased. The TDS content of ginger wines increased but the TSS content and sugar content of ginger wines decreased when their life increased.

Antioxidant Activity of Ginger Wines

The antioxidant activity of ginger wines was determined when ginger wines reached six days. Different analytical approaches have been applied to assess the antioxidant activity in wine. The DPPH method allowed to obtain a fast quantification of total polyphenol content and the data produced showed to be highly correlated with antioxidant activity measured by spectrophotometric assays.

Table 12. % Inhibition on 0.002 % DPPH with 1.5 mL Wines from Different Amounts of Sample

Day	% inhibition				
	10 g	15 g	20 g	25 g	30 g
6th day	61.0655	58.4016	66.8032	58.1967	65.1939
12th day	67.5635	60.0409	73.9910	66.1885	68.6475
18th day	73.0932	67.3728	78.3258	72.2457	76.0593
24th day	77.8688	78.3958	79.6711	80.9426	82.5819

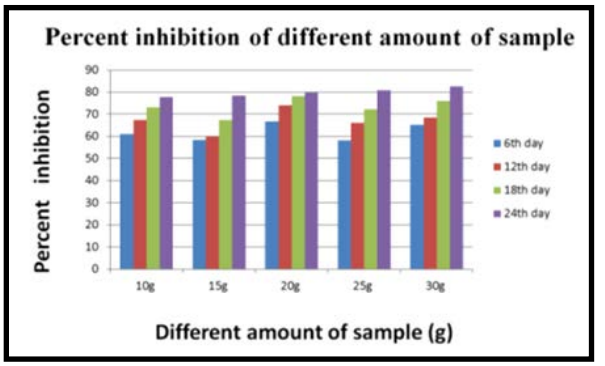

Figure 6. Percent inhibition of different amounts of sample

Table 13. % Inhibition on 0.002 % DPPH with 1.5 mL Wines from Different Amount of Commercial Yeast

Day	% inhibition				
	0.5 g	1 g	1.5 g	2 g	2.5 g
6th day	52.0491	54.2600	54.5590	45.1420	42.4320
12th day	74.5901	72.0930	66.2790	47.6067	46.8305
18th day	75.9379	79.1720	68.4426	50.3234	47.6067
24th day	78.9133	83.0627	71.1065	60.0409	67.9172

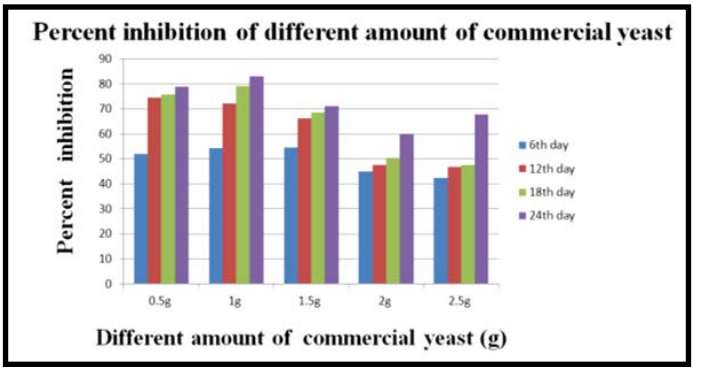

Figure 7. Percent inhibition of different amounts of commercial yeast

The antioxidant activity followed by spectrophotometric methods was useful to obtain preliminary information on the phenolic composition of wines and the associated antioxidant activity. The results of two types of wine (different amounts of sample and different amounts of yeast) have high antioxidant activity when their life increases.

Antimicrobial Activity of Ginger Wine

The Agar Well Diffusion method was used to test the antimicrobial activity of the wine after one month. The results are shown in Table 14.

Table 14. Antimicrobial Activity of Ginger Wine

Microorganisms	Inhibition zone (mm)	Microorganisms	Inhibition zone (mm)
Agrobacterium tumefaciens	35.26 +++	*Escherichia coli*	35.59 +++
Bacillus pumilus	32.87 +++	*Pseudomonas fluorescens*	–
Bacillus subtilis	35.80 +++	*Staphylococcus aureus*	35.87 +++
Candida albicans	36.58 +++		
Agar Well - 8 mm		13 mm ~ 17 mm	(++)
8 mm ~ 12 mm	(+)	18 mm above	(+++)

The key finding of this study is that bacterial resistance to wine appears to be closely associated with bacterial resistance to antimicrobial drugs. This indicates that bacterial resistance to wine and medicinal antibiotics share, at least in part, the same mechanisms. According to experimental results, the highest antimicrobial activity was responded on *Agrobacterium tumefaciens, Bacillus pumilus, Bacillus subtilis, Candida albicans, Escherichia coli* and *Staphylococcus aureus.*

Conclusion

In this study, the ginger can be converted into a value-added product through fermentation. Ginger wines were determined for their physicochemical properties, antioxidant activity, and antimicrobial activity. The physicochemical parameters of ginger wine having different TSS at 3 and 27 days have been shown in Tables 10 and 11, depicting a significant difference among various treatments. The TDS content of ginger wines increased but the TSS content and sugar content of ginger wines decreased when their life increased. During storage, there was a reduction in the TSS and alcohol which may be attributed due to sedimentation and volatility. The pH of the products was found to corroborant with titratable acidity. It could be acidified before the initiation of desirable fermentation by yeast culture. The amount of reducing sugar depends on the conditions for fermentation and 27 days of storage indicating that the same has been utilized for alcohol production. In a suitable environment and substrate, the amount of alcohol produced depends upon the amount of sugar present and the efficiency of the yeast in converting the sugar to alcohol. Ginger wine versions have relatively low alcohol content than commercially available wines, so ginger wines are not harmful to health and are acceptable for daily use. In fact, it has many health benefits. Ginger wine is acidic, sweet to dry, and low to a high alcoholic. Therefore, ginger wine is suitable for drinking and good for health.

Furthermore, the antioxidant activity of ginger wines with different amounts of samples is better than the that of ginger wines with different amounts of commercial yeast. However, the antimicrobial activity of wine and its constituents involves many modes of action. The relationship between bacterial multidrug resistance and various mechanisms of antibacterial action of wine and its constituents is practically unexplored.

From the experimental results, their data coincided with each other. This study proves that acceptable wine can be prepared from ginger. The results of process monitoring and final analysis will help a small-scale wine industry or can refer to the results to develop a small-scale wine industry.

Acknowledgements

We would like to express many thanks to Rector Dr San San Mar and Pro-rector Dr Myat Nyunt of Kyaing Tong University for their permission to do this research. I wish to mention my deepest thanks to my Professor and Head, Dr Mya Mya Khine and Professor, Dr Nwe Thin Ni, Department of Chemistry, Kyaing Tong University for their interest, valuable guidance and encouragement throughout this research work.

References

Alverz, M., I.M. Moreno, A.M. Ios, A.M. Camean and A.G. Gonzolez. (2007). "Study of mineral profile of Morntilla-Moriles "fino" wines using inductively coupled plasma atomic emission spectrometry methods ". *Journal of Food Composition and Analysis*, 20(5), 391-395.

Amerine, M.A., R. Kunkee, K.C.S. Ough, V.L. Singleton and A.D. Webb. (1980). *The technology of wine making.* Nigeria, Westport, Connecticut, 4th edn., 185-703.

Andrietta, M.G.S., S.R. Andrietta, C . Stecklberg and E.N.A. Stupiello, (2007). "Bioethanol-30 years of Proalcool". *Int Sugar*, 1(109), 195-200.

AOAC,(1990), *Official Methods of Analysis*, Washington, DC., USA., 15th edn, Association of Official Analytical Chemists, 200-210.

Attri, B.L., (2009). "Effect of initial concentration on the physico-chemical characteristics and sensory qualities of cashew apple wine". *Nat. Prod-Radiance*, 8, 374-379.

Blois, M.S., (1958). "Antioxidant determination by the use of a stable free radical". *Nature*, 29, 1199-1200.

Browne, C.A., John Wiley and Sons, (1912). *Handbook of sugar analysis.* New York.

Chen, B.H., P.Y. Wu, K.M. Chen, T.F. Fu, H.M. Wang and C.Y.Chen, (2009). "Antiallergic potential on RBL-2HS cells of some phenolic constituents of *Zingiber officinale* (Ginger)". *I. Nat. Prod.* 72, 950-953.

Degen, J. and F.E. Nussberger, (1956). "Notes on the determination of suspended solids. Sewage". *Ind. Wastes*, 28- 237.

Guganani, H.C., Ezenwanze, Aeschbach, R., Loliger, J and Scott B., (2015). "Antioxidant actions thymol, carvacrol,6-gingerol, zingerone and hydroxytyrosol". *Food Chem.Toxicol*, 31:36.

Shukla, Y. And Singh, M., (2007). "Cancer preventive properties of ginger a brief review". *Food Chem Taxicol*, 683-690.

Isolation, Characterization and Identification of Bioactive Constituents and Screening of Antimicrobial Activity (MIC) of *Tectona grandis* L. (Kyun)

Htay Htay Yee[1] & Daw Hla Ngwe[2]

Abstract

The present research, *Tectona grandis* L erbenaceae (Kyun) heart-wood was chosen to study some bioactive phytoconstituents and antimicrobial activity. The heart wood of *Tectona gradis* L. (Kyun) as saw dust were collected from Yangon, Myanmar, during November to December in 2004. The preliminary phytochemical investigation of saw dust revealed the presence of steroid, terpenoids, flavonoids, glycosides phenolic compound, α-amino acid, saponins, organic acids, tannins alkaloids, anthraquinones and the absence of reducing sugar and cyanogenic glycosides. On silica gel column chromatographic separation, 0.01% of 2-methyl anthraquinone (**'A'**, m.pt 173-174 ºC) was isolated from pet-ether extract of Kyun heart wood (KHW). The identities of all isolated compounds were made by joint application of physico-chemical properties and modern spectroscopic techniques (UV, FT IR and ^{1}HNMR). The minimum inhibitory concentrations (MIC) of 2-mehtyl-anthraquinone **(A)** against 8 microorganisms such as *Proteus morganni, Escherichia coli, Staphylococcus aureus, Escherichia coli* ATCC 25922, *Shigella flexneri, Vibrio cholerae, Staphylococcus aureus* and *Bacillus subtilis* were also determined by employing microplate dilution method. The MIC of '**A**' against *E. coli* ATCC 25922 strain was found to be 0.0156 mg ml^{-1} and the MIC of '**A**' against remaining 7 bacterial strains were observed to be >1 mg ml^{-1}. Therefore, it is suggested that these findings will contribute in the development of finding drugs used for the diseases caused by the above organisms.

Keywords: *Tectona grandis* L. (Kyun), phytochemicals, UV, FT IR, ^{1}H NMR, antimicrobial activity

Introduction

In Myanmar, there are many medicinal plants which have been claimed to be useful for their potential therapeutic value in medicine. Medicinal plants are important for Pharmacological research and drug

[1] Lecturer, Dr, Department of Chemistry, Dagon University
[2] Professor (Retired), Dr, Department of Chemistry, University of Yangon

development, not only when plant constituents are used directly as therapeutic agents, but also as starting materials for the synthesis of drugs or as models for pharmacologically active compounds (WHO, 1998). *Tectona grandis* L. is a native of southeast Asia, where it occurs naturally in Myanmar, Laos, Thailand and was introduced hundred years ago to Indonesia Now it is cultivated in many countries both inside and outside the region, including China, Vietnam and the Philippines (Chopra *et al*, 1956).

Tectona grandis L. (kyun) heart-wood is acrid, cooling, laxative, sedative, to gravid uterus and useful in treatment of piles, leucoderma and dysentery. Wood is good for headache, biliousness, burning sensation and pain and liver related trouble properties. Teak has the resistance to termites and fungi (Cruickshank *et al*, 1975).

(a)

(b)

Figure 1. Image of (a) Kyun Tree and (b) saw dust of *Tectona grandis* L.(Kyun heart-wood)

Material and Methods

Collection and Preparation of the Samples

The heart wood of *Tectona grandis* L. (Kyun) as saw dust (Figure.1) was collected from Yangon, Myanmar, during November to December, in 2004. After being collected, the scientific name of these plant were identified at Botany Department, University of Yangon. The Kyun heart-wood (KHW) powder was dried again at room temperature. The dried powder samples were separately stored in the airtight containers to prevent the moisture and other contaminations. The dried powder sample was used for chemical and biological investigations.

Preliminary Phytochemical Investigation of Kyun Heart-wood

The prepared dried powder samples were then firstly subjected to preliminary phytochemical tests in order to find out the types of organic compounds present in these samples by using appropriate reported methods. The presence and absence of phytochemical constituents such as steroids, terpenoids, flavonoids, glycosides, phenolic compounds, α- amino acids, reducing sugars, saponins, organic acids, cyanogenic glycosides, tannins, alkaloids and anthraquinones are determined by test tube method.

Preparation of Crude Extracts from Kyun Heart Wood by Successive Percolation Method

The dried KHW powder (300 g) was percolated in 1500 mL of pet-ether (60 – 80 ºC) for one week and filtered. This procedure was repeated for further two times. The combined filtrates were then evaporated under reduced pressure by means of a vaccum rotary evaporator. Consequently, concentrated pet-ether extract of KHW was obtained.

Separation and Isolation of Some Organic Constituents from Pet-ether Crude Extract of Kyun Heart-wood

The pet-ether crude extract from KHW was firstly separated by silica gel column was thoroughly stirred. A portion of the slurry was poured into the column and at the same time the tap was opened so that the solvent flowed at a slow but constant rate. As the column material slowly settled to the bottom, the column was lightly tapped with a rubber tubing around the outside wall so as to achieve an air bubble free, uniform packing. Column material sticking to the upper walls of the column was washed down with the solvent. When the level of solvent had fallen to reach a few millimeters above the top of the silica gel column, the tap was closed.

4 g of petroleum ether crude extract were weighed and made as a mixture with 2 g of silica gel. The mixture was allowed to dry with continuous agitation so that a free flowing dry silica gel on which the sample was uniformly adsorbed. By careful pouring of the sample adsorbed gel down into the above column through a small funnel and adjusting the position of the upper surface of the adsorbed gel, a uniform layer of adsorbed gel was obtained on the top of the column. The top of the layer must be emerged in the solvent. Any extra depth of the solvent above the

top was allowed to enter the gel by opening the top. The column was then completely filled with the solvent system and fractionation was started. Flow rate was adjusted to about one drop per 4 seconds. Gradient elution was performed successively with (PE : EtOAc 40:1, 20:1, 9:1 v/v) and a total of 118 fractions were collected.

Chromatographic Method Eluting with Various Ratios of PE/EtOAc Solvent Systems

The column was packed by the wet method. The column was plugged by pushing a small pieces of cotton wool through the solvent with a glass rod. Care was taken so that no air bubbles were trapped in the cotton wools. Silica gel (80 g) was measured and placed in a beaker and made into a slurry by adding (PE : EtOAc, 40 : 1v/v) and the suspension

The fractions that gave some appearance on TLC chromatograms were combined. Finally five main fractions (FI-FV) were obtained. Fractions FI, F III, F IV and F V occurred as mixtures, and from fraction F II, compound '**A**' (3 mg, 0.01 %) was obtained after removal of the solvent. The compound '**A**' obtained as a yellow solid was purified by washing with PE followed by crystallization from PE/EtOAc to give a yellow crystal.

Identification of Isolated Compounds "A"

The isolated compound: '**A**' from KHW PE extract was identified by the application of modern spectroscopic methods such as UV visible, FT-IR and ^{1}H NMR.

Study on Physico-chemical Properties of Isolated Compounds

Some physico-chemical properties of the isolated compounds such as R_f values (UV 254 nm and 365 nm), melting points (Gallentemph melting point apparatus), solubilities (PE, chloroform, ethyl acetate, ethanol and methanol solvent) and some colour tests (5 % H_2SO_4, anisaldehyde – H_2SO_4, vanillin–H_2SO_4, 1% $FeCl_3$, I_2, LB reagent and KOH solution) anisaldehyde were studied.

Modern Spectroscopic Studies on the Isolated Compounds

For the identification of isolated compounds, the ultraviolet absorption spectra of the isolated compounds was recorded and examined. A Shimadzu UV-240 UV-Visible spectrophotometer at University Research Centre, YU, was used.

To identify the isolated compound, their infrared spectra were recorded on a Shimadzu perkin Elmer spectrum GX FT IR spectrophotometer at Universities' Research Centre, YU and MU. The isolated compounds were sampled with 1% KBr pellet.

The nuclear magnetic resonance spectra were also studied to examine the types and numbers of protons or carbon present in the isolated compound. The ^{1}H NMR spectra were recorded by $CDCl_3$ with TMS internal standard on a JEOL JNM-GX 400 (MHz) at Department of Natural Product Chemistry, Institute of Natural Medicine, University of Toyama in Japan.

The Minimum inhibitory concentration of Isolated compounds A by Agar disc Diffusion Method

The compound from *Tectona grandis* L. (Kyun) was prepared. The compound was tested against eight strains of microorganism serial dilution method. This include *Proteus morganni, E. coli, S. aureus* WS DMR 1D15, *E. coli* ATCC 25922, *Shigella flexneri, Vibrio cholera, S. aureus* ns DMR 1DM96 and *B. subtilis.*

Results and Discussion

Phytochemical Investigation of Kyun Heart-wood

The results obtained from these experiments were summarized in Table 1. According to these results, it was observed that steroids, terpenoids, flavonoids, glycosides, phenolic compounds, α-amino acids, saponins organic acids, tannins, alkaloids and anthraquinones present in saw dust of kyun.

Separation and Isolation of Compound "A" from Petether Extract of Kyun Heart-wood

4 g of pet-ether crude extract were separated column chromatographically by using silica gel adsorbent with increasing the polarity of eluent ethyl acetate in pet-ether. An anthraquinone compound "**A**" (yellow crystal, 3 mg, 0.01% yield,

R_f = 0.57, PE. EtOAc = 9 : v/v) was isolated as a main constituent from KHW PE extract.

Characterization and Classification of Isolated Compounds "A"

To identify the structures of isolated compound, it was firstly characterized by appropriate physical and chemical examinations followed by classification. The resultant physico-chemical properties are summarized in Table 2.

The appearance of the isolated compounds: A is illustrated in Figure 2 (a) and their thin layer chromatograms are illustrated in Figure 2 (b).

(a) (b)

Figure 2. (a) Appearance of isolated compounds (A) and (b) Co-TLC chromatograms of isolated compounds

Table 1. Results of Preliminary Phytochemical Tests on Kyun Heart-wood

Tests	Extracts	Test Reagents	Observation	Results
Steriod	Toluene	Acetic anhydride and S/A	Colouration	+
Terpenoids	$CHCl_3$	Acetic anhydride and S/A	Colouration	+
Flavonoids	EtOH	conc: HCl and Mg	Pink colour	+
Glycosides	EtOH	10% lead acetate	White ppt	+
Phenolic compound	EtOH	$FeCl_3$ solution	Deep Blue colour	+
α-Amino acid	H_2O	Ninhydrin	Pink colour	+
Reducing sugars	dil.H_2SO_4	Benidict solution	Brick Red ppt.	-
Saponins	H_2O	Distilled water	Frothing	+
Organic acids	H_2O	Bromocresol green solution (in alcohol)	Dark Blue colour	+
Cyanogenic glycosides	H_2O	Sodium picrate	Brick red	-
Tannins	H_2O	1% $FeCl_3$ and Gelatin	White ppt.	+
Alkaloids	1%HCl	Mayer's reagent	Yellow ppt.	+
		Dragendorff's reagent	Oragne ppt.	+
		Wagner's reagent	Brown ppt.	+
Anthraquinones	Benzene	KOH Solution	Red colour	+

Table 2. Some Physicochemical Properties of Isolated Compounds A from Kyun Heart wood

UV	254 nm – active,365 nm – active						
Observation	5% SA Δ	AΔ	VΔ	LB *	I_2	1% $FeCl_3$	KOH
	Yellow	ND	ND	ND	yellow	ND	Red
Melting point (°C)	173 – 174						
Solubility	PE	EtOAC	EtOH	MEOH	$CHCl_3$	H_2O	
	-	+	+	+	+	-	
Remark	Anthra quinone – derivatives						

+ soluble, - insoluble , A - Anisaldehyde , V – vanillin, LB – Lieberman Burchard , * tested in $CHCl_3$ solution

Structural Identification of Isolated Compounds

After the classification of the isolated compounds by physico-chemical characteristics, the structures were then identified by joint application of modern spectroscopic methods such as UV-visible, FT-IR, ^{1}H NMR, ^{13}C NMR and MS spectroscopies.

Compound 'A'

Compound '**A**' has the anthraquinone character. It was studied by UV-visible spectral data. The UV-visible spectra recorded in MeOH as well as in the presence of NaOH are illustrated in Figure 4. The absorption maxima were found at 206, 256, 275 and 325 nm in MeOH solvent and observed to be identical with the characteristic absorption maxima of anthraquinone at 252, 272 and 325 nm (Mohan, 2000). This observation confirmed the compound '**A**' to be an anthraquinone derivative. In addition, the absorption maxima of '**A**' were not shifted by the effect of NaOH, indicating the absence of phenolic group in '**A**'. These UV-visible spectral data of '**A**' and anthraquinone are described in Table 3.

The functional groups of compound '**A**' were also identified by FT-IR specrum shown in Figure 5 and spectral data assignments are summarized in Table 4.

The band appeared at 3015 cm^{-1} represents the aromatic C-H stretching and that at 1589 cm^{-1} was attributed to aromatic C=C stretching, indicating the presence of aromatic ring in '**A**'. The absorption bands at 2924 cm^{-1} and 2854 cm^{-1} were appeared due to asymmetric and symmetric C-H stretching, confirmed the presence of $–CH_3$ group. The sharp band at 1674 cm^{-1} was attributed to C=O stretching of 1, 4 – quinone and the bands occurred at 1327 and 1296 cm^{-1} due to C-CO-C Skeletal in diaryl ketones. The strong band at 700 cm^{-1} appeared due to O-H out of plane bending of monosubstituted benzene ring. All of these IR spectral data assignments are described in Table 4 and these observations lead to the compound '**A**' to be a monosubstituted anthraquinone as follows.

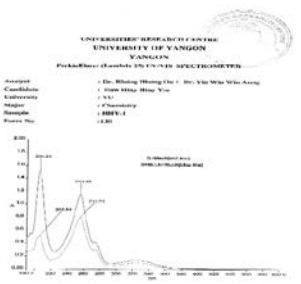

Figure 4. UV-visible spectrum of isolated compound “A”

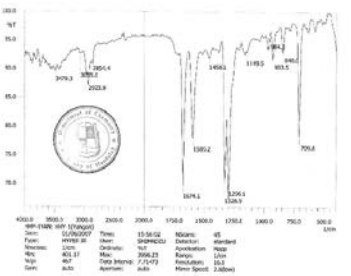

Figure 5. FT-IR spectrum of isolated compound “A” (KBr)

Table 3. UV-visible Absorption Maxima of Isolated Compound 'A' and Anthraquinone

Reagent	λ_{max} (nm)	
	Compound 'A'	Anthraquinone *
MeOH	206, 256 275, 325	252, 275, 325
MeOH + NaOH	206, 256 275, 325	-

* Mohan, 2000

Table 4. FT-IR Spectral Data of Isolated Compound 'A'

Wave Number (cm^{-1})	**Group Assignment**
3015	aromatic C-H stretch
2923, 2854	asymmetric and symmetric C-H stretch of alkyl group
1674	C=O stretch of 1,4 – quinone
1589	aromatic C=C stretch
1326, 1296	Stretch of - C - C - C - diaryl ketone skeletal
709	out of plane bending of monosubstituted ıatic ring

Furthermore, '**A**' was also structurally identified by ^{1}H NMR spectrum (400 MHz, $CDCl_3$) shown in Figure 6, and Figure 7. illustrates the expanded ^{1}H NMR spectrum between δ 7.5 ppm and 8.4 ppm. The ^{1}H NMR spectral data were interpreted from the spectra as shown in Table 5. The singlet signal appeared at δ 2.54 ppm was due to sp^3 methyl protons, indicating the presence of a methyl group substituented in '**A**'. The double-doublet signal at δ 7.60 ppm, appeared with a medium and a large coupling constants was due to the H-3 proton. The multiplet signal centered at δ 7.79 ppm was related to H-6 and H-7 protons. The signal at δ 8.12 ppm appeared with a medium coupling constants (meta protons coupling) was assigned due to H-1 proton. The signal at δ 8.21 ppm was appeared with a large coupling constant (ortho coupling) due to H-4 proton. The multiplet signal centered at δ 8.31 ppm was due to H-5 and H-8 protons. From the above ^{1}H NMR interpretation, the compound '**A**' may be assigned as 2-methyl anthraquinone with the following structure.

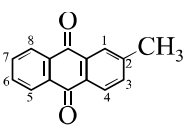

Compound **A** = 2 methyl anthraquinone

The melting point of '**A**' (173 – 174 °C) was also found to be identical with that (173 – 174 °C) of 2-methyl anthraquinone (El-Gamal, 1995). Therefore, on the basis of its physico-chemical properties and spectral data studies, the isolated compound '**A**' could be identified as 2-methyl anthraquinone with molecular formula of $C_{15}H_{10}O_2$.

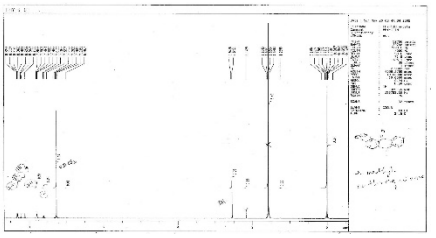

Figure 6. ^{1}H NMR spectrum (400 MHz, $CDCl_3$) of isolated compound 'A'

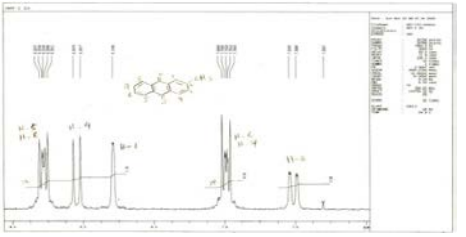

Figure 7. ^{1}H NMR spectrum expended between δ 7.5~7.84 ppm of compound 'A'

Table 5. ^{1}H NMR (400 MHz, $CDCl_3$) Spectral Data of Isolated Compound 'A'

δ (ppm)	Multiplicity	Integration	Remark
2.54	s	3H	Methyl protons
7.60	dd	1H	H-3
7.79	m	2H	H-6, H-7
8.12	d	1H	H-1
8.21	d	1H	H-4
8.31	dd	2H	H-5, H-8

Study on Antibacterial Activity of Isolated Compounds A by (Micro Plate Dilution Method)

Compounds (A) was taken to be studied their antibacterial activity, since these were isolated as main constituents from KHW. The value was obtained in larger amounts than others. Their antibacterial powers were determined in terms of minimum anhibitory concentration (MIC) values by

employing micro plated dilution method. Eight strains of microorganisms were used and these were *Proteus morganni*, *E. coli*, *S. aureus* WS DMR 1D15, *E. coli* ATCC 25922, *Shigella flexneri, Vibrio cholerae, S. arureus* ns DMR 1DM96 and *B. subtilis*.

The resultant MIC values are reported in Table 6. The MIC of compound "**A**" against *E.coli* ATCC 25922 strain was found to be 0.0156 mgml^{-1} and its MIC values against the remaining 7 strains of microorganisms were observed to be > 1 mg ml^{-1}.

This indicated that compound "**A**" possessed good antibacteiral activity, especially against *E.coli* ATCC 25922 as shown in Figure 8 and Table 6.

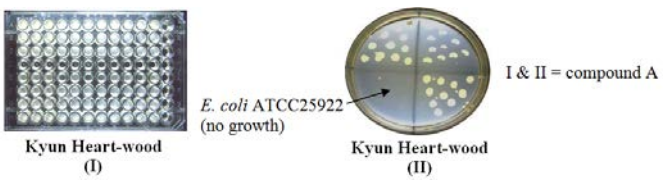

Figure 8. A presentation for determination of MIC values of compound 'A' on *E. coli* ATCC 25922 bacterial strains

Table 6. Bacteria Strains and MIC Values of Compounds 'A'

Code No.	Bacteria strains	MIC values (mg mL^{-1}) Compound A
A	*Proteus morganii* DMR 1D01	> 1
B	*Eschericha coli* DMR 1D12	> 1
C	*Staphylococcus aureus* ws DMR 1D15	> 1
D	*Escherichia coli* ATCC 25922	0.0156
E	*Shigella flexneri* DMR 1D75	> 1
F	*Vibrio cholerae* 01DMR 1D93	> 1
G	*Staphylococcus arureus* ns DMR 1DM 96	> 1
H	*Bacillus shbtilis* DMR Bs	> 1

Conclusion

From the present chemical and pharmacological investigation into Kyun heart-wood, the following inferences could be deduced: Kyun Heat-wood (KHW) was collected from Yangon Division. The samples were identified by authorized botanist at Botany Department, Yangon University. The preliminary phytochemical investigation on KHW revealed the presence of alkaloids, flavonoids, glycosides, saponin, α-amino acids, steroid, terpenoids, tannins, organic acid, phenolic compound and anthraquinonein.

2-methyl anthraquinone (**A**, 0.01 %, m.pt 173-174 ºC (EtOAc);

R_f = 0.57; PE:EtOAc, 9:1 v/v) was isolated from PE crude extract of KHW by employing silica gel column chromatographic methods. The structures of isolated compound were elucidated by joint-application of modern spectroscopic techniques such as UV, FT IR, and ^{1}H NMR spectroscopy and their corresponding physicochemical characters.

The MIC of compound "A" against *E.coli* ATCC 25922 strain was found to be 0.0156 $mgml^{-1}$ and the MICs of compound "A" against remaining seven species were observed to be > 1 $mgml^{-1}$. Compound "A" possessed good antibactieral activity, especially against *E.coli* ATCC 25922.According to these observations, it can be inferred that since *Tectona grandis* linn. (Kyun) heart-wood showed good antimicrobial activity, it can be effectively used as antimicrobial agent in the treatment of diarrhoea.

Acknowledgements

I would like to express my sincere gratitude to Dr Cho Cho Win, Department of Chemistry, Dagon University, for the permission to use various department facilities for present research paper.

References

Anthana, A.R and C.K.J.Paniker.(1983). *Text Book of Microbiology*. Longman Ltd, New Delhi, 584

Balakrishna, S., T.R.Seshadri and B.Venkataramani.(1961)."Special Chemical compounds of Commercial Woods and Related Plant Materials". *J. Sci. Industr.Res.*, **20 B**, **I**, 1-42.

Briggs, L.H and G.A.Nicholls.(1949).“Chemistry of the Coprosma Genus: The Non-glycoside Anthraquinone Compounds from Coprosma Lucida”.*The Chemical Society, London*, **II**, 1241-1246

Chopra, R.N., (1956), "Glossary of Indian Medicinal Plant". *New Delhi, Council of Scientific and Industrial Research*, 255.

Cruickshank, Ri, J.P.Duguid, B.P. Marmior and R.H.A.Swaiw.(1975).*Medicinal Microbiology*.Churchill livingstone Ltd., London.

El-Gamal, A.A.; K.Takeya, H.Itokawa, A,F,Halam, M.M. Amer, H.E.A. Saad and S.A.Awad.(1995).*Anthraquinones from Galium sinaicum, Phytochemistry*. Elsevier Science Ltd., Great Britain Press, **40**(1),

Harbone, J.B., (1973*). Phytochemistry Dictionary*,*A Hand-book of Biacltive Compounds from Plants*. Taylor & Francis Ltd., London, Washington Dc, 743

Medicinal Plants of Myanmar, (2000), Ministry of Health, Department of Traditional Medicine, Myanmar.

Merck Index, (2001).*An Encycloopedia of Chemicals, Drugs and Biologicals*. USA, Merck & Co., Inc., 13rd Ed

M-Tin Wa, (1970)."Phytochemical Screening, methods and Procedures". *Phytochemical Bulletin of Botanical Society of America*, In., **5(3)**, 4-10

Thomson, R.H., (1971).Naturally Occurring Quinones New York, Academic Press.,2nd Ed,

Isolation of (22*E*,24*R*)-24-Methyl Cholesta-5,22-Diene-3β,7β-Diol of Terrestrial Fungus *Hypocrea lutea*

Yin Yin Myint[1] & Dongho Lee[2]

Abstract

Many oxysterols exhibit therapeutic properties that were isolated from microbial sources that have been reported. Several sterol compounds from microbes possess an alkyl group at C-24 of the sterol skeletal side chain. (22*E*, 24*R*)-24-methyl cholesta-5, 22-diene-3β, 7β-diol was isolated from ethyl acetate extract of terrestrial fungus *Hypocrea lutea* by chromatographic methods using various eluents. The structure of the metabolite was identified on the basis of the spectroscopic analysis, including 1D and 2D Nuclear Magnetic Resonance (NMR) data. This is the first time that compound is reported with that fungus. The ethyl acetate extract of that fungus exhibited less cytotoxicity (40% mortality) against brine shrimps.

Keywords: (22*E*,24*R*)-24-methyl cholesta-5,22-diene-3β,7β-diol, *Hypocrea lutea*, cytotoxicity

Introduction

Fungi are remarkable organisms that readily produce a wide range of natural products often called secondary metabolites. Since the time of the pharaohs, fungi have been utilized for simple food processing. The last century has seen the development of fungal biotechnology for the subsequent production of valuable commodities such as antibiotics, enzymes, vitamins, pharmaceutical compounds, fungicides, plant growth regulators, hormones and proteins. The majority of antibiotics obtained from fungi are produced by fermentation and most are secondary metabolites, production of which occurs in the stationary phase and is linked to sporulation (Calvo, et al., 2002).

The kingdom of genus *Hypocrea* is fungus, phylum is Ascomycetes, order is Hypocreales and family is Hypocreaceae. The *Hypocrea* form typically presents itself as a cushion-shaped, brightly or lightly coloured, fleshy stroma that is no more than 5 mm in diameter, although stromata of

[1] Associate Professor, Dr, Department of Chemistry, Pathein University
[2] Associate Professor, Dr, Metabolomics and Natural Product Chemistry, College of Life-Science and Biotechnology, Korea University

some species may be several centimeters in extent and may even be club shaped or turbinate. All investigated *Trichoderma* species are intimately related to *Hypocrea*, and, increasingly, named *Trichoderma* species are being shown to be the anamorphs of *Hypocrea* species (Chaverri and Samuels, 2003). *Hypocrea*/*Trichoderma* is a genus of soil-borne or wood-decaying fungi containing members important to mankind as producers of industrial enzymes and biocontrol agents against plant pathogens, but also as opportunistic pathogens of immune compromised humans (Irina and Christ, 2005). *Hypocrea* species are economically important because of the effect that some of them have on disease-causing fungi. In addition to the use of *Hypocrea*/*Trichoderma* species in the biological control of plant pathogenic fungi, many species have the ability to break down cellulosic materials through the production of cellulases. This ability has led to the commercial exploitation of some *Hypocrea* species in the production of enzymes used in the manufacture of clothes washing detergent, animal feed and fuel (Chaverri and Samuels, 2003).

The objective of this study was to isolate and identify the secondary metabolite of fungi *Hypocrea lutae*.

Weete and Gandh, 1996, were reported that sterols and triterpenoids are in all major groups of organisms, from fungi to humans, as secondary metabolites. Sterols; such as ergosterol and lanosterol are found in membranes from a wide range of species, whereas cholesterol is an abundant membrane component, and bacteria lack sterols altogether. Sterols are widely distributed in nature, where they are required for the growth and reproduction of essentially all eukaryotic organisms.

Materials and Methods

Collection and Identification of Collected Samples

Fungus *Hypocrea lutea* was collected from Laboratory of Metabolamic and Natural Product and scientific name was confirmed according to the authorized microbiologist of College of Life Science of Biotechnology, Korea University.

Biological and Chemical Investigation of Selected Fungi

Chemical and Reagents

Chloroform, dichloromethane, ethyl acetate, tri fluro acetic acid, methanol, ethanol, dimethyl sulphoxide (EP grade solvent, Duksan and Dae-Jung chemical Co., Ltd. Korea) and HPLC grade solvents (J.T. baker) were used. Vanillin, sulphuric acid, were also used for reagent tests. For NMR analysis, deuterated solvents (CIL, USA) were used. For separation of metabolites, silica gel 60 (230-400 mesh, Merck), Sephadex LH-20 (18~111 μm, GE Healthcare), RP-18 gel, TLC percoated silica gel 60 F254 (Merck) and gel 60 RP-18 F254(Merck) were used.

Apparatus and Equipment

The following equipment and apparatus were used throughout this experiment; beakers, conical flasks, funnels, measuring cylinders, pasture pipette, bulb, clips, water bath, micropipette (Ependroff), 1L of Scholt Duran Flask, petridish (ø150×h25 mm, D, Duran, Stariplan), an electronic balance (Mettler), a refrigerator, Rotavapor R-210 (BUCHI, Switzerland), vacuum pump PC 3001 VARIO (Germany), HPLC (Varian system Prostar 210, USA).

Cultivation by solid culture

The fungal strains number F- 45 (H*ypocrea lutae*) was cultivated with 1200 mL petridish (ø150×h 25 mm, D, Duran, Stariplan) each containing Potatoes Dextrose Agar (PDA) medium at 25 ˚C for 14 days.

Extraction

The well-grown agar culture was extracted using ethyl acetate solvent four times to get the ethyl acetate layer and aqueous layer. The resulting ethyl acetate layer was evaporated using a rotary evaporator. The obtained crude extract was used for biological and chemical screenings.

Preliminary biological screening on fungal extract by brine shrimp lethality assay

Cytotoxic activity of ethyl acetate extract of *Hypocrea lutae* was monitored by the brine shrimp lethality test (Meyer, et al.,1982). Brine shrimp (*Artemia salina*) were used for test animals and geldanamycin for positive control for this test. Brine shrimp eggs were hatched with artificial sea water in rectangular dishes at 48 hours. Each 2 mg/mL of fungal extract

with 20 µL of DMSO was separately added into each of three dishes. After that, 1 mL of seawater was added in each plate of extract before adding brine shrimps (nauplii). Ten brine shrimps were added by using pasture pipette in each plate. The three replication were used for this concentration. A parallel series of tests with the standard geldanamycin for positive control was conducted. Observations were recorded after 24 hours and survivors were counted and percent death at each was calculated. Extracts causing mortality higher than 60 % were considered active.

Chemical Screening

Firstly, the bioactive extract of fungus was analyzed by using High Performance Liquid Chromatographic (HPLC) technique to know the including of major secondary metabolites. Ethyl acetate extract of *Hypocrea lutae* was analyzed with 20-100 % methanol: water solvent system, at 20 minutes.

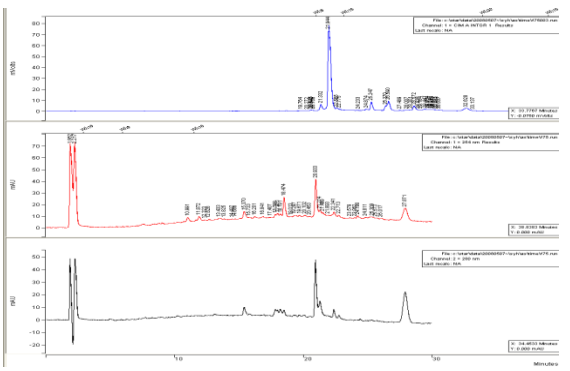

Figure 1. HPLC chromatogram for activity guided ethyl acetate extract of *Hypocrea lutea*, 20-100 % methanol, 20 minutes

Isolation and structural identification of secondary metabolites from ethyl acetate extract of *Hypocrea lutea*

Ethyl acetate extract (357 mg) of *Hypocrea lutea* was fractionated by Sephadex LH-20 gel column using isocratic elution of chloroform-methanol (1:1) solvent system to yield five fractions (F-1 to F-5). The fraction F-2 was two times rechromatographed with silica gel column by chloroform -methanol (9:1) elution and followed by *n*-hexane and

increasing *n*-hexane in ethyl acetate (1:1-1:2) as eluent to get purify secondary metabolites. Isolated secondary metabolite as white powdered was purified and conducted with a Varian-NMR (VNMR-500) spectrometer under the frequency 500 MHz in $CDCl_3$ solvent, temperature 30 °C.

Results and Discussion

Brine shrimp lethality test of ethyl acetate extract of *Hypocrea lutea*

The cytotoxic effect of ethyl acetate extract of *Hypocrea lutea* was determined using brine shrimps. This method was applied for the general toxicity of extract. It was found that the extract of *Hypocrea lutea* had 40 % of mortality on brine shrimp which can be considered it has less toxic.

Structural elucidation of one isolated secondary metabolite from *Hypocrea lutea*

According to the preliminary chemical analysis of ethyl acetate extract of *Hypocera lutea* by HPLC, it possessed one major component at 20-100 % methanol-water solvents at 20 minutes. Thus, chromatographic methods were applied to isolate the secondary metabolite from ethyl acetate extract of *Hypocrea lutea* using different polarities eluents.

One secondary metabolite (4 mg), white powdered, gave positively responded to vanillin/sulphuric acid test for steroids see Figure 6. The R_f value in chloroform/methanol solvents (10:1) is 0.24. 1D and 2D NMR spectra of isolated metabolite were applied to elucidate the chemical structure.

^{1}H NMR and ^{13}C NMR spectra revealed that the character of the isolated compound is a steroidal nucleus. ^{1}H NMR spectrum indicated that two tertiary methyl signals at δ_H 0.63 ppm (s,3H) and 1.08 ppm (s, 3H), corresponding to H-18 and H-19, two secondary methyl signals appeared at δ_H 0.93 (d, *J* 6.5 Hz, 3H) and δ_H 1.02 ppm (d, *J* 6.5 Hz, 3H) corresponding to H-21 and H-28, two distortion doublet methyl signals at δ_H 0.82 (d, *J 7.0* Hz, 3H) and 0.84 (d, *J 7.0* Hz, 3H) corresponding to H-27 and H-26. Two oxygenated methine protons are suggested at δ_H 3.54 ppm (s, 1H, H-7) and δ_H 4.09 ppm (s, 1H, H-3). Three olefinic protons were found at δ_H 5.23 ppm (dd, *J* 15, 7.5 Hz, 2H) for H-22 and H-23, and 5.35 ppm (distortion d, 1H, H-6) see Figure 2.

The ^{13}C NMR spectrum indicated 28 carbon atoms, which suggested that one trisubstituted double bond at δ_C 144.0 ppm (C-5) and 117.5 ppm (C-6) and one disubstituted double bond at δ_C 132.2 ppm(C-23) and 135.3 ppm (C-22). In addition to hydroxyl group attached two methine carbons suggested at δ_C 67.7 (C-7) and 73.7 ppm(C-3) see Figure 3.

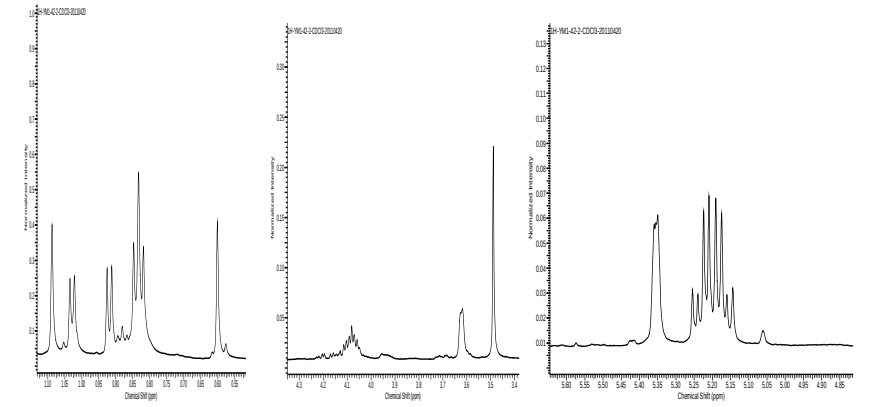

(a) (b) (c)

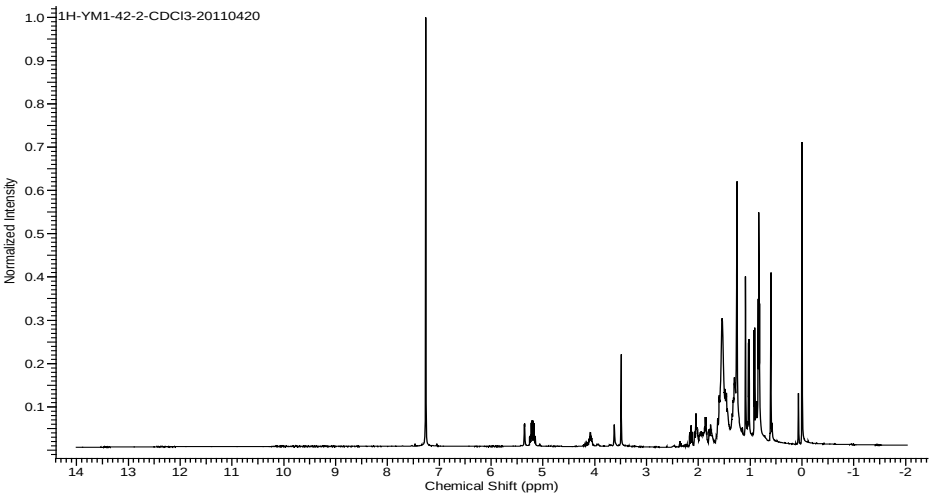

(d)

Figure 2. ^{1}HNMR spectra for (22*E*, 24*R*)- 24-methyl cholesta-5,22-diene -3β,7β-diol
(a) 0.06-1.10 ppm,
(b) 3.0-4.3 ppm,

(c) 4.85- 5.60 ppm, and
(d) 0-14 ppm

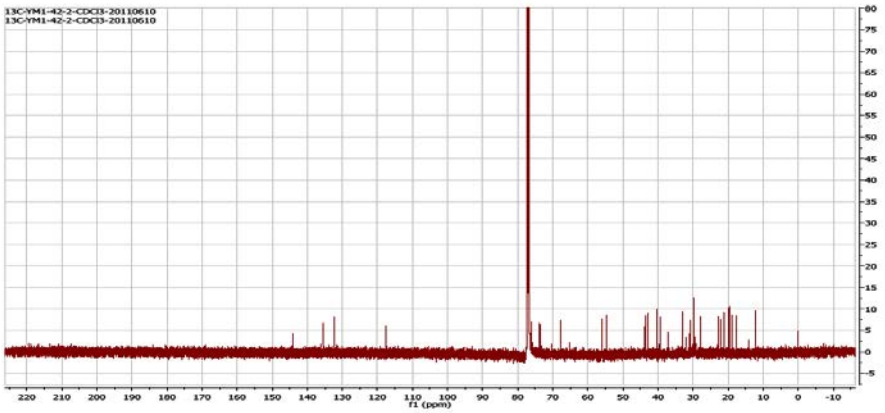

Figure 3. ^{13}CNMR spectrum for (22*E*, 24*R*)-24-methyl cholesta-5,22-diene-3β, 7β-diol

HSQC spectrum revealed ^{1}H-^{13}C direct correlation between the protons of six methyl groups; 0.6 ppm and 12.33 ppm (C-18), 0.92 ppm and 17.58 ppm (C- 28), 1.08 ppm and 18.82 ppm (C-19), 0.83 ppm and 19.94 ppm (C-26), 1.03 ppm and 21.11 ppm (C-21). The carbons attached to the hydroxyl groups and their corresponded protons; 4.09 ppm and 67.73 ppm, 3.62 ppm and 73.73 ppm were determined in that spectrum see Figure 4.

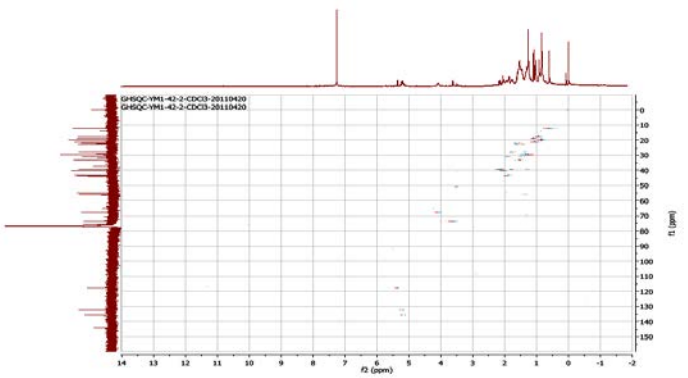

Figure 4. HSQC spectrum (^{1}H-^{13}C correlation) for (22*E*, 24*R*)- 24-methyl cholesta- 5,22-diene -3β,7β-diol

Table 1. ^{1}H and ^{13}C NMR Spectral Data of (22*E*, 24*R*)- 24-Methyl Cholesta-5, 22-Diene -3β,7β-diol with References Data

Caron position	^{1}HNMR, δ value (ppm),*J* in Hz		^{13}C NMR, δ value (ppm)	
	Observe value in $CDCl_3$, 500MHz	*(22*E*, 24*R*)-24 methyl cholesta -5, 22-diene-3β,7β diol in $CDCl_3$, 400MHz	Observe value in $CDCl_3$, 125MHz	**(22*E*, 24*R*)-24 methyl cholesta-5, 22-diene -3β ol in $CDCl_3$, 25.16 MHz
1			37.17	37.36
2			30.89	31.69
3	4.09, m	3.54,bm	73.71	71.76
4		2.25, bdd, 13.7, 13.7	40.37	42.30
5			144.02	140.79
6	5.35, distortion d,	5.29,dd, ,2.2, 2.2	117.57	121.60
7	3.62	3.85, bdd, 7.7, 2.2	67.73	31.97
8			29.69	31.97
9			43.79	50.27
10			33.09	36.58
11			22.07	21.13
12			39.25	39.77
13			43.51	42.35
14			56.03	56.96
15			22.89	24.39
16			27.89	28.58
17			54.77	56.06
18	0.60, s	0.70, s	12.34	12.09
19	1.09,s	1.05, s	18.82	19.42
20			39.52	40.24
21	1.03, d, 6.7	1.02, d, 6.6	21.12	21.06
22	5.23, dd,	5.18, m	135.38	135.83

Caron position	^{1}HNMR, δ value (ppm),*J* in Hz		^{13}C NMR, δ value (ppm)	
	Observe value in $CDCl_3$, 500MHz	*(22*E*, 24*R*)-24 methyl cholesta -5, 22-diene-3β,7β diol in $CDCl_3$, 400MHz	Observe value in $CDCl_3$, 125MHz	**(22*E*, 24*R*)-24 methyl cholesta-5, 22-diene -3β ol in $CDCl_3$, 25.16 MHz
	15.0, 7.5			
23			132.22	131.76
24			42.83	42.90
25			32.99	33.16
26	0.83, distortion d, 6.5	0.83,d,6.6	19.94	20.02
27	0.82, distortion d, 6.5	0.82,d, 6.6	19.64	19.69
28		0.91, d, 6.6	17.59	17.86

*Notaro, et al., 1992 and **Wright, et al., 1978

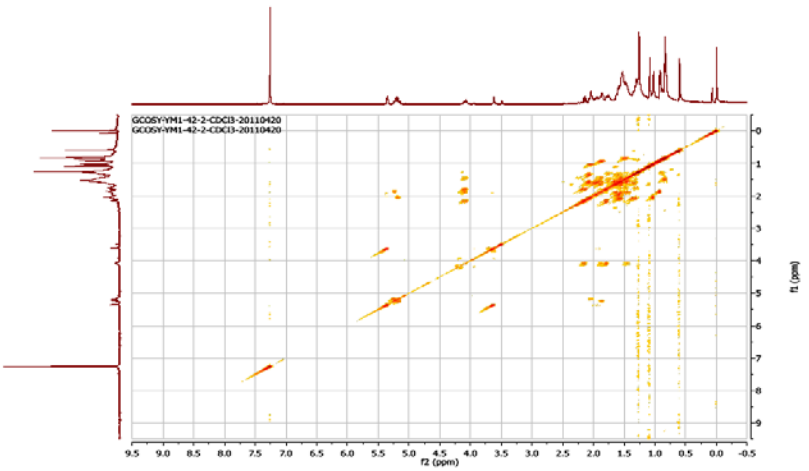

Figure 5. ^{1}H-^{1}H COSY spectrum of or (22*E*, 24*R*)-24-methyl cholesta-5, 22-diene-3β, 7β-diol

In ^{1}H-^{1}H COSY spectrum, the correlation between δ 4.09 ppm (H-3) and δ 5.35 ppm (H-6) of isolated compound indicated the olefinic proton is located next to a hydroxyl group see Figures 5 and 6.

The stereochemistry of the side chain was determined by comparison of the ^{1}H and ^{13}C NMR spectral data of isolated compound and reported data. According to the *J* values of C-22 and C-23 were large coupling constant (15.0 Hz), thus the configuration of the double bond between C-22 and C-23 was determined to be *trans*-disubstituted (an *E*-configuration of the double bond at C-22). Wraight, et al., 1987 presented that many sterols of plants and micro-organisms contain a methyl or ethyl group at C-24, and both C-24 diastereoisomers have been found to occur in nature. In general, algae and fungi produce sterols with the 24*R* configuration (24*S* if a saturated side chain, 24*R* if the Δ^{22} derivatives). Besides, that research paper was described at δ_C 17.6 ppm for the C-28 methyl resonance that the characteristic of the compound is 24*R* configuration in sterols possessing an unsaturated side chain (Wraight, et al., 1987).

Thus, the isolated compound can be considered that it possesses (22*E*, 24*R*)-24-methyl-Δ^{22}-sterol side chain. All compilation of the spectral data, the isolated compound can be deduced as (22*E*, 24*R*)-24-methyl cholesta-5, 22-diene -3β,7β-diol. Comparing the observed data of isolated compound with reported data of (22*E*, 24*R*)-24-methyl cholesta-5, 22-diene -3β,7β-diol were presented in Table 2.

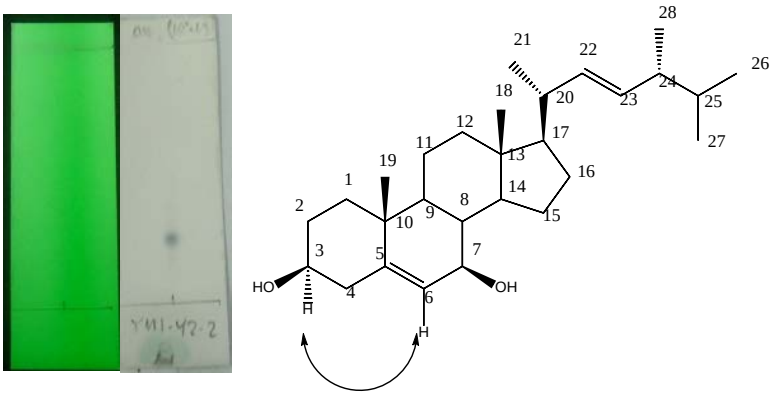

(a) (b) (c)

Figure 6. Chromatogram of (22*E*,24*R*)-24-methyl cholesta-5,22-diene-3β, 7β-diol, chloroform/methanol (10:1)
(a) under 254 nm
(b) after spraying with vanilline/sulphuric, heated
(c) ^{1}H-^{1}H correlation H-3 and H-6

Conclusion

Ethyl acetate extract of *Hypocrea lutea* had less cytotoxicity against on brine shrimps. White powder, 4.0 mg of (22*E*, 24*R*)-24-methyl cholesta-5, 22-diene-3β, 7β-diol was firstly reported for ethyl acetate extract of fungus *Hypocrea lutea*. Metabolomics of sterols in microorganisms has provided insight into the biology of microorganisms. Additionally, sterols play an important role in drug discovery, through validation of drug targets, and by confirmation of small molecule mechanisms. Thus, the investigation of sterol from microbiota will inform chemical biology, ecology, and pharmacology.

Acknowledgement

This research work was financially supported by the International Scholar Exchange Fellowship (ISEF 2010-2011) of the Korea Foundation for Advanced Studies (KFAS). I thank Cooperative Centre for Analytical Instruments Center at Korea University for providing some of the instruments used in this research.

References

Calvo, A. M., A.W.Richard, W. B. Jin and P. K.Nancy.(2002). "Relationship between Secondary Metabolism and Fungal Development. *Microbiology and Molecular Biology Reviews*, **66 (**3), 447–459

Chaverri, P., and G.J. Samuels. (2003). *Hypocrea/Trichoderm* (Ascomycota, Hypocreales, Hypocreaceae): Species with Green Ascospores. Maryland 20705, U.S.A, Cebtraalbureau voor Schimmelcultures, 1-36

Irina, D. and K.P. Christ. (2005). "Species Concepts and Biodiversity in *Trichoderma* and *Hypocrea*: from Aggregate Species to Species Clusters. *Journal of Zhejiang University Science*, **6B** (2), 100-112

Meyer, B. N., N. R. Ferrigni, J. E. Putnam, L.B. Jacobsen, D. E. Nichols, and J. L. McLaughin. (1982). "Brine Shrimp: A Convenient General Bioassay for Active Plant Constituents ". *Journal of Medicinal Plant Research*, **45**, 31-34

Nataro,G., V.Piccalli,D. Sica. (1992). "New Steroidal Hydroxyketones and Closely Related Diols from the Marine Sponge *Cliona copiosa". Journal of Natural Products*, **55 (**11), 158-1594

Weete, J.D. and S.R. Gandhi. (1996). Biochemistry and Molecular Biology of Fungal Sterols, The Mycota III, Biochemistry and Molecular Biology, Brambll Marzluf (Eds.), New York, Springer-Verlag Berlin Heidelberg, 421-422

Wright, J. L. C., A.G. Mcinnes, S. Shimizu, D.G Smith, and J.A. Walter, A. (1978). "Identification of C-24 Alkyl Epimers of Marine Sterols by ^{13}C Nuclear Magnetic Resonance Spectroscopy. *Canadian Journal Chemistry*, **56**, 1898- 1903

Environmental Studies on Water Qualities of Attaran River Near Kaw Pa Naw Village, Mon State

War War Nyein[1] & Zune Pwint Phyu[2]

Abstract

This research was conducted to study the water qualities of Attaran River near Kaw Pa Naw village in Kyaikmayaw Township, Mon State. The collection of river water samples were carried out in 2019 during winter, summer and rainy seasons. The water parameters such as pH, temperature, color, electrical conductivity, turbidity, total dissolved solids, dissolved oxygen, biochemical oxygen demand, sulphate, chloride, total hardness, total alkalinity, iron, fluoride and manganese respectively by using conventional and modern instrumental methods. Results of microbiological examination of river water samples during three seasons by plate count method, total coliforms were found to be in the range of 154 CFU/mL (rainy season) to 176 CFU/mL (summer season). *E. coli* value 1 CFU/mL (summer season) and 0 CFU/mL (rainy season) were observed. However, total coliform and *E. coli* were not detected in winter season. Some elements present in river water samples were determined by using Energy Dispersive X-Ray Fluorescence method and some toxic heavy metal contents of river water samples during three seasons were found to be in the ranges of lead (ND - 0.10 ppm), arsenic (0 - 3.566 ppm) and cadmium (ND - 0.139 ppm) by atomic absorption spectrophotometric method. The results of river water samples in both seasons were compared with the water quality standards by WHO guideline.

Keywords: Attaran River, physicochemical parameters, microbiological parameters, heavy metals

Introduction

Water plays an important role in the world economy. Approximately 70 % of the freshwater used by humans goes to agriculture. Water is an excellent solvent for a wide variety of chemical substances; such as it is widely used in industrial processes, and in cooking and washing (Yadav *et al*., 2013). Most of the rivers in the urban areas of the developing countries are the ends of effluents discharged from the industries. Highly impure water has various effects on human being, domestic purpose as well as

[1] Associate Professor, Dr, Department of Chemistry, Pathein University
[2] MSc student, Department of Chemistry, Mawlamyine University

industrial use. Human beings get infections due to presence of different bacteria and heavy metals present in water (Patil *et al*., 2012).

River water quality is a key concern as it is used for drinking and domestic purpose. Rivers are the most important freshwater resource for man. Social, economic and political development has been largely related to the availability and distribution of freshwaters contained in riverine systems (Su *et al*., 2004). The ecological balance maintained by the quantity and quality of water determines the way of life of a people. With increasing industrialization, urbanization and technological advance in all fields, source of water are getting more and more seriously polluted. Industrial effluents of different origins containing toxic metals, pesticides, etc. and anthropogenic sources create water pollution problems through discharges into river water. The utility of river water for various purposes is governed by physico-chemical and biological quality of the water (Hatje and Bidone, 1998).

To access the quality of river water for the purpose of irrigation, health, domestic and fisheries, we need to identify the physicochemical characteristics that are important for respective field, and their acceptable levels of concentrations. The chemical constituents of irrigation water can affect plant growth (Roborts *et al*., 2002).

Materials and Methods

Sample Collection

Water samples were collected from Attaran River near Kaw Pa Naw village in Kyaikmayaw Township, Mon state. The collection of river water samples were made on 19th January, 2019 (winter season), 15th May, 2019 (summer season) and 29th June, 2019 (Rainy season). Water samples were collected from the surface and 3 feet below from the surface of water and stored in the clean polythene bottles. After the samples have been taken a label describing the sample names, date, time and exact location were fixed to the bottles and then water samples were carefully transported to the laboratory and are preserved for physical and chemical analysis. The photograph of collecting river water samples near Kaw Pa Naw village was shown in Figure 1.

Figure 1. Sampling point of Attaran River near Kaw Pa Naw village in Kyaikmayaw Township, Mon state

Water Quality Analysis

Conventional methods are utilized in monitoring pH, temperature, color, electrical conductivity (EC), turbidity, total dissolved solids (TDS), dissolved oxygen (DO), and biochemical oxygen demand (BOD). Total hardness, total alkalinity and chloride values were tested by titrimetric methods. The content of iron, manganese, sulphate and fluoride were anlayzed by spectrophotometric methods. The presence of silicon, potassium, sulphur, iron, calcium, titanium, copper and zinc were identified by Energy Dispersive X-Ray Fluorescence (EDXRF) method. The contents of arsenic, lead and cadmium were analyzed by atomic absorption spectrophotometric (AAS) method. In addition, microbiological examination such as total coliforms and *E. coli* were also determined by plate count method.

Results and Discussion

Physical Parameters

pH

pH is one of the most common water quality tests performed. Basically, the pH value is a good indicator of whether water is hard or soft. The pH of pure water is 7. The observed pH values of the river water samples during three seasons were found to be in the range of 6.44 to 7.05

as shown in Table 1. From the results, it was observed that in winter season (pH is 6.74), in summer season (pH is 6.44), and in rainy season (pH is 7.05). Hence, the pH values of river water samples during three seasons were in the permissible range of pH value recommended by WHO standards (6.5 - 8.5).

Temperature

Water temperature plays a limiting role on the feeding and recruitment success of fish and crustacean larvae. It is one of the most important physical factors affecting marine and estuarine organisms. In general, the sensitivity of aquatic organisms to toxic substances increases with increasing water temperature (Abida and Harikrishna, 2008). The observed temperature values of the river water samples during three seasons higher than the standard guideline value of WHO (15 °C) and were recorded in Table 1. High temperature values indicated that increasing demand of dissolved oxygen.

Color

All surface water possesses some degree of color. The observed color values of river water sample during three seasons were found to be in the range of 186 HU to 750 HU as shown in Table 1. The observed color values in winter, summer and rainy seasons were 206 HU, 750 HU and 186 HU respectively. These values exceeded the standard guideline value of WHO(5 HU). The observed color values indicated that more suspended materials contained in these river water samples.

Electrical conductivity (EC)

The electrical conductivity (EC) measures the concentration of ions in water. The observed electrical conductivity values of river water samples during three seasons were found to be in the range of 106.60 μS/cm to 340 μS/cm as shown in Table 1. The observed electrical conductivity values 245 μS/cm (in winter), 340 μS/cm (in summer) and 106.60 μS/cm (in rainy season) were lower than the standard guideline value of WHO (≤ 1500 μS/cm). From the EC results, it was observed that the presence of ions within river water samples were low.

Turbidity values

Turbidity is the cloudiness or haziness of a fluid caused by suspended solids that are usually invisible to the naked eye. The measurement of turbidity is an important test when trying to determine the quality of water. At World Health Organization (WHO) prescribe the highest desirable limit to be 5 NTU and maximum permissible limit 25 NTU. The observed turbidity values of river water samples during three seasons were found to be in the range of 42.70 NTU to 179 NTU as shown in Table 1. It was found that all turbidity values were exceeded than the standard guideline value of WHO (5-25 NTU). Turbidity values 54.70 NTU and 42.70 NTU of winter and rainy seasons were slightly murky. The highest turbidity values 179 NTU were found to be in summer season and it was very murky.

Total dissolved solids (TDS)

Total dissolved solids refer to the sum of all the components dissolved in water. According to literature, the water was classified as excellent (< 300 ppm), good (300-600 ppm) and poor (600-900 ppm). In this research, total dissolved solids values of river water samples during three seasons were found to be in the range of 81 to 183 ppm as shown in Table 1. TDS values observed were in winter season (128 ppm), summer season (163 ppm) and rainy season (81 ppm) and they were in the range permitted by WHO (< 300 ppm). According to literature and present results data, these river water samples were excellent.

A village and a cement industry were closed by at the time of the research. Due to human activities and environmental consequences, turbidity, color, electrical conductivity, and total dissolved solids were all high throughout the summer season.

Dissolved oxygen (DO)

The oxygen content in water samples depends on a number of physical, chemical, biological and microbiological processes. In this research, DO values of river water samples during three seasons were found to be in the range of 2.00 to 5.78 ppm as shown in Table 1. The results for summer and rainy seasons were observed as 2.00 ppm and 3.00 ppm and they were below the permissible limit of WHO guideline. DO value in winter season (5.78 ppm) was within the limit permitted by WHO standards (4-8 ppm). According to literature, fish need at least 5-6 ppm DO to grow

and thrive. If DO levels drop below about 3.00 ppm in summer season, the microorganisms in water will not survive.

Biochemical oxygen demand (BOD)

BOD is the amount of oxygen required by the living organisms engaged in the utilization and ultimate destruction or stabilization of organic water. The observed biochemical oxygen demand values of river water samples during three seasons were found to be in the range of 4.60 to 4.80 ppm as shown in Table 1. The values for BOD were found to be maximum 4.80 ppm in both winter and rainy seasons. In summer season, BOD value was recorded as 4.60 ppm. These values were agreed with the standard guideline value of WHO (3-5 ppm). The results showed that these river water samples were moderately clean.

Table 1. Physical Parameters of River Water Samples

Physical Parameters	Seasons			Standard Guideline Values of WHO
	Winter	Summer	Rainy	
pH	6.74	6.44	7.05	6.5 - 8.5
Temperature (°C)	26.90	33.10	28.05	15
Color (HU)	206	750	186	5
Electrical conductivity (μS/cm)	245	340	106.60	≤ 1500
Turbidity (NTU)	54.70	179	42.70	5-25
Total dissolved solids (ppm)	128	163	81	excellent (< 300) good (300-600) poor (600-900)
Dissolved oxygen (ppm)	5.78	2.00	3.00	4-8
Biochemical oxygen demand (ppm)	4.80	4.60	4.80	1-2 (very good) 3-5 (moderately clean) 6-9 (polluted)

Chemical parameters

Sulphate

The sulphate content of natural waters is an important consideration in determining their suitability for public and industrial supplies. The resultant sulphate values of river water samples during three seasons were found to be in the range of 5 to 27 ppm as shown in Table 2 and sulphate was recorded as in winter season (12 ppm), in summer season (27 ppm) and in rainy season (5 ppm). These values were lower than the standard guideline value of WHO (150 ppm). According to the results, these river water samples were suitable for public uses.

Chloride

Chloride occurs naturally in all types of water. High concentration of chloride is considered to be the indicators of pollution due to organic wastes of animal or industrial origin. Chloride contents are troublesome in irrigation water and also harmful to aquatic life (Rajkumar *et al*., 2004). The chloride values of river water samples during three seasons were recorded in Table 2. The chloride values were recorded as winter season (ND), summer season (3.49 ppm) and rainy season (ND). These values were lower than the standard guideline value of WHO (250 ppm). Hence, low concentrations of chloride in river water samples indicated that these were not hazardous to human consumption.

Total hardness

Hardness of water is an important consideration in determining the suitability of water for domestic and industrial uses. Total hardness is a characteristic of water which represents the total concentration of the calcium and magnesium ions expressed as calcium carbonate. The total hardness values of river water samples during three seasons varied from 1.28 to 64 ppm as shown in Table 2. Total hardness values observed were in winter season (1.28 ppm), summer season (64 ppm) and rainy season (1.36 ppm). All these hardness were agreed with permissible range of WHO standard guideline (≤ 100 ppm). The results indicated that the class of hardness in river water samples was soft.

Total alkalinity

Alkalinity is composed primarily of carbonate and bicarbonate, alkalinity acts as a stabilizer of pH. Alkalinity of natural water is typically a

combination of bicarbonate, carbonate and hydroxide ions. Alkalinity between 50 and 500 ppm is generally acceptable to fish and shrimp production and alkalinity between 20 and 50 ppm will permit plankton production for fish culture. The observed total alkalinity values of river water samples during three seasons were recorded in Table 2. The total alkalinity range of river water samples from 2 to 2.82 ppm [winter season (2.12 ppm), summer season (2.82 ppm) and rainy season (2 ppm)] were observed. These values were very low under standard guideline value of WHO (200 ppm) and thus these river water samples were acceptable to fish culture.

Iron

Iron is an essential mineral. The standard limit for iron in drinking water is 0.30 ppm, which is very high but not dangerous. The observed iron values of river water samples during three seasons were described in Table 2. The observed iron concentrations in winter season (0.11 ppm), in rainy season (ND) were lower and in summer season (0.89 ppm) were higher than the standard guideline values of WHO (0.30 ppm). The results showed that higher concentrations of iron in summer season may have adverse effects on humans.

Fluoride

Fluoride is mainly used to improve dental health. It also helps with slowing down or stopping the decay process. The observed fluoride values of river water samples during three seasons were found to be in the range of 0.16 to 5.70 ppm as shown in Table 2. Fluoride values in winter (0.17 ppm) and rainy seasons 0.16 ppm) were lying below the standard guideline values of WHO. Fluoride values in summer season (5.70 ppm) exceeded the WHO standard (1.50 ppm). From the results, higher concentrations of fluoride in summer season can damage bone and joints of humans.

Manganese

Manganese values of river water samples during three seasons were described in Table 2. The values of manganese ranged from 0.007 ppm in summer season followed by 0.086 ppm in winter season and 0.107 ppm in rainy season, respectively. From the results, manganese values were below the permissible limit in summer season and exceeded than the standard guideline values of WHO (0.05 ppm) in winter and rainy seasons. Higher

concentrations of manganese in winter and rainy season can impart undesirable taste and odour.

Microbiological Parameters

Total coliforms

In water, coliform bacteria have no taste, smell or color. Coliform bacteria may not cause disease, but used as one of the indicators of pathogenic contamination that can cause diseases such as intestinal infection, dysentery, hepatitis, typhoid fever, cholera and other illness (Emmanuel *et al*., 2009). The observed total coliforms values of river water samples were in Table 3. It was found that total coliforms values were recorded in summer season (176 CFU/mL) and rainy season (154 CFU/mL). Results of microbiological examination of river water samples for total coliforms were not detected in winter season. The results showed bacterial contaminations in summer and rainy seasons due to the presence of total coliforms bacteria.

Table 2. Chemical Parameters of River Water Samples

Chemical Parameters	Seasons			Standard Guideline Values of WHO
	Winter	Summer	Rainy	
Sulphate (ppm)	12	27	5	150
Chloride (ppm)	ND	3.49	ND	250
Total hardness (ppm)	1.28	64	1.36	soft (0 – 60) moderate(61 – 120) hard (121 – 180) very hard (> 180)
Totalalkalinity (ppm)	2.12	2.82	2	200
Iron (ppm)	0.11	0.89	ND	0.30
Fluoride (ppm)	0.17	5.70	0.16	1.50
Manganese(ppm)	0.086	0.007	0.107	0.05

ND = Not Detected

E. coli

Escherichia coli (*E. coil*) is the only member of the total coliforms group of bacteria that is found only in the intestines of mammals, including humans. The presence of *E. coli* in water indicates recent fecal contamination and may indicate the possible presence of disease-causing pathogens such as bacteria, viruses and parasites. The observed *E. coli* values of river water samples were recorded in Table 3. *E. coli* values were in summer season (1 CFU/ mL), in rainy season (O CFU/mL) and not detected in winter season. The results showed that very low concentration of *E. coli* in summer season may not have adverse effects on humans.

Qualitative determination of some elements by EDXRF method

The EDXRF elemental analysis is a powerful technique for analysis of the various samples. One of the advantages is a multi-elemental analysis, i.e, it can indicate all elements in a given sample by one measurement. According to the results of the relative abundance, six elements such as Si, S, K, Ca, Fe and Cu were detected in winter season. Eight elements like Si, K, S, Fe, Ca, T,i Cu and Zn were observed in summer season. Six elements such as Si, S, K, Ca, Fe and Cu were observed in rainy season. These elements are vital elements for human health needs. The resultant EDXRF data were described in Table 4.

Table 3. Microbiological Parameters of River Water Samples

Microbiological Parameters	Seasons			Standard Guideline Values of WHO
	Winter	Summer	Rainy	
Total coliforms (CFU/mL)	ND	176	154	0
E. coli (CFU/mL)	ND	1	0	0

ND = Not Detected

Table 4. Relative Abundance of some Elements in River Water Samples

Elements	Relative Abundance (%)		
	Winter season	**Summer season**	**Rainy season**
Si	0.407	1.845	0.403
K	0.022	0.104	0.026
S	0.079	0.080	0.068
Fe	0.010	0.058	0.007
Ca	0.013	0.035	0.010
Ti	ND	0.013	ND
Cu	0.004	0.004	0.009
Zn	ND	0.002	ND
H_2O	99.465	97.859	99.837

ND = Not Detected

Quantitative determination of some elements by AAS method

Some toxic elements in river water samples during three seasons were determined quantitative by Atomic Absorption Spectrophotometric method. The results were recorded in Table 5 and it was shown graphically in Figure 2. The results showed that arsenic and cadmium in winter and summer seasons and lead in rainy season exceeded the standard guideline value of WHO. Result of arsenic (0 ppm) in rainy season was below WHO standards. Lead was not detected in winter and summer seasons. Cadmium was not detected in rainy season. From the results, these river water samples during three seasons were not suitable for drinking due to the presence of some toxic metals.

Table 5. Comparison of some Toxic Metals of River Water Samples and WHO Standards

Sr. No	Seasons	Elements	Concentrations (ppm)	WHO Standards
1	Winter	Pb	ND	0.05
		As	0.790	0.05
		Cd	0.139	0.01
2	Summer	Pb	ND	0.05
		As	3.566	0.05
		Cd	0.046	0.01
3	Rainy	Pb	0.1	0.05
		As	0	0.05
		Cd	ND	0.01

ND = Not Detected

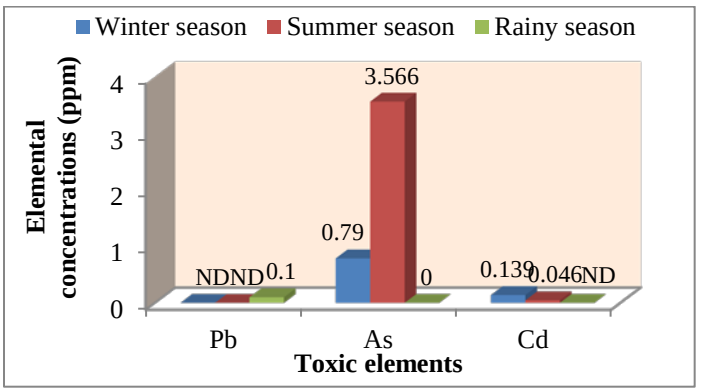

Figure 2. A bar graph of toxic elements vs. concentration (ppm) in river water for the three seasons

Conclusion

From the overall analysis on the water quality of Attaran river near Kaw Pa Naw village during three seasons, results of some physicochemical properties of river water samples were consistent to the WHO standards except temperature, color, turbidity, dissolved oxygen, manganese (both in winter and rainy seasons), fluoride and iron (in summer season). Results

of microbiological examination of river water samples showed that these river water samples were suitable for domestic water due to the presence of low contaminations of some bacteria. Relative abundance of elements such as Si, K, S, Fe, Ca Ti, Cu and Zn were observed during three seasons. Some toxic elemental concentrations of river water samples showed that arsenic and cadmium in winter and summer seasons exceeded than WHO standards. Result of arsenic was below and lead concentration was slightly exceeded than WHO standards in rainy season. Lead (in winter and summer seasons) and cadmium (in rainy season) were not detected. The results indicated that the river water samples contained some heavy metals analyzed and hence may have adverse effects with heavy metals toxicity on people. Therefore, these river water samples were not suitable for drinking. In summary, the river water samples may not be suitable for drinking due to the presence of some heavy metals and bacterial contaminations. However, the overall results revealed that almost all the physicochemical parameters, microbiological indicators and elemental contents are in fair status, expressing their safety for domestic purpose.

Acknowledgement

The authors would be grateful thanks Professor Dr Si Si Hla Bu, Rector, Dr Than Tun, Pro-rector, Pathein University, for their encouragement, permission and suggestions. Then, the authors would like to thanks professor Dr Ye Myint Aung, Head of Department, Pathein University for his reviewing to this research paper and kind permission.

References

Abida, B. and Harikrishna (2008). "Study on the Quality of Water in some Streams of Cauvey River" *E-Journal of Chemistry*, **5,** 377 –384

Emmanuel, E., M.G. Pierre and Y. Perrodia. (2009). "Groundwater Contamination by Microbiological and Chemical Substances Released from Hospital Wastewater Consumers". *Environmental International Journal*, **35**, 718 – 726

Hatje, V. E. D. and J. L. Bidone. (1998). "Estimation of the Natural and Anthropogenic Components of Heavy Metal Fluxes in Fresh Water, Sinos River, Rio Grande do Sul State, South Brazil" *Environmental Technology*, **19**, 483-487

Patil, P. N., D. V. Sawant and R. N. Deshmukh. (2012). "Physicochemical Parameters of Water Testing of Water Review". *International Journal of Environmental Science*, **3**, 110-121

Rajkumar, S., Velmurugan, K. Shanthi, P. M. Ayyasamy and Lakshmana-perumalasamy (2004). "Water Quality of Kodaikanal Lake, Tamilnadu in Relation to Physicochemical and Bacteriological Characteristics" *Capital Publishing Company, Lake,* 339-346

Roborts, R. D., A. S. Fraser, K. M. Hodgson and J. M. Paquette. (2002). "Monitoring and Assessing Global Water Quality". *Ecohydrol.Hydrobiol*, **2**, 19-27

Su, S. X., L. Kang, P. Tong, X. Shi and J. Shen. (2004). "The Impact of Water Related Human Activities on the Water Land Environment of Shiyang River Basin, An Arid Region in Northwest China". *Hydro.Sci.des.Hydro.J.*, **49**, 413-427

Yadav, P., A. K. Yadav and P. K. Khare. (2013). "Physicochemical Characteristics of a Freshwater Pond of Orai, U.P, Central India". *Octa Journal of Bioscience*, **1**, 177-184

Effects of pH Value and Sintering Temperature on Structural and Mechanical Properties of Beta-Tricalcium Phosphate Bioceramics

Cho Cho Khin[1] & Kyaw Kyaw Wynn[2]

Abstract

β-tricalcium phosphate (β-TCP) powders were prepared by the wet chemical precipitation method with calcium nitrate tetrahydrate $Ca(NO_3)_2.4H_2O$ and diammonium hydrogen phosphate $(NH_4)_2HPO_4$. In this research, β-TCP powders were prepared with two different pH values of 8 and 10. After filtration, the thermal behavior of two types of products pH-8 and pH-10 were investigated by using Thermogravimetric and Differential Thermal Analysis (TG/DTA). The synthesized β-TCP pellets were sintered at four different sintering temperatures. The phase formations of these samples were characterized by using X-ray Diffraction (XRD) analysis. The crystallite size has increased with the larger pH value. The mechanical behaviors of the samples were investigated by undertaking hardness testing in this research. The compressive strength increased with increasing pH value. The bulk density and porosity of β-TCP pellets were measured by using Archimedes' method. It was found that the sample β-TCP for pH-10 at 1100°C exhibits the largest bulk density with the smallest porosity. In this research, the β-TCP sample for pH-10 at a sintering temperature of 1100°C provided the largest mechanical properties which may be applicable as bone substitutes.

Keywords: Beta-tricalcium phosphate, pH, sintering, mechanical Properties

Introduction

Tricalcium phosphate (TCP) is one of the variations of the calcium phosphate compounds with more applications In bone tissue regeneration due to its chemical composition $Ca_3(PO_4)_2$ being similar to the natural bone tissue. TCP is widely used in the biomedical field because of its excellent biocompatibility, high bioactivity, non-toxicity, non-inflammatory behavior, and non-immunogenic properties. It can exist in two possible forms, α, and

[1] Lecturer, Department of Physics, Mawlamyine University
[2] Professor, Dr., Department of Physics, Mawlamyine University

β (Massit, A., *et al*, 2018). The β-TCP is bioresorbable, and bio-resorption occurs through osteoclastic activity. It has good biodegradability and a higher dissolution rate in the body's environment after implantation, which is absorbed and replaced by new bone. Many methods are used to synthesize such biomaterials including wet chemical method, solid-state process, microwave irradiation, sol-gel, etc. In particular, the wet chemical precipitation route is the most talented route owing to its ease in experiment operations, low working temperature, high percentages of pure products, and inexpensive equipment requirement (Asril, A., *et al*, 2017). In the present research, a wet chemical precipitation method was carried out to prepare β-TCP and the effects of pH value and sintering temperature on its structural and mechanical properties were investigated.

Materials and Method

Experimental Procedure

β -TCP powders were synthesized by wet chemical precipitation method with calcium nitrate tetrahydrate with diammonium hydrogen phosphate. The Ca:P molar ratio of β-TCP is 1.5. Keeping that ratio constant, the amounts of required raw materials were calculated. Calcium nitrate tetrahydrate and diammonium hydrogen phosphate solutions were prepared by dissolving the crystals in distilled water. The prepared solution of $(NH_4)_2HPO_4$ was added slowly drop-wise into the $Ca(NO_3)_2.4H_2O$ solution. The pH was controlled by adding sodium hydroxide (NaOH) solution. After filtration of the paste, the thermal behavior of two types of products pH-8 and pH-10 were investigated by using Thermogravimetric and Differential Thermal Analysis (TG/DTA). The filter paste was dried at 80°C for 24 h and calcined at 700°C for 2 h. The synthesized β-TCP powders were pressed into pellets by hydraulic press. The pellets were sintered at 800°C, 900°C, 1000°C, and 1100°C for 6 h each. The phase formations of these samples were characterized by using X-ray Diffraction (XRD) analysis. The crystallite sizes and lattice parameters were estimated from the XRD data. The values of hardness were measured by using a hardness tester (EH-01). The compressive strengths were calculated from the hardness data. The bulk density and porosity were measured by using Archimedes' method. Figure 1 shows the flowchart of the wet chemical precipitation process used for the preparation of β-TCP samples.

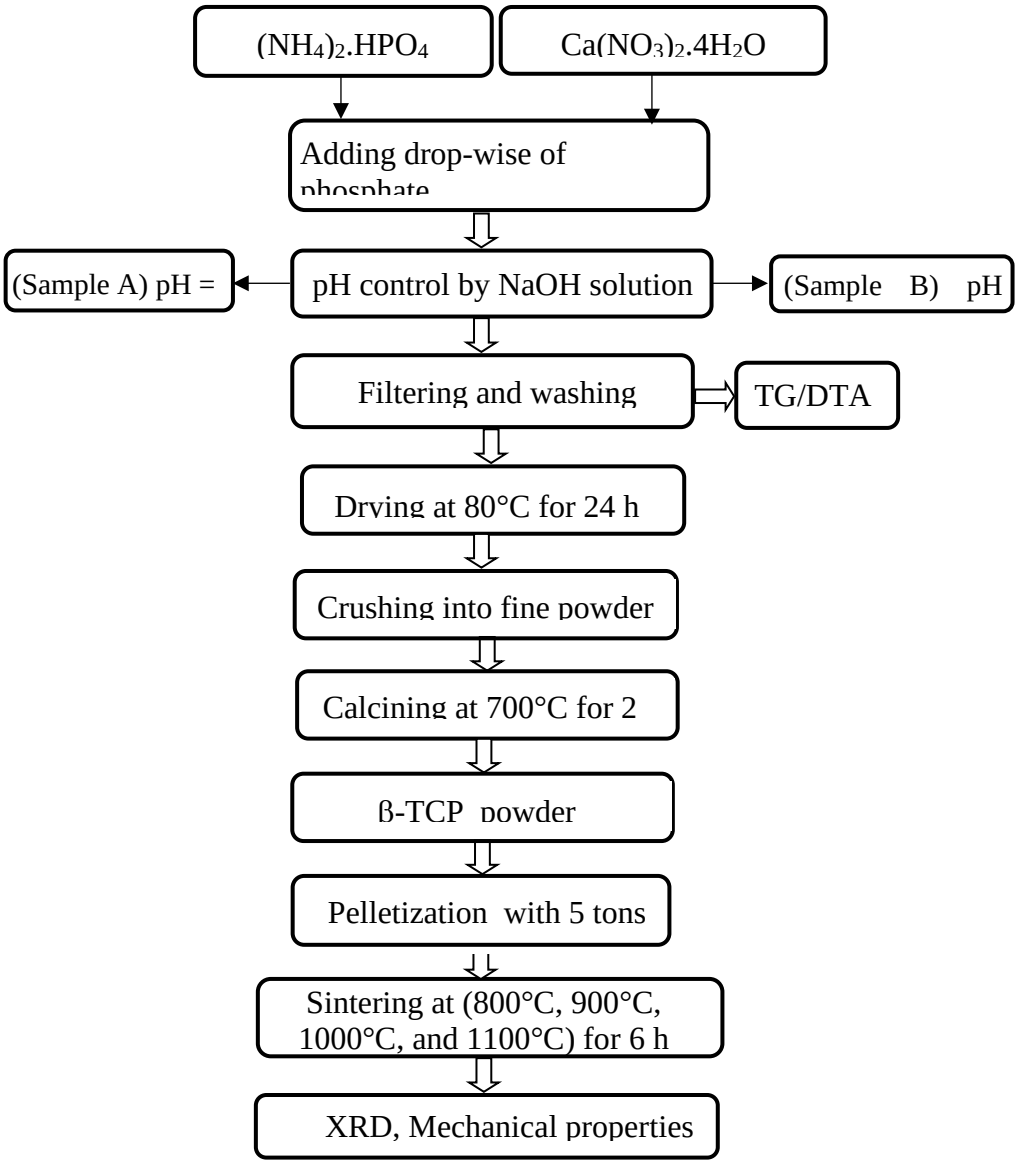

Figure 1. Flowchart of the wet chemical precipitation process used for the preparation of β-TCP samples

Results and Discussion

TG/DTA Analysis

For TG/DTA measurement, the sample is heated in a pan at 15°C/min from 0°C to 600°C in a nitrogen atmosphere with the flow rates of 50ml/min. Figure 2 shows the TG/DTA results of sticky filter paste for pH-8. At the temperature range of 37.11°C to 124°C, there is a change in mass that occurred on the TG curve which corresponds to dehydration and this dehydration shows up on the DTA curve as a first endothermic reaction at 113.47°C. The weight loss started from 37.11°C to 210°C and the total weight loss was 64.229%. The second endothermic event took place at 205.4°C due to the decomposition of phosphate, nitrate, and base groups.

Figure 3 shows the TG/DTA results of sticky filter paste for pH-10. TG curve shows the weight loss started from 35.19°C to 160°C and the total weight loss has been found to be 76.891% over the heating time as the amount of NaOH is twice in the mixture solution compared to that with pH-8.

DTA curve shows a broad endothermic peak at 130.29°C. It has been investigated that the overall decomposition temperature becomes lower with the pH value of 10 of the mixture solution.

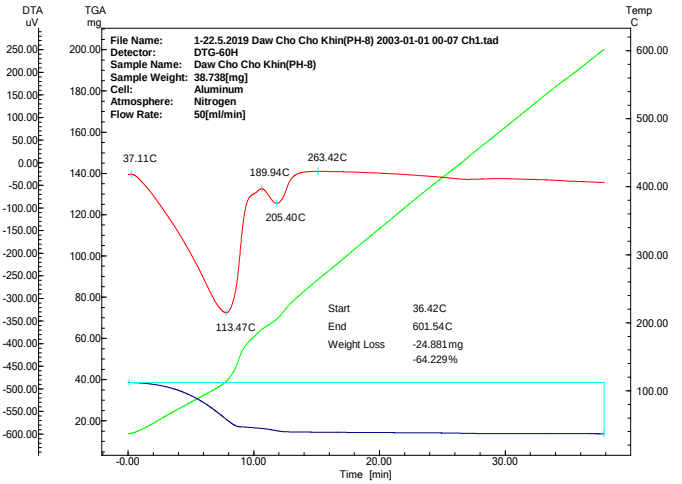

Figure 2. TG/DTA analysis curve of sticky filter paste for pH-8

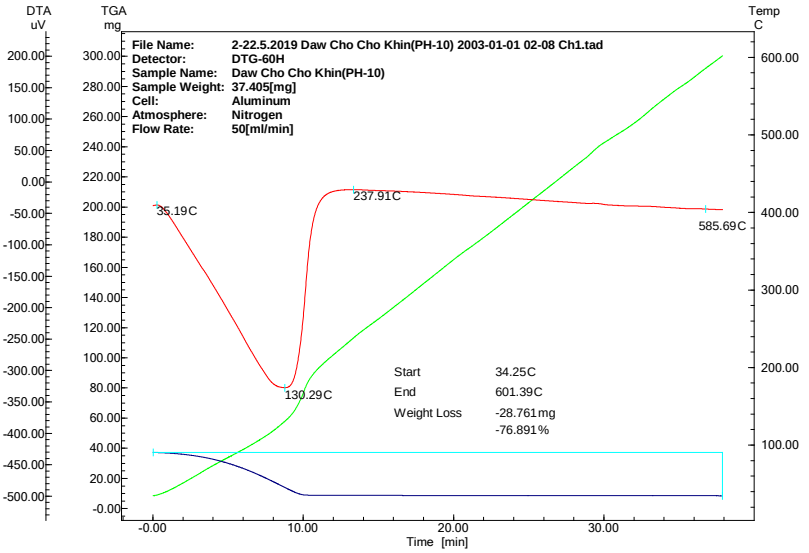

Figure 3. TG/DTA analysis curve of sticky filter paste for pH-10

Phase Formation by XRD analysis

The phase formations of these samples were characterized by using X-ray Diffraction (XRD) analysis. The XRD patterns of β-TCP pellets (pH 8 and pH 10) were sintered at 800°C, 900°C, 1000°C, and 1100°C for 6 h each are shown in Figure 4 and Figure 5 respectively. The XRD patterns exhibit that phase in each sintered pellet is the rhombohedral structure of β-TCP. The peaks were sharper as the sintering temperature was increased. The results show that the sintered pellets for both pH-8 and pH-10 contain only a single-phase β-TCP structure.

Determination of Lattice Parameters and Crystallite Size

The values of lattice parameters and crystallite sizes of sintered pellets at different temperatures for both pH-8 and pH-10 are summarized in Table1 and Table 2. It was investigated that the lattice parameters of the samples for pH-8 and pH-10 well agree with the typical values for β-TCP structure as discussed in other research on β-TCP.

The crystallite size of β-TCP is in the nano-range and increased with increasing temperatures shown in Figure 6. Moreover, it was found that the crystallite size has increased with the larger pH value.

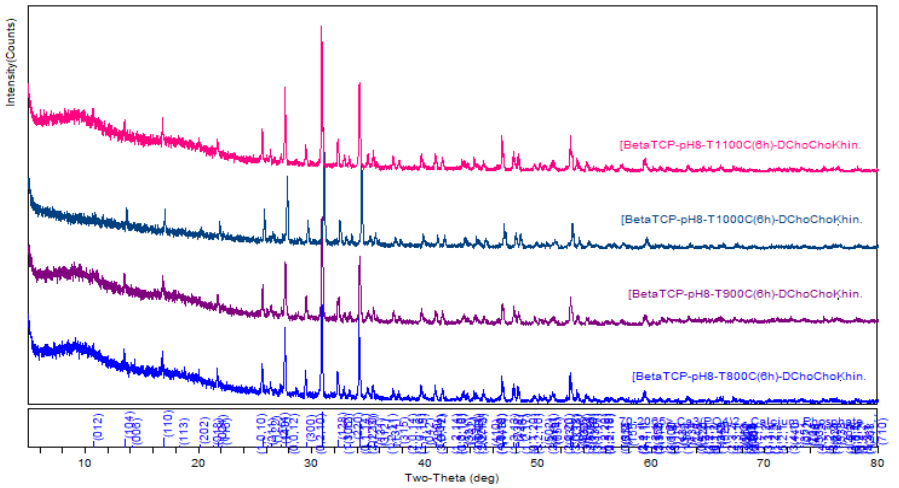

Figure 4. XRD patterns of β-TCP pellets sintered at 800°C, 900°C , 1000°C and 1100°C for pH-8

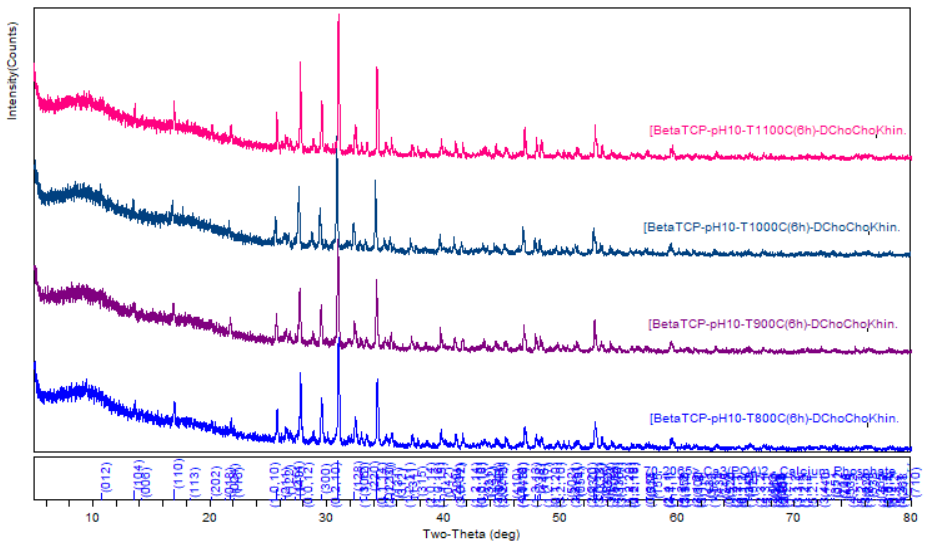

Figure 5. XRD patterns of β-TCP pellets sintered at 800°C, 900°C, 1000°C and 1100°C for pH-10

Table 1. The values of lattice parameters of β-TCP for pH -8 and pH -10

Sintered Temperature (°C)	Lattice Parameters (Å)			
	pH-8		pH-10	
	a	c	a	c
800	10.48	37.57	10.44	37.38
900	10.47	37.50	10.46	37.44
1000	10.42	37.29	10.48	37.60
1100	10.47	37.57	10.44	37.40

Table 2. The values of crystallite sizes of β-TCP for pH-8 and pH-10

Sintered Temperature (°C)	Crystallite Size D (nm)	
	pH-8	pH-10
800	57.61	58.15
900	60.26	62.52
1000	67.82	69.21
1100	69.38	71.83

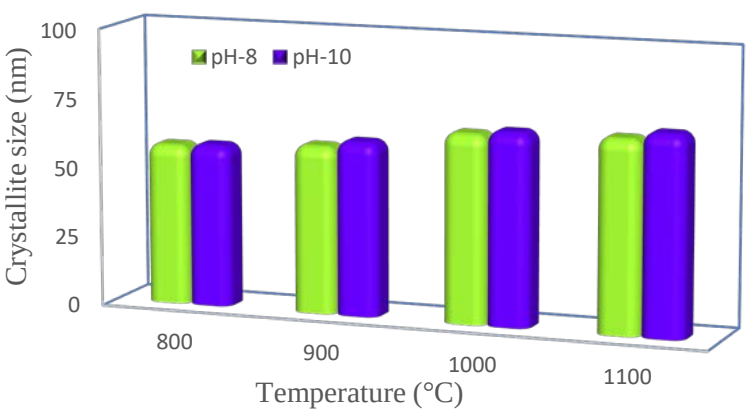

Figure 6. Comparison between crystallite size of β-TCP for pH-8 and pH-10

Study on Mechanical Properties of Sintered β-TCP

The hardness and compressive strength of β-TCP for pH-8 and pH-10 were investigated and the data are summarized in Table 3. The variation of hardness and compressive strength of β-TCP pellets with different temperatures for pH-8 and pH-10 are shown in Figure 7 and Figure 8 respectively.

It was found that the hardness increases with increasing sintering temperature in both samples. The compressive strength of the samples which were determined from the hardness values show the same trend as the hardness accordingly. It was found that the hardness and compressive strength of the β-TCP (pH-10) exhibits a larger value compared to that of the β-TCP (pH-8). Therefore, it can be said that the hardness and compressive strength were increased with increasing pH value, and the maximum compressive strength of the β-TCP pellet was obtained at 1100°C of pH-10.

Table 3. The values of hardness and compressive strength of β-TCP for pH-8 and pH-10

Sintered Temperature (°C)	Hardness P (N)		Compressive Strength σ_{comp} (MPa)	
	pH-8	pH-10	pH-8	pH-10
800	102.0	139.8	2.09	2.86
900	139.1	172.3	2.88	3.56
1000	155.9	263.3	3.27	5.52
1100	475.4	484.8	10.09	10.29

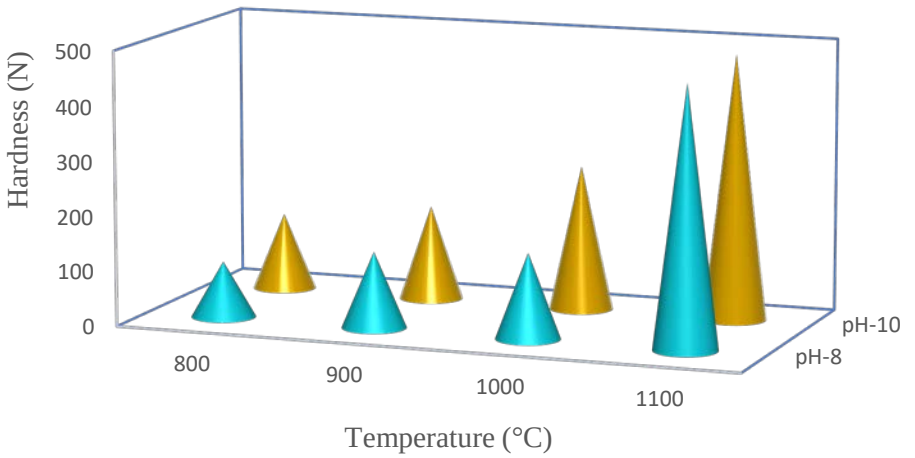

Figure 7. Comparison between hardness value of β-TCP for pH-8 and pH-10

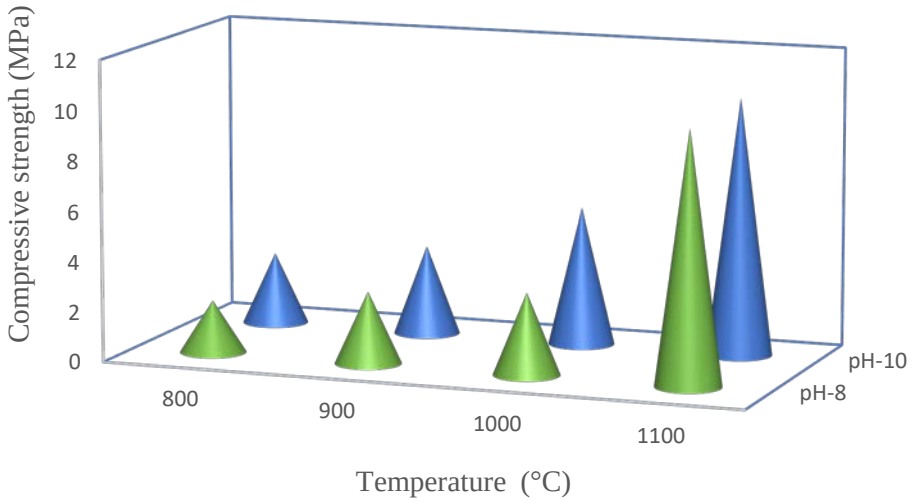

Figure 8. Comparison between compressive strength of β-TCP for pH-8 and pH-10

Estimation of Bulk Density and Porosity

The porosity and bulk density of the samples were estimated in this work. The measured bulk density and porosity of β-TCP were represented in Table 4. Comparison between bulk density and porosity of β-TCP sample for pH-8 and pH-10 are shown in Figure 9 and Figure 10 respectively. It was found that the sample β-TCP for pH-10 exhibits the largest bulk density with the smallest porosity.

Table 4. The values of theoretical density, apparent porosity, and bulk density

Sintered Temperature (°C)	Bulk density ($g\ cm^{-3}$)		Porosity (%)	
	pH-8	pH-10	pH-8	pH-10
800	2.60	2.65	28.57	26.47
900	2.66	2.71	25.71	23.53
1000	2.71	2.76	20.59	18.18
1100	2.84	2.88	15.63	9.37

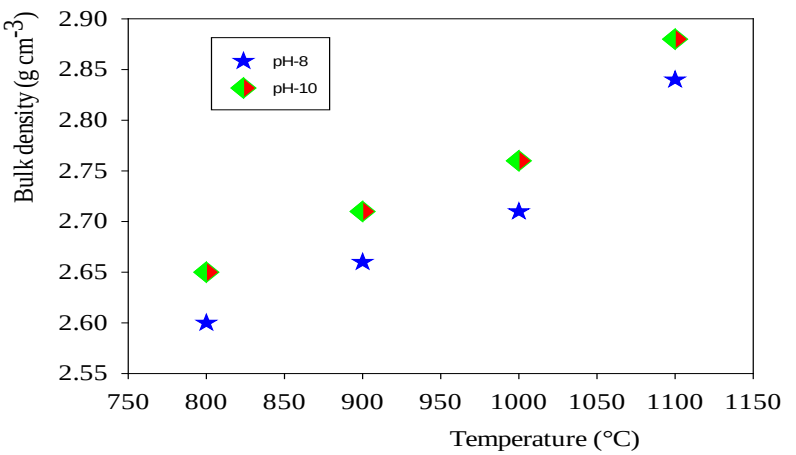

Figure 9. Comparison between the bulk density of β-TCP sample for pH-8 and pH-10

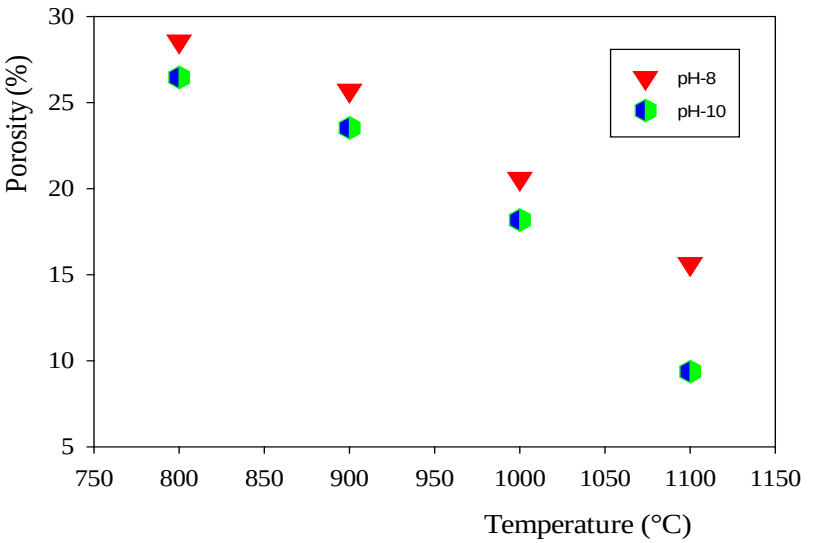

Figure 10. Comparison between the porosity of β-TCP sample for pH-8 and pH-10

Conclusion

β-TCP powders were prepared by wet chemical precipitation method by using calcium nitrate tetra-hydrate $Ca(NO_3)_2.4H_2O$ and diammonium hydrogen phosphate $(NH_4)_2HPO_4$ with high purity.

TG/DTA analysis reveals the thermal response of the mixture solution to crystallize as β-TCP. The overall decomposition temperature becomes lower with the pH value of 10 of the mixture solution.

The XRD analysis has revealed that the phase precipitated out in the samples is rhombohedral for both samples with pH-8 and pH-10. The lattice constants well agree with the typical values for β-TCP structure. It was confirmed the formation of homogeneous powders via the wet chemical precipitation method. The crystallite size was increased with increasing temperature. Importantly, the variation of pH value and different sintering temperatures could produce a range of crystallite sizes and therefore, there may be variation in mechanical properties in the characterization of β-TCP samples.

The hardness and compressive strength of β-TCP (pH-8 & pH-10) were found to increase with increasing sintering temperature in both samples. The hardness and compressive strength of β-TCP (pH-10) exhibit a larger value compared to those of β-TCP (pH-8). The maximum compressive strength of the β-TCP was obtained at 1100°C of pH-10.

The bulk density increases with increasing temperature and the porosity decreases with increasing temperature accordingly. It was found that the sample β-TCP for pH-10 exhibits the largest bulk density with the smallest porosity. It is believed that the sintered β-TCP sample for pH-10 at 1100°C possesses the largest mechanical properties.

Based on the results obtained, it is concluded that the pH value and sintering temperature could effect on structural and mechanical properties of beta-tricalcium phosphate and it can tune the applications for bone replacement.

Acknowledgements

We would like to thank Dr Aung Myat Kyaw Sein, Rector, and Dr San San Aye, Pro-Rector of Mawlamyine University for their permission to present our research paper.

References

Asril, A., *et al*, (2017), "pH Effect in Synthesize of Tricalcium Phosphate from Eggshell via Precipitation Method", Journal of Chemical and Pharmaceutical Research, vol. 9, pp. 224-227.

Behzad, M., *et al*, (2012), "Sintering effects on the hardness of β-TCP", Journal of Ceramic Processing Research, vol. 13, pp. 486-490.

Laasri, S., *et al*, (2012), "Manufacturing and mechanical properties of calcium phosphate biomaterials", C. R. Mecanique 340, pp. 715-720.

Massit, A., *et al*, (2018), "Effect of physical and chemical parameters on the β-Tricalcium phosphate synthesized by the wet chemical method ", Mediterranean Journal of Chemistry, vol. 7, pp. 234-242.

Nahar, U. K., *et al*, (2017), "Characterization of Beta-Tricalcium Phosphate (β-TCP) Produced at Different Process Conditions", J Bioengineer & Biomedical.

Shriver, D. F., *et al*, (2006), " Differential thermal analysis (DTA)/ Thermogravimetric analysis (TG) " 4th edition, Oxford University Press.

Yashima, M., *et al*, (2003), "Crystal structure analysis of β-TCP $Ca_3(PO_4)_2$, by neutron powder diffraction", Journal of Solid State Chemistry, vol. 175, pp. 272-277.

Investigation on Shielding Characteristics of Different Wood Samples in Myanmar

Win Mar[*]

Abstract

Radiation protection is one of the most important topics in various fields of industry, medicine and research. The purpose of this research is to reduce the dose rate from radioactive sources. The exposure to gamma radiation is leading to several health effects as the result of absorption by the human body. Woods are readily available radiation shielding sources which complement traditional shielding materials such as lead, concrete and steel. The measurements are carried out for Kyun, In, Pyinkado, Kokko, Rubber Wood, Tinyu and Yemane as shielding materials. The dependence of gamma attenuation coefficient on different kinds of wood sample is taken into account. From the result, it is found that the attenuation coefficient increases with the increasing the absorber thickness of high density and decreasing the half value layer (HVL) of the absorber. Finally, it is concluded that Pyinkado of highest density and lowest half value layer (HVL) may be used for gamma ray shielding.

Introduction

Radiations and gamma rays are present all around us. These are present since the birth of our planet and are part of our natural world. Radiations can be classified into ionizing and non-ionizing radiations and ionizing radiations are further classified into direct or indirect ionizing radiation. The interaction of radiation with matter is useful in applications of nuclear physics detectors, material modification, analysis, radiation therapy. The interaction can damage the materials, especially living tissues. The effects of interaction depend greatly on the intensity, energy and type of the radiation as well as the nature of absorbing material. Gamma rays interact with matter in a completely different way as that of alpha and beta rays i.e. ionizing radiations. This is because of the fact that γ-rays have large penetrating power and obey different absorptions rules. To detect gamma rays and their attenuation, study of γ- rays interactions are of great importance.

[*] Professor and Head, Department of Physics, Kalay University

The Natural Composite of Wood Sample and Radiation Protection

Wood consists of a large number of small cells, which are generally tubular in shape. The cells in a living tree always contain water. It is in the form of 'free' water in the cell cavities, and 'bound' water in the cell walls, which are fully saturated. When a tree fell and sawn into timber the wood starts to dry. The free water evaporates first. The stage where all the free water has gone, but the cell walls are still fully saturated, is known as the fiber saturation point. The cell walls then lose water until the wood has dried to a condition where the amount of bound water is in equilibrium with the moisture in the air around the wood. This moisture content is known as the equilibrium moisture content (EMC).

Gamma attenuation coefficient is an important parameter for study of interaction of radiation with matter that gives us the fraction of energy absorbed or scattered. Some wood materials with a thin lead lining have earlier been tried for shielding X-ray facilities. So wood by itself can be studied for its radiation shielding property. In this context the study of wood materials with regards to its ability to absorb radiation for different types of wood materials based on their hardness. Attenuation coefficient data for wood materials are useful for radiation shielding characteristics.

It is an exponential function of the path length through the medium. Attenuation coefficient is a significant factor for study of interaction of radiation with matter that gives us the amount of energy scattered or absorbed. The attenuation of gamma rays expressed as:

$$I = I_0 e^{-\mu x} \quad (1)$$

Where I_0 is the count of particles of radiation during a certain time duration without any absorber, I is the number counted during the same time with a thickness x of absorber between the source of radiation and the detector and μ is the attenuation coefficient. Shielding is often expressed by thickness that provided a certain shielding factor, such as a "half-value layer". An HVL is the thickness of a given material required to reduce the dose rate to one half the unshielded dose rate. The half value layer (HVL) can be expressed as

$$HVL = \frac{\ln 2}{\mu} \quad (2)$$

Experimental Setup

Source for Gamma Ray and Equipment

In the present work, gamma-ray source Cs-137 forms gamma disc shape from Nuclear Lab in University of Yangon is chosen. ^{137}Cs has one energy. It has an activity of 5μCi, half-life is 30.17 years and energy of the source is 0.662 MeV. In the present work, the equipment used in gamma ray spectrometry was described as:

- Thallium Activated Sodium Iodide detector (Model 802-5)
- High Voltage Power Supply (Model 3002)
- ST-360 Radiation Counter (Model ST-360)

Sample Collection, Sample Preparation and Elemental Analysis

Kyun was collected in Oktwin township, Bago Division. Kokko and Yemane were collected in Taungoo township, Bago Division. Tinyu was collected in Kalaw, Shane State. Pyinkado and In were collected in Myanmar. Rubber Wood was collected in Than Daung Gyi township, Kayin State. Each wood sample has area of (11.5x6.5)cm^2. Kyun has a thickness of 1.4cm, Pyinkado has 1.9cm, Rubber Wood has 1.1cm, Yemane and Tinyu have 1.6cm, Kokko has 0.9cm and In has 1.5cm. Elemental analysis was done at Forest Research Institute in Yezin. Equilibrium moisture content and the density for each wood sample were shown in Table (1).

Table 1. Equilibrium moisture content (EMC) and density of seven different wood samples

Sr. No	Species	Scientific Name	English Name	Equilibrium Moisture Content(EMC)	Density (kgm^{-3})
1	Pyinkado	Xylia dolabriformis	Flowers of India	10.3	897
2	In	Dipterocarpus tuberculatus	Dawngding	12.4	895
3	Kyun (Plantation 20 yrs)	Tectona grandis	Teak	12.0	731
4	Kokko	Albizia lebbeck	Lebbek tree	12.0	633

Sr. No	Species	Scientific Name	English Name	Equilibrium Moisture Content(EMC)	Density (kgm^{-3})
5	Rubber Wood	Hevea brasiliensis	Para Rubber tree	12.0	617
6	Tinyu (thone-khwa)	Pinus	Finus Khasia	12.8	572
7	Yemane	Gmelina arborea	Beechwood	12.0	551

Experimental Setup and Procedure

The wood samples were used as absorbers for gamma radiation. These samples were placed midway position between the source and detector. The detector was placed horizontally and the distance between the source and detector was 20 cm. The Cs-137 source was fixed in the lead shield. First the gamma intensity I_0 (in the absence of the shield sample) was measured by the detector as shown in Figure (1). Then, the sample position was placed at the center of the source and detector. The detector was located forward direction of gamma beam. Measurements were made with different thickness of wood samples. The above procedures were repeated for seven types of wood shield sample. The transmitted gamma counts collections were done for 60s. Detector working voltage is 900V (positive bias). For each thickness of wood shield samples, the gamma intensity reaching the detector was measured and the results obtained were recorded.

Figure 1. The operating system of NaI (Tl) detector and ST-360 radiation counter with high voltage power supply in the form of narrow beam

Determination of Errors

For every atom of the source there is a probability, not a certainty, that an electron will be emitted during the next unit of time. One can never measure the "exact" number. The number of particles emitted per unit time is different for successive units of time. Therefore, one can only determine the average number of particles emitted. That average, like any average, carries with it an uncertainty, an error. The determination of this error is an integral part of any radiation measurement. Let p(x) be the probability function of a "history" of value x. Mx variable is given by p(x).

$$\mathrm{Mx} = \int_{a}^{b} \mathrm{x}\ \mathrm{p(x)dx} \tag{3}$$

The value of p(x) and thus Mx are not known exactly, but the true mean; (x) can be estimated using the Monte Carlo method.

$$\overline{x} = \frac{1}{N}\sum_{i=1}^{N} x_i \tag{4}$$

where (x_i) value of corresponding to the "history" (i), and (N) is the total number of "histories". The variance (σ^2) can be estimated using following formula.

$$\mathrm{var}\,iance = \sigma^2 = \frac{1}{N-1}\sum_{i=1}^{N}(x_i - \overline{x})^2 \tag{5}$$

The quantity $\overline{(x_i - m_i)(x_j - m_j)}$ is called the "covariance X_i and X_j:

$$\mathrm{cov}(\mathrm{x_i}, \mathrm{x_j}) = \overline{(\mathrm{x_i} - \mathrm{m_i})(\mathrm{x_j} - \mathrm{m_j})} \tag{6}$$

The covariance is divided by the product of the standard deviations σ_i, σ_j and the resulting ratio is called the correlation coefficient $\rho(x_i, x_j)$. Thus,

$$\rho_{ij} = \rho(\mathrm{x_i}, \mathrm{x_j}) = \frac{\mathrm{cov}(\mathrm{x_i}, \mathrm{x_j})}{\sigma_i \sigma_j} \tag{7}$$

Results

In the case of carrying out of the shielding characteristics calculation for the radiation shielding, seven different wood samples collected in Myanmar are used. From the experiment, the transmission data without absorber, with absorber and net count rate of various thicknesses for Pyinkado , In, Kyun, Kakko, Rubber wood, Tinyu and Yemane absorbers are described in Table (2), (3), (4), (5), (6), (7) and (8). Using experimental data in Table (2), logarithm of intensity ($\ln \frac{I_0}{I}$) versus the various thickness for Pyinkado wood sample is drawn and as shown in Figure (2). The linear attenuation coefficient for Pyinkado wood sample (the slope of linear graph) is obtained 0.57 cm^{-1} and then recorded in Table (9). Similarly, the linear attenuation coefficient for In, Kyun, Kokko, Rubber, Tinyu and Yemane wood samples are also obtained 0.53cm^{-1}, 0.48cm^{-1}, 0.42cm^{-1}, 0.36cm^{-1}, 0.31cm^{-1} and 0.25cm^{-1} and then recorded in Table (9). It is cleared that Pyinkedo has highest attenuation coefficient while Yemane having the lowest.

From the experimental data, the mean count rate and standard deviation for each wood sample are calculated by using equation (4) and (5). And then the correlation between the net count rate and various thickness of each wood sample are calculated by using equation (7). The correlation coefficient are positive and in the range from 0.32 to 0.34. A linear correlation coefficient has an absolute value between 0 and 1. With one is indicated a perfect linear relationship exists. In our case, there is a positive correction of less than 0.5.

The half value layer (HVL) for seven different wood samples are calculated by using equation (2) and also recorded in Table (9). It is found that Pyinkado has lowest half value layer while Yemane having the highest. It means that at only one energy of incident radiation; a lesser thickness of Pyinkado will be required to attenuation of gamma radiation (or) to half its original intensity, when compared with other wood samples used in this experiment.

The densities at equilibrium moisture contents for seven different types of wood sample indicate in Table (9). It is seen that the gamma attenuation coefficient depends on the densities of wood samples. Figure (3) shows a linear proportionality exists between attenuation coefficients and

the densities of different wood samples. This means that a high attenuation coefficient corresponds to a high density wood sample.

Discussion

Gamma attenuation coefficient is an important for the study of interaction of radiation with matter that gives us the fraction of energy absorbed or scattered. Some wood materials with a thin Lead lining have earlier been tried for shielding facilities. So wood by itself can be studied for its radiation shielding property. In this context the study of wood materials with regards to its ability to absorb radiation of different types of wood samples based on their radiation shielding characteristics.

From the research work, wood sample (Pyinkado) of high attenuation coefficient and high density would have low half value layer (HVL), this implies a good absorber of radiation. While, a wood sample (Yemane) of low attenuation coefficient and low density would have high half value layer (HVL), this shows that the wood sample (Yemeane) is a bad absorber of radiation.

Table 2. Total count and net count rate for increasing Pyinkado wood sample thickness

Sr. No	Thickness (cm)	Total Count	Net count rate (C/s)
1	0	6782	91.98
2	1.9	6069	80.10
3	3.8	5550	71.45
4	5.7	5206	65.72
5	7.6	4632	56.15
6	9.5	4479	53.60

Table 3.Total count and net count rate for increasing In wood sample thickness

Sr.No	Thickness (cm)	Total Count	Net count rate (C/s)
1	0	6717	90.90
2	1.5	6408	85.75
3	3.0	5930	77.78
4	4.5	5467	70.07
5	6.0	5299	67.27
6	7.5	4824	59.35

Table 4. Total count and net count rate for increasing Kyun wood sample thickness

Sr. No	Thickness (cm)	Total Count	Net count rate (C/s)
1	0	6857	93.23
2	1.36	6325	84.36
3	2.72	5829	76.10
4	4.08	5584	72.02
5	5.44	5395	68.87
6	6.80	5089	63.77

Table 5. Total count and net count rate for increasing Kokko wood sample thickness

Sr.No	Thickness (cm)	Total Count	Net count rate (C/s)
1	0	6680	90.28
2	0.9	6508	87.42
3	1.8	6284	83.68
4	2.7	6155	81.53
5	3.6	6110	80.78
6	4.5	6107	80.73

Table 6. Total count and net count rate for increasing Rubber wood sample thickness

Sr. No	Thickness (cm)	Total Count	Net count rate (C/s)
1	0	6625	89.37
2	1.1	6403	85.67
3	2.2	6296	83.88
4	3.3	5922	77.65
5	4.4	5720	74.28
6	5.5	5575	71.87

Table 7. Total count and net count rate for increasing Tinyu wood sample thickness

Sr.No	Thickness (cm)	Total Count	Net count rate (C/s)
1	0	6706	90.72
2	1.6	6393	85.50
3	3.2	6071	80.13
4	4.8	5928	77.75
5	6.4	5803	75.67
6	8.0	5338	67.92

Table 8.Total count and net count rate for increasing Yemane wood sample thickness

Sr.. No	Thickness (cm)	Total Count	Net count rate (C/s)
1	0	6756	91.55
2	1.6	6500	87.28
3	3.2	6304	84.02
4	4.8	5919	77.60
5	6.4	5821	75.97
6	8.0	5646	73.05

Table 9. Density, linear attenuation coefficient and half value layer for seven different wood samples

Sr. No	Samples	Density (kgm^{-3})	μ (cm^{-1})	HVL (cm)
1	Pyinkado	897	0.57	1.22
2	In	895	0.53	1.31
3	Kyun	731	0.48	1.51
4	Kakko	633	0.42	1.58
5	Rubber	617	0.36	1.93
6	Tinyu	572	0.31	2.24
7	Yemane	551	0.25	2.77

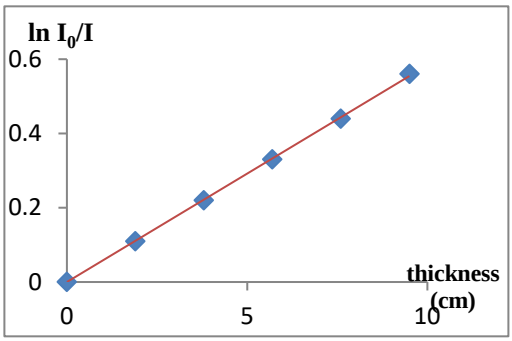

Figure 2. Logarithm of intensity versus the various thickness of Pyinkado wood sample for good geometry

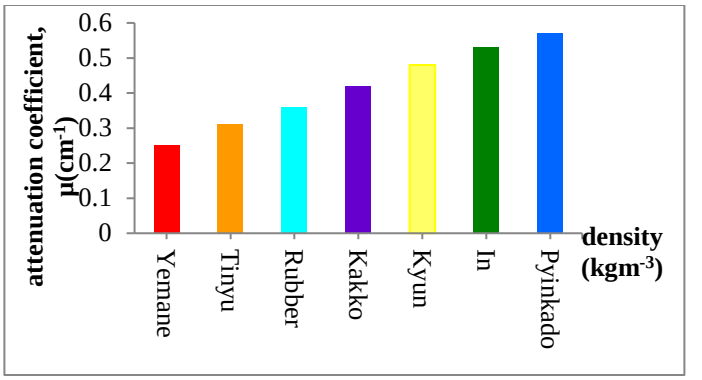

Figure 3. Attenuation coefficient versus density for Seven different wood samples

Conclusion

To sum up, attenuation coefficient, density and half value layers are characteristics that can best be used in composing the γ-radiation shielding abilities of materials. In the research work, one can say that the best attenuation is the wood with the highest attenuation coefficient, the highest density and the lowest half value layer (HVL). It is concluded that, all of wood sample investigated in this research, the highest attenuation coefficient of Pyinkado wood sample is considered a very good absorber and a good quality material for radiation shielding.

Acknowledgements

The author would like to express my gratitude to Ministry of Education, the department of Higher education in Myanmar, University of Yangon, and Universities' Research Centre (URC) for all necessary facilities.

References

Bradley DA, Tajuddin AA, Chewan A, Chewan S and Bauk S .,1991. Photon Attenuation studies on Tropical Hard woods. *Int J Radiat Appl Radiat Isot 42:771-73.*

Celiktas C.,2011. A method to determine the gamma-ray linear attenuation coefficient. *Ann Nucl Energ 38:5.*

Chafe SC., 1991. A relationship between equilibrium moisture content and specific gravity of wood.

Elias, S. et al., 1990. Characterization of Rubber using Gamma-rays Attenuation Technique.

Evans PO., 1991. The strength properties of clear wood materials Forum. J Wood Sci 15:231-244.

Kharita M.H ., Takeyeddin M., Alnassar M., Yousef M.S., 2008. Development of Special Radiation Shielding characteristics, Prog. In Nuclear Energy 50:33-36.

Physical Analysis of the Concentration of Elements in the Pyar Mee Leaves (*Gynura Procumbens* Merr) due to Metamorphosis

Wint Shwe War Hlaing*

Abstract

Pyar Mee Leaves (*Gynura Procumbens Merr*) can be used to control hypertension and diabetes. The objective of this study was to determine the concentration of elements and fundamental of the mineral water of Pyar Mee Leaves and their possible effects on the health of the human. The samples were analyzed using Energy Dispersive X-Rays Fluorescence (EDXRF) spectroscopy to determine the concentration of elements and Fourier Transform InfraRed (FTIR) spectroscopy is used to get more sufficient recommendations chemical bonding existed in molecular structure of those leaves should be studied. The major composite was to detect potassium, calcium and sulphur. The study showed that the mineral juices should not be consumed and stored for a long time.

Keywords: Pyar Mee Leaves, EDXRF spectroscopy, FTIR Spectroscopy

Introduction

Now a day, People are suffered for many diseases. Among them, they suffered hypertension and diabetes. A people needed to well control blood glucose levels, which is controlling blood pressure, eating less salt, lipids (cholesterol) and weight.

Some people to treatment some western medicine. Some were to eat remedial medicinal leaves for controlling blood glucose levels and for lowering blood pressure.

In this research paper, remedial medicine of Pyar Mee Leaves (*Gynura Procumbens Merr*) are to be elemental analysed with EDXRF spectroscopy and to study of chemical bodings existed in molecular structure of those leaves with FTIR spectroscopy.

* Associate Professor, Dr., Department of Physics, Yangon University of Education

Pyar Mee Leaves are measured in three ways such as fresh mineral water, overnight mineral water and two nights mineral water. The fresh mineral water of Pyar Mee leaves was more useful for various disease conditions which may be taken out to get comparative description.

Background Theory

Pyar Mee is a group of *Gynura procumbens* (Lour.) Merr. It also a family of Asteraceae. It is a small plant ~1–3 m in height. The stems are fleshy and the leaves are ovate-elliptic or lanceolate. It has scientific synonym names such as *Gynura sarmentosa* DC and *Cacalia sarmentosa* Blume. The plant leaf is commonly consumed and scientifically it has been shown to be safe for consumption [Merrill., et. al., 1922].

In Malaysia, the fresh leaves of *G. procumbens* are commonly eaten raw and in Thailand, the leaves are also used for cooking. In Malay, *G. procumbens* is called Sambung Nyawa which means “prolongation of life” whereas in Chinese, it is called Bai Bing Cao which means “100 ailments” [Bodeker et. al., 2009]. This is because it has been utilized in traditional medicine both systemically and for topical application for treatment of different types of illnesses and diseases [Krishnan et. al., 2015].

It is widely used to relieve kidney discomfort in Indonesia. In Vietnam, people have been using it for the treatment of fever. In Thailand, it is commonly used to alleviate inflammation, rheumatism, and to cure viral ailments. The beneficial properties of *G. procumben*s have been attributed to the presence of bioactive compounds such as flavonoids and glycosides in this plant [Akowuah et. al., 2001].

Figure 1. Pyar Mee Tree (*Gynura procumbens* Merr)

Materials and Methods

Sample preparation

The samples of Pyar Mee leaves were collected in a well-cultivated house. First, the Pyar Mee leaves are washed with water. The leaves are then dried in the shade. When the leaves are dry, they are grinded to obtain mineral water.

Sample (1): Pyar Mee leaves measured the fresh mineral water,

Sample (2): Overnight in a room at 24°C and

Sample (3): Two nights in a room at 24°C

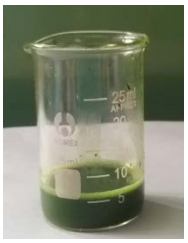

Sample (1)

Sample (2)

Sample (3)

Sample extraction

The mineral water of Pyar Mee leaves samples were placed in the sample chamber of EXD-7000 system. Again, these samples were placed in sample champer of FTIR spectroscopy.

Results and Discussions

The results shows the FTIR absorption peaks at certain wave numbers are assigned in the functional groups obtained in the literature previously.

Table 1. Infrared spectra of extract from the fresh mineral water of Pyar Mee leaves

Wave number (cm^{-1})	**Assignment**
1017.03	C-N stretching
1098.58	C-N stretching
1241.15	C-N stretching
1315.78	O-H bending
1369.51	C-H bending
1419.52	C-H bending
1624.48	C=C stretching
1734.20	C=O stretching
2848.68	Carbonyl Aliphatic Aldehyde C-H stretching
2916.91	Asymmetric C-H stretching
3273.64	Secondary amide N-H stretching

Table 2. Infrared spectra of extract from overnight mineral water of Pyar Mee leaves

Wave number (cm^{-1})	**Assignment**
1015.11	C-N stretching
1076.36	C-N stretching
1151.70	C=S thiocarbonyl; P=O phosphine; SO_2 symmetric stretching; C-N stretching
1320.96	phenol, O-H bending; sulfide, S=O stretching; aromatic amine, C-N stretching
1541.64	N-O stretching

Wave number (cm^{-1})	**Assignment**
1636.95	alkane, C=C stretching; amine, N-H bending
2921.22	C-H stretching
3279.61	Secondary amide N-H stretching

Table 3. Infrared spectra of extract from two nights mineral water of Pyar Mee leaves

Wave number (cm^{-1})	**Assignment**
1636.24	alkane, C=C stretching; amine, N-H bending
3277.51	Secondary amide N-H stretching

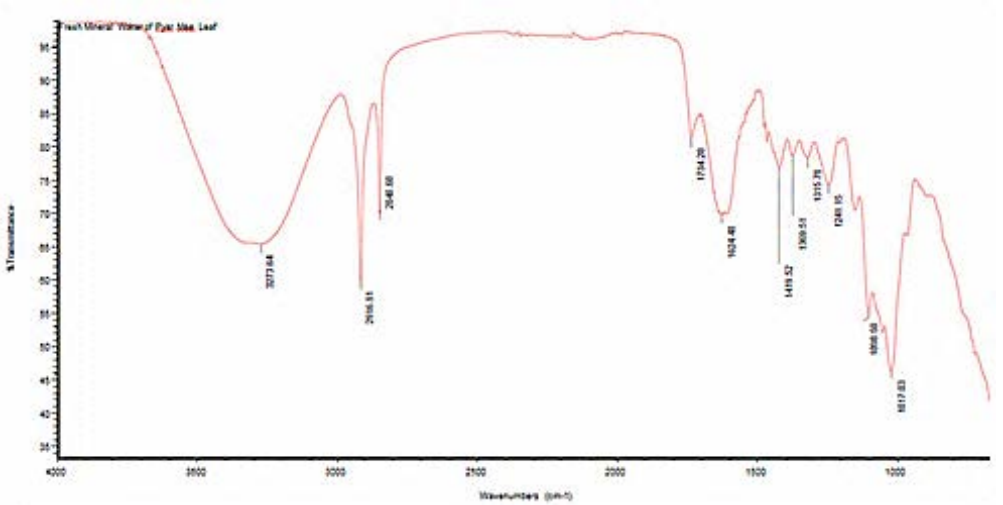

Figure 1. Fresh mineral water of Pyar Mee leaves with FTIR

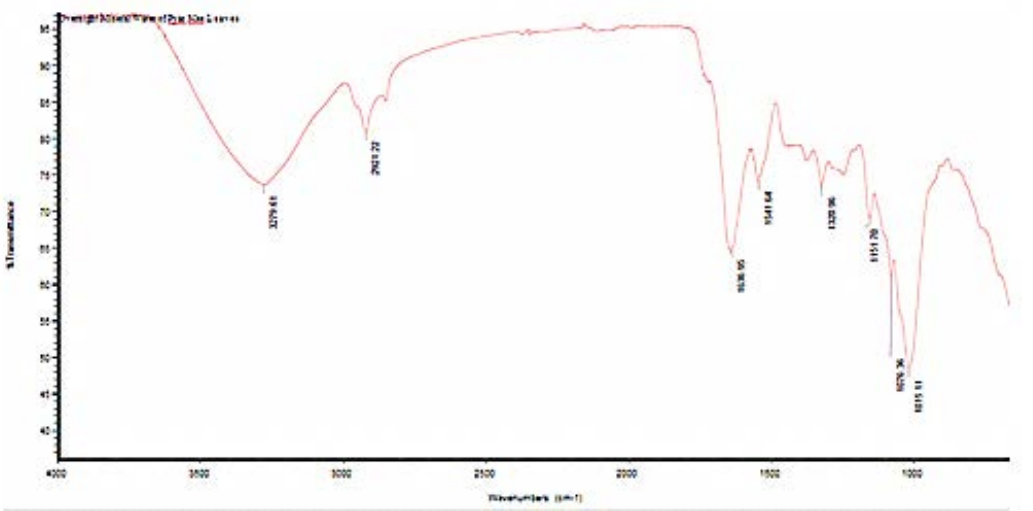

Figure 2. Overnight mineral water of Pyar Mee leaves with FTIR

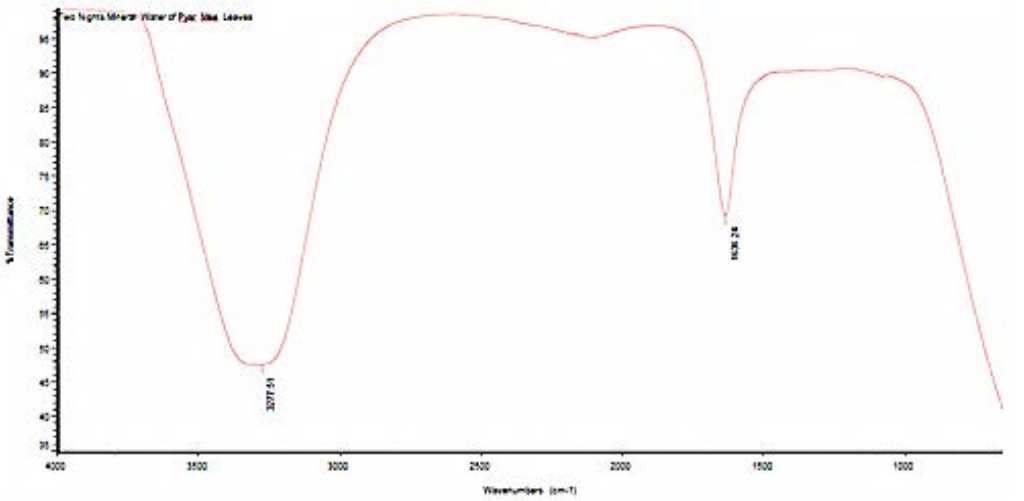

Figure 3. Two nights of Pyar Mee leaves at 24°C with FTIR

Table 4. Measurement data for Mineral Water of Pyar Mee leaves

Sample No.	Concentration (%)										
	K	Ca	P	S	Hf	Cu	Fe	Zn	Br	Os	Rb
Sample (1)	50.35	20.69	14.48	13.10	0.69	0.69	0	0	0	0	n.d
Sample (2)	49.75	21.61	n.d	26.63	1.01	0.50	0.50	0	0	n.d	0
Sample (3)	37.65	32.94	n.d	26.47	n.d	1.18	1.18	0	0.59	n.d	0

n.d = not detected

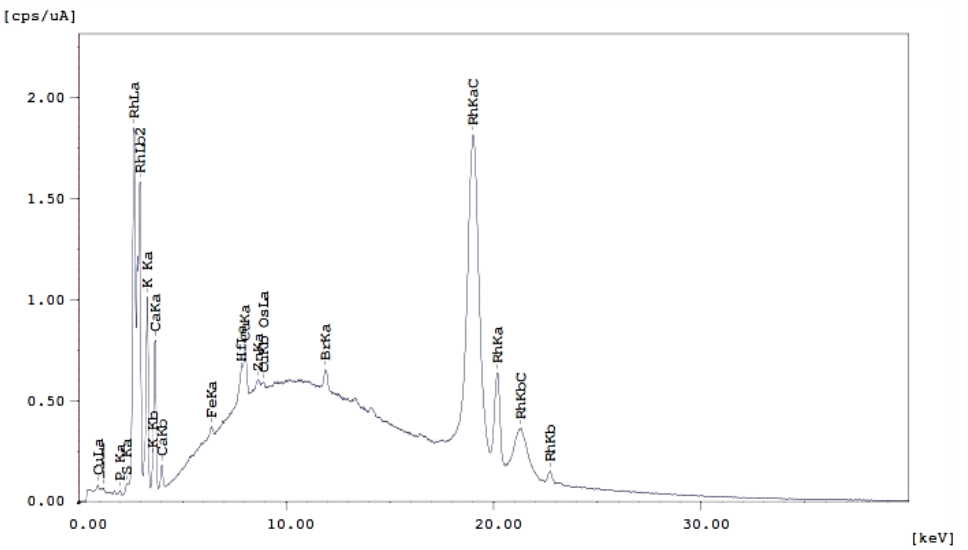

Figure 4. The graph of fresh mineral water of pyar mee leaves measured by using EDXRF analysis

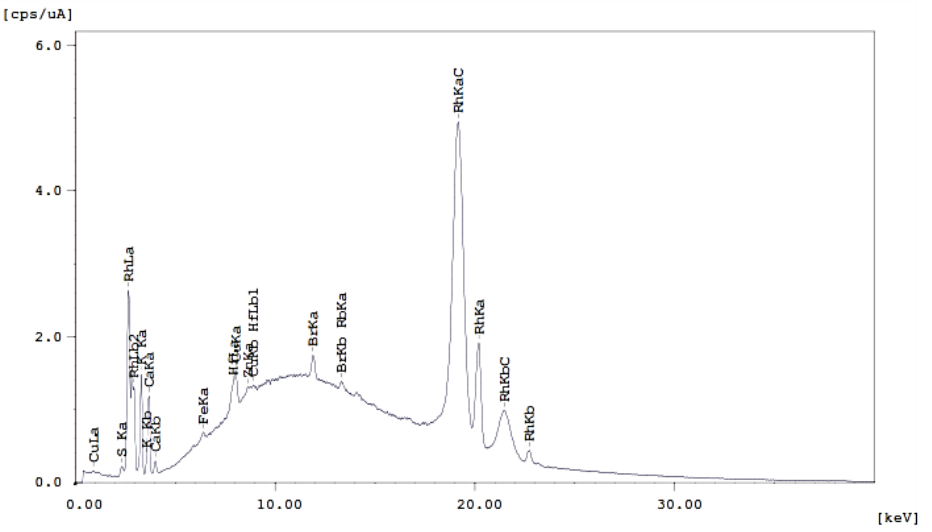

Figure 5. The graph of overnight mineral water of pyar mee leaves measured by using EDXRF analysis

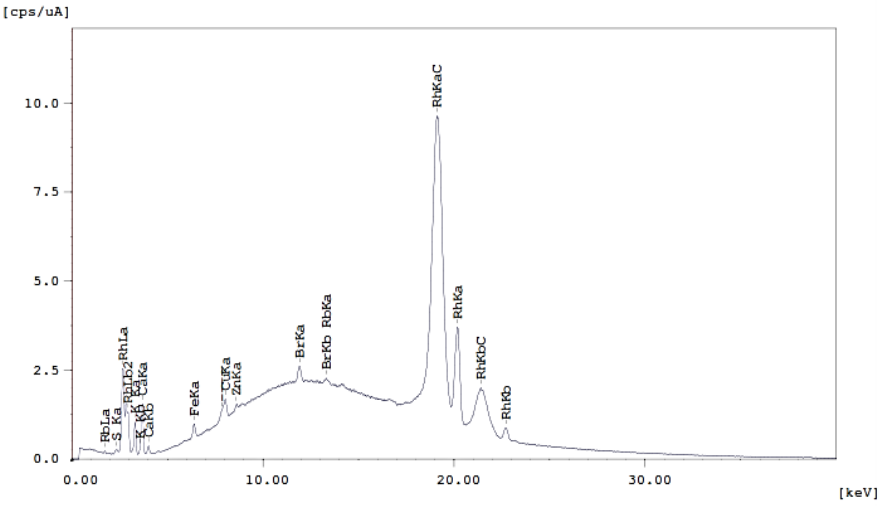

Figure 6. The graph of two nights mineral water of pyar mee leaves measured by using EDXRF analysis

Discussions

Due to Figure (2), Figure (3) and Figure (4) at the wave numbers of 3273.64, 2916.91, 2848.68, 1734.20, 1624.48, 1419.52, 1369.51, 1315.78, 1241.15, 1098.58, 1017.03, 3279.61, 2921.22, 1636.95, 1541.64, 1320.96, 1151.70, 1076.36, 1015.11, 3277.51, and 1636.24 cm^{-1} the absorption peaks are seen. When it was compared with the standard, the FTIR spectrums confirmed the presence of alkane, aldehyde, carboxylic acids, alcohol, oxygen compounds, and nitrogen compounds, sulphur compounds, and phosphorous compounds in the extractions of the mineral water of Pyar Mee leaves.

EDXRF spectrum for the mineral water of Pyar Mee leaves provided the qualitative result which can be seen that potassium, calcium and sulphur are the major composite in Pyar Mee leaves. Phosphorus contains in sample (1). The toxic elements can be seen. But the concentrations are less.

Conclusion

It is found that the elements involved in the transformation are different. Sample (1) have phosphorous in the EDXRF spectrums. Phosphorous plays an important role for human body. It makes protein for growth, maintenance, and repaired of cells and tissues. Prolonged exposure to mineral water of Pyar Mee leaves has been shown to increase copper and iron levels. In the FTIR spectrums, only then this allow for an accurate comparison of products as well as their efficiency in the clinical setting. Comparative study found that the preparation of samples by grinding leaves increases aliphatic primary amines and alkyne compounds. So that it can even be exposed as medicinal valuable compound. But the mineral juices should not be consumed for a long time.

Acknowledgements

I am highly grateful thanks Professor Dr Yin Maung Maung, Head of Department of Physics, University of Yangon for his permission to do and encouragement throughout this paper.

References

Afandi A., Sadikun A., Ismail S., (2014), Antioxidant properties of *Gynura procumbens* extracts and their inhibitory effects on twomajor human recombinant cytochrome

P450s using a high throughout Iuminescence assay. Asian J. Pharm. Clin. Res. 7, 36-41.

Akowuah G., Amirin S., Mariam A., Aminah I., (2001), Blood sugar lowering activity of *Gynura procumbens* leafextracts. J. Trop. Med. Plants 2, 5-10.

Arthur Winter, (2020), How to Find Functional Groups in the IR Spectrum. Wiely, 2nd ed., Iowa State University.

Bodeker G., Salleh H., Shekar S. C., (2009), Health and Beauty from the Rainforest: Malaysian Traditions of Ramuan. Kuala Lumpur: Editions Didier Millet Pty Ltd.

Dole M.N., Patel P.A., Sawant S.D., Shedpure P.S., (2011), Advance Applications of Fourier Transform Infrated Spectroscopy. Int.J.Pharm. Sci.Rev. Res.7,159-166.

Griffiths P., de Hasseth, J. A., (2007), Fourier Transform Infrared Spectrometry. United State.

Jenkins, Gould R.W., Gedcke D., (1981), Quantitative X-ray Spectrometry. New York.

Krishnan V., Ahmand S., Mahmood M., (2015), Antioxidant potential in different parts and callus of *Gynura procumbens* and different parts of *Gynura bicolor.* 1Biomed Res. Int.2015, 1-7.

Merck KGaA, Darmstadt, (2020), IR Spectrum Table & Chart. Germary and/or its affiliates.

Merrill, Elmer Drew, (1922), Enumeration of Phillippine Flowering Plants 3:618. Manila, Bureau of Printing, Vol.1, New York Botanical Garden, LuEsther T. Mertz Library.

Reusch William, (2020), Virtual Textbook of Organic Chemistry. East Lansing: Michigan State University.

Investigation on Impact Parameters and the Differential Cross Sections of Alpha Particle Scattering

Lae Lae Kyaing*

Abstract

In this research, elastic scattering and inelastic scattering are studied. Electron elastic scattering and optical elastic scattering are also studied. The impact parameters and the differential scattering cross sections of alpha particle are calculated by using Coulomb potential and central potential. The alpha particles arescattered from Coulomb potential and central potentialusingquantum mechanics and classical Newtonian mechanics respectively.

Keywords: Coulomb potential, scattering cross sections, impact parameter.

Introduction

The term "cross section" is a measure of the probability for the scattering reaction at a given angle. From a dimensional standpoint, cross section is expressed by units area. This seems reasonable since the relative probability of an alpha striking a gold nucleus is proportional to the effective area of the nucleus. The cross section defined here is referred to as the differential cross section, and it represents the probability per unit solid angle that an alpha will be scattered at a given angle θ.

Application of Scattering Cross Section

Generally, elastic scattering describes a process where the total kinetic energy of the system is conserved. In nuclear physics and particle physics, inelastic scattering is a fundamental scattering process in which the kinetic energy of an incident particle is not conserved.

Alpha Particle Scattering

Figure (1) shows the trajectory of an α -particle of mass m, velocity v_0, and charge Z'e while passing a positive charge Ze at O which is taken as the origin of the coordinate system .When the α -particle is far away from

* Associate Professor, Dr., Department of Physics, Lashio University

the nucleus, the path of the particle will be a straight line with constant speed v_0. As it approaches the nucleus, it experiences the Coulomb force which causes the particle to move in a different direction. In other words, the particle is said to be scattered. The angle between the original direction and scattered direction of the α-particle is referred to as the scattering angle θ. The perpendicular distance from the axis to the line of initial motion is called the impact parameter b.

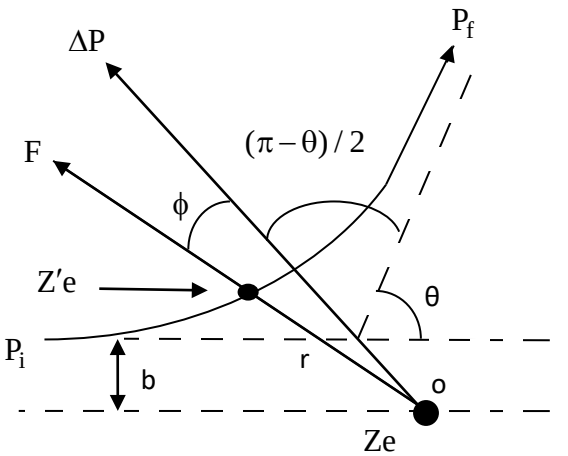

Figure 1. The trajectory of an α-particle scattered by a stationary positive charge Ze at the origin O.

For elastic scattering $|p_i| = |p_f| = mv_0$.

$$\sin\frac{\theta}{2} = \frac{(\Delta p)/2}{p_f} = \frac{(\Delta p)/2}{mv_0}$$

$$\Delta p = 2mv_0 \sin\frac{\theta}{2} \qquad (1)$$

By momentum –impulse theorem,

$$p_f - p_i = \Delta p = \int F dt \qquad (2)$$

From Eq(1) and Eq(2)

$$Fdt = 2mv_0 \sin\left(\frac{\theta}{2}\right) \tag{3}$$

Where F is the Coulomb force given by

$$F = \frac{1}{4\pi\varepsilon_0}\frac{q_1 q_2}{r^2} = \frac{1}{4\pi\varepsilon_0}\frac{Z'eZe}{r^2} = \frac{kZ'Ze^2}{r^2} \tag{4}$$

The repulsive force F is directed outward and makes an angle ϕ with the vector Δp. Hence, F dt can be resolved into two components, one parallel to Δp and the other perpendicular .The perpendicular component when integrated over the entire time interval vanishes:

$$\int_{-\infty}^{\infty} F\sin\phi \, dt = 0 \tag{5}$$

The parallel component adds when integrated over the time interval.

From Eq (3), we have

$$\int_{-\infty}^{\infty} F\cos\phi \, dt = 2mv_0 \sin\left(\frac{\theta}{2}\right) \tag{6}$$

The angular momentum of the α–particle about O at any particular r is $mr^2\omega$ and long before scattering is $mv_0 b$ .The conservation of angular momentum,

$$mv_0 b = mr^2\omega, \tag{7}$$

By changing the variable from t to, ϕ From Eq (6) ,

$$\int_{(n-\theta)/2}^{(n-\theta)/2} F\sin\phi\frac{dt}{d\phi}d\phi = 2mv_0\sin\left(\frac{\theta}{2}\right) \tag{8}$$

From Eq (8),

$$\frac{dt}{d\phi} = \frac{r^2}{bv_0} \tag{9}$$

With this value of $(dt/d\phi)$, Eq (8) takes the form,

$$\int_{-(\pi-\theta)/2}^{(\pi-\theta)/2} \frac{r^2}{bv_0} F\cos\phi\, d\phi = 2mv_0 \sin\frac{\theta}{2} \tag{10}$$

Substituting the value of F from Eq (4) into Eq (10)

$$kZZ'e^2\ 2\cos(\frac{\theta}{2}) = 2mv_0^2 b\ \sin(\frac{\theta}{2})$$

$$b = \frac{kZZ'e^2}{2KE}\cot(\frac{\theta}{2}) \qquad (\because KE = \frac{1}{2}mv_0^2) \tag{11}$$

To find the number of particles scattered at an angle θ, consider a foil of thickness t having n number of atom per unit volume. If the α-particles fall in an area A of the foil, the number of nuclei encountered in the fall in ntA. Associated with each nucleus, there is an area πb^2 which is effective in causing scattering. The total effective area is $\pi b^2 ntA$. As a result, the fraction f of the incident α- particles that is scattered through an angle θ or more is equal to the ratio of effective area to the target area A.

$$f = \frac{\pi b^2 ntA}{A} = \pi b^2 nt \tag{12}$$

Substituting the value of b from Eq (11),

$$f = \pi\left(\frac{kZZ'e^2}{mv_0^2}\right)^2 nt\ \cot^2(\frac{\theta}{2}) \tag{13}$$

Then the number of particles that are scattered within a come between angle θ and θ + dθ is given by

$$df = -\pi nt\left(\frac{kZZ'e^2}{mv_0^2}\right)^2 \cot(\frac{\theta}{2})\ \mathrm{cosec}^2(\frac{\theta}{2}) \tag{14}$$

Where the negative sign indicates that F decreases as θ increase.

The number of particles scattered into unit area at angle θ, denoted by N(θ),

$$N(\theta) = N_i \frac{|df|}{dA}$$

$$N(\theta) = \frac{N_i \pi nt \left(\frac{kZZ'e^2}{mv_0^2}\right)^2 \cot(\frac{\theta}{2}) \operatorname{cosec}^2(\frac{\theta}{2})}{2\pi r^2 \sin\theta \, d\theta}$$

$Z' = 2$, $K = \frac{1}{2}mv_0^2$, the kinetic energy of the α- particle

$$N(\theta) = \frac{N_i \, nt \, k^2 Z^2 e^4}{4r^2 K^2 \sin^4 \frac{\theta}{2}} \qquad (15)$$

$N(\theta)$ is directly proportional to t and Z^2 and $N(\theta)$ is inversely proportional to K^2 and $\sin^4(\frac{\theta}{2})$. In a scattering experiment, the α-particles reach closest to the nucleus when the incident particles are along the axis. In such a case, the expected scattering angle is 180º. At the point of closest approach, the α-particles come to rest momentarily and then turn back. The energy at that point is simply the Coulomb potential energy. The distance of that point from the origin ber$_c$ which is approximately the radius of the scattering nucleus. The Coulomb potential at a distance r_c is $\frac{(k2eZe)}{r_c}$. Equating the potential energy to the initial kinetic energy, we get

$$\frac{1}{2}mv_0^2 = \frac{2kZe^2}{r_c} \text{ This implies, } r_c = \frac{4kZe^2}{mv_0^2} \qquad (16)$$

The distance of closest approach is when the scattering angle θ is 180º. At the point of closest approach the α-particle comes to rest momentarily and the energy is simply the Coulomb potential energy $\frac{kZZ'e^2}{d}$, where d is the distance of the closest approach. Equating this potential energy to initial kinetic energy.

$$\frac{kZZ'e^2}{d} = \frac{1}{2}mv_0^2 \quad , \; d = \frac{2kZZ'e^2}{mv_0^2}. \qquad (17)$$

Comparison of Impact Parameter by Using Coulomb Potential and Central Potential

The Coulomb potential is that produced by a fixed charge q_B acting on incident particles having a charge q_A,

$$V_c(r) = \frac{q_A q_B}{(4\pi\varepsilon_0)\, r} \tag{18}$$

and we shall treat the repulsive case for which $q_A q_B > 0$. The distance of closest approach r_0 is the largest root of the equation

$$E - \frac{q_A q_B}{(4\pi\varepsilon_0)\, r} - \frac{L^2}{2mr^2} = 0 \tag{19}$$

Setting, $A = \frac{q_A q_B}{(4\pi\varepsilon_0)\, 2E}$, $\quad B = \frac{1}{2mE}$ (20)

The deflection function is given by, $\Theta = \pi - \alpha$

$$\alpha = 2\int_{r_0}^{r} \frac{L}{mr^2}\left\{\frac{2}{m}[E - V_c(r)] - \frac{L^2}{m^2 r^2}\right\}^{-\frac{1}{2}} dr$$

$$\Theta = \pi - 2\int_{r_0}^{r} \frac{L}{mr^2}\left\{\frac{2}{m}[E - V_c(r)] - \frac{L^2}{m^2 r^2}\right\}^{-\frac{1}{2}} dr \tag{21}$$

We solved Eq (21), we obtain

$$\Theta = \pi - 2\int_{r_0}^{r} \frac{b}{r}\left\{r^2 - 2Ar - b^2\right\}^{-\frac{1}{2}} dr \tag{22}$$

The integral on the right-hand side of this equation is a standard one and we have

$$\Theta = 2\cos^{-1}\left[\frac{1}{\left[1 + A^2/b^2\right]^{\frac{1}{2}}}\right] = 2\tan^{-1}\frac{A}{b} \tag{23}$$

The scattering angle θis, $b = A \cot \frac{\theta}{2}$ (24)

We choose the kinetic energy is 4.8 MeV and the angle θ is 50°. We calculate the impact parameter b by using Eq (11) and Eq (24). These results are shown in Table (1).

Table 1. The values of impact parameters for quantum mechanics and classical Newtonian mechanics

Impact parameter	quantum mechanics(m)	classical Newtonian mechanics(m)
b	5.0825×10^{-14}	3.2124×10^{-16}

The number dN′of incident particles emerging per unit time in the solid angle dΩ is proportional to N, n and dΩ, so that one can write

$$dN' = N\, n\sigma(\theta, \phi)\, d\Omega \quad (25)$$

The proportionality factor $\sigma(\theta, \phi)$, which is also often written as

$$\sigma(\theta, \phi) \equiv \frac{d\sigma}{d\Omega}(\theta, \phi) \quad (26)$$

Above equation is called the differential scattering cross-section.

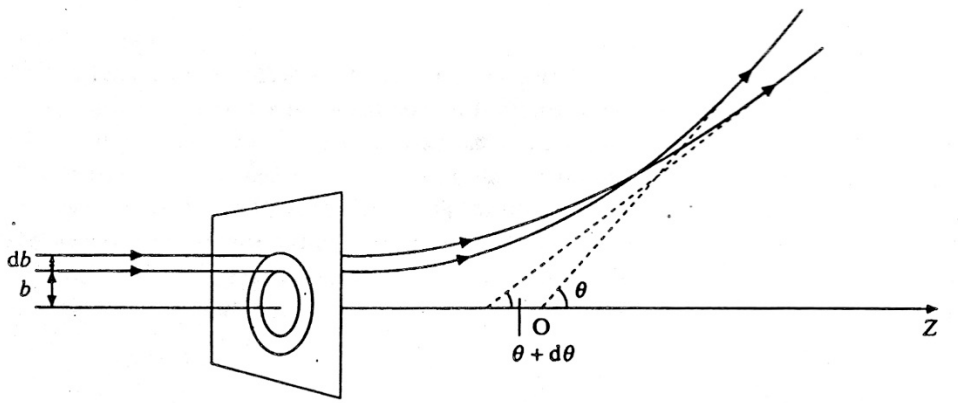

Figure 2. The number of particles scattered with impact parameters between b and b + db is equal to N 2πbdb, where N is the incident flux. These particles are scattered with scattering angles between θ and $\theta + d\theta$.

Let us now consider the classical scattering of a beam of particles by a centre of force, assuming that the force is central and vanishes for large r. The position of each incident particle can then be specified by giving its cylindrical coordinates (b,ϕ, z),where b is the impact parameter and ϕ the azimulthal angle. Since the particles do not all have the same impact parameter b or angular momentum L = mvb, they will in general be scattered differently. Indeed, each value of L (or b) defines a deflection function Θ and a corresponding angle of scatteringθ. Thus the particles scattered at angles betweenθ and $\theta + d\theta$, independently ofϕ, are those having an angular momentum between L and L + dL or an impact parameter between b and b + db. In other words they are the particles falling on the ring of area2πbdbshown in figure (2). Now, since N is the flux of incident particles, the number of particles passing per unit time through the ring is N 2πbdb, and the number of particles per unit time having angular momentum between L and L + dL is $\frac{N\,2\pi L\,dL}{(m^2v^2)}$. This is the same as the number dN′ of particles scattered per unit time within the solid angle$d\Omega$, so that

$$dN' = N\,2\pi bdb = \frac{N\,2\pi L\,dL}{(m^2v^2)} \qquad (27)$$

Since n = 1 and $d\Omega = 2\pi \sin\theta\, d\theta$

$$\frac{dN'}{N(1)\,2\pi\sin\theta d\theta} = \frac{d\sigma}{d\Omega}$$

$$\therefore \frac{d\sigma}{d\Omega} = \frac{b}{\sin\theta}\left|\frac{db}{d\theta}\right| \tag{28}$$

If more than one value of b (or L) contributes to a given value of θ, the differential cross section is the sum over all values of b (or L) that contribute, namely

$$\frac{d\sigma}{d\Omega} = \sum_i \frac{b_i}{\sin\theta}\left|\frac{db_i}{d\theta}\right| \tag{29}$$

Substituting the value of impact parameter, b from Eq (11) into Eq (29), we get,

$$\frac{d\sigma}{d\Omega} = \left[\frac{kZZ'e^2}{2KE}\right]^2 \frac{\cot\frac{\theta}{2}}{\sin\theta}\left|\frac{d}{d\theta}\cot\frac{\theta}{2}\right| \tag{30}$$

$$\frac{d\sigma}{d\Omega} = \left[\frac{kZZ'e^2}{4KE}\right]^2 \frac{1}{\sin^4\frac{\theta}{2}} \tag{31}$$

This equation is the differential scattering cross section by using coulomb potential.

$$\frac{d\sigma_c}{d\Omega} = \frac{A\cot\frac{\theta}{2}}{\sin\theta}\left|\frac{d}{d\theta}A\cot\frac{\theta}{2}\right| \tag{32}$$

$$\frac{d\sigma_c}{d\Omega} = \left(\frac{A}{2}\right)^2 \frac{1}{\sin^4(\frac{\theta}{2})}, \text{where } A = \frac{q_A q_B}{(4\pi\varepsilon_0)2E} \tag{33}$$

$$\frac{d\sigma_c}{d\Omega} = \left(\frac{q_A q_B}{4\pi\varepsilon_0}\right)^2 \frac{1}{16E^2\sin^4(\frac{\theta}{2})} \tag{34}$$

This equation is differential scattering cross section by using central potential. We calculate the differential scattering cross section by using Eq (31) and Eq (34). We choose the angle θ is 50º and some different kinetic energy. These results are shown in Table (2).

Table 2. Comparison of differential scattering cross section by using quantum mechanics and classical Newtonian mechanics

Kinetic Energy (MeV)	quantum mechanics(cm^2)	classical Newtonian mechanics(cm^2)
3	1.1269×10^{-22}	4.5018×10^{-27}
4	6.3388×10^{-23}	2.5323×10^{-27}
5	4.0568×10^{-23}	1.6206×10^{-27}
6	2.8172×10^{-23}	1.1254×10^{-27}
7	2.0698×10^{-23}	8.2686×10^{-28}
8	1.5847×10^{-23}	6.3306×10^{-28}

Conclusion

Firstly, the impact parameters are calculated by using quantum mechanics and classical Newtonian mechanics. The results of impact parameter are shown in Table (1). And then, I also calculate the differential scattering cross section by using quantum mechanics and classical Newtonian mechanics. These results are shown in Table (2). By using quantum mechanics, the impact parameter and the differential scattering cross section equations contain the atomic numbers of gold foil and the alpha particle. By using classical Newtonian mechanics, the impact parameter and the differential scattering cross section equations do not contain the atomic numbers of gold foil and the alpha particle. The results of differential scattering cross section are compared with theoretical value of reference [6].This theoretical value is $2.46\times10^{-25}cm^2$for kinetic energy 4MeV. Calculated results are slightly different from theoretical results of reference [6].

Acknowledgements

I wish to express my deepest gratitude to Dr. Kyaw Tun, Rector, Lashio University and Dr. Hla Hla Tin, Pro-Rector, Lashio University for their kind permission to do this work. I would like to express sincere thanks to Professor Dr. Ko Ko Naing, Head of Department of Physics, Lashio University and Dr. Cho Cho Aung, Professor, Department of Physics, Lashio University for their permission and moral support throughout the paper. I also grateful to all teaching staffs of Physics Department, Lashio University.

References

Arludhas, G. &Rajaopal, P., (2005), "Modern Physics", Prentice Hall of India Private Limited, New Delhi.

Bransden. B.H and Joacham. C.J (1988) "Physics of Atoms and Modecules", India.

Enge. H.A, (1966), "Introduction to Nuclear Physics", Addison-Wesley Publishing Co., Massachusetts.

https://en.m.wikipedia.org/wiki/Elastic_scattering

https://en.m.wikipedia.org/wiki/Inelastic_scattering

web.mit.edu>ruther paper.PDF.

Enge. H.A, (1966), "Introduction to Nuclear Physics", Addison-Wesley Publishing Co., Massachusetts.

https://en.m.wikipedia.org/wiki/Elastic_scattering

https://en.m.wikipedia.org/wiki/Inelastic_scattering

Influence of Cu Substitutions on Crystallite Size and Grain Size of Magnesium Copper Zinc Ferrites

Su Su Tha[1], Hsan Htoo[2] & Kyaw Kyaw Wynn[3]

Abstract

Magnesium copper zinc ferrites with the general formula $Mg_{0.5}Cu_xZn_{0.5-x}Fe_2O_4$ (x=0, 0.1, 0.2, 0.3, 0.4, 0.5) were prepared by mixing stoichiometric proportions of magnesium, copper, zinc and ferrite nitrates with calculated amount of citric acid. Before mixing, four raw samples were checked by XRD to confirm these samples are pure or not. Four raw samples, magnesium nitrates: copper nitrate: zinc nitrates: ferric nitrates ($Mg(NO_3)_2.6H_2O$, $Cu(NO_3)_2.6H_2O$, $Zn(NO_3)_2.6H_2O$, $Fe(NO_3)_3.9H_2O$) were mixed with citric acid ($C_6H_8O_7$) in different ratios in the beaker and stirring at 70°C until to get viscous gel. And then the samples were calcined at 800˚C for 2 hr. The structural analysis, crystallize size and surface morphology investigation of as prepared samples were studied by Powder X-ray Diffractometer (XRD) and Scanning Electron Microscopy (SEM) techniques.

Keywords: Magnesium copper zinc, XRD and SEM

Introduction

With the rapid development of mobile communication and information technology, small, inexpensive, high performance electronic devices are in high demand. Recently, we have witnessed the rapid development of surface mounting devices (SMD) using multilayer chip inductors (MLCI), which utilize alternating coats of ferrite and electrical paste, followed by cofiring. High temperature co-firing (normally higher than 1000 °C) causes a decrease in inductance due to the interfacial reaction (via diffusion) between ferrite and silver, usually use as electrode material. This interfacial reaction can be suppressed by co-firing at a temperature lower than the melting point of Ag (approximately 960 °C). Therefore, low temperature sintering is of great importance to suppress the interfacial diffusion. Whereas, Mg-Cu-Zn ferrites are more suitable to overcome these problems. The citrate precursor method is a promising technique for the synthesis of certain technical ceramics. Since all the reactants are solutions,

[1] Lecturer, Department of Physics, Mawlamyine University.
[2] Associate Professor, Dr, Department of Physics, Kalay University.
[3] Professor, Dr, Department of Physics, Mawlamyine University.

they can be uniformly mixed on an atomic or molecular level, and the amount of the reactants can be accurately controlled. This wet chemical method has unique advantages over conventional sintering processes in terms of obtaining nanoparticles that can be densified easily at lower temperature. The aim of this work is to present a novel and economical method of preparation of Mg-Cu-Zn ferrite by the citrate precursor method in order to achieve sintering at lower temperatures.

Materials and Method

Experimental Procedure

The samples of $MgCuZnFe_2O_4$ mixed ferrite were prepared by mixing magnesium nitrate, zinc nitrate, copper nitrate and ferric nitrates with calculated amount of citric acid. Four raw samples were checked by XRD to confirm these samples are pure or not. The different ratios of the six mixtures were staring at 70˚C to get viscos gel. And then the samples were pre sintering at 70˚C until to get dry powder. Then the powder samples were sintering at 800˚C for 2 hours. During heating the crucible, the crystal water was gradually vaporized. When a crucible temperature was reached to the critical temperature, large amounts of foams produced with appearance of spark at one corner which spread through the mass in the container.

Results and Discussion

Structure Analysis

In X-ray diffraction (XRD) measurement, a beam of X-ray directed on a crystalline material may experience diffraction (constructive interference) as a result of its interaction with a series of atomic plane according to Bragg's law. Since interplanar spacing is a function of the miller indices, lattice gathering much useful information relating the crystal structure. The value of interplanar spacing, d_{hkl} is function of miller indices (h, k and l) as well as the lattice parameter. The lattice parameters of the unit cell of the cubic represent:

$$\frac{1}{d^2} = \left[\frac{h^2 + k^2 + l^2}{a^2} \right]$$

where, d = interplanar spacing,

a = lattice parameter(Å)

(hkl) = Miller indices

The crystallite size can be measured as following Debye-Scherrer formula.

$$D = \frac{k\ \lambda}{B\ \cos\ \theta}$$

where, D = Crystallite size (nm)

λ = The wavelength of X-ray use (1.5405 Å)

B = Full Width Half Maximum of dominant peak (radians)

θ = Angle of diffraction (radians)

k = Scherrer constant

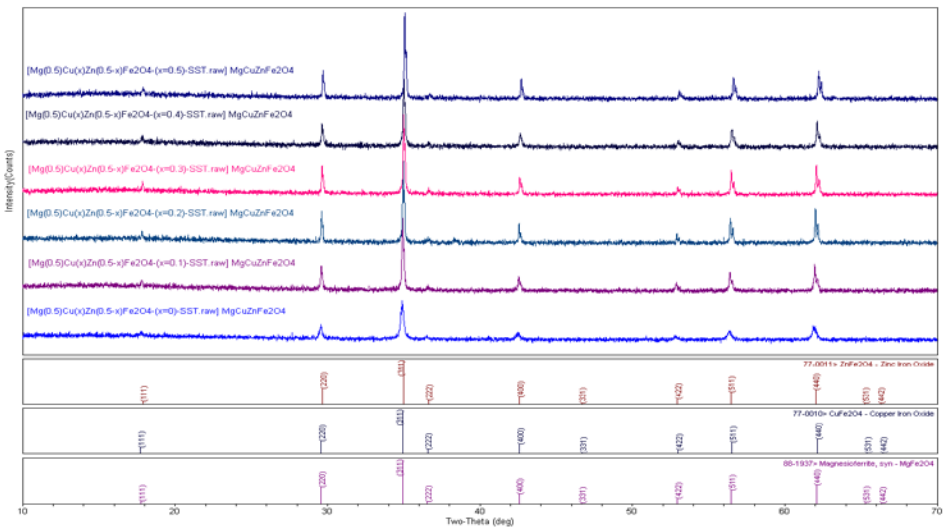

Figure 1. Peak comparisons of XRD patterns for $Mg_{(0.5)}Cu_{(x)}Zn_{(0.5-x)}Fe_2O_4$ samples

Table 1. Comparisons of lattice parameters and crystallite sizes for $Mg_{(0.5)}Cu_{(x)}Zn_{(0.5-x)}Fe_2O_4$ sample

x	Lattice (a) (Å)	Crystalize Size (nm)
0.00	8.5489	20.73
0.10	8.6126	47.19
0.20	8.5334	44.68
0.30	8.5632	44.61
0.40	8.5483	29.63
0.50	8.5192	37.26

Surface Morphology Investigation using SEM

Scanning electron microscopy (SEM) as shown in the following figure is a widely spread technique, used in materials and biological sciences as well as in industry. Modern scanning electron microscopies combine high spatial resolution imaging and analysis capabilities with easy to handle hardware and user- friendly computer-based interface. The scanning electron microscope (SEM) is a type of electron microscope that creates various images by focusing a high energy beam of electrons onto the surface of a sample and detecting signals from the interaction of the incident electrons with the sample's surface. The type of signals gathered in a SEM varies and can include secondary electrons, characteristic X-rays, and back scattered electrons. The focused electron beam is scanned across the sample surface, generating different signals. The richness in signal opens up the possibility to investigate a wide range of materials properties. The two most commonly used signals for imaging in the SEM are secondary electrons and back scattered electrons.

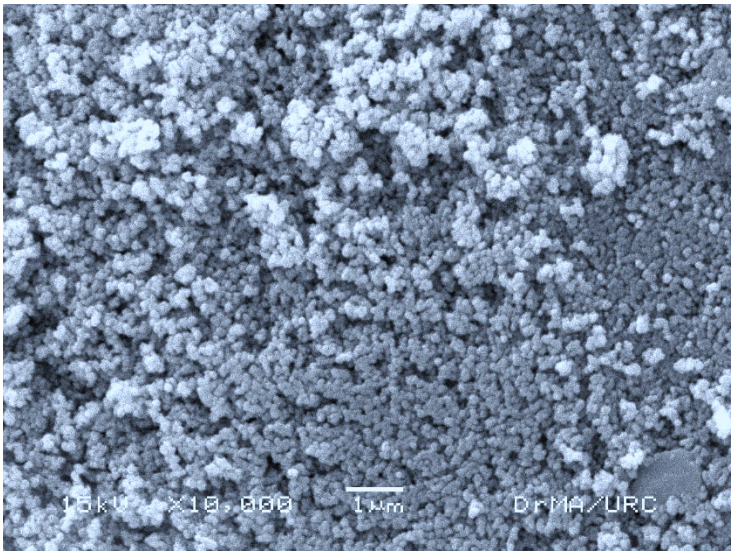

Figure 2. SEM image of $Mg_{(0.5)}Zn_{(0.5)}Fe_2O_4$ (800°) sample

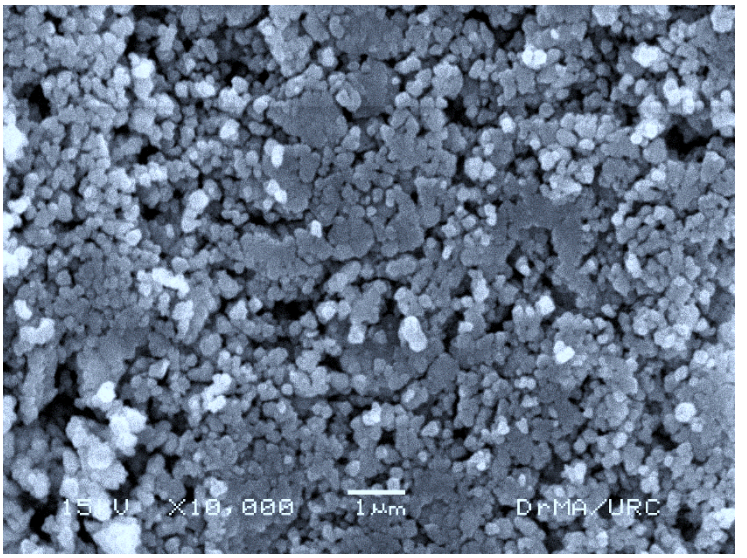

Figure 3. SEM image of $Mg_{(0.5)}Cu_{(0.1)}Zn_{(0.4)}Fe_2O_4$ (800°C) sample

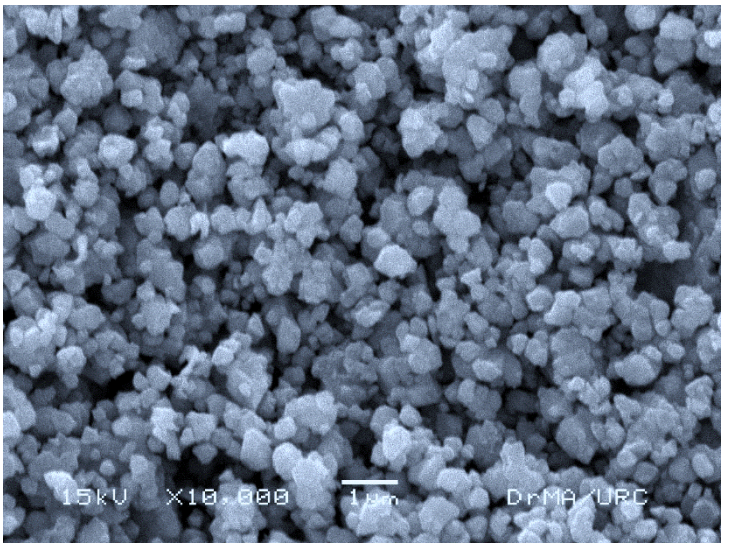

Figure 4. SEM image of $Mg_{(0.5)}Cu_{(0.2)}Zn_{(0.3)}Fe_2O_4$ (800°C) sample

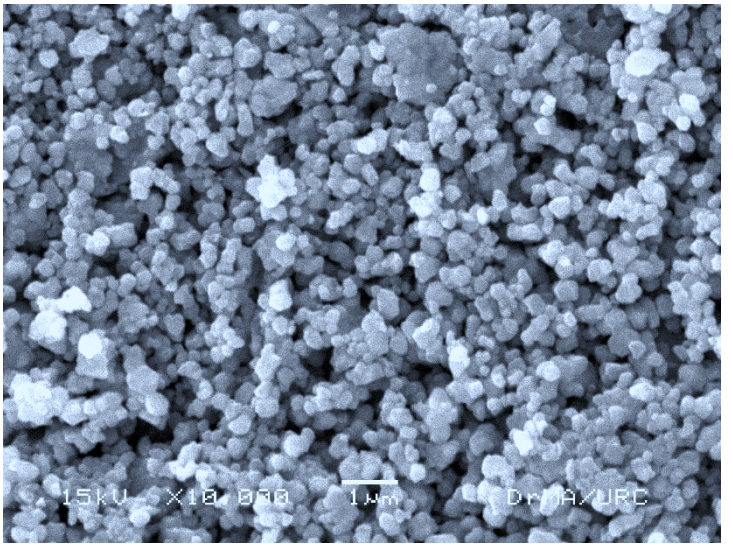

Figure 5. SEM image of $Mg_{(0.5)}Cu_{(0.3)}Zn_{(0.2)}Fe_2O_4$ (800°C) sample

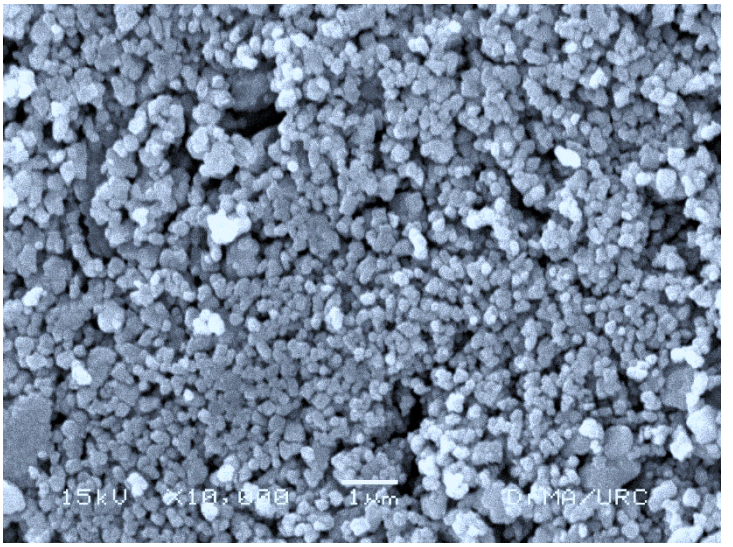

Figure 6. SEM image of $Mg_{(0.5)}Cu_{(0.4)}Zn_{(0.1)}Fe_2O_4$ (800°C) sample

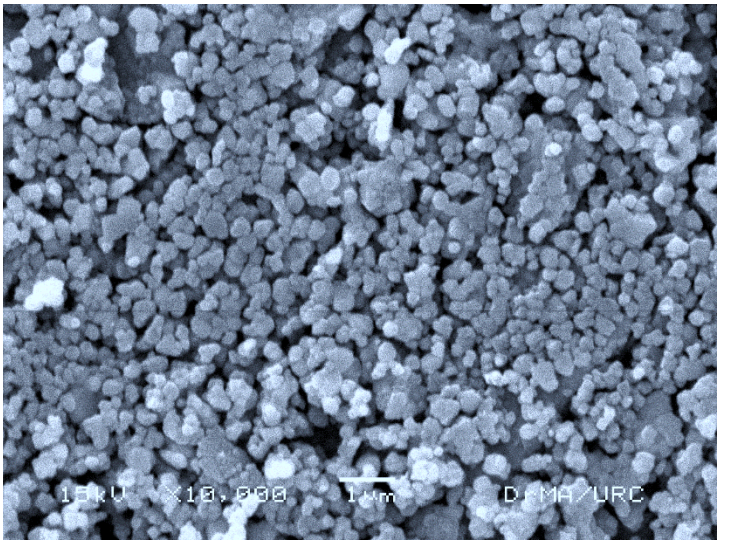

Figure 7. SEM image of $Mg_{(0.5)}Cu_{(0.5)}Fe_2O_4$ (800°C) sample

Table 2. Comparisons of grain size for $Mg_{(0.5)}Cu_{(x)}Zn_{(0.5-x)}Fe_2O_4$ sample

x	Grain size (μm)
0.0	0.186
0.1	0.199
0.2	0.205
0.3	0.209
0.4	0.232
0.5	0.269

The microstructure and morphology have an important role in determining the magnetic and electric transport properties and those were examined by a high resolution scanning electron microscope. These studied for the materials are essential in order to understand the relationship between their processing parameters as well as the behavior when used in practical applications. The morphology of the as prepared sample was achieved by using SEM technique. SEM images with same magnification for the $Mg_{(0.5)}Cu_{(x)}Zn_{(0.5-x)}Fe_2O_4$ samples are given in Figure 9. These images display formation of spongy and homogeneous material. Average grain size was determined using Image J software. The surface morphology of the $Mg_{(0.5)}Cu_{(x)}Zn_{(0.5-x)}Fe_2O_4$ (calcined at 800˚C) sample as seen from the SEM photographs consists of grain size varying from (0.186) to (0.269) μm and it was generally uniform in grain size. There can be concluded that the grain size increases with increasing the molar ratio of Cu substitution.

Conclusion

Magnesium copper zinc ferrites $Mg_{(0.5)}Cu_{(x)}Zn_{(0.5-x)}Fe_2O_4$ has been determined in various ratios as (x = 0.0, 0.1, 0.2, 0.3. 0.4, 0.5). The preparation method for the investigated system is solgel method. According the XRD results, the crystallite sizes of ferrite samples were calculated to be 20.73, 47.19, 44.68, 44.61, 29.63 and 37.26 nm at the various ratios of (x=0.0, 0.1, 0.2, 0.3, 0.4, 0.5) respectively. And lattice parameters are nearly the same as 8.6 Å. It was clear that the crystallite size of ferrite sample with

mixed ratio of (x = 0.0) (or) $Mg_{(0.5)}Zn_{(0.5)}Fe_2O_4$ was smallest crystallite size about 20.73nm among all samples. But the crystallite size of ferrite sample

with mixed ratio of (x=0.4) (or) $Mg_{(0.5)}Cu_{(0.4)}Zn_{(0.1)}Fe_2O_4$ was smallest crystallite size about 29.63 nm among four mixed samples. X-ray diffraction analysis clearly revealed that all the ferrites have the structure cubic spinel. According of SEM results, grain size of as prepared samples are varying from (0.186) to (0.269) μm and it was generally uniform in grain size. It can be concluded that the grain size increases with increasing the molar ratio of Cu substitution.

Acknowledgements

We wish to show our sincere thanks to Dr Aung Myat Kyaw Sein, Rector, Mawlamyine University and Dr San San Aye, Pro-rector, Mawlamyine University for their suggestion and comments for this work.

References

Bondyopadhyay, A. K. (2010). "Nano Materials" (New Delhi: New Age)

Kittle, C, (2005). "Introduction to Solid State Physics", (New York : Wiley)

Nakamura, T. (2017). "Journal of Magnetism and Magnetic Material". Mater. 168, 285-291.

Pillai S. O. (2006). "Solid State Physics" (New Delhi: New Age)

Qi, X., Zhou, J., Yue, Z., Gui, Z., Li, L. (2002). "Journal of Magnetism and Magnetic Material". Mater. 251, 316-322.

Zhang, H., Li, L., Wu, P., Zhou, J., Ma, Z. & Gui, Z. (2000). "Journal of Magnetism and Magnetic Materials". Mat. Res. Bull. 352, 207-2215.

Zhang, H., Ma, Z., Zhou, J., Yue, Z., Li, L. & Gui, Z. (2000). "Journal of Magnetism and Magnetic Materials". Mater. 213, 304-308.

Growth and Structural Analysis of Ammonium Tetrachlorozincate Single Crystal

Thidar Nyunt[1], Thet Mar Win[2], Than Zaw Oo[3] & Pho Kaung[4]

Abstract

Single crystal of ammonium tetrachlorozincate $(NH_4)_2ZnCl_4$ (AZC) was grown from aqueous solution by slow evaporation technique. Precise X-ray structural analysis on the single crystal of AZC was carried out to study the structural details and the bond lengths, bond angles and torsion angles. The crystal is monoclinic (pseudo orthorhombic) with the space group Pc with Z = 16. The structure was solved by direct methods and refined by full- matrix least- squares using SHELXTL- 97. The final values of R-factor (all data) and R_w (reflection weighted -factor) are 0.1368 and 0.3607 respectively.

Keyword: $(NH_4)_2ZnCl_4$ single crystal, X-ray diffraction , structure analysis.

Introduction

Ammonium tetrachlorozincate $(NH_4)_2ZnCl_4$ (AZC) is one of A_2BX_4 type crystals having the orthorhombic structure or monoclinic structure (pseudo-orthorhombic). Crystals of A_2BX_4 type compounds, where A is K, Rb, Cs, NH_4 ion, B is Zn, Co, Hg and X is Cl or Br, are known as ferroelectrics. Most crystals grow from liquid solutions. Crystals grow from liquid in response to changes in temperature, pressure or liquid composition. Single crystals were grown from aqueous solution by slow evaporation method at room temperature. Preparing the saturated solution is to add the salt according to their molecular weight ratio and stirring at the elevated temperature until there is excess that will not dissolve. The temperature is then slowly increased until all of the salt dissolve. The best condition for growth crystal was dependent on temperature constant, pressure constant and used slow evaporation method with distilled water as solvent [Leduc F X et al., 1998].

[1] Lecturer, Department of Physics, Meiktila University
[2] Professor and Head, Faculty of Natural Science, University of Computer Studies (Thaton)
[3] Professor, Department of Physics, University of Yangon
[4] Rector, University of Yangon

Phase transition sequence of AZC crystal

X-ray studies assigned the INC-COM transition to $ZnCl_4$ tetrahedra rotation. They have a common sequence of phase transitions; with decreasing temperature, the paraelectric-orthorhombic normal phase (N) changes to the INC phase followed by the commensurate (COM) phase of three-fold cell dimension along the c-axis (ferroelectric/ antiferroelectric phases).The existence of an INC lattice instability in these compounds depend basically on the effective volume of the A cations compared with the size of the BX_4 tetrahedra.

Above 406K the structure of AZC is orthorhombic with space group (Pnam). By cooling an INC, space group (Pnma) has been detected between 406K and 364K. The crystal undergoes another transition at 319K. The phase between 319K and 364k is orthorhombic with space group ($Pn2_1a$). The room temperature phase is antiferroelectric with a monoclinic structure (pseudo-orthorhombic) with space group (Pa). Down 270K the phase is ferroelectric [Gaffar M A et al., 2003]. The phase transition sequences were summarized as shown in Figure 1.

The interplanar distances change weakly with the temperature. The successive phase transitions in AZC have different character. The ferroelectric phase transition is a first order one. Differential thermal analysis successfully detected this phase transition at 270K in addition to the phase transition at 406K, while it failed to detect the phase transition at 319K. However, the phase transition at 319K was assigned as due to change in the ferroelectric domains and it is not a structural phase transition. In general a domain structure appears when the crystal changes its phase form high symmetry (orthorhombic) phase to low (monoclinic) one [Takesda M,et al 1944].

In the literature, there are observed discrepancies in reported data about structure and physical properties of AZC. The structure of AZC at room temperature is orthorhombic with lattice constants a = 7.184 Å , b = 12.56 Å, c = 27.83 Å, and space group $P2_1cn$ [ICDD (The International Centre for Diffraction Data) card no.75-2326].

In the ICDD data bank, there is also monoclinic structure with lattice parameters a = 12.62 Å, b = 7.211 Å, c = 37.09 Å, β = 90˚ and space group Pc [ICDD card no. 76-1633] and orthorhombic structure with a = 9.281 Å, b = 12.63 Å, c = 7.215 Å, and space group Pnnm [ICDD card

no.12-0304] [Bruker AXS 1999].Uses and properties of zinc chloride, ammonium chloride and ammonium tetrachlorozincate are shown in Table 1.

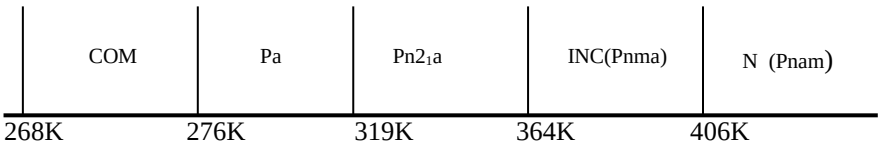

Figure 1. Phase transition sequence of AZC crystal.

Table 1. Uses and properties of ammonium chloride, zinc chloride and ammonium tetrachlorozincate

Chemical Name	Ammonium chloride	Zinc chloride	Ammonium tetrachlorozincate
Synonyms	Azanium chloride	Zinc dichloride	Diammonium tetrachlorozincate (or) Ammonium Zinc Chloride
Molecular Formula	NH_4Cl	$ZnCl_2$	$(NH_4)_2ZnCl_4$
Molecular Weight	53.49146	136.315	243.28 g/mol
Melting point	338 ^oC	290^oC	~ 150 ^oC
Boiling Point	520 ^oC.	732^oC	340 ^oC
Density	1.5274 g/cm^3	2.907 g/cm^3	1.879 g/cm^3
Appearance	White solid	White deliquesce granular powder	White orthorhombic plates, White crystalline solid

Chemical Name	Ammonium chloride	Zinc chloride	Ammonium tetrachlorozincate
Solubility	Non-volatile matter	Acid- insoluble matter	Soluble in water
Uses	-soldering fluxes, - textile printing, -baking,etc.....	-the manufacture of various dyes, -dry cell batteries as an electrolyte, etc.....	-welding, soldering flux, -dry batteries, galvanizing, etc.....

Experimental Procedure

Sample Preparation of AZC crystal

AZC crystal was grown by the slow evaporation technique from an aqueous solution. The reagents of ammonium chloride NH_4Cl and zinc chloride $ZnCl_2$ were dissolved with stoichiometric ratio of 2:1 in water. Because $ZnCl_2$ is a highly hygroscopic material, excess of $ZnCl_2$ was found necessary to compensate the water content and to be sure of the chemical reaction stoichiometry. The excess $ZnCl_2$ was 10 weight % for the present sample. To obtain the crystal, the saturated solution was placed into the oven at 100˚C. Allow it to sit in an undisturbed location for several hours or overnight. After three months, seed crystal was obtained. The crystal was transparent and colorless.

Goniometer Performance

The term ‘four-circle’ refers to the number of rotational motions available and in the instrument shown three of these are associated with the crystal and one with the counter. The counter rotates about the 2θ axis in one plane and the crystal may be oriented in any way by the three axes of rotation χ, ω and ϕ. The omega, phi and chi axes correlate to the independent x, y, and z axes of a cartesian coordinate system. The 2θ axis positions the detector at the optimum detection angle according to Bragg’s law. Photograph of four circle diffractometer and goniometer head adjustments are shown in Figure 2. A typical four-circle diffractometer and axes of the four-circle goniometer are shown in Figure 3. The specimens having single domain with clear optical axis were cut under a polarizing

microscope and shaped as a sphere with a diameter 0.35 mm [Woolfson MM, 1970].

The X-ray diffraction (XRD) experiment have been performed on the AZC crystal. X-ray single crystal study is carried out using the Siemens P4 Single Crystal Diffractometer with MoKα radiation of wavelength 0.71073 Å with the X-ray power of 40 kV x 40 mA. The unit cell parameters were determined by least- squares refinement of 25 reflections with the diffraction angles 2θ =10 ~ 30˚. Intensity measurements were carried out in the ω - scan mode. The maximum 2θ in which intensity data were collected was 50.0˚. Three standard reflections were monitored after every hundred reflections to check the stability of the measurements. After processing the raw data, Lorentz and Polarization corrections were made, absorption correction is also applied. Positional parameters and individual isotropic temperature factors were refined by a full-matrix least-squares method ORTEP-3 [Farrugia L J, 2005] and SHELXS-97 [Sheldrick G M, 1997].

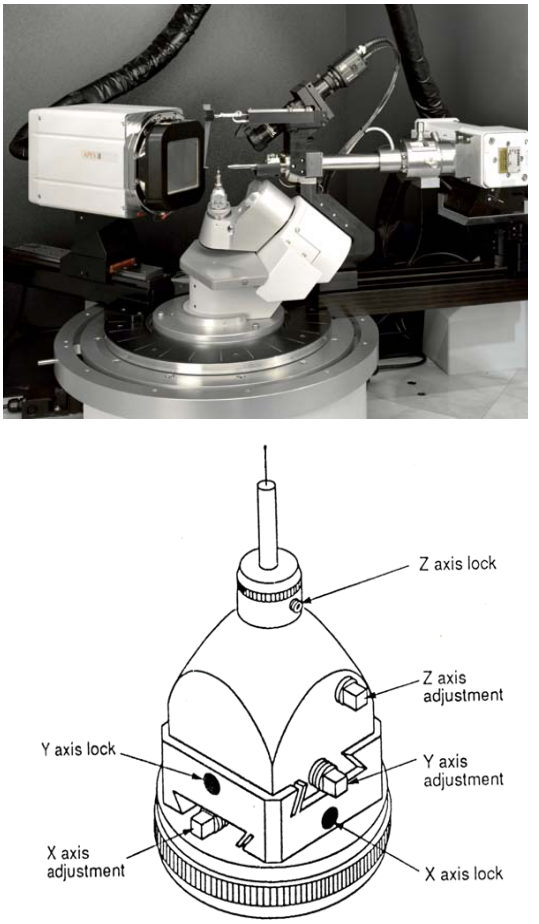

Figure 2. Photograph of four circle diffractometer and goniometer head adjustments

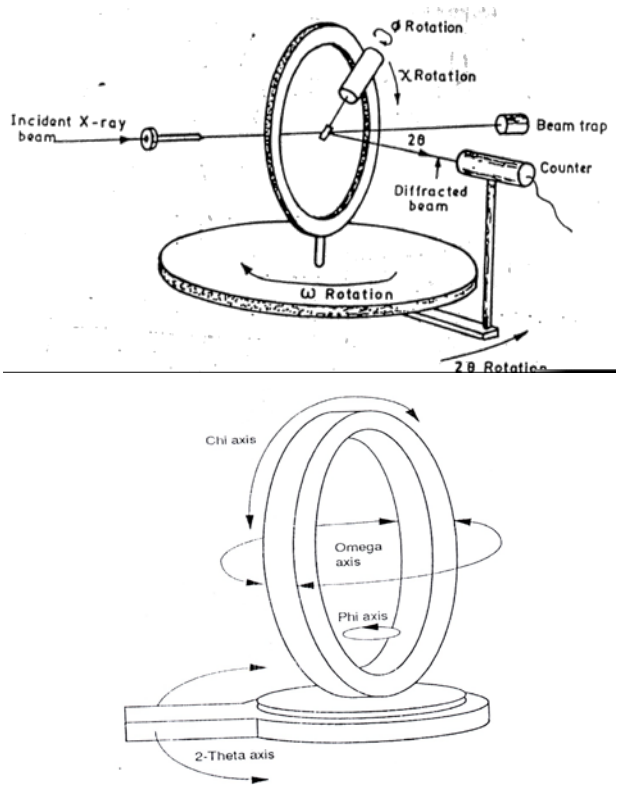

Figure 3. A typical four-circle diffractometer and axes of the four-circle goniometer

Results and Discussion

The projection normal to (100), (010) and (001) of AZC structures are shown in Figure 4. A group consists of NH_4 molecule and $ZnCl_4$ tetrahedron. One group lies on the mirror plane (z = 1/4) and another group on the mirror plane (z=3/4). Fractional atomic coordinates and equivalent isotropic displacement parameters are shown in Table (2). Bond angles of $ZnCl_4$ in AZC single crystal at room temperature are shown in Table (3). Selected bond distances of the tetrachlorozincate ions are shown Table (4).

Model summary concerning unit cell Information and SHELXTL refinement for AZC as shown in Table 5. X-ray Fourier map presents charge density distribution. The contour map view of around Zn5 and 3D-relief view of Zn5 position in AZC crystal are shown in Figure 5 and Figure 6. The function minimized was $\Sigma w(|F_0|-|F_c|)^2, w = 1/\sigma^2(|F_0|)$.

Anisotropic displacement parameters were used for non- H atoms The two discrepancy factors are defined as $R = \Sigma (|F_0| - |F_c|) / \Sigma |F_0|$ and $R_w = \{\Sigma w(|F_0| - |F_c|)^2 / \Sigma w |F_0|)^2\}^{1/2}$, respectively. The calculations were performed using SHELXS 97 [Leduc F X et al.,1998] and ORTEP- III [Clegg W ,2003].

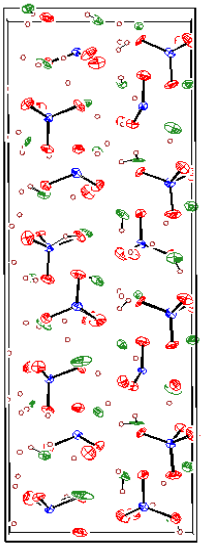

(b) (c)

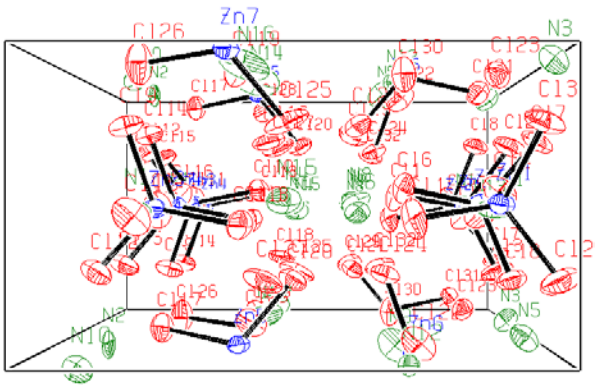

Figure 4. Projection normal to (a) (100) (b) (010) and (c) (001) for AZC crystal

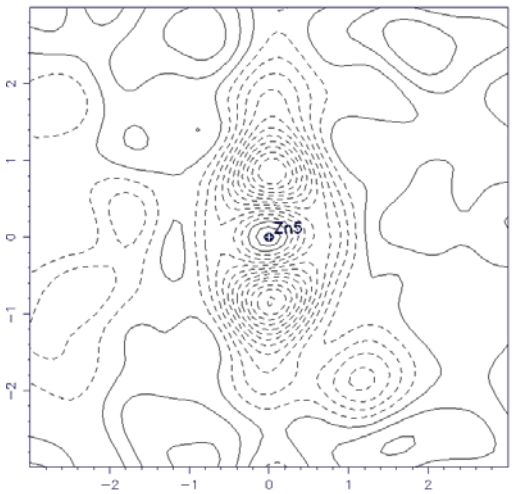

Figure 5. The contour map view of around Zn5

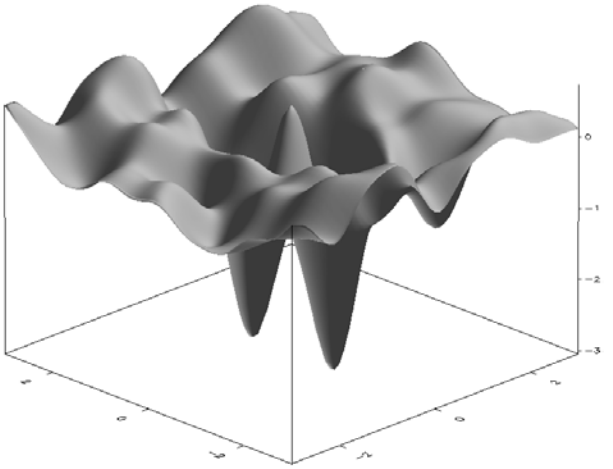

Figure 6. 3D- relief view of Zn5 position in AZC crystal

Table 2. Fractional atomic coordinates and equivalent isotropic displacement parameters(Å^2)

$U_{eq}= (1/3)\sum_i\sum_j U_{ij}a^*_i a^*_j a_i a_j$

Atom	X	Y	z	Ueq
Zn1	0.87573	0.50487	-0.07174	422
Zn2	0.87489	0.49497	0.17917	412
Zn3	0.22435	0.50943	0.30304	361
Zn4	0.22463	0.49924	0.05398	359
Zn5	0.37570	0.99840	0.19036	383
Zn6	0.72602	-0.00143	0.31554	304)
Zn7	0.37777	-0.00850	-0.05945	379
Zn8	0.72338	0.00705	0.06508	330
N1	0.20012	0.49086	-0.09308)	634
N2	0.12252	0.98357	0.25000	395
N3	0.98245	0.02462	0.37744	546
N4	0.48748	0.49010	0.23914	449
N5	0.97673	-0.01052	0.12838	646
N6	0.61618	-0.52293	-0.13146	404
N7	0.20037	0.48856	0.15657	479
N8	0.61924	0.48746	0.11807	550
N9	0.69688	-0.00556	0.21441	692
N10	0.12568	0.00404	-0.00146	491
N11	0.89006	0.50991	0.28282	746
N12	0.70517	0.00614	-0.03443	575
N13	0.89681	0.52718	0.03413	729
N14	0.40454	0.02516	0.08659	1167

Atom	X	Y	z	Ueq
N15	0.48433	0.51536	-0.00916	574
N16	0.40089	0.03055	0.33782	1082
Cl1	0.71605	0.45850	-0.04913	678
Cl2	0.98015	0.26288	-0.05522	925
Cl3	0.94861	0.76230	-0.04501	753
Cl4	0.88358	0.54582)	-0.13231	621
Cl5	0.88906	0.51686	0.11840	919
Cl6	0.71567	0.43752	0.20007	575
Cl7	0.98932	0.27077	0.19887	743
Cl8	0.93612	0.76468	0.20395	648
Cl9	0.17291	0.23314	0.32663	646
Cl10	0.3907	0.56490	0.32512	628
Cl11	0.21867	0.51538	0.24331	738
Cl12	0.11614	0.72284	0.32507	634
Cl13	0.39064	0.55902	0.07557	589
Cl14	0.17197	0.23292	0.08033	47
Cl15	0.11579	0.72539	0.07061	765
Cl16	0.21819	0.46628	-0.00584	749
Cl17	0.21518	0.94274	0.16777	56
Cl18	0.43684	1.26580	0.16371	740
Cl19	0.38227	1.01947	0.25045	760
Cl20	0.48687	0.76849	0.16974	612
Cl21	0.61949	0.22804	0.29884	570
Cl22	0.73087	-0.05164	0.37394	723
Cl23	0.89143	0.05361	0.29276	555

Atom	X	Y	z	Ueq
Cl24	0.67281	-0.26533	0.28754	476
Cl25	0.48566)	-0.23175	-0.08557	845
Cl26	0.21742	-0.04861)	-0.08123	740
Cl27	0.44216	0.26089	-0.08006	774
Cl28	0.38608	-0.04076	0.00054	722
Cl29	0.61687	0.22723	0.04384	703
Cl30	0.72186	0.01225	0.12447	694
Cl31	0.89090	0.06520	0.04272	542
Cl32	0.67402	-0.26579	0.04034	599

Table 3. Bond Angles of $ZnCl_4$ in AZC single crystal at room temperature

Atom	A B C	Angle		Atom	A B C	Angle
	Cl3 - Zn1 - Cl4	107.70			Cl18 - Zn5 - Cl17	107.13
	Cl3 - Zn1 - Cl2	105.94			Cl18 - Zn5 - Cl19	111.08
	Cl3 - Zn1 - Cl1	108.82			Cl18 - Zn5 - Cl20	104.87
	Cl4 - Zn1 - Cl2	109.94			Cl19 - Zn5 - Cl20	111.04
	Cl4 - Zn1 - Cl1	115.97			Cl17 - Zn5 - Cl19	114.80
	Cl2 - Zn1 - Cl1	108.02			Cl17 - Zn5 - Cl20	107.35
	Cl8 - Zn2 - Cl7	105.18			Cl24 - Zn6 - Cl21	108.68
	Cl8 - Zn2 - Cl6	109.10			Cl24 - Zn6 - Cl22	108.69
	Cl8 - Zn2 - Cl5	108.26			Cl24 - Zn6 - Cl23	104.20
	Cl7 - Zn2 - Cl6	109.29			Cl21 - Zn6 - Cl22	114.44
	Cl7 - Zn2 - Cl5	108.42			Cl21 - Zn6 - Cl23	108.59
	Cl6 - Zn2 - Cl5	116.04			Cl22 - Zn6 - Cl23	111.71
	Cl10 - Zn3 - Cl11	112.48			Cl26 - Zn7 - Cl25	107.14

Atom	A B C	Angle		Atom	A B C	Angle
	Cl10 - Zn3 - Cl12	108.14			Cl28 - Zn7 - Cl26	113.15
	Cl10 - Zn3 - Cl9	106.14			Cl28 - Zn7 - Cl25	108.45
	Cl11 - Zn3 - Cl12	109.69			Cl28 - Zn7 - Cl27	114.39
	Cl11 - Zn3 - Cl9	113.16			Cl25 - Zn7 - Cl27	104.27
	Cl12 - Zn3 - Cl9	106.94			Cl26 - Zn7 - Cl27	108.83
	Cl13 - Zn4 - Cl15	109.30			Cl29 - Zn8 - Cl32	108.26
	Cl13 - Zn4 - Cl14	106.23			Cl29 - Zn8 - Cl31	107.14
	Cl13 - Zn4 - Cl16	113.61			Cl29 - Zn8 - Cl30	109.61
	Cl15 - Zn4 - Cl14	108.84			Cl32 - Zn8 - Cl31	105.29
	Cl15 - Zn4 - Cl16	109.47			Cl32 - Zn8 - Cl30	114.71
	Cl14 - Zn4 - Cl16	109.25			Cl31 - Zn8 - Cl30	111.48

Table 4. Selected bond distances of the tetrachlorozincate ions

Atom	A B	Distance	Atom	A B	Distance
	Zn1 -CL 3	2.2950		Zn5 -CL 18	2.3003
	Zn1 -CL 4	2.2675		Zn5 -CL 17	2.2233
	Zn1 -CL 2	2.2687		Zn5 -CL 19	2.2345
	Zn1 -CL 1	2.2064		Zn5 -CL 20	2.3020
	Zn2 -CL 8	2.2845		Zn6 -CL 24	2.2684
	Zn2 -CL 7	2.2848		Zn6 -CL 21	2.2178
	Zn2 -CL 6	2.1913		Zn6 -CL 22	2.1961
	Zn2 -CL 5	2.2662		Zn6 -CL 23	2.2848
	Zn3 -CL 10	2.2839		Zn7 -CL 28	2.2386
	Zn3 -CL 11	2.2160		Zn7 -CL 26	2.1927
	Zn3 -CL 12	2.2133		Zn7 -CL 25	2.3201

Atom	A B	Distance	Atom	A B	Distance
	Zn3 -CL 9	2.2710		Zn7 -CL 27	2.2403
	Zn4 -CL 13	2.2785		Zn8 -CL 29	2.2218
	Zn4 -CL 15	2.2189		Zn8 -CL 32	2.2576
	Zn4 -CL 14	2.2552		Zn8 -CL 31	2.3074
	Zn4 -CL 16	2.2320		Zn8 -CL 30	2.2025

Table 5. Model summary concerning unit cell Information , data collection and SHELXTL refinement for AZC single crystal

Cell axes [A˚]	$(NH_4)_2ZnCl_4$
a	12.5962 Å
b	7.2115 Å
c	37.08 Å
Cell angles [deg]	$\alpha = \gamma = 90^{\circ}, \beta = 90.134^{\circ}$
Cell Volume [$A^{\circ 3}$]	3368.02
Crystal system	Pseudo orthorhombic (monoclinic)
Space group	Pc
F(000)	1859.7
Density [gcm^{-3}]	1.85
Formular Weight	235.1
No.form.units Z	16
Abs.coeff: [mm^{-1}]	3.745
Reflection read	4461
Number rejected	300
Systematic absence violation	44
Inconsistent equivalents	169

Cell axes [A˚]	$(NH_4)_2ZnCl_4$
Unique reflections	3569
R(all data)	0.1368
R_w (reflection weighted - factor)	0.3607
R (int) & R (sigma)	0.1683 & 0.0428
Data with F0>4 sig (F0)	2779

Conclusion

In AZC single crystal, theoretical value and experimental value of the densities are 1.879 g/cm^3 and 1.85 g/cm^3. These values are nearly equal. The NH_4 ions form linear chain whose periodicity is incommensurate with that of the arrangement of the $ZnCl_4$ tetrahedron. The Zn atom shifts away from one of Cl atoms in the tetrahedral molecules and carries an electric dipole moment parallel to the Zn-Cl bond. Similarly, NH_4 ions shows slightly distorted tetrahedral form having an electric dipole moment. Such a formation of dipole moments becomes the antiferroelectric structural characteristic of AZC crystal. The crystal structure of AZC is pseudo orthorhombic (monoclinic) system. The lattice parameters and interaxial angles are a=12.5962 Å, b =7.2115Å, c = 37.08 Å,

$\alpha = \gamma = 90^{\circ}$, $\beta = 90.134^{\circ}$.

Acknowledgements

We wish to our deepest gratitude to Dr. Ba Han, Rector, Meiktila University and Dr. Tin Tun Aung Pro-Rector, Meiktila University for their kind permission to do this work. I would like to express sincere thanks to Professor and Head Dr. Hla Hla Than and Professor Dr Daw Hla Win, Department of Physics, Meiktila University for their kind permission to carry out this research work.

References

Bruker AXS, Inc (1999) “XSHELL User Guide” (Wisconsin: Bruker)

Clegg W (2003) “Crystal Structure Determination” (New York: O U P)

Farrugia L J (2005) "ORTEP-3 for Windows- version 1.08"(Glasgow: University of Glasgow)

Gaffar M A, Abu El-Fadl A and Bin Anooz (2003), Cryst. Res. Technol. 38(1), pp 83-93

Leduc F X, Hedoux A and Kiat J M (1998) Phys Rev B 57 p11023-11026

Sheldrick G M (1997) " SHELXS- 97 and SHELXL- 97" (Germany: University of Gottingen)

Takesda M and Mashiyama H (1994) J. Phys. Soc. Jpn. 63(7), pp.2618- 2626

Woolfson MM (1970) “An Introduction to X-ray Crystallography” (New York: C U P)

Fabrication and I-V Characteristics of Perovskite Solar Cells

Hsan Htoo[1] & Su Su Thar[2]

Abstract

Fabrication of layers of perovskite solar cells in different temperatures and I-V characteristic of these solar cells were investigated. The first layer, compact TiO_2 layer was deposited using a spray pyrolysis method. The second mesoporous TiO_2 layer was deposited by the screen printing of the TiO_2 slurry. The third ZrO_2 space layer was printed on the top of the TiO_2 layer using ZrO_2 paste. Then, a carbon counter electrode was coated on the top of the ZrO_2 layer by printing carbon slurry. The $CH_3NH_3PbI_3$ perovskite layer was prepared by a two-step solution method. The unit cell structure of the perovskite layer is tetragonal and the crystallite sizes lie between 22.30 nm to 27.40 nm. From XRD results, the lattice constants of $CH_3NH_3PbI_3$ are 8.86 Å and 12.66 Å. I-V characteristics of methylammonium lead iodide perovskite thin films were also studied.

Keywords: perovskite, crystallite size, lattice constants

Introduction

Work on solar cells using perovskite material has advanced rapidly as a result of the material's excellent light absorption, charge-carrier mobilities, and lifetimes, resulting in high device efficiencies with significant opportunities to realize a low-cost, industry-scalable technology. This potential for low cost and scalability requires overcoming barriers related to stability and environmental compatibility.

A perovskite solar cell is a type of solar cell that includes a perovskite structured compound, most commonly a hybrid organic-inorganic lead or tin halide-based material, as the light-harvesting active layer. Perovskite materials such as methylammonium lead halides and all-inorganic cesium lead halide are cheap to produce and simple to manufacture.

[1] Associate Professor, Department of Physics, Kalay University
[2] Lecturer, Department of Physics, Mawlamying University

Methylammonium lead iodide is a direct bandgap semiconductor, with an energy bandgap of around 1.55eV making it an efficient absorber of light across the visible spectrum. Herein, 'Perovskite' will generally refer to methylammonium lead iodide, $CH_3NH_3PbI_3$ (Adam Pockett *et al*, 2016).

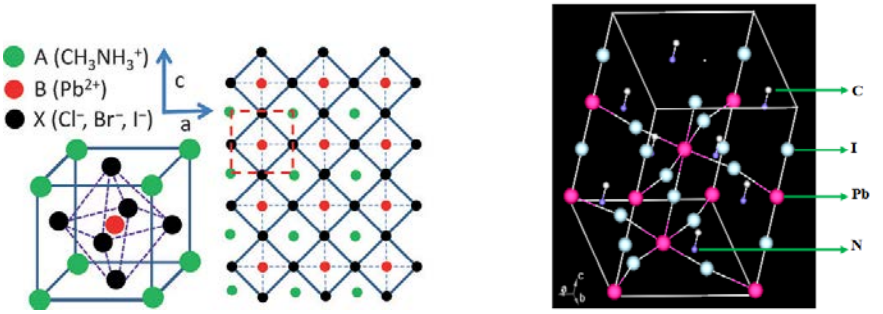

Figure 1. Crystal structure of perovskites

Materials and Method

Materials

The materials fluorine-doped tin oxide (FTO) glass, titanium dioxide (TiO_2), zirconium oxide (ZrO_2), graphite, methylammonium iodide (MAI) (98% Sigma-Aldrich), lead II iodide (PbI_2), hydrochloric acid (HCl), ethanol, isopropanol, acetylacetone, acetic acid, acetonitrile, ethylene glycol and dimethylformamide (DMF) were used in this research.

Experimental Procedure

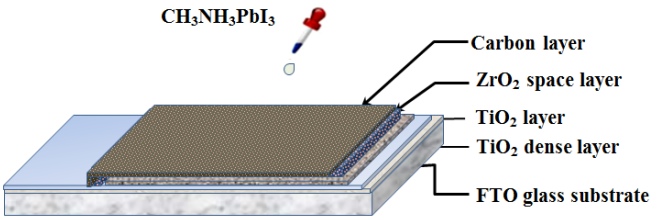

Figure 2 Layers of Perovskite Solar Cells

FTO glass cleaning

Fluorine-doped tin oxide (FTO) coated glass substrates were cleaned by soaking in the mix solution of HCl and distilled water (1:10 ratio) for

30 minutes. And then it was rinsed in DI water. Then it was dried at room temperature.

Preparation of compact and mesoporous TiO_2 films (Electron Transporting Layer)

4g of TiO_2 powder, 40 ml of ethanol and 20 ml of distilled water were mixed in the beaker. Then it was continuously stirred by magnetic stirrer at 70°C for 2 h. Thereafter, the TiO_2 solution was deposited onto the glass substrate by spray pyrolysis method for a compact layer. After that, the substrates annealed at 300°C, 400°C and 500°C for 30 minutes respectively.

TiO_2 paste for mesoporous layer was prepared by the addition of a few 10-20 ml of ethanol to the TiO_2 powder and continuously stirred by a magnetic stirrer until the desired paste is formed. Then TiO_2 mesoporous layer was printed on the TiO_2 fine layer by using the screen printing method. Then they were sintered at 300°C, 400°C, and 500°C for 30 minutes respectively.

Preparation of ZrO_2 film (Space layer)

2 g of ZrO_2 powder was mixed with 20 ml of ethanol and 2 ml of isopropanol in the beaker. Then the solution was stirred by magnetic stirrer at 70°C to make a viscous paste for screen printing on the mesoporous TiO_2 layer. After that, the ZrO_2 space layer was printed by screen printing, and the films were sintered at 300°C, 400°C, and 500°C for 30 minutes respectively.

Preparation of graphite layer (Counter Electrode –CE)

2g of graphite powder, acetylacetone, acetic acid, acetonitrile, ethylene glycol 1.5 ml each were ground by using motor and pestle for 3h to form a paste for blade coating (doctor blading) method. After cooling down the space layer, graphite CE was prepared by doctor-blade coating on the ZrO_2 space layer and followed by heating at 300°C, 400°C and 500°C for 30 minutes respectively.

Making the perovskite precursor solution

In the case of the inter-diffusion reaction (sequential deposition) of the inorganic and organic precursors, the PbI_2 precursor is dissolved in dimethylformamide (DMF) (400 mg/ml) and stirred at 70°C for 30 minutes.

CH_3NH_3I precursor is dissolved in isopropanol (IPA) at a concentration of 10 mg/ml.

To prepare $CH_3NH_3PbI_3$ perovskite films, the PbI_2 solution (460 mg/ml in DMF) was spin-coated on the mesoporous graphite layer at 3000 rpm for 30 seconds. The layer is then dried by heating the substrate at 70°C for 30 minutes. Then the substrates were dipped into CH_3NH_3I solution (10 mg/ml in isopropanol) for 40 seconds. After that, it was heated for 15 minutes at 100º C on a hot plate. During the procedure, the coated electrode changed color from light yellow to dark brown, indicating the formation of the perovskite film. The films were characterized by an I-V measurement for electrical characterization.

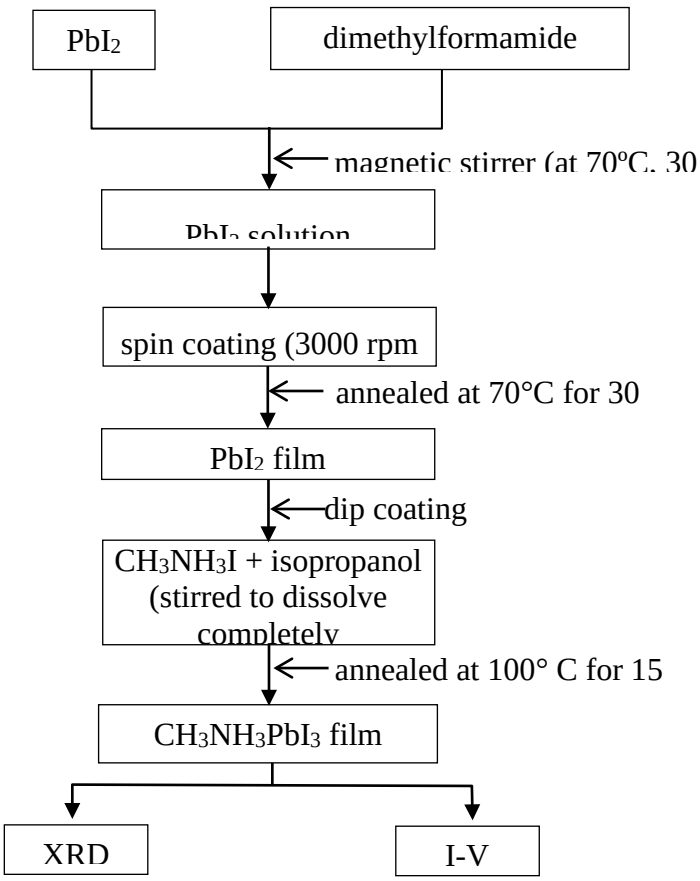

Figure 3. Block diagram for preparation of perovskite film

Fabrication of Photovoltaic Devices

The (FTO) coated glass substrates were cleaned by soaking in the mixed solution of HCl and distilled water (1:10 ratio) for 30 minutes. And then it was rinsed in deionized water and dried at room temperature. After that, the substrates were coated with compact TiO_2 layer by aerosol spray pyrolysis and annealed at 300°C, 400°C, and 500°C for 30 minutes respectively. After that, the mesoporous TiO_2 layer was deposited on top of the compact layer by screen printing and sintered at 300°C, 400°C, and 500°C for 30 minutes respectively. Followed, the ZrO_2 space layer was printed by screen printing and the films were sintered at 300°C, 400°C, and 500°C for 30 minutes respectively. After cooling down, graphite CE was prepared by doctor-blade coating on the ZrO_2 space layer and followed by heating at 300°C, 400°C, and 500°C for 30 minutes respectively. To prepare $CH_3NH_3PbI_3$ perovskite films, the PbI_2 solution (460 mg/ml in DMF) was spin-coated on the mesoporous graphite layer at 3000 rpm for 30 s and dried at 70°C for 15 minutes. Then the substrates were dipped into CH_3NH_3I solution (10 mg/ml in isopropanol) for the 40s. After that, it was heated for 15 minutes at 100º C on a hot plate. During the procedure, the coated electrode changed color from light yellow to dark brown, indicating the formation of the perovskite film.

X-ray Data Collection and Characterization

XRD data collection was carried out using a SmartLab X-ray diffractometer. As an X-ray source, Cu-Kα radiations were used with the X-ray power of 50kV, 40 mA. The detector was a semiconductor detector. All measurements were performed by a 2θ scan method. The range of 2θ was between 10˚ to 70˚ when intensity data were collected.

The structures of crystals and molecules are often being identified using x-ray diffraction studies, which are explained by Bragg's Law. The law explains the relationship between an x-ray light shooting into and its reflection off from crystal surface. Bragg's law states that when the x-ray is incident onto a crystal surface, its angle of incidence, θ, will reflect with the same angle of scattering, θ. And, when the path difference, d is equal to a whole number, n, of wavelength, constructive interference will occur. Knowing the wavelength and the diffraction angle of a reflection, its resolution *d* can be easily calculated:

$$d = 1/2(n\lambda / \sin\theta)$$

This is just a reformulation of the famous Bragg equation $n\lambda = 2d \sin\theta$.

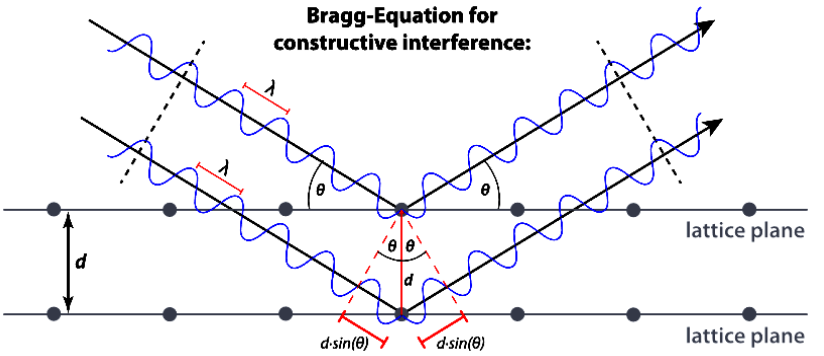

Figure 4. Bragg-Equation for Constructive Interference

The structural analysis of the perovskite layer was performed using SmartLab Studio II software. The crystallite size of solar cell layers was carried out by using the Debye-Scherrer formula.

$$D = \frac{0.9\ \lambda}{B \cos\theta}$$

Where D = Crystallite size (nm)

λ = the wavelength of X-ray used (1.54056 Å)

B = Full-Width Half Maximum of dominant peak (radian)

θ = Angle of diffraction (radian)

Results and Discussion

In this work, a two-step spin coating method was used for the preparation of the $CH_3NH_3PbI_3$ perovskite layers. The XRD patterns of the perovskite layer were as follows.

XRD pattern of $CH_3NH_3PbI_3$ layers for the temperature of 300°C, 400°C, and 500°C was shown in Figure 4. Dominant peaks of (110), (004), (220), (114), (224), (400), (404) occur at diffraction angles of 13.957˚,

19.96˚, 23.339˚, 31.711˚, 40.298˚, 40.744˚, 50.045˚. The other peaks were PbI_2. The crystallize size and lattice constant were tabulated in Table 1. From the XRD results, the crystal structure of the $CH_3NH_3PbI_3$ layer was tetragonal.

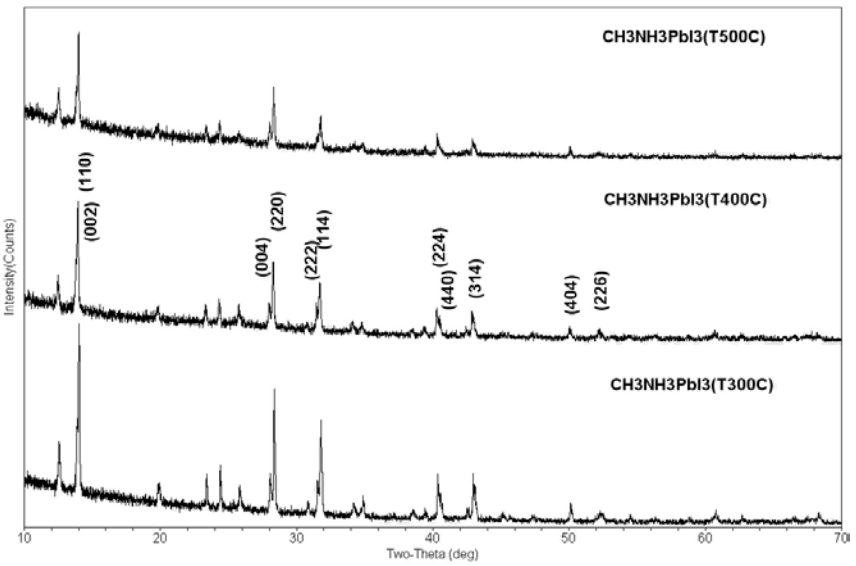

Figure 5. XRD patterns of the perovskite layer at different temperatures

Table 1. The average crystallize size and lattice parameter of perovskite layers at 300˚C, 400˚C, 500˚C

No.	Temperature (˚C)	Lattice constant (Å)		Crystallize size (nm)	
		a	c	XRD	Calculation
1.	300	8.89	12.66	26.8	24.9
2.	400	8.89	12.66	30.0	27.4
3.	500	8.86	12.66	23.4	22.3

In this research, the hole transporting layer free perovskite solar cell with a graphite counter electrode was successfully fabricated by the infiltrating of $CH_3NH_3PbI_3$ which consisted of four layers including compact TiO_2, mesoporous TiO_2, ZrO_2, and graphite layers. The perovskite layer was deposited by the two-step deposition technique. The crystallize

sizes of methylammonium lead iodide perovskite layers at different temperatures 500˚C, 400˚C, and 300˚C were 23.41 nm, 30 nm, and 26.75 nm. It was found that the perovskite layer at 500˚C has the smallest crystallize size of 23.41 nm. From XRD results, the lattice constants of $CH_3NH_3PbI_3$ are 8.86 A˚ and 12.66 Å. The bond distances among the atoms of the perovskite layer are 2.66 Å at Pb1-I1, 3.15 Å at Pb1-I2, and 1.13 Å at C1-N1.

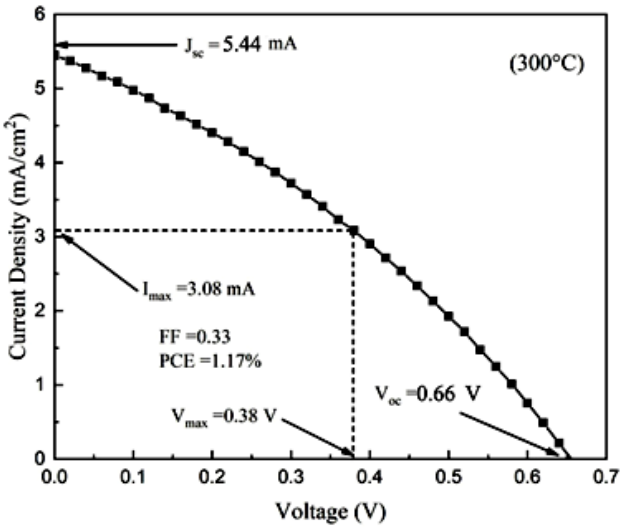

Figure 6 (a). I-V characteristics of $CH_3NH_3PbI_3$ film under illumination condition at a substrate temperature of 300°C

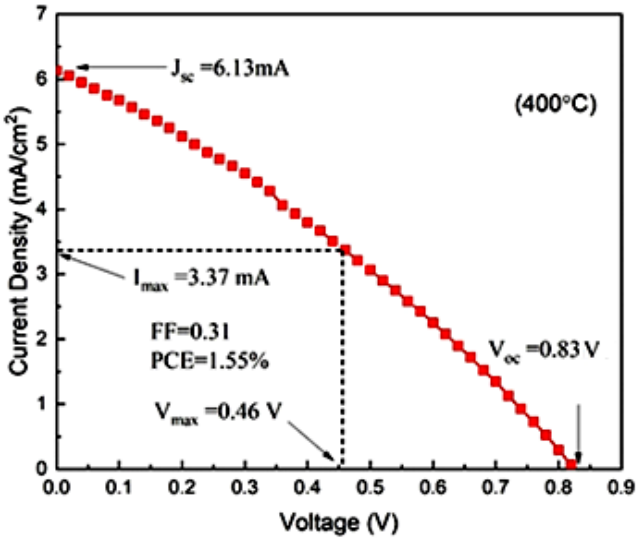

Figure 6 (b). I-V characteristics of $CH_3NH_3PbI_3$ film under illumination condition at a substrate temperature of 400°C

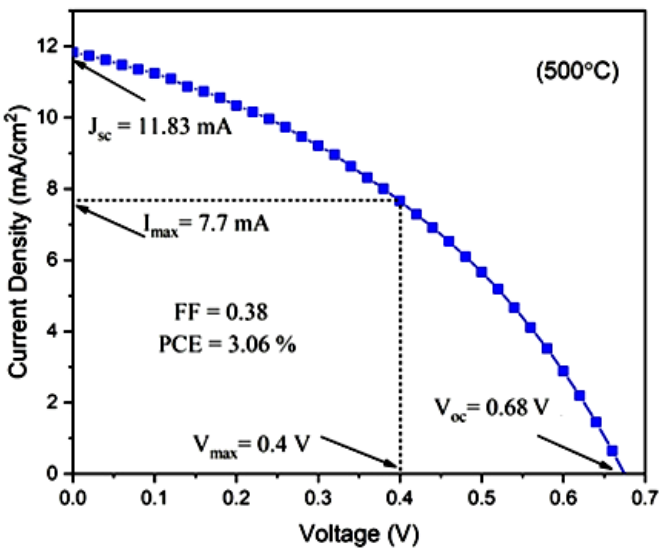

Figure 6 (c). I-V characteristics of $CH_3NH_3PbI_3$ film under illumination condition at a substrate temperature of 500°C

I-V characteristics of methylammonium lead iodide perovskite thin films were also measured. From the I-V characteristics, the current flow through the device was exponentially increased with the increasing voltage

across the fabricated film in the forward region and reverse region. An ln I-V characteristic was also determined in I-V characteristics. According to ln I-V characteristics, diode parameters such as saturation current, barrier height, and diode ideality factor are evaluated. From I-V measurement, photovoltaic parameters: power conversion efficiency (PCE) and the fill factor (FF) were also determined. The fill factor of $CH_3NH_3PbI_3$ perovskite solar cell was 0.328 at 300°C, 0.306 at 400˚C, and 0.384 at 500˚C. The conversion efficiency of 1.172 %, 1.552 %, and 3.064 % were observed at temperatures of 300°, 400°, and 500°C. The results showed that the power conversion efficiency was up to 3.064% at 500˚C, the open-circuit voltage of 0.675 V, current density of 11.83 mA/cm^2, and the fill factor of 0.384 was the best characteristic and also it has smallest crystallize size (23.41 nm). By the conclusion, the methylammonium lead iodide perovskite photovoltaic cells at various annealing temperatures were credible and promising use for thin- film solar cells by non-expensive and simple methods.

Acknowledgements

The authors would like to thank to Professor Dr. Thar Tun Maung, Rector of Kalay University for his kind permission to carry out this work. The authors would like to sincere thanks to Professor Dr. Saw Naing, Professor and Head, Department of Physics, Kalay University, for his kind encouragement.

References

Adam Pockett, 2016. “Characterization of Perovskite solar cell”. (pp.10)

F. Hao, C. C. Stoumpos, D. H. Cao, R. P. H. Chang, and M. G. Kanatzidis (2014), Vol. 8, pp. 489-494.

H. Mashiyama, Y. Kurihara, and T. Azetsu, (1998), Journal of the Korean Physical Society, Vol. 32, pp. S156–S158

K. P. Ong, T. W. Goh, Q. Xu, and A. Huan, J. Phys. Chem. A, (2015)

R. K. Singh, R. Kumar, N. Jain, J. Singh and S. K. Mishra, AIP Conference Proceedings, (2018)

T. Baikie, Y. Fang, J. M. Kadro, M. Schreyer, F. Wei, S. G. Mhaisalkar, Grätzel, M. & Whitec, T. J. (2013). Journal of Materials Chemistry A, Vol. 1, pp. 5628–5641

W. Geng, C. Tong, J. Liu, W. Zhu, W. Lau, and L. Liu, Sci Rep. (2016) 6

Y. Kawamura, H. Mashiyama, and K. Hasebe, (2002). Journal of the Physical Society of Japan, Vol. 71, pp.1694–1697.

https://en.wikipedia.org/wiki/crystal_structure

Analysis of Life Time of ^{8}Li via Hammer-like Track in Nuclear Emulsion at E373 Experiment

Kyaw Thu[1], Shwe Zin Aung[2], & Khin San Htay[3]

Abstract

In analysis lifetime of ^{8}Li via hammer track event in nuclear emulsion with photo-emulsion nuclei, these results are presented in this paper. Presented in this report are lifetime estimates for hypernuclei ^{8}Li based upon data obtained from an emulsion stack exposed to 1.67 GeV/c K^- mesons. The lifetime is: T (^{8}Li) = (845.49 ± 3) sec. Hammer-like track events were analyzed when we were getting in nuclear emulsion from E373 experiment. The kinetic energy of two alpha of hammer-like track event was obtained from range-energy relation by using their (average) ranges. Moreover, the masses and momentums of two alpha of hammer were also obtained by range-energy relation with use their ranges. Hammer-like track events in nuclear emulsion were analyzed by using computer-aided microscope system to study the life time of ^{8}Li nuclei.

Keywords: J-PARC E373 Experiment, ^{8}Li nuclei, Hammer-like track events, Range-energy relation, Computer-aided microscope system

Introduction

The β-decays of stopped ^{8}Li and ^{8}B fragments were produced by high-energy particles. Another example is the first observation of the ^{9}C nucleus from the decay 2α + p [M. S. Swami et al]. When used with sufficiently pure secondary beams, NTE appears to be an effective means for a systematic study of the decay of light nuclei with an excess of both neutrons and protons. More than half a century ago, hammer-like tracks from the decay of ^{8}Be nuclei through the first excited state 2+ of about 2.0 MeV were observed in NTE. The hammer-like tracks make the identification of ^{8}He fragments very simple and unambiguous. In March 2012 exposure of NTE to nuclei ^{8}He of energy of 60 MeV [3] is performed

[1] Lecturer, U, Department of Physics, Monywa University

[2] Professor, Dr, Head of Department of Physics, Monywa University

[3] Professor, Dr, Department of Physics, Monywa University

at the fragment separator [A.CCULINNA] in the G. N. Flerov Laboratory of Nuclear Reactions, JINR. Similarly, there have been quite an E373 experiments on the emission of ^{8}Li fragments from K^- interactions with nuclear emulsion at various incident beam energies. The experiments are helpful in understanding the nuclear structure and also the mechanism of fragmentation. For studying ^{8}Li fragments with a charge greater than that of α-particle, ^{8}Li (also ^{8}He, ^{8}Be) fragments have been chosen because of their characteristic decay into two α-particles, usually known as 'hammer-like tracks'.

Then the ^{8}Li nucleus with its half-life $\tau_\beta = (838 \pm 6) \times 10^{-3}$ sec undergoes β decay to the 2+ level of the ^{8}Be nucleus (3.03 MeV) with 100% probability and energy ΔE = 13 MeV [A. CCULINNA]. Finally, the ^{8}Be nucleus decays from its 2+ state with the width of 1.5 MeV to a pair of α-particles. In this paper we present the analysis on hammer-like track produced in the interaction of 1.67 GeV/c K^- with the nuclear emulsion. Features of decays of the ^{8}He isotope are shown in Figure1, according to the compilation [F. Ajzenberg-Selove]. Figure2 shows a macrophotograph of a decay of a nucleus ^{8}He stopped in NTE and ^{8}Li stopped in emulsion. It is typical one among thousands observed in this study. Video recordings of such decays taken with the microscope and camera are collected [A. CCULINNA]. When scanning the NTE pellicle with a 50× objectives on the microscope-aided computer system a primary search for β-decays of ^{8}Li nuclei was focused on hammer-like events Figure 2.

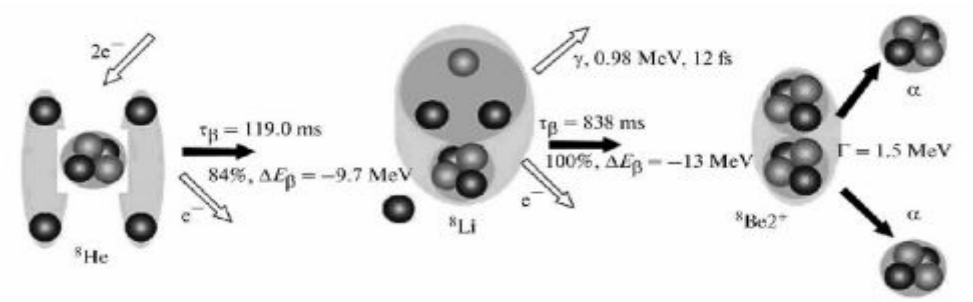

Figure1. Scheme of a major channel of the cascade decay of ^{8}He and ^{8}Li isotope; light circles correspond to protons, dark ones -neutrons.

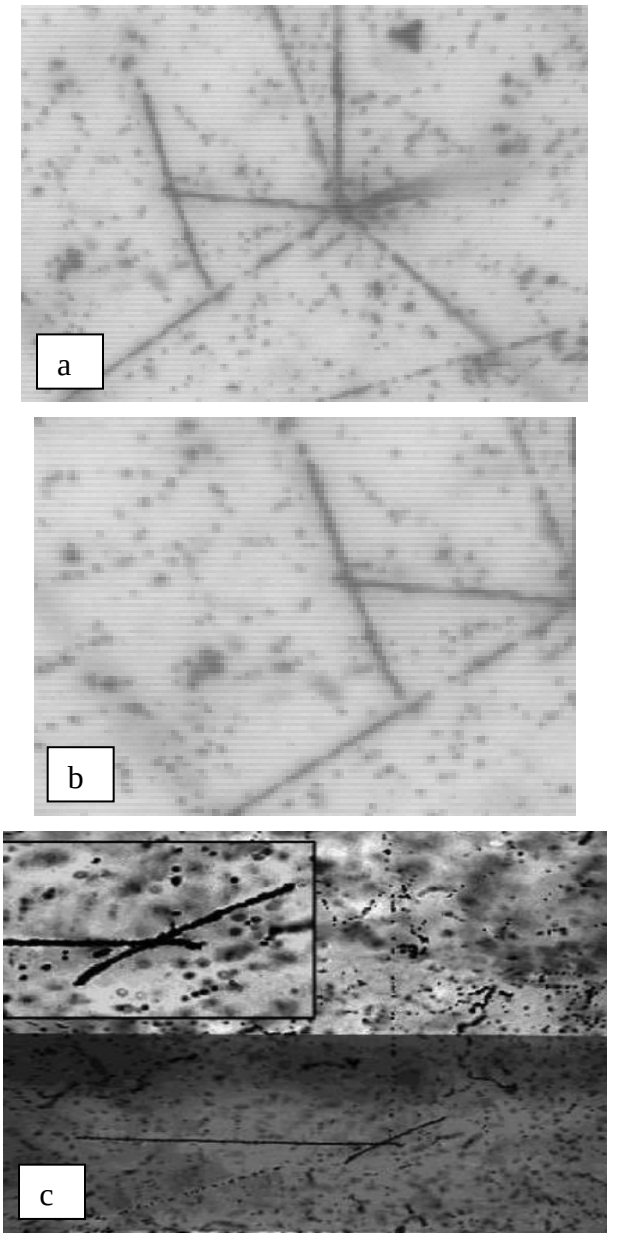

Figure 2. Macrophotography of a hammer-like decay of ^{8}He nucleus Fig. (c) stopped in nuclear track emulsion with compare ^{8}Li of hammer like track Fig. (a, b). Pair of electrons and pair of α-particles (short opposite tracks) for Fig. (a, b, c).

Experimental Procedure

This work was done using a stack consisting of 12 nuclear pellicles, each of size 25cm*24.5cm exposed to the K^- beam of momentum 1.67 GeV/c at Kazuma Nakazawa Laboratory. Hammer-like tracks were picked up by an area scan using 50x magnifications with computer-aided microscope system in Figure3. Each grey or black track which originated from a beam star was followed within the emulsion pellicle containing the primary star. The centre of each star was examined under a magnification of 50 x to detect the presence of a short hammer (hammer like) or recoil. All hammer and hammer-like tracks were assumed to be due to ^{8}Li, ^{8}Be fragments. Only those ^{8}Li, ^{8}Be fragments which decayed at rest into two colinear α-particles were picked up.

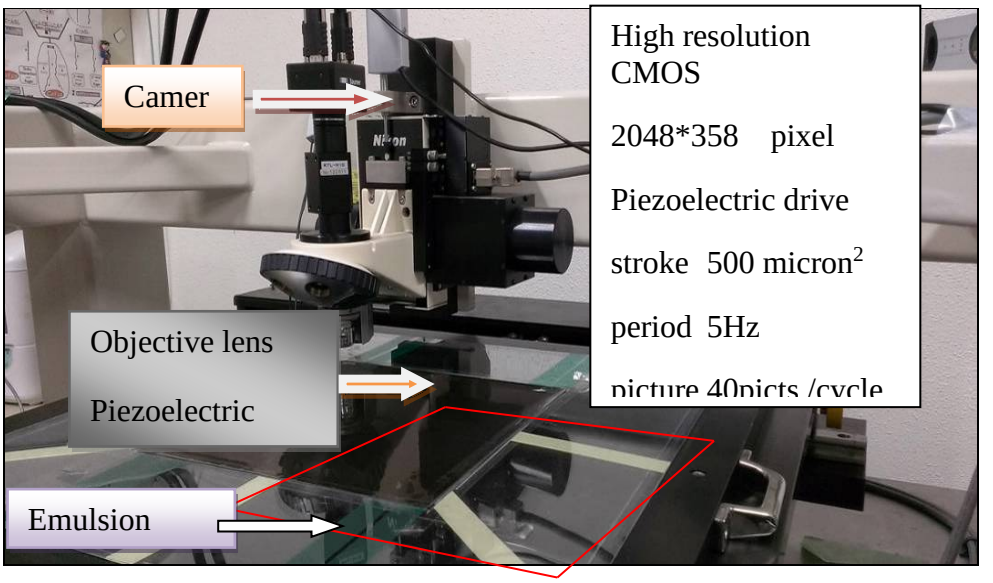

Figure 3. Computer-aided microscope

Analysis of Hammer-like Decays

As the pellicle was scanned using a computer-aided microscope system with a 50× lens, the primary search for alpha decays of ^{8}Li nuclei was focused on hammer-like events Figure 2 (a, b). The absence of tracks of a decay electron in the observed event was interpreted as a consequence of the inadequately effective observation of all decay tracks in the emulsion pellicle. The most problematic background for selection by this criterion

could arise from decays of ^{8}Li nuclei. In addition, for the decay of the ^{8}Be 2+ state to be hammer-like, it must populate the ^{9}Be level at energy no lower than 4.7 MeV. Otherwise, the decay proceeds via the ground state of the ^{8}Be nucleus and is therefore hardly observable even in emulsion. Thus, the background from decays of ^{8}Li and ^{9}Li nuclei could be ignored. There is often a gap observed between the stopping point and the hammer-like decay itself.

The events that included at least one electron were further measured using the 50× microscopes. The average length of the beam track events was $\langle L\ (^{8}Li)\rangle = 14.167 \pm 1.178$ μm. The Rang-Energy Relation simulation program allows the kinetic energy of the ^{8}Li nuclei that penetrated into the emulsion pellicle to be evaluated on the basis of the range measurements. Its average value is $\langle E\ (^{8}Li)\rangle = 7.124$ MeV. Coordinates of decay vertices and stops of decay α particles were determined for the hammer-like decays event.

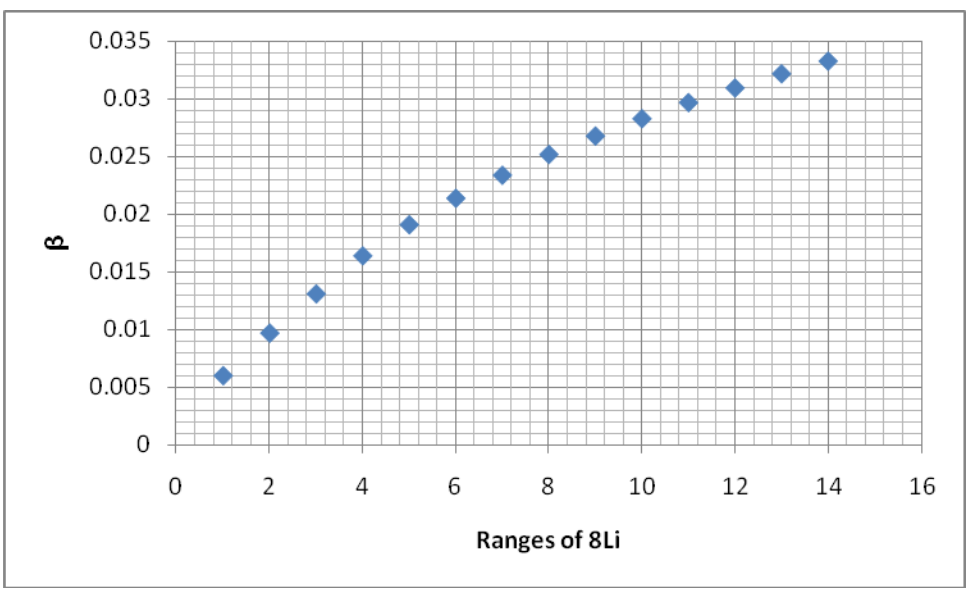

Figure 4. Determination of the beta from the measured ranges of ^{8}Li.

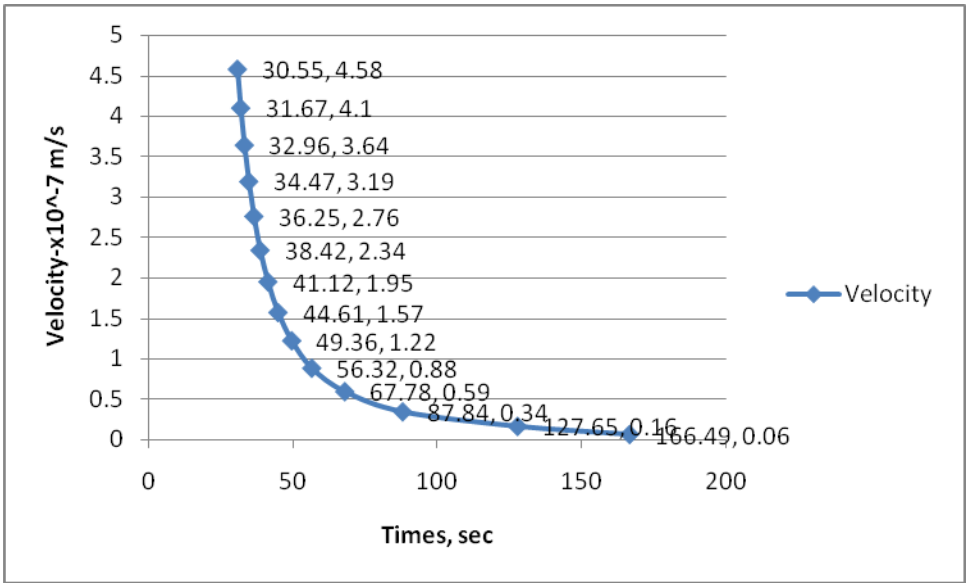

Figure 5. Calculation of lifetime with the velociy of ^{8}Li.

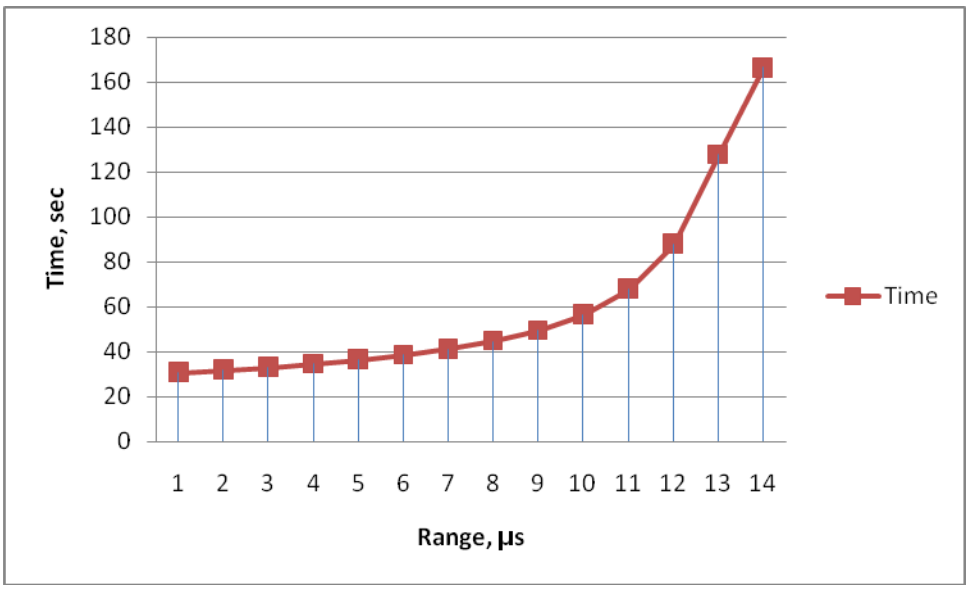

Figure 6. Estimating of lifetime with the measuring of range

Figure 4 express the relation between the ranges of ^{8}Li from the hammer-like decays and the beta decay from the range–energy relation. The average of the ^{8}Li ranges is 14.167 ± 1.17 μm which corresponds to the average kinetic energy ⟨E (^{8}Li)⟩ = 7.124 MeV. We may be calculating the velocity of ^{8}Li from the range and time of ^{8}Li as shown in Figure 5. The energy and momentum of ^{8}Li, we can obtain the beta decay of ^{8}Li. The relativity invariant of lifetime is defined as a divided by the beta (β) to the range of the ^{8}Li (R),

$$T = \frac{2\left(R - R^{*}\right)}{\beta + \beta^{*}}$$

Here T is defined as a lifetime of ^{8}Li,

The resolution of the nuclear track emulsion is enough to find the distances L (^{8}Li–^{8}Be) between the ^{8}Li stopping points and the ^{8}Be (2+) decay vertices in the hammer-like events Figure 2. The average value ⟨L (^{8}Li)⟩ = 14.167 ± 1.17 μm can be associated with the average drift length of ^{8}Li atoms. This hammer like track indicates the possibility of generating radioactive ^{8}Li atoms and pumping them out from sufficiently thin targets. The drift rate and length can be increased by heating the target. The ^{8}Li can be used for measuring the ^{8}Li life time at a new range of accuracy for the ^{8}Li. This paper is investigated the thin films by pumping ^{8}Li atoms with their particular penetrating power and depositing them onto detectors.

Conclusion

This analysis proves the life time of ^{8}Li reproduced nuclear track emulsion exposed to a beam of ^{8}Li nuclei. The experiment observed radioactive ^{8}Li nuclei to be identified by their decays as they stopped in the emulsion, the possibility of carrying out α spectrometry of these decays to be estimated, and the ^{8}Li atoms to be analysis for life time. The experiment proved the high purity of the beam of radioactive nuclei formed at the E373 facility with an energy ranging from 10 to 30 MeV/nucleon. The analysis of decay of ^{8}Li nuclei can be investigating decays of ^{8}He, ^{8,12}B, ^{9}C, and ^{12}N nuclei in which the ^{8}Be nucleus serves as a center point. This nuclear track can also be estimate to analysis the ^{8}He of time of flight. The hammer-like decays analysis in this work is a small fraction of the ^{8}Li nuclei, and the measured decays of hammer-like track. The nuclear track emulsion with radioactive nuclei analysis the basis using computer aided microscopes and

image processing programs at the same time. This paper may be possible to hope for new statistics of analyzed decays.

Acknowledgements

The author would like to thank Professor Dr Shwe Zin Aung, Head of Department of physics, Monywa University for her kind permission to carry out this work. And then, I would like to special thank Professor Dr Yin Maung Maung, Head of Department of physics, University of Yangon, and we would like to gratefully acknowledge Dr. Than Than Win, Pro-Rector, Monywa University for her collaboration in our research as well as for her guidance, Myanmar. And then, I also would like to thank Professor KazumaNakazawa, Head of Department of Physics, Gifu University, Japan.

References

Artemenkov D. A. et al., Phys. Part. Nucl. Lett. 10, 415 (2013).

Ajzenberg-Selove, F. Nucl. Phys. A, 490 1 (1988).

Powell, C. F. P. H. Fowler and D. H. Perkins “The Study of Elementary Particles by the Photographic Method”, Pergamon Press, 1959.

Rodin et al., A. M. Nucl. Instr. & Meth. B, 204, 114 (2003).

Swami M. S. et al., Phys. Rev., 103, 1134 (1956).

A. CCULINNA Project. Available: http://aculina.jinr.ru/

Synthesis and Characterization of Nano-Structured Nickel Cobalt Ferrites by Sol-gel Method

Khin Nwe Oo[1] , Kyaw Kyaw Winn[2] , Nila[3] & Khin Win Mu[4]

Abstract

Nickel substituted Cobalt Ferrites with the general formula $Ni_xCo_{1-x}Fe_2O_4$ (x = 0.0, 0.1, 0.2 and 0.3) were prepared by sol-gel method. The X-ray diffraction (XRD) analysis was carried out to investigate the crystalline phase formation, which indicated the formation of cubic spinal in single phase and no other impurity phases. Microstructural properties and Elemental composition characterization of prepared samples were determined by SEM-EDS. The broader size distribution in these samples was characteristics of mechanically activated nano-sized particles. The vibration bond structure was also analyzed by FTIR

Keyword: Ni-Co Nano ferrites ;auto combustion and solgel;, XRD, SEM , EDS and FTIR .

Introduction

Insulating magnetic materials are in growing demand for certain applications as they have the ability to suppress various losses, particularly the hysteresis loss. In this respect spinel ferrites have been a source of attraction for researchers for their strong magnetic behavior with insulating in nature. Nano ferrites have been observed with drastic change in magnetic properties counter to their bulk part. Ferrites crystallize in three different crystal structures, namely, spinels, garnets and magnetoplumbites by many methods, and the feasibility to prepare a virtually unlimited number of solid solutions opens the means to tailor their properties for many applications. Several Nano ferrites are rigorously studied and tuned their magnetic behavior with suitable dopants[1]. Cobalt ferrite (CFO) has been emerged as the highly studied material in this case. For many applications, ferrites cannot be substituted by ferromagnetic metals; for other, ferrites often compete with metals on economic reasons. $CoFe_2O_4$ is one of the members

[1] Lecturer, Department of Physics. University of Mawlamyine
[2] Professor, Department of Physics . University of Mawlamyine
[3] Lecturer, Department of Physics. University of Mawlamyine
[4] Lecturer, Department of Physics. University of Mawlamyine

of spinel ferrite family which has been extensively studied for its intrinsic properties of large spin polarization, good chemical stability, high resistance and high magnetic critical temperatures; typically well above the room temperature [1-2]. Number of modifications have been carried out to enhance on it both magnetically and electrically to make a potential material for wide range of applications such as magnetic recording and storage, spin filters, spintronics and phase shifters. Ferrites in the form of ceramics and composites find applications in magnetic memories, TV yokes and in many other devices.

In present work, nickel (Ni^{3+}) as dopant to substitute Fe^{3+} in $CoFe_2O_4$ system was performed by sol-gel combustion method. Structural, microstructure properties and atomic and weight concentration of fabricated nano-ferrite were studied by X-ray diffraction (XRD), scanning electron microscopy(SEM), Energy Dispersive Spectrometer(EDS) and Fourier Transform Infranred (FTIR).

Experimental Details

In this research spinel like ferrites belonging to the series $Ni_{1-x}Co_xFe_2O_4$, where x varies from 0.0 to 0.3 in steps of 0.1 were prepared by self-combustion method and sol-gel method. $Ni(NO_3)_2.6H_2O$, Nickel nitrate hydrate, $Fe(NO_3)_2.9H_2O$, iron nitrate hydrate and $Co(NO_3)_2.6H_2O$, cobalt nitrate hydrate were used as raw materials for $Ni_{1-x}Co_xFe_20_4$ ferrite. Before preparation of spinel like ferrites the purification of starting materials was checked by X-ray diffraction.

Experimental Sequence for Nano-ferrites by Sol-Gel Method

Sol-gel processing, which is based on chemical engineering methods, is a technique to manufacture ceramic powders, especially oxides. The term *sol* refers to the initial solution of the chemical components for the final powder; whereas the term *gel* describes the final consolidation stage that forms the ceramic product. Sol-gel procedures have been successful in the preparation of bulk metal oxides, e.g., ceramics, glasses, films and fibers and, therefore, they have been applied for nanoparticle synthesis.

The sol-gel process consists of the following five prime steps.

(i) Preparation of a homogeneous solution either by dissolution of metal organic precursors in an organic solvent that is miscible with water, or by dissolution of inorganic salts in water.

(ii) Conversion of the homogeneous solution into a sol by treatment with a suitable reagent that is generally water with or without an acid base.

(iii) Aging of the solution.

(iv) Shaping of the gel.

(v) Thermal treatment or sintering of the final product.

Firstly, Metal precursors were prepared by using $Ni(NO_3)_2.6H_2O$, Nickel nitrate hydrate, $Fe(NO_3)2.9H_2O$, ion nitrate hydrate and $Co(NO_3)_2.6H_2O$, cobalt nitrate hydrate and deionized water. The chelating agent was prepared by dissolving the necessary powders in distilled water at 70 °C. The chelating agent solutions were maintained at 70 °C for 2 h, the solution became clear. Metal precursors were dissolved into the chelating agent solution under magnetic stirring. Ammonia (NH_3) was added drop by drop to maintain the pH at 7. The sol-gel reaction was continued for 3 h and the temperature increased to 100 °C for 10 h or until the gel dried into the form of a powder. Finally, all samples were sintered at 800 °C for 5 h and then ground and sieved, nano ferrite powder was obtained. The experimental sequence for nano ferrite powder by sol-gel method was shown in figure 1.

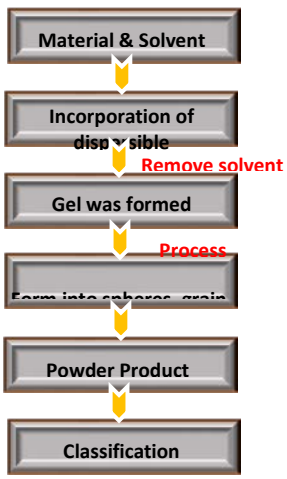

Figure 1. The production steps for sol-gel production route

Results and Discussion

Structural Investigation of Nano-ferrite

The method of X ray diffraction was used to evaluate the purity of raw materials and the various structural parameters namely inter atomic spacing (d), relative intensity ($1/1_0$) and lattice parameter. The identification of the phase was carried out by comparing the observed structural parameters with that of the standard values reported in the literature. The diffractograms of the samples were recorded on a X ray diffractometer using Cuk_α radiation ($\lambda = 1.54056$Å).

The XRD spectra of the cobalt Doped Nickel ferrites, Ni_{1-x} Co_x Fe_2 O_4 (x = 0.1, 0.1, 0.2 and 0.3) nano-ferrite were investigate by X-Ray Diffractometer. Figure 3(a-b) showed XRD profile of nano-ferrite fabricated by sol-gel method with different Co concentration.

In these figures, eight diffraction patterns were clearly observed and all of these patterns were consistent with JCPDS library file No 01-077-9720. It can be seen that all the compounds thus prepared show crystallinity and the diffraction pattern is characteristic of a spinel structure. The interatomic spacing (d) values were in good conformity with that of the reported values. Moreover no other impurity lines corresponding to possible oxides of precursors used for synthesis were noticed. Thus it was ensured that the prepared compounds were single phasic in nature and they exhibit an inverse/ normal spinel structure.

In figure 3(b), all the reflections in the XRD patterns correspond to that of cobalt ferrite and no additional reflections were observed for the samples indicating the phase purity of the samples. The X-ray diffractograms clearly indicate the formation of single phase spinel structure. The XRD patterns were compared and indexed using JCPDS library file no 00-003-0875 for Ni ferrites. The reflections of the samples synthesized by sol-gel methods were shaper than that of the sample prepared by the self-combustion route, indicating the presence of larger crystallites. But their intensities were more intense than nano ferrite by self-combustion method.

The X-ray density of all the $Ni_{1-x}Co_xFe_2O_4$ ($0 \leq x \leq 0.3$) ferrites has been calculated from the molecular weight and the volume of the unit cell using the relation;

$$d_x = \frac{8M}{Na^3}.$$

The calculated values were also listed in Table1.

The average particle size of the synthesized ferrite samples was estimated from X-ray peak broadening of diffraction peaks using Scherrer formula. The calculated average crystallite sizes of these starting materials were listed in Table 2. From this results, the average crystallite size was decreased with the increasing of Co content. But at the Co content (0.3%), the average crystallite size increased again due to the material concentration. Average crystallite size of fabricated nano ferrite by sol-gel method was a little larger than that of self-combustion method. Generally the sol-gel technique yields nano size grains in the ferrite systems. But, as the sintering temperature and sintering time (800˚C for 5 h) were very high, this resulted for larger grain size in the prepared ferrite samples. Likelihood, all of fabricated nano ferrite confirmed nanometer range.

Table 1. Variation of X- ray density values and The crystallite size of starting materials for $Ni_{1-x}Co_xFe_2O_4$ nano-ferrite

$Ni_{1-x}Co_xFe_2O_4$ Nano-ferrite	Crystallite Size(nm)	X-ray density (gcm^{-3})
x =0.0	46.3617	5.3900
x =0.1	45.6355	6.7070
x = 0.2	45.1332	6.7029
x= 0.3	45.7477	6.7244

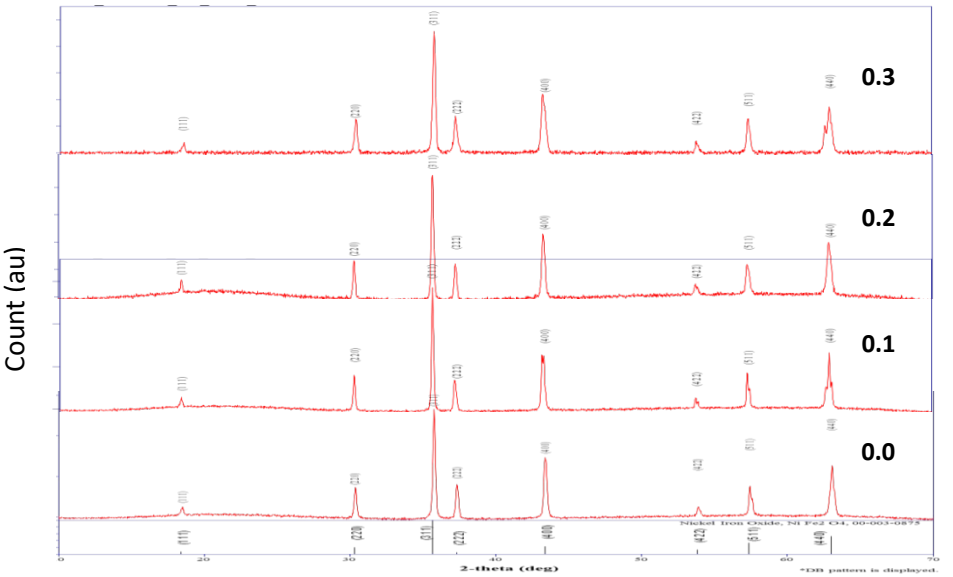

Figure 2. XRD Spectrum of $Ni_{1-x}Co_xFe_2O_4$ ferrites with different Co concentration

Microstructural Determination

Microstructural properties of Ferrite samples were studied by Scanning Electron Microscopy(SEM). The scanning electron image of ferrite samples by self-combustion method and sol-gel method were shown in figure 4(a&b). In these figures, it can be seen that the morphology of particles for SEM micrographs of various composition is similar. They reveal largely agglomerated, well defined nano particles of the sample powder with inhomogeneous broader grain size distribution. Such broader size distribution is characteristics of mechanically activated nano sized particles.

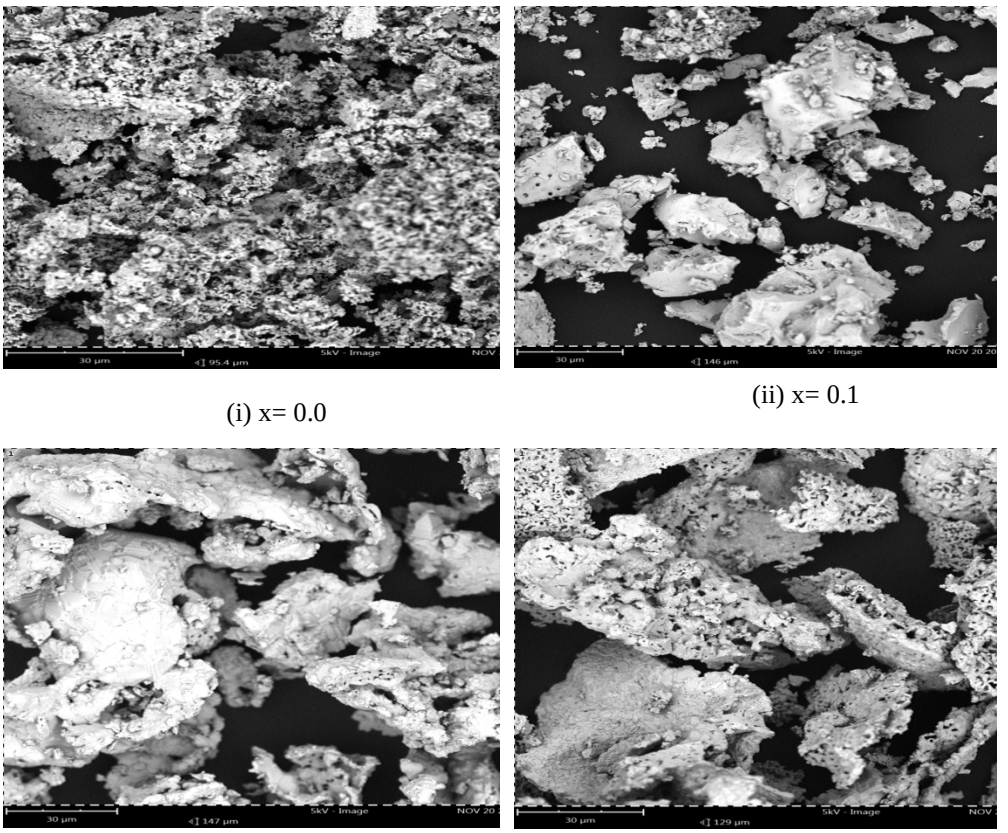

(i) x= 0.0 (ii) x= 0.1

(iii) x= 0.2 (iv) x= 0.3

Figure 3. Scanning electron images of $Ni_{1-x}Co_xFe_2O_4$ nano ferrite with different Co concentration

Elemental Analysis by EDS

The elemental analysis of ferrite samples with different compositions by two different methods were analyzed by Energy Dispersive Spectrometer(EDS).The EDS pattern of nanoferrites samples were shown in figure 4. In these figure, it was indicated that the elemental and atomic composition.The fabricated nanferrite showed the present of Ni, Co, Fe and O without precipitating cations.The elemental % and atomic % of different elements were shown in Table 2.

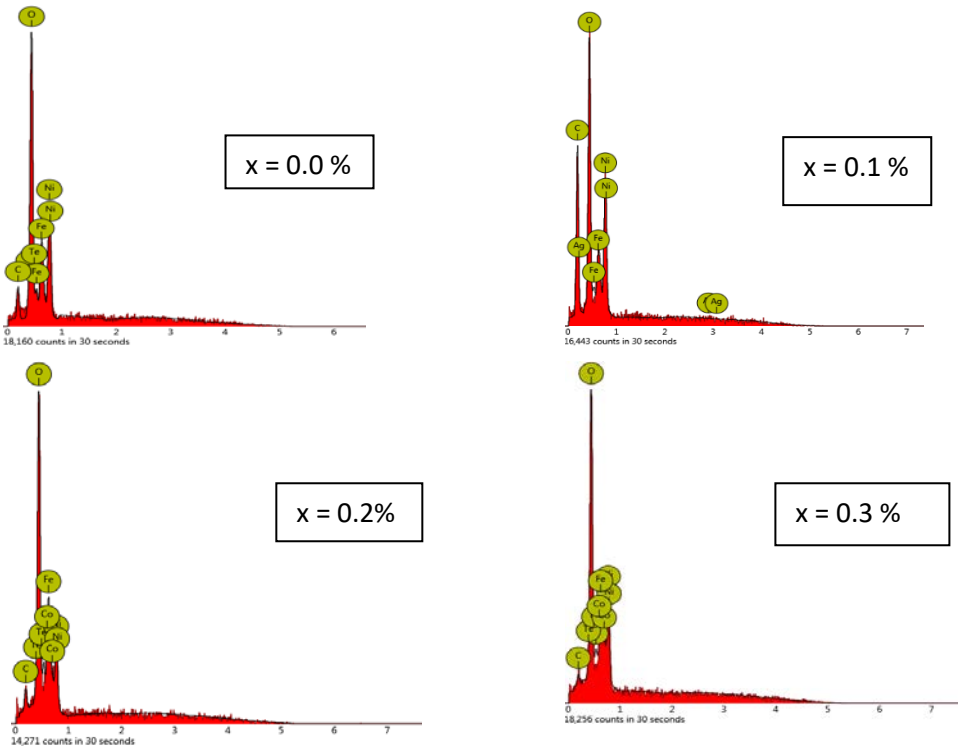

Figure 4. EDS pattern of $Ni_{1-x}Co_xFe_2O_4$ nanoferrite with different Co concentration

Table 2. Atomic and weight concentration of nano-ferrite sample

Element	Ni		Co		Fe		O	
Ferrite Composition	Atomic Conc. %	Weight Conc.%	Atomic Conc. %	Weight Conc.%	Atomic Conc. %	Weight Conc.%	Atomic Conc. %	Weight Conc.%
NiFe $_2$O4	20.43	39.90			14.38	26.73	50.56	26.92
Ni0.9Co0.1Fe $_2$04	14.50	37.05			6.36	15.46	35.18	24.50
Ni0.8Co0.2Fe $_2$04	13.09	24.01	5.34	9.83	20.87	36.41	52.37	26.18
Ni0.7Co0.3Fe $_2$04	19.25	33.88	6.98	12.33	15.59	26.11	53.46	25.65

Fourier Transform Infrared Spectroscopy Studies (FTIR)

Chemical functional groups of Nickel substitutes Cobalt ferrites were characterized by FT-IR spectroscopy and shown in the figure 6. The same FT-IR peaks were observed in all of ferrite samples. The absorbing bands at 1076.22 cm^{-1} was assigned to the positions of metal-oxide stretching vibrations. The peaks at 1374.95, 1447.82, and 1637.29 cm^{-1} were related to the O-H vibrations due to the adsorbed water. The peak at 3331.20 cm^{-1} was attributed to the adsorbed CO_2 on the surface of these samples. FT-IR result showed that all the carbonic functional groups related to the precursors were eliminated. The vibration frequency of tetrahedral and octahedral sites was also shown in table 3.

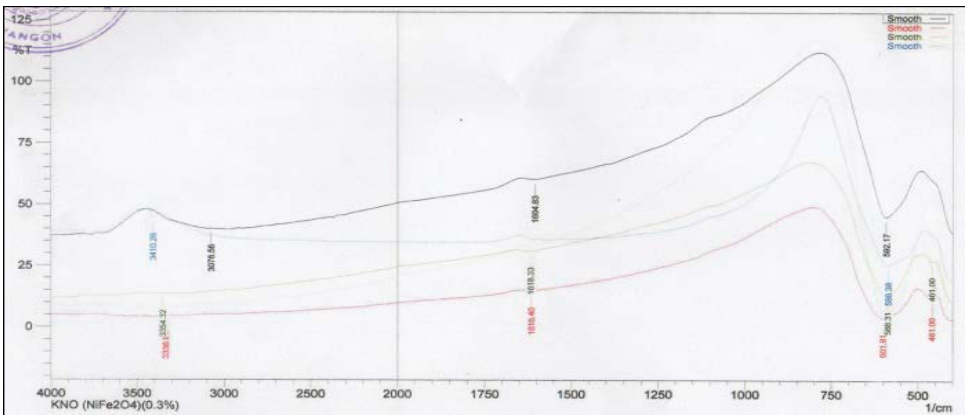

Figure 5. The FTIR spectrum of nickel substitutes cobalt ferrites

Table 3. The vibration frequency of tetrahedral and octahedral sites

Ni content 'x'	Composition	$\nu_{1\ tetra}$	$\nu_{1\ octa}$
x = 0.0	$CoFe_2O_4$	592.17	460.88
x = 0.1	$Ni_{0.1}Co_{0.9}Fe_2O_4$	586.38	460.92
x = 0.2	$Ni_{0.2}Co_{0.8}Fe_2O_4$	588.31	461.00
x = 0.3	$Ni_{0.3}Co_{0.7}Fe_2O_4$	601.81	461.00

Conclusion

Nanocrystalline Cobalt Doped Nickel Ferrites, Ni_{1-x} Co_x Fe_2 O_4 (where x = 0.0, 0.1, 0.2 and 0.3) samples were successfully prepared by self-combustion method and sol-gel method. Their structural analysis was reported by using XRD. The process involved no impurity pick up and material loss. It was a very simple and economical method where no specific heating or cooling rate is required. X-ray diffraction pattern confirms the formation of cubic spinel structure in single phased without any impurity peak. The lattice parameter was not remarkablely changed with the increase of Co substitution in Ni-Co ferrites which indicates that Co content was totally substituted in Ni. Average crystallite size of fabricated nano ferrite observed that in the range between 41 and 46 nm. SEM micrographs of various compositions indicate the morphology of particles is similar and largely agglomerated and inhomogeneous broader grain size distribution. EDS data gives the present of Ni, Co, Fe and O without precipitating cations. The FT-IR measurement for the ferrite powders shows two characteristic bands in the range 500-600 cm^{-1} and 385-450 cm^{-1}, which could be attributed to the tetrahedral and octahedral complexes respectively.From the results, it is concluded that, the two fabrication methods used in this research provided improvement of crystallinity and pronounces of nano particle size.

Acknowledgement

I would like to express my deep and sincere thanks to my Professor Dr Khin Khin Win, Head of Department of Physics, University of Yangon, for her kind permission to carry out this research .I would like to thank Professor Dr Kyaw Kyaw Winn, Department of Physics, University of Mawlamyine, for his valuable suggestion for this work.I wish to express my warmest thanks to my Co-supervisor Dr Min Mg Mg Associate Professor, Department of Physics, University of Yangon, for her valuable guidance.

References

Gopathi Ravi Kumar& et.al.,(2012), “Synthesis, Structural and Magnetic Properties of Copper Substituted Nickel Ferrites by Sol-Gel Method”, Materials Sciences and Applications, 3, 87-91.

Jiang K, Li K, Peng C, Zhu Y., (2012) “Effect of multi-additives on the microstructure and magnetic properties of high permeability MnZn ferrite”, Journal of Alloys and Compounds, 541, 472-476.

Manjura Hoque, S. Md. Amanullah Choudhury and Md.Fakhrul Islam, (2002), "Characterization of Ni-Cu Mixed Spinel Ferrite," Journal of Magnetism and Magnetic Materials, 251, (3), 292-303.

Pardavi-Horvath, M. (2000), "Microwave applications of soft ferrites" Journal of Magnetism and Magnetic Materials, 215, 171–183.

Raul Valenzuela, (2011), "Novel Applications of Ferrites", Physics Research International, 2012, 9.

Venkataraju, C., Sathishkumar, G. and Sivakumar, K. (2010), "Effect of Cation Distribution on the Structural and Magnetic Properties of Nickel Substituted Nanosized Mn-Zn Ferrites Prepared by Co-Precipitation Method," Journal of Magnetism and Magnetic Materials, 322, (2), 230-233.

Fourier Transforming of Acoustic Signal

Shwe Zin Aung*

Abstract

The constructed system implements the fast Fourier transform of the real world acoustic signal, various notes produced by casio musical instrument and voice of human. C programming is essential tool for fast Fourier transforming and the system offers to display the signal and its spectrum and to store for further processing. Data acquisition is made efficient by AT89S51 based 8 bit successive approximation logic (SAL) type analog to digital converter (ADC). While AT89S51 microcontroller is doing analog to digital conversion of the input signal, the personal computer (PC) processes the digital data, and particularly does the fast Fourier transforming and displays the signal and its spectrum. Self-developed firmware embedded in microcontroller can perform the analog to digital conversion and send parallel digitized signal to the PC. The sampling time of the parallel processing system is 60 μs and sampling frequency(f_s) is 16 kHz. So the maximum frequency that can be measured by the constructed system is ($f_s/2$) 8 kHz and frequency resolution of the system is 8 Hz. Fundamental frequency and its overtones for various notes produced by casio musical instrument and the resulting Fourier transform output were observed and compared with the 100MHz, RIGOL DS 5102CA, two channel digital oscilloscope. Voice of men and women were also analyzed by the constructed system and it was found that the fundamental frequency of woman is higher than that of man. The system allows the storage of both signal and its spectrum in the PC for further analysis and is intended to make synthesizing and recognition process.

Keywords: sampling frequency(f_s), frequency resolution, synthesizing and recognition process

Background Theory of Fourier Transform

Transforms are orthogonal expansions of functions such that a given function can be represented uniquely by a combination of some elementary basic functions. The linear independence of orthogonal functions provides the advantage of identifying or recognizing a particular function uniquely by means of its transforms. Very often, transforms lead to an easy way of performing certain operation that are otherwise difficult to perform. For

* Professor and Head, Physics Department, Monywa University

example, to avoid the mathematical difficulty of performing a convolution operation, one might prefer to do a simple multiplication in the Fourier transform domain. For example, input-output relationship of a system may be described by a simple product of input Fourier transform and the system transform. Fourier (1768-1830), a French mathematician, was famous for his contribution to the theory of heat conduction by what came to know as Fourier expansion [H. Hutchings (1995)].

So, Fourier theory is of central importance in a vast of application in engineering, physical science, electrical and electronics engineering, computer science and applied mathematics. Electronic engineers routinely use Fourier transforms to examine the effects of noise or bandwidth on the signal being processed through a particular system. The usual concern in electronics signal analysis is with time to frequency domain transforms, although numerous other application exits [H. Hutchings (1995)]. The block diagram of the system is illustrated in Figure 1.

Fast Fourier Transform (FFT)

The Fast Fourier Transform is not a new transform. It is an algorithm which, when applied to a data set of 2^M samples, reduces the number of multiplications from N^2 to $N \log_2 N$. This is a huge saving of computations times. Its existence generally becomes known in the mid 1960. It followed the matrix theory of Cooley and Tukey, who returned to the computation of "schedules" originally undertaken at Los Alamos as part of the Manhattan Project. Retrospectively, it is acknowledged that a few clever people had been using the FFT as early as 1942 [H. Hutchings (1995)].

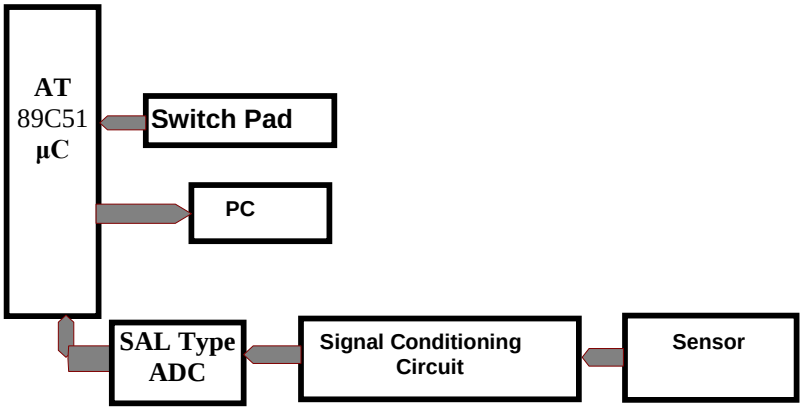

Figure 1. The block diagram of the system

Examination of the DFT algorithm indicates that approximately N complex multiplications and about the same numbers of additions are required to calculate the frequency coefficient for a particular value of m. Since there are N/2 unique spectral components, the total number of multiplications required to compute the complete spectrum is approximately N^2. This is a considerable calculated coefficients are redundant and can be factored out. Evaluating the FFT by hand is an exercise in tedious calculation. Nevertheless, insight into the inner workings of the FFT only comes with real understanding of the more straightforward DFT. Modern notation tends to present the DFT in the form;

$$X(m) = \sum_{n=0}^{N-1} x(n) e^{\frac{-j2\pi mn}{N}}$$

$$X(m) = \sum_{n=0}^{N-1} x(n)\, W^{mn} \qquad m = 0, 1,2,\ldots,(N-1)$$

Material and Method

This section presents the general explanations for the hardware and firmware of the implemented system. The system consists of signal conditioning unit, software controlled successive approximation logic (SAL) type analog to digital converter (ADC) and AT 89S51 microcontroller.

AT89S51 Microcontroller

For the analog to digital conversion, Atmel's AT89S51 microcontroller is used. The 89S51 is an 8-bit, low power, high-performance microcontroller. There are large numbers of devices in the 89S51 family with similar architecture and each member of the family is downward compatible with each other. The pin diagram of AT89S51 microcontroller is shown in Figure 2 [Ad.www.all.datasheet.com/at 89C51].

Amplifier Circuit Using LF 353 IC

LF-353 IC consists of two operational amplifiers (op amp). These operational amplifiers can be used as comparator and integrator, such as Schmitt trigger or squaring circuit, zero crossing detector, voltage level

detector and oscillator. The gain of the op amp is easily set by the ratio of the feedback and input resistors by the equation A_V(voltage gain)= – R_f / R_{in} [https://www.ti.com, LF353N]. The schematic diagram of LF 353 and amplifier circuit are shown in Figure 3 (a) and (b).

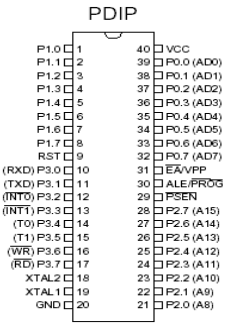

[Ad.www.all.datasheet.com/at 89C51]

Figure 2. Pin layout diagram of AT89S51 microcontroller

Low Power Dual Voltage Comparator (LM-393)

The LM-393 series consists of two independent precision voltage comparators with an offset voltage specifications as low as 2mV maximum or all two comparators. There were designed specifically to operate from a single power supply over a wide range of voltages.

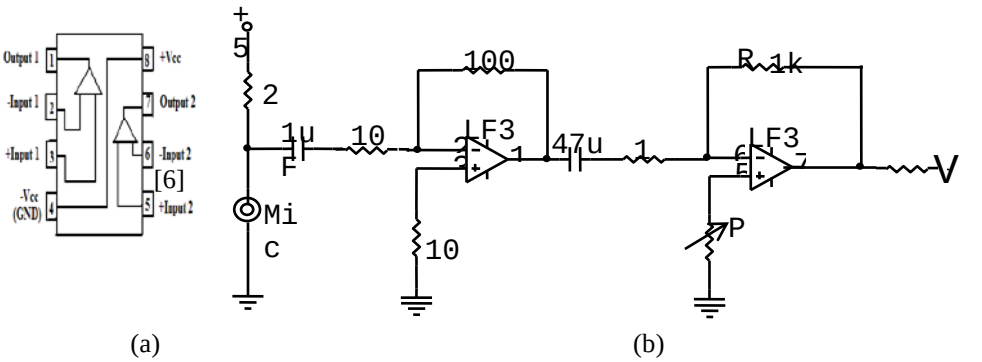

(a) (b)

Figure 3 (a). Schematic diagram of LF-353 IC (b) The first and second amplifier stage

These comparators also have a unique characteristic in that the common-input mode voltage range includes ground, even though operated

from a single power supply voltage. Applications areas include simple analog to digital converters, wide range VCO (voltage control oscillator), MOS (metal oxide semiconductor), clock generator, multivibrators and high voltage logic gate. It can be used with single supply voltage over range 2.0 V_{DC} to $36V_{DC}$ or dual supplies over a range of $\pm 1.0V_{DC}$ to ± 18 V_{DC} [https://www.ti.com, LF353N].

R-2R Ladder Type Digital to Analog Converter (DAC)

R-2R ladder type digital to analog converter (DAC) is most popular (DAC). It uses a ladder network containing series and parallel combinations of two resistors of values R and 2R. Hence the name R-2R ladder type DAC [Li Tan (2008)].

The stabilized voltage reference source sees a total resistance of R ohm's and delivers a current of V/R amps, with the switches in the positions shown, the topology of the circuit is such that the current divides into two at each node. Thus, the current flowing into the op-amp is given by the expression for 4-bit is by the equation.

$$I = -\frac{V}{2R} - \frac{V}{4R} - \frac{V}{8R} - \frac{V}{16R},$$ and the output voltage V_0 of the op-amp is given by,

$$V_0 = -I.R_f = -\left[\frac{V}{2R} + \frac{V}{4R} + \frac{V}{8R} + \frac{V}{16R}\right]R_f$$

$$= -\frac{R_f}{R}\left[\frac{V}{2} + \frac{V}{4} + \frac{V}{8} + \frac{V}{`16}\right].$$

This result in 0 mapping to the maximum negative value of (-2.5V) and 255 mapping to the maximum positive value of + 2.5V. A zero output is achieved when an input of 128 is applied to the converter. This section consists of eight 20 kΩ resistors, nine 10 kΩ resistors. This section converts the digital data from port 2 of microcontroller to the analog voltage. The output waves are generated by this section [T. L. Floyd (2007)].

Hardware and Software Development of The System

The desired program for AT89S51 was developed in keil µvision2 software and its compiler generates the machine code as .HEX file. The resultant .HEX file was downloaded from PC to µC via MP929

programmer. The microcontroller sends the data to PC via the Line Printer Terminal (LPT1). C^{++} program in PC implements the digital signal processing, Fast Fourier transforming of the input signal and displaying the signal and its spectrum, while the microcontroller does the analog to digital conversion.

Signal Conditioning Unit and Level Shifter

Signal Conditioning Unit consists of two LF353ICs. First LF353IC used as an inverting amplifier. Incoming-signal pass through R_{37}. The gain of this op amp is the ratio of the feedback resistor R_{35} by input resistor R_{37}. The output of first LF 353 is fed to the input of second op amp. The gain of second op amp is adjustable by means of second preset (PR2). Second LF353 IC is used as level shifter and buffer.

In the case of microcontroller and PC interfacing the negative voltage level of the signal cannot be recognized by microcontroller and PC. So level shifting circuit is needed and the level shifter is simply a non-inverting adder with unity voltage gain. In this circuit the voltage signal emerged from the preceding section (signal conditioning circuit) is fed through the 10k resistor (R_{38}) to the non-inverting terminal of the op amp (LF 353) connected as voltage adder. The voltage level to be added is obtained from second preset (PR 2) and R_{39}.

Microcontroller-Based SAL Type ADC

In software the various bit patterns from $1000\ 0000_2$ down to $0000\ 0001_2$ can be added to the subtotal and sent out to the DAC. The resulting analog equivalent is compared to the incoming voltage. The "sum" is initialized to zero (nothing on the pan) and the "count" is initialized to 128 (largest known weight $1000\ 0000_2 = 128_{10}$). The while loop adds the test weight (count) to the trial pattern to form aggregate, sends it out to the DAC and checks the comparator output. The comparator answers the equation if the trial pattern is larger, then the test weight is removed (subtracted). Each new test weight is generated by shifting weight right once. After eight passes through the loop, the state of the aggregate is the digital equivalent to V_{in}. The program will pass through the loop 8 times. The first time through the loop sends $128_{10} = 1000\ 0000_2$ to port 2. For instance, if V_{out} is greater than V_{in}. Port 0.1 is high and the latest bit is reset. If V_{out} is less than V_{in},

port 0.1 is low and the next bit is added to the successive approximation. After 8 passes through the loop, the software conversion is finished and the program is ready to take the next data. The calibration curve of digital reading from PC and analog voltage for microcontroller based SAL type ADC is shown in Figure 4.

User Interface

The system performs the real time data acquisition, real time data saving, fast Fourier transforming and Fourier data saving. The user interface of the system is shown in following. Data of time domain and frequency domain data can be saved as file in computer hard disk for long time analyzing.

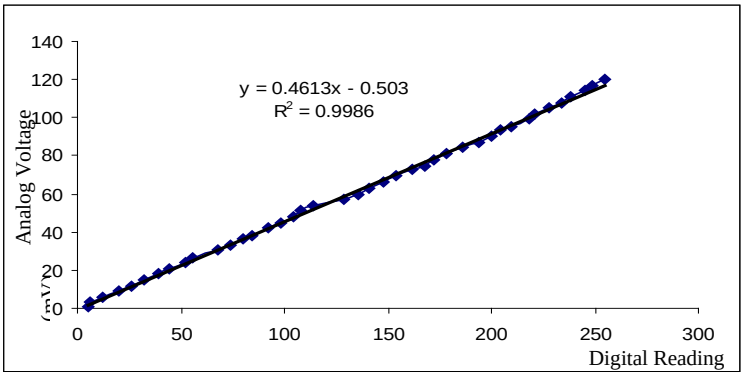

Figure 4. The calibration curve of digital reading from PC and analog voltage for Microcontroller-based ADC.

Microcontroller-based Spectrum Analyzer

R-->Real time data acquisition

C-->Data signal storage

F-->Spectrum analyzer

S-->Save Signal and its spectrum

O-->Open saved signal and spectrum files

Esc-->Press Esc to quit

Chose R, C, F, S, O, Esc:

Frequency Calibration

First of all, we have to determine the time (or) frequency scaling. So the sampling time (time interval between two data points) and sampling frequency (the number of samples per second) are determined for the constructed system. In this case, we used the sinusoidal signal of frequencies ranging from 100 Hz to 3 kHz generated by a signal generator.

To determine the sampling time and sampling frequency, a digitized graphical signal on PC monitor was used. Sampled data from software controlled SAL type ADC sends discrete time signal to the PC. The numbers of sampled data points are recorded. The period and frequency of applied sine wave is noted using the calibrated time base of the oscilloscope. The sampling time can be achieved by dividing the period by the number of data points in one period. This can be calculated by the following equation.

$$\text{Sampling time} = \frac{\text{Period}}{\text{No: of data points in one period}}$$

Then the sampling frequency is determined by following equation.

$$\text{Sampling frequency} = \frac{1}{\text{Sampling time}}$$

Sine waves with frequencies ranging from 400Hz to 1000Hz from the signal generator are used as input signals. A file of digitized signal was created and graphically analyzed by C^{++} programming.

To obtain the reliable value of sampling time and sampling frequency for various signals of the frequency range between 400Hz and 1 kHz would be observed in this way. The sampling frequency of the system is 16 kHz.

The frequency resolution is determined by the following equation.

$$\text{frequency resolution} = \frac{\text{sampling frequency}}{\text{FFT Length}}$$

$$\text{frequency resolution} = \frac{\text{sampling frequency}}{2048}$$

frequency resolution = 16kHz/2048 = 8 Hz

Frequency resolution of this system is 8Hz. After calibrating with the sinusoidal measurements, it is now ready to find the frequency contents in the input signal. The Fourier Transform spectrum is calibrated using the RIGOL DS 5102CA, two channel digital storage oscilloscope. The whole circuit diagram for microcontroller-based spectrum analyzer is shown in Figure 5. Figure 6 shows photograph of sine wave input signal and its Fourier spectrum (f = 300Hz, V_{pp} 1.4V) display of constructed analyzer and display of digital oscilloscope.

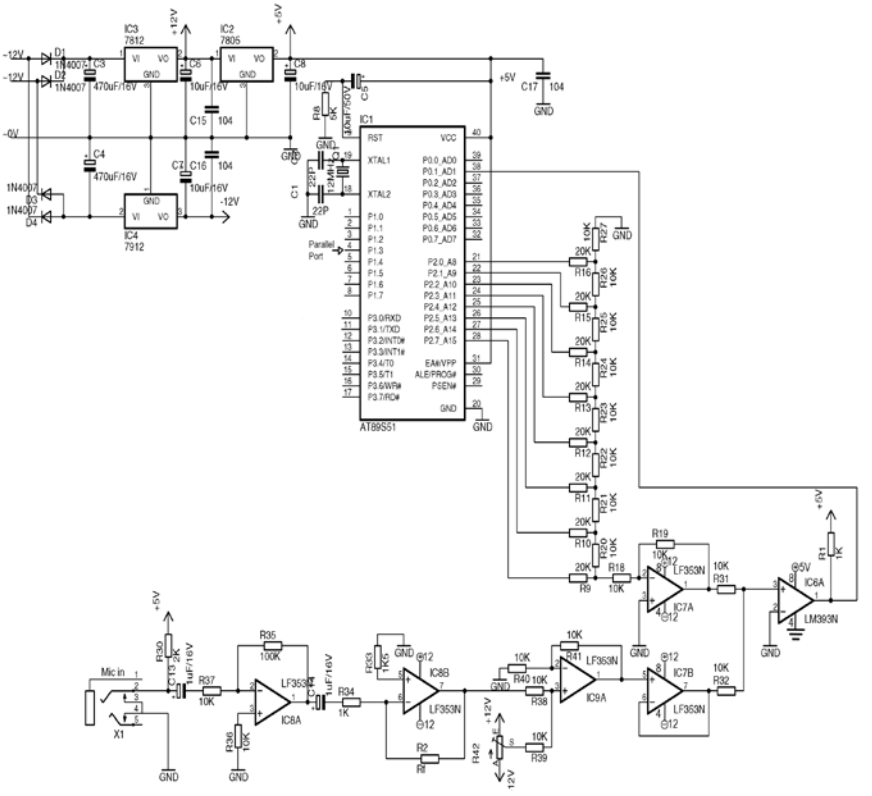

Figure 5. The whole circuit diagram for microcontroller-based spectrum analyzer

Discussions

The spectrum analyzer has been constructed using readily available electronic components. The basic idea of parallel processing system is introduced in this work. While the microcontroller is doing analog to digital conversion, personal computer processes these data and makes the digital signal processing. PC monitor is used to make the best presentation for the

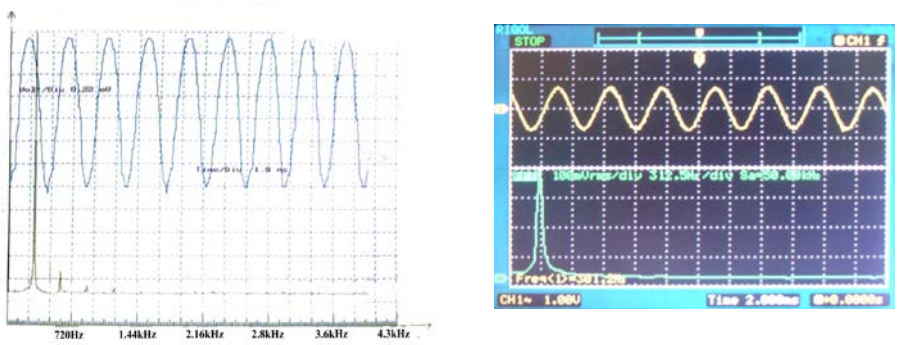

(a) (b)

Figure 6. Photograph of sine wave input signal and its Fourier spectrum (f = 300Hz, V_{pp} 1.4V) (a) display of constructed analyzer (b) display of digital oscilloscope

shape of signal and spectrum and also used for the user interface. Real time data acquisition is also available in this system. Long time data storage can be obtained in this work. Then the transform of Casio tones of C, D, E, F, G, A, B, C' and voice of women and men are also shown in Figure 7 (a) and (b) and Figure 8(a) and (b). Figure 9 (a) shows the array of components and inter connections between Printed Circuit Boards (PCBs). The whole microcontroller-based spectrum analyzer system when it is operating is shown in Figure 9 (b).

Quantization and Resolution of the System

The constructed 8-bit ADC has the resolution of 1/255 x its maximum voltage (5V) = 0.02V. The quantization level of the system is 0.02V. The resolution of the ADC can be increased by increasing bits of ADC. If one uses 16 bits ADC the resolution is down to 1/65535 of its maximum.

The analog output from the microphone is 120 mV and pre conditioning was performed with operational amplifier. To obtain the desired accuracy it is the one of important parts of the system. For higher performance applications some form of special amplifier, instrumentation amplifier and filtering are needed to use.

Observation on Fourier Spectrums and Harmonics

By using the constructed spectrum analyzer fundamental frequencies and overtones were observed on the graphic screen for various notes C, D, E, F, G, A, B and C´ of Casio MT45 (Electronic Musical Instrument). One can also determine the ratio of their contribution. Signals were simultaneously inputted to personal computer, 50 MHz analog oscilloscope (Yokogawa AL510) and 100 MHz digital oscilloscope (Rigol DS5102CA). The signals and its spectrums can be observed on the PC monitor as well as on the reference oscilloscopes.

And voices of man1, man2, man3 and voices of woman1, woman2, woman3 are analyzed and compared when they said the same word "**Hello**". It is found that the fundamental frequency of woman is greater than that of man.

Conclusion

Microcontroller based spectrum analyzer that can measure the minimum frequency 20 Hz up to maximum frequency 8 kHz was designed, programmed and developed. The present design is intended to analyze the frequencies of voice of women and men. Since the system can perform lower frequency range, it is suitable for our work. Sound of women and men are analyzed. Voice synthesizer and voice recognition process can be made for further research. And then we can also develop the two dimensional Fourier transforms for pictures, signatures and human faces from these analyzing processes and we can carry on the pattern recognitions.

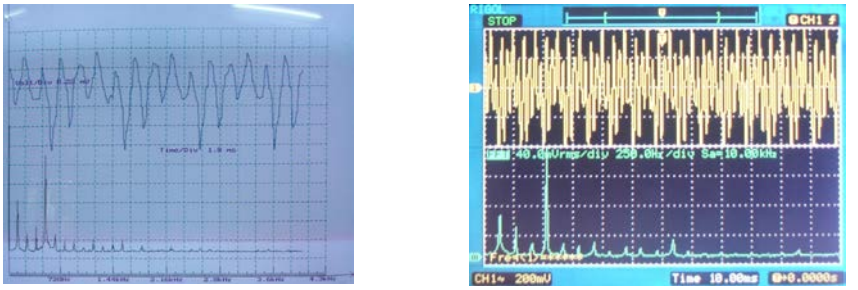

(a) (b)

Figure 7. Photograph of input signal and Fourier Spectrum of C note of Casio MT45 (a) display of constructed analyzer. (b) display of digital oscilloscope

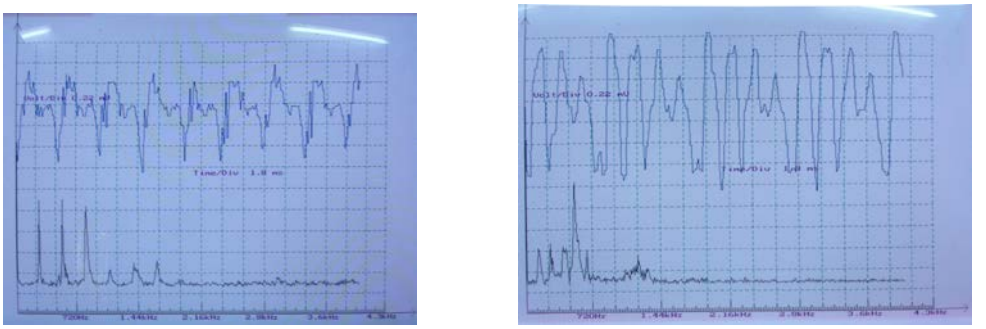

(a) (b)

Figure 8. Photograph of Time domain signal and frequency domain spectrum for voice of woman 1 (b) man1

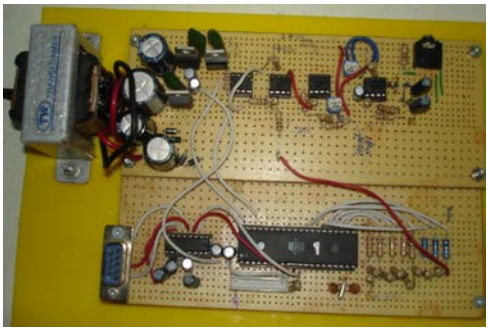

(a)

(b)

Figure 9. (a) Photograph of the array of the components and interconnections between PCBs (b) The whole system of microcontroller based spectrum analyzer

Acknowledgements

I would like to give my heartfelt thanks to Professor Dr. Thura Oo, Rector, Monywa University, for his permission to do this work.

References

Floyd T. L. (2007).Electronic Devices, 7th Edition. Prentice - Hall International Inc, New Jersey.

Hutchings H. (1995) "*Interfacing with C*" (London : Butterworth).

Li Tan (2008) DeVry University Decatur, Georgia, “Digital Signal Processing Fundamentals and Applications.

Tom Duncan, (1997). “Success In Electronics”, 2nd Edition, John Murray ltd. Ad.www.all.datasheet.com/at 89C51.

https://www.ti.com, LF353N.

Encapsulation of Oil Soluble Food Colorant

Soe Soe Than*

Abstract

Spray drying is considered as an appropriate technique to convert fluid foods to powders enabling encapsulation of color materials. In this study, several types of coating materials such as gelatin, soyprotein, gum arabic, albumin, and pectin were used for encapsulation of oil soluble colorant, curcumin. Spray drying of emulsion solutions was carried out to obtain powder form of encapsulated curcumin products. Color stability and powder functionalities such as dispersibility, solubility, and sedimentation of the encapsulated products were evaluated. Based on the color stability and powder functionalities under different conditions of pH and UV light, gum arabic represented the most suitable coating material for curcumin.

Keywords: curcumin, coating materials, encapsulation, spray drying

Introduction

Both synthetic and natural food colors play a significant role in enhancing the aesthetic appeal of processed foods as well as in food manufacture, storage and quality control (Ghorpade et al., 1995). Natural colorants are attractive colors for use in the food industry. Annatto and turmeric are widely used in everyday foodstuffs among five natural colors. Oil soluble colorant, curcumin (E100) is the fluorescent yellow extract of the dried, ground rhizome of turmeric (*Curcuma longa*). It is widely used in dairy and flour confectionery industries, sugar and frozen products and desserts (Hendry and Houghton, 1997). Curcumin has poor stability and low aqueous solubility, especially insoluble in acidic solutions. It is unstable in basic pH solutions and breakdowns easily (Wang et al., 2009). Due to undesirable and harmful toxicological effects of synthetic colorants, natural colorants are greatly demanded. The natural pigments are subjected to adverse physical and chemical conditions during processing that cause their partial degradation. Processing often results undesirable changes in color and thus diminishes the visual perception of foods (Ghorpade et al., 1995). Being confronted with the various drawbacks of some commercial

* Professor, Department of Industrial Chemistry, University of Yangon

natural food colorants (instability to light, heat, or adverse pH), microencapsulation provides such protection as a sophisticated technique (Beatus, Raziel and Rosenb (1985). Microencapsulation consists of packaging liquid droplets or solid small particles in individual shells as known as walls. Proper choice of wall material and structure makes possible a variety of service conditions from controlled gradual release of capsule content under specific conditions to retention of the capsule intact until its final use when the capsules are dissolved or raptured (Ré, 1998). Different biopolymers such as carbohydrates, proteins and lipids are used as coating materials. Carbohydrates are suitable coating materials under high temperature process while lipids and proteins can be melt and be denatured when subjected to high temperature (De Boer et al., 2019). Spray drying offers the attractive advantages of producing microcapsules in a relatively simple continuous processing operation involving atomization of liquid feed stocks, hot air flowing and evaporation of water (Ré, 1998).

The present research was focused on encapsulation of curcumin with different coating materials. Spray drying of encapsulated emulsions was carried out for dried encapsulated products.

Materials and Methods

Materials

Curcumin (CDH Ltd., India) was used as the core material. Soyprotein isolate (ADM company, USA), pectin (DCH Ltd., India), albumin (Aqua Phoenix Scientific, Germany), gelatin (Merck, Germany) and gum arabic (Fisher Scientific, USA) were used as the coating materials.

Methods

Preparation of Curcumin Microcapsules

The flow diagram for the preparation of curcumin microcapsules is shown in Figure 1. Curcumin (2%, 10%) was dissolved into tween 80 with the ratio of 1:4 as the oil phase. The water phase of coating material was also prepared by dissolving gelatin (1:5 ratio relatively to natural colorant) into 800 mL of distilled water. Emulsions were prepared by the addition of the oil phase of core material into the water phase of coating materials. The mixture was homogenized using ultra turrax (IKA, T25 digital, USA) for 10 min. The emulsions were spray dried in a laboratory type spray dryer with

drying chamber 140 mm dia and length of 600 mm, spray nozzle of 0.7 mm, keeping air inlet temperature of 160-180°C and outlet air temperature of 60-65°C. The color powders were collected from the base of the cyclone. Likewise, encapsulation with the other coating materials such as soyprotein isolate, pectin, albumin and gum Arabic was conducted.

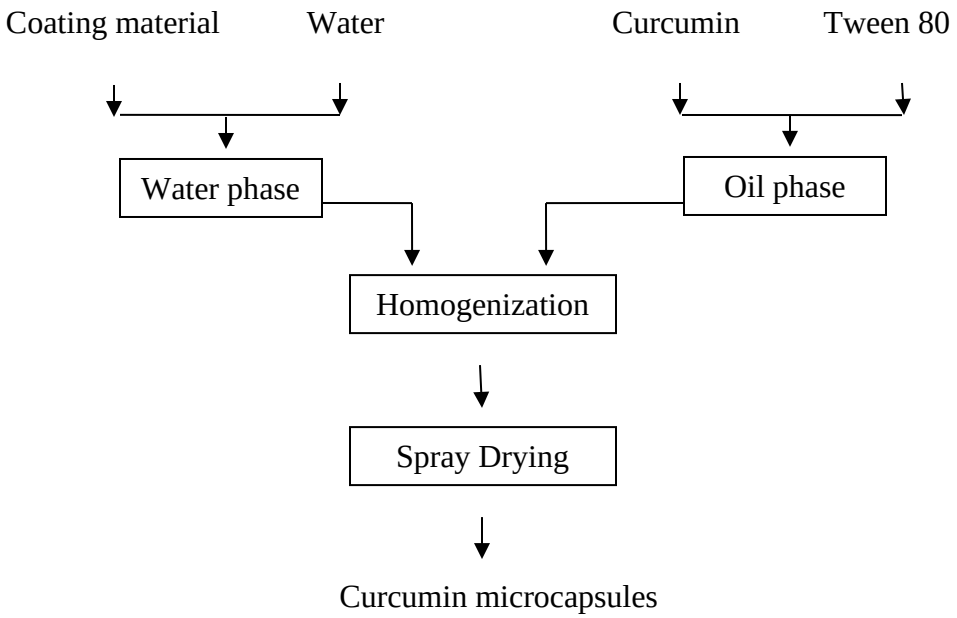

Figure 1. Process Flow Diagram for the Preparation of Curcumin Microcapsules

Evaluation of Color Stability of Encapsulated Curcumin Products

The color stability of encapsulated curcumin products at different pH and under UV light was studied using an instrumental colorimeter (Minolta meter, CR-310, L* a*b* color system). The colorimeter represents the color of the samples in terms of three dimensional, L, a, b color space system where + L is white direction, - L is the black direction, + a is the red direction, - a is the green direction, + b is the yellow direction, - b is the blue direction and the color values are expressed with reference to the illuminant D65 and a visual angle of 2°.

Effect of pH on Color Stability

Encapsulated sample 1 g was dissolved in 100 mL of distilled water using a magnetic stirrer and allowed to stand for 24 hr. The color solutions were adjusted to pH 3 and pH 5 using hydrogen phosphate solution. pH was measured using Benchtop pH meter (EUTECH pH 700). Changes in color were measured at 24 hr interval for 7-day period. The results were expressed as lightness (L value) and brightness or chroma C* ($C^* = \sqrt{a^{*^2} + b^{*^2}}$) where C* is the attributes of color perception by means of which an object is exactly judged for its location in the color space.

Effect of UV light on Color Stability

Encapsulated sample 0.4 g was dissolved in 40 mL of agar solution at 60 ± 1°C and poured into pertridishes. After hardening, the plates were exposed to UV light (UV light, 254 nm, UV output 8 W and intensity 90µWcm^{-2}, Sylvania, Japan). Average distance from dishes to light source was 310 mm. Changes in color were observed at one hr interval for a 12 hr period. Likewise, 0.04% of curcumin solution was also prepared in agar plates and its color stability was observed. The observed color values were presented as L and C* values.

Evaluation of Functionality of Encapsulated Curcumin Products Dispersibility, Solubility and Sedimentation

Encapsulated sample 0.25 g was dissolved into 50 mL of distilled water using a magnetic stirrer at 25 ± 1°C, 40 ± 1°C, and 65 ± 1°C respectively. The powder functionalities such as dispersibility, solubility and sedimentation were observed. The solubilities of encapsulated color products are represented as very good (VG) (soluble between 0 and 2 min), good (G) (soluble between 3 and 8 min), Fair (soluble between 5 and 10 min), and Poor (soluble more than 10 min).

Results and Discussion

Pure 95% curcumin cannot be directly used in food industry since it is insoluble in water and has poor solubility in other solvents. Generally, curcumin is used as its convenient form with a carrier (Hendry & Houghton, 1996). Spray-dried curcumin products containing 2% and 10% curcumin were processed with gelatin, soy protein isolate, gum arabic, albumin and pectin as the carrier or coating materials in this work.

Figure 2 to Figure 5 indicate the color values of encapsulated 2% and 10% curcumin products at different pH of pH 3 and pH 5 as the form of L (lightness) and C* (hue) values. It was observed that soyprotein isolate encapsulated curcumin products revealed their good stabilities under acidic condition especially, at pH 3 for the lightness (L value) until the 6-day storage period. As regards in hue (both a color and a shade of a color), soyprotein isolate also kept good retention of hue until the 6-day storage. At pH 5, the instability was shown by the lightness of the other coating materials while good retention of color shade belongs to all encapsulated products. Their L values decreased in the decreasing order: green> yellow> red. Color shade of curcumin at pH 3 is lemon yellow. Curcumin gives a lemon yellow color in acidic media with a distinct green shade. As the pH increases, the green shade becomes less distinct (Hendry & Houghton, 1996). Generally, encapsulated curcumin products in acidic media showed their keeping color shades of curcumin during 7-day storage at pH 5. In addition, the color solubility of solubilized form of curcumin in different pH 3 and pH 5 was observed. It was also found that more water dispersible form of encapsulated curcumin products gave a slight decreased stabilized position in color space in acidic media which agreed with the data: curcumin as suspended pigment is more stable than the solubilized color (Knewstubb & Rayner, 1991).

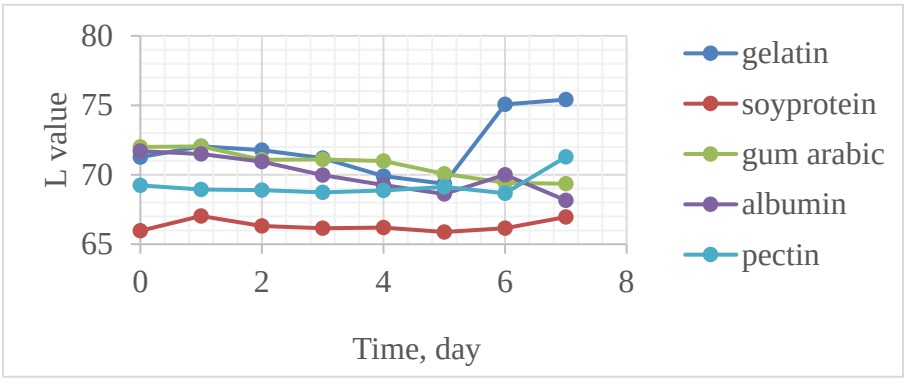

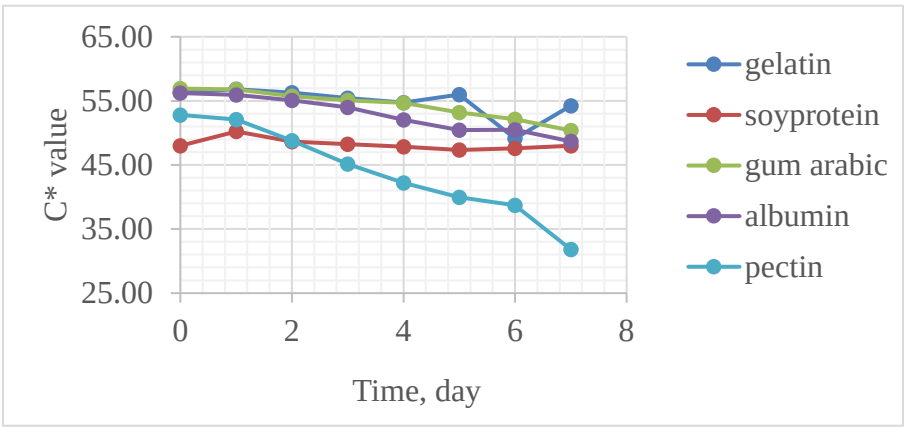

Figure 1. Color Values of Encapsulated 2% Curcumin Products at pH 3

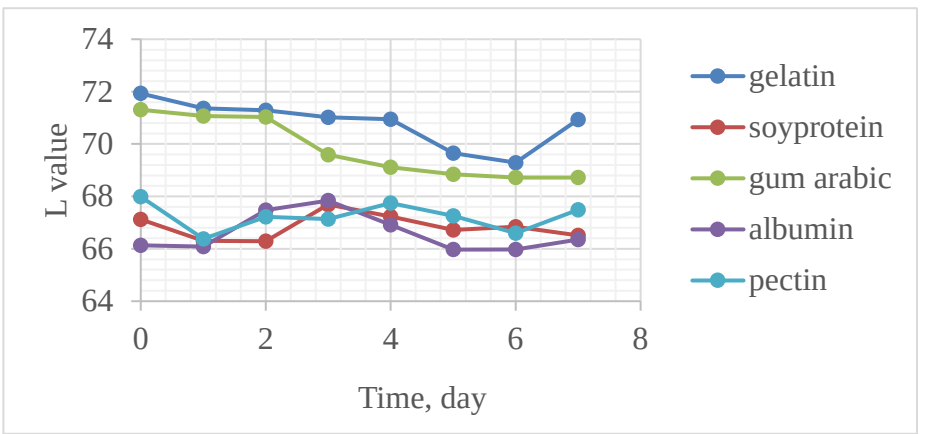

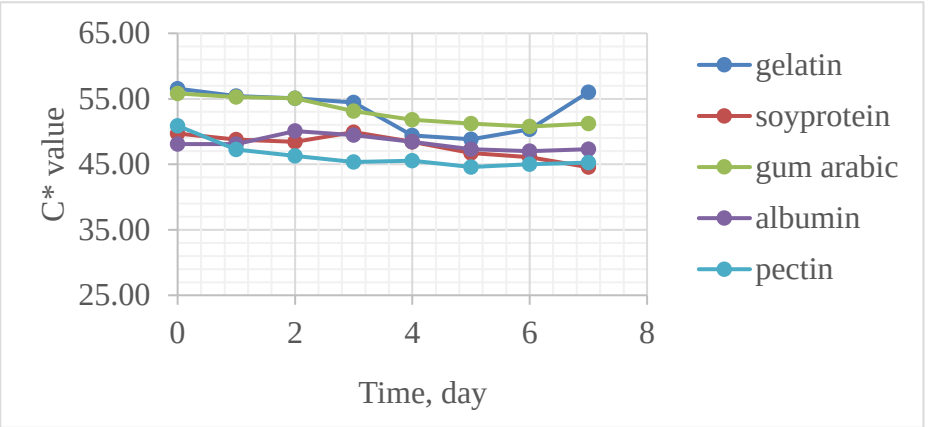

Figure 2. Color Values of Encapsulated 2% Curcumin Products at pH 5

Figure 6 and Figure 7 represent the color values of encapsulated curcumin products exposed to UV light. Table 1. also shows the change in color during the exposure to UV light. Their lightness in color decreased in the decreasing order: green>yellow>red. When the color a values increased slightly, the color b values decreased. It meant that with decreased lightness, color negative a values of encapsulated 2% and 10% curcumin products moved to color positive a values according to their loss of color shade (C* values). It can also be predicted that the direction of color change depends on its individual spectral energy distribution and the color intensities of encapsulated products. The loss of color (fading of color shade) in encapsulated products was presented by the change in color a and b values as shown in Table 1.

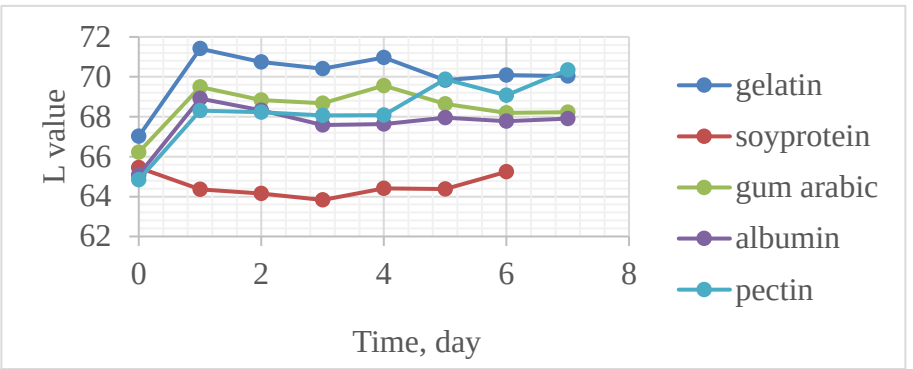

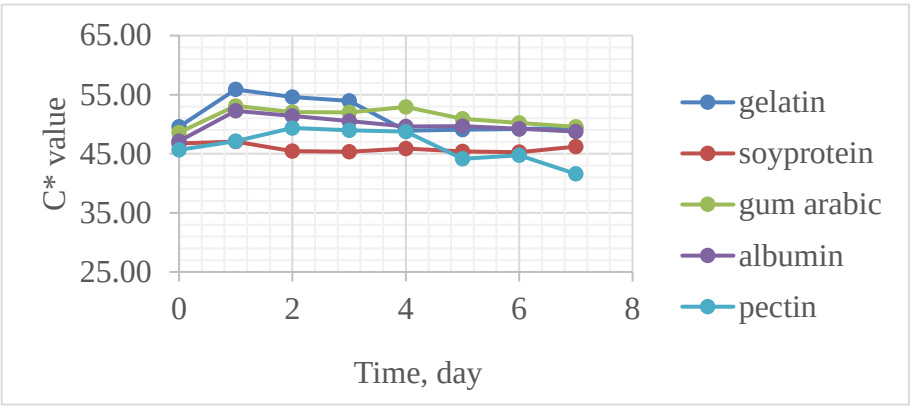

Figure 3. Color Values of Encapsulated10% Curcumin Products at pH 3

Table 2 and Table 3 describe the functionalities of encapsulated curcumin products. It indicated that the encapsulated curcumin products had very good dispersibility. No sedimentation was observed for gelatin, gum arabic, and pectin encapsulated 2% curcumin products, but some sedimentation took place for encapsulated 10% curcumin products. Diffusional release depends upon the possible interactions between the core and the wall material and the rate at which the active core is able to pass through the outer wall. Core diffusion rate varies according to the characteristics of the microcapsules wall such as chemical structure, thickness. pore size and surface integrity. High retention of core material during processing relies on successful spray drying microencapsulation (Ré, 1998). In this work, the amount of coating materials ranged from 50 to 54% and the encapsulation efficiency was influenced by the composition of core to wall (coating material). Among the encapsulating agents, gum arabic was the most appropriate material for oil soluble colorant curcumin with a quality of not only dispersibility but also solubility in water aside from no precipitation or no sediment in acidic media.

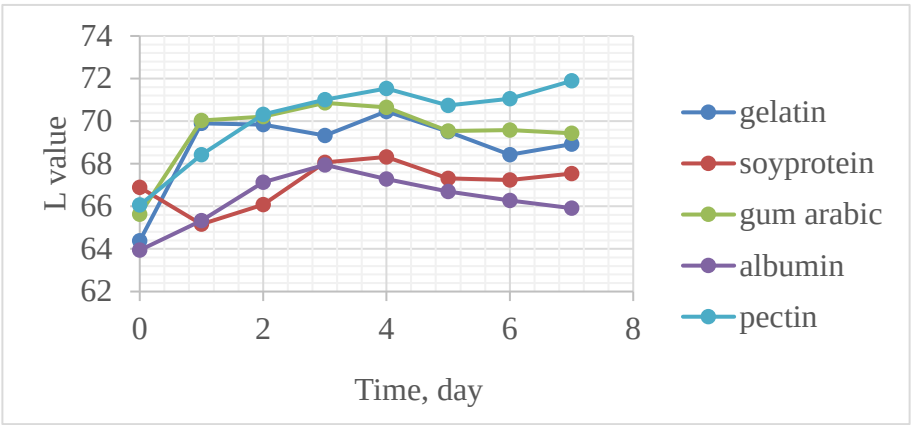

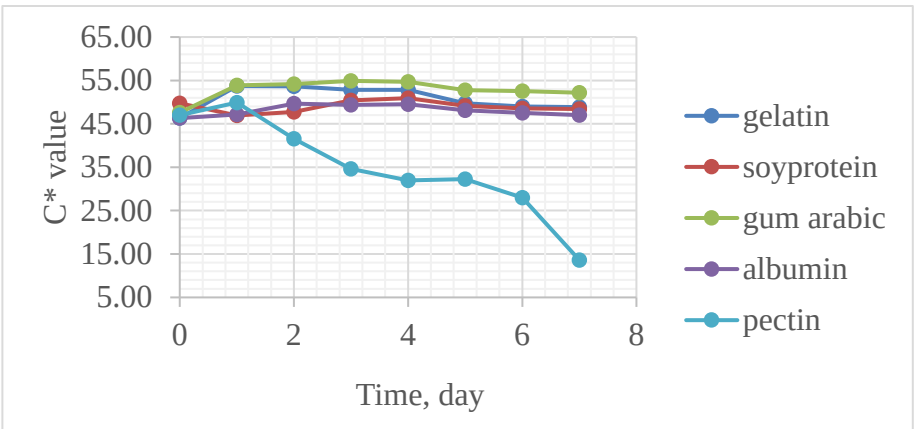

Figure 4. Color Values of Encapsulated10% Curcumin Products at pH 5

Gum arabic has been the encapsulating agent of choice for many years due to its specific characteristics like film forming and emulsifying properties. It composes of D-glucuronic acid. L-rhamnose. D-galactose and L-arabinose with about 5% protein (Ré, 1998). The protein fraction of gum arabic acts as an interface between oil and water, forming the film around oil droplets. That has resulted from the highly branched arabinogalactan-protein structure containing both protein and polysaccharide moieties. A stabilization mechanism is obtained from the polysaccharide-protein system that leads the polysaccharide onto the surface of the oil droplet and the hydrophilic carbohydrate chains by forming a thick charged layer (Nakamura, 2006; Adamiec et al., 2012). Gum arabic is soluble in water

and widely used in food industry as stabilizer. It was also recommended for effective encapsulating agent for better stability (De Boer et al., 2019).

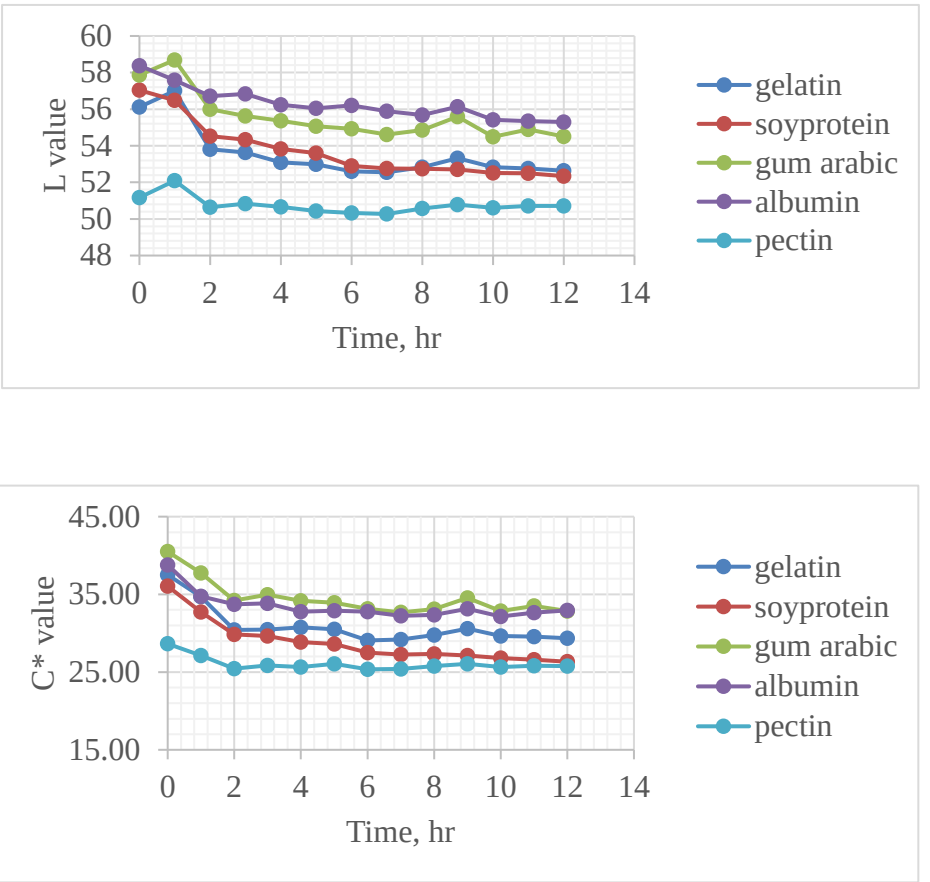

Figure 5. Color Values of Encapsulated 2% Curcumin Products Under UV Light

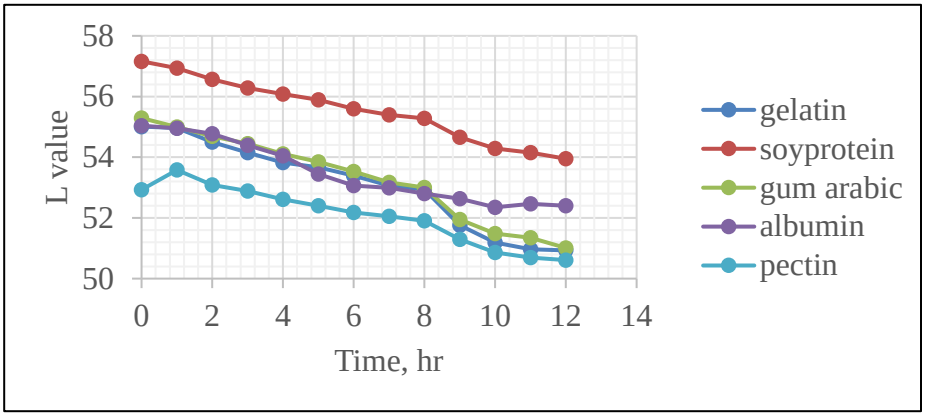

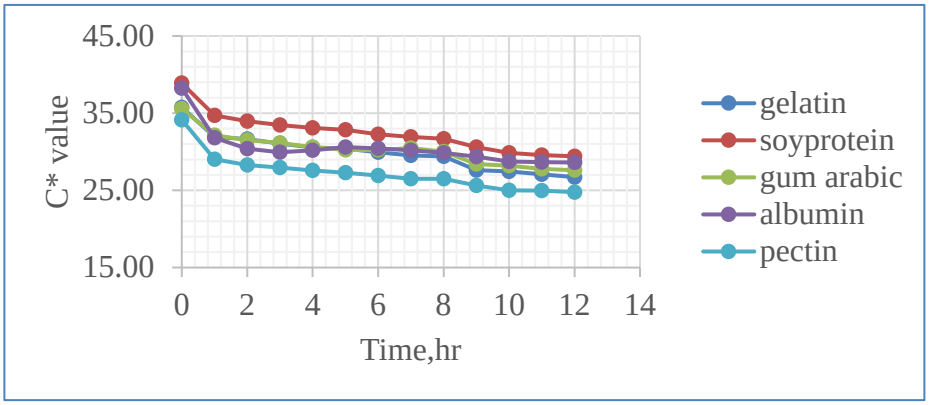

Figure 6. Color Values of Encapsulated 10% Curcumin Products Under UV Light

Table 1. Change in Color Under UV Light

	Color values before exposure		Color values after 12 hr exposure	
	a	b	a	b
0.04% curcumin (suspended form)	5.36	33.61	6.41	26.87
0.4% encapsulated curcumin products (dispersible form)	4.23 -6.96	33.65-38.65	4.93-8.39	23.44-29.00

Table 2. Functionality of Encapsulated 2% Curcumin Products

Temperature, °C	Functionality	2% Curcumin with				
		Gelatin	Soy protein	Gum arabic	Albumin	Pectin
25 ± 1	Dispersibility	VG	VG	VG	VG	VG
	Solubility	poor	Fair	VG	VG	Fair
	Sedimentation	+	+	-	-	-
40 ± 1	Dispersibility	VG	VG	VG	VG	VG
	Solubility	VG	Fair	VG	VG	Fair
	Sedimentation	-	+	-	-	-
65 ± 1	Dispersibility	VG	VG	VG	VG	VG
	Solubility	VG	Fair	VG	Poor	VG
	Sedimentation	-	+	-	+	-

(+) Sediment fall out (-) No sediment

Table 3. Functionality of Encapsulated 10% Curcumin Products

Temperature, °C	Functionality	10% Curcumin with				
		Gelatin	Soy protein	Gum arabic	Albumin	Pectin
25 ± 1	Dispersibility	VG	VG	VG	VG	VG
	Solubility	Fair	VG	VG	VG	Fair
	Sedimentation	+	+	-	-	-
40 ± 1	Dispersibility	VG	VG	VG	VG	VG
	Solubility	VG	VG	VG	VG	G
	Sedimentation	+	+	-	+	-
65 ± 1	Dispersibility	VG	VG	VG	VG	VG
	Solubility	VG	VG	VG	Fair	G
	Sedimentation	+	-	-	+	-

(+) Sediment fall out (-) No sediment

By encapsulating of oil soluble colorant curcumin, more water dispersible form of encapsulated color products was observed for 2% and 10% curcumin. Encapsulated 2% curcumin products had still visual intense color even though the large range of coating material and emulsifier was used in emulsions.

Conclusion

Oil soluble colorant, curcumin (suspended in water) was converted to water dispersible colorant as improved solubilized form by spray drying microencapsulation. Encapsulated curcumin products with several coating materials displayed as solubilized color products and their color retention was gauged to some extent. Certain color stability for 7-day storage in acidic media and 12 hr exposure to UV light was evaluated by observing tri-stimulus color values of L and C*. Gum arabic showed a suitable capsule material based on the powder functionalities.

Acknowledgement

The author is grateful to Carl Duisberg Gesellshaft e.V for scholarship support to conduct this research work at the Institute of Food Technology, Bonn University.

References

Adamiec. J, Borompichaicharkul. C, Srzednicki. G, Panket. W, Piriyapunsakul. S and Zhao. J, (2012). Microencapsulation of Kaffir Lime Oil and Its Functional Properties, Drying Technology, 30, 914-920.

Beatus. Y, Raziel. A and Rosenb. M, (1985). Spray Drying Microencapsulation of Paprika Oloresin, Lebensmittel Wissenshaft & Technologie, 18, 28.

De Boer. F. Y, Imhof. A, and Velikov. K. P, (2019). Ecapsulation of Colorants by Natural Polymers for Food Applications, retrieved from https:// doi.org/ 10.1111/cote.12393

Ghorpade. V. M, Deshpande S.S, and Salunkhe, D.K, (1995). Food Colors, Food Additive Toxicology, 179-227.

Hendry G. A. F, and Houghton J.D, (1996). Natural Food Colorants, second edit., 47-51.

Knewstubb. C. K, and Rayner. P.B, (1991). The practicalities of Using Natural Food Colors, Food Technology International, 207-208.

Nakamura. A, Yoshida. R, Maeda. H, Corredig. M, (2006). Soy Soluble Polysaccharide Stabilization at Oil-Water Interfaces, Food Hydrocolloids, 20, 277-283.

Ré. M. I, (1998). Microencapsulation by Spray Drying, Drying Technology, 16:6, 1195-1236, DOI: 10.1080/07373939808917460

Wang. Y, Lu. Z, Wu. H and Lv. E, (2009). Study on the Antibiotic Activity of Microcapsule Curcumin against Foodborne Pathogens, International Journal of Food Microbiology, 136, 71-74.

Ultrasound Image Edge Detection Using Python

Myat Su Hlaing[1] & Soe Mya Mya Aye[2]

Abstract

Edges occur in images with various resolutions or scales and represent transitions of different degrees, or gradient levels. Edge detection techniques draw attention of many researchers because they can be used in several computer vision and image processing applications such as object recognition, semantic content description, image segmentation and image compression. In this research, edge detection is performed in ultrasonic images with the help of Anaconda Navigator python3 language. Edge detection results with Robert Edge detection, Sobel edge detection, Canny Edge Detection and Prewitt edge detection are demonstrated with the comparison of elimination performance on different image sizes. Experimental results suggest that Sobel edge detector gives the best edge detection. The experimental result and the implications drawn in this paper will benefit the medical development in the field of ultrasound imaging technology.

Keyword: edge, edge detection, ultrasound images

Introduction

An image can be defined a collection of pixels that are generally sampled into a rectangular array. A monochrome image is represented as a discrete matrix F:

$$F = \{f(x, y) \mid x = 0,...N-1, y = 0,...M-1\} \qquad (1)$$

Images are represented at spatial coordinates that are corresponded to the sample index (x,y). It can be denoted by the function f(x,y), where x is the column number and y is the row number. An example of an image matrix is shown in “Figure 1”.

[1] Associate Professor, Department of Computer Studies, University of Yangon
[2] Professor(Head), Department of Computer Studies, University of Yangon

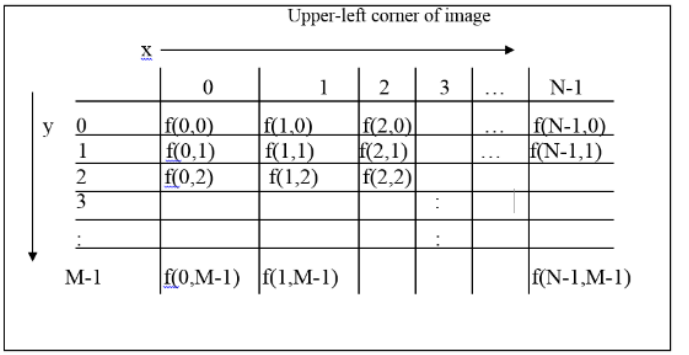

Figure 1. Image matrixes

Ultrasound Imaging

Ultrasonic image is a sonography that uses high-frequency (~1–10 MHz) sound waves. Their echoes produce images to demonstrate organ movement in real time. Ultrasound images are constructed by calculating the time taken for ultrasound pulses to travel into the body and return after reflections of a tissue surface. A typical pulse, just over 1μs in duration with a frequency of 5MHz, contains 5 cycles of the wave as shown in "Figure 2". Nimrod M. T told that ulses can be separated by perhaps 1ms, resulting in a pulse repetition rate of 1000 Hz; they travel through soft tissue at a speed of about 1540ms^{-1} compared with the speed of sound in air of about 330ms^{-1}. Kutz,M. and Thomenius, K expressed that a typical ultrasound system is shown in "Figure 3". Ultrasound images are the most widely used medical images varying from confirming and dating a pregnancy to diagnosing certain conditions.

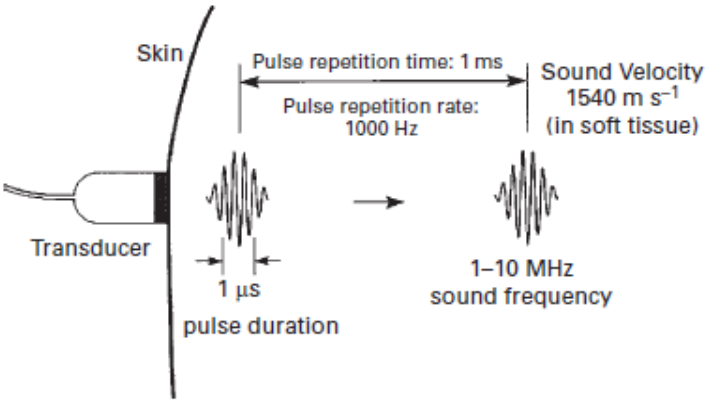

Figure 2. Schematic diagram of a typical clinical ultrasound beam

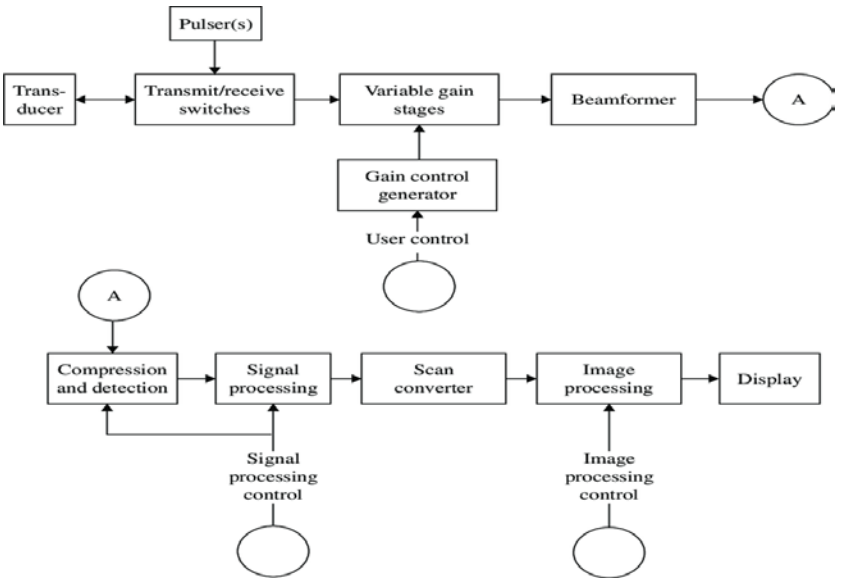

Figure 3. Block diagram of a typical ultrasound system

Edge Detection

Edges or edge points in an image are the points where changes significantly occur. Gonzalez, R.C and Woods. Proposed that edges present critical changes of intensity in an image that helps with segmentation and object recognition. An edge has both magnitude and direction. Edge detection is a fundamental process for low-level image processing. Good edge detection is necessary for higher level image processing to distinguish the boundaries of regions in an image based on image properties such as intensity and texture. Mehena,J. proposed that the steps of edge detection. They are smoothing, enhancement, detection and localization.

Edge Detection Techniques

The quality of edge detection depends on several conditions such as lighting, the presence of objects of similar intensities, thickness of edges in the scene and noises. Edge detection is detecting the presence of intensity transitions among adjacent pixels and their pixel locations in a sub-window. Among several edge detection techniques, Roberts, Sobel, Prewitt and Canny edge detector techniques are used in this research.

Roberts Edge Detector

Roberts edge detector is typically used to find the approximate absolute gradient magnitude at each point of an input grayscale image. It performs a 2-D spatial gradient measurement on an image and emphasizes regions of high spatial frequency that correspond to edges. In this technique, diagonal edge gradients can be obtained by forming running differences of diagonal pairs of pixels. The Robert crosses difference operators are defined in magnitude form as follows:

$$G(x,y)=|G1(x.y)+G2(x,y)| \quad (2)$$

In square root means form it can be defined as:

$$G(x,y)=\{|G1(x.y)|2+|G2(x,y)|2\}2 \quad (3)$$

Where

$$G1(x,y) = F(x+1, y+1) - F(x,y) \quad (4)$$

And

$$G2(x,y) = F(x, y+1) - F(x+1, y) \quad (5)$$

G1 and G2 are two images with at each point contain the horizontal and vertical derivative approximations.

Sobel Edge Detector

Sobel operator is typically used to find the approximate absolute gradient magnitude at each point in an input grayscale image by creating image emphasizing edges. Sobel edge detector detects vertical and horizontal edges separately and these directional edges are combined finally. Like the other gradient operator, Gx and Gy can be implemented using convolution masks where two masks are separately convoluted with image. The magnitude and direction of edge is calculated by using convolution results of two masks. These are as follows:

$$G = \sqrt{G^2x + G^2y} \quad (6)$$

$$\text{Arg}(G)=\tan^{-1}(|Gy|/|Gx|) \quad (7)$$

Prewitt Edge Detector

Prewitt operator is a discrete differentiation operator that computes an approximation of the gradient of the image intensity function. The operation Prewitt detector is based on convolving the image with a small, separable, and integer valued filter in horizontal and vertical direction. Therefore, it relatively inexpensive in terms of computations. Prewitt operator is limited to 8 possible orientations; however experience shows that most direct orientation estimates are not much more accurate.

$$G(x,y)=\{|G_1(x.y)|^2+|G_2(x,y)|^2\}^2 \quad (8)$$

with

$$G_R(x,y)=1/(k+2)[(A_2+KA_3+A_4)-A_0+KA_7+A_6)] \quad (9)$$

And

$$G_C(x,y)=1/(k+2)[(A_2+KA_1+A_2)-A_0+KA_5+A_4)] \quad (10)$$

Canny Edge Detector

In Canny edge detector, the detection is performed by finding the image gradient to highlight regions with high spatial derivatives. Canny edge detection algorithm is given by the following steps. Ruba, A.was found that the best algorithm for displaying edge and removing Gaussian noise is the Canny algorithm after using the median filter.

Step 1: Convolve the image with a Gaussian kernel G.

Step 2: Compute the gradient ∇(G*f) at each pixel.

Step 3: If the gradient is nonzero, compute f, the second derivative of the smoothed image in the direction of the gradient. $D\frac{\nabla G*f}{\|\nabla G*f\|}$

Step 4: Detect the pixels where f changes the sign, these pixels are edge points. $D\frac{\nabla G*f}{\|\nabla G*f\|}$

Implementation

For this research, Anaconda Navigator Python3 was used to test the edge detection techniques in ultrasound images. Python language is a powerful scripting language that can be used for image processing. Juypter Notebook is launched while detecting edge in conventional 2D ultrasound images and 3D ultrasound images. Python Standard Library and Matplot library are used for visualization. The implementation used Standard Skimage library, to convert RGB image to gray image. Standard Scipy library provides operations on n-dimensional NumPy arrays. Skimage library is used to detect edges in the images. Figure 4 shows the architecture of the system.

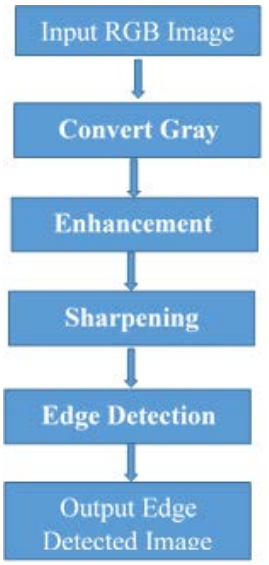

Figure 4. Architecture of Edge Detection system

There are six steps for the tasks of image edge detection system. They are:

Step 1: Read Input image

Step 2: Convert RGB image to Gray image

Step 3: Make enhancement image

Step 4: Make sharpening image

Step 5: Detect Edge among different detection techniques

Step 6: Output the resultant edge detected image.

Step1: Reading input image

Matplot library is used to import ultrasound image. The submodule *pyplot* provides reads the imported image. The syntax for reading image is shown in the following line.

```
import matplotlib.pyplot as plt
image =plt.imread('input_img.jpg')
```

Step 2: Convert RGB image to Gray image

Skimage library is used to convert the imported ultrasound image to gray image. The submodule *rgb2gray* is used to convert color images into gray image. The syntax for converting color image is shown in the following line.

```
from skimage.color import rgb2gray
image=rgb2gray(image)
```

Step 3: Make enhancement image

If the ultrasound image has noises, the image is filtered and enhanced. *Scipy* library is used for Gaussian Image filtering and the blurred image is enhanced in that way. The syntax for Gaussian filtering image and resultant filtered image are shown in the following line.

```
from scipy import ndimage
blurred_f=dimage.gaussian_filter(image,3)
```

Step 4: Make sharpening image

If the ultrasound image has blurred image, the image is sharpened to get better detection. Scipy library is used for sharpening the blurred image. The syntax for filtering image and resultant filtered image are shown in the following line. The value of alpha may change for better sharpening.

```
filter_blurred_f= ndimage.gaussian_filter(blurred_f, 1)
alpha =25
sharpened=blurred_f+alpha*(blurred_f- filter_blurred_f)
```

Step 5: Detect Edge on different edge detection techniques

Skimage library is also used to import edge operators to detect edge of ultrasound image. The submodule *Roberts* and *Sobel* are used to detect edges of gray image. *Robert* edge detection algorithm compute approximations of the gradient by the following syntax. *Sobel* edge detection algorithm also compute approximations of the gradient by the following syntax.

```
from skimage.filters import roberts, sobel
sedge_roberts = roberts(sharpened)
sedge_sobel = sobel(sharpened)
sedge_prewitt = prewitt(sharpened)
```

The submodule is used to detect edges of gray image by *canny* sharpening algorithm. Canny edge detection algorithm also compute approximations of the gradient by the following syntax.

```
from skimage import feature
sedge_canny= feature.canny(sharpened)
```

Step 6: Output the resultant edge detected image.

For the resulting visual image, *matplotlib library* is used to provide the visual output of images.

```
import matplotlib.pyplot as plt
fig, ax = plt.subplots(ncols=5, sharex=True, sharey=True, figsize=(20,10))
ax[0].imshow(image, cmap=plt.cm.gray)
ax[0].set_title('Original Image')
ax[1].imshow(edge_roberts,cmap=plt.cm.gra)
ax[1].set_title('RobertsEdge Detection')
ax[2].imshow(edge_sobel, cmap=plt.cm.gray)
ax[2].set_title('Sobel Edge Detection')
ax[3].imshow(edge_canny,cmap=plt.cm.gray)
ax[3].set_title('Canny Edge Detection')
ax[4].imshow(sedge_prewitt)
ax[4].set_title('Prewitt Edge Detection by Sharpening')
```

Result and Discussion

Edge detection techniques are applied on 3D ultrasound images and 2D ultrasound image of broken heal images. Edge detection results in Robert Edge detection, Sobel edge detection, Canny Edge Detection and Prewitt edge detection are demonstrated. The resulting edge detected images are shown in the following Jyupter page. It is found that enhanced and sharpened image achieved better quality images. “Figure 5” shows Edge Detection of 3D ultrasound image. Edges of ultrasound heal broken bones are shown in “Figure 6”. Those figures describe better detected images among different edge detection techniques.

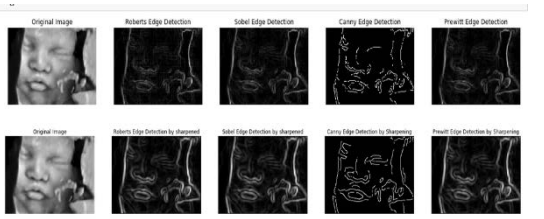

Figure 5. Edge Detection of 3D ultrasound image

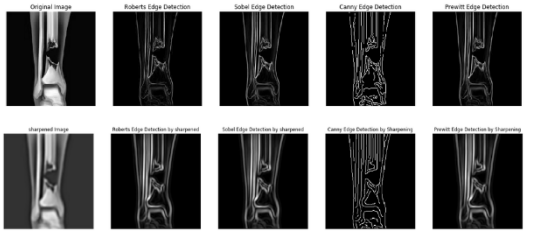

Figure 6. Edge Detection of 2D ultrasound image

In this paper, 2D ultrasound image and 3D ultrasound image are tested to evaluate the impact and the performance of the edge detection techniques. Two important parameters of Peak signal-to-noise ratio (PSNR) and Mean Squared Error (MSE) are measured to measure the quality of different detected images. Table 1 shows PSNR value of 3D Ultrasound image of different detection type among different techniques and MSE values are shown in Table 2.

Table 1. PSNR of Edge Detection techniques on different Detection type

Techniques	Simple Edge Detection	Edge Detection with Enhancement
Roberts	58.71434643	58.75758587
Sobel	58.8303451	58.91188403
Prewitt	58.82820875	58.91088627
Canny	57.57763332	57.52629551

Table 2. MSE of Edge Detection techniques on different Detection type

Techniques	Simple Edge Detection	Edge Detection with Enhancement
Roberts	0.0874	0.08656
Sobel	0.08512	0.08354
Prewitt	0.08516	0.08356
Canny	0.11358	0.11493

PSNR values among different techniques are plotted in “Figure 7” and MSE values of different techniques are plotted in “Figure 8”.

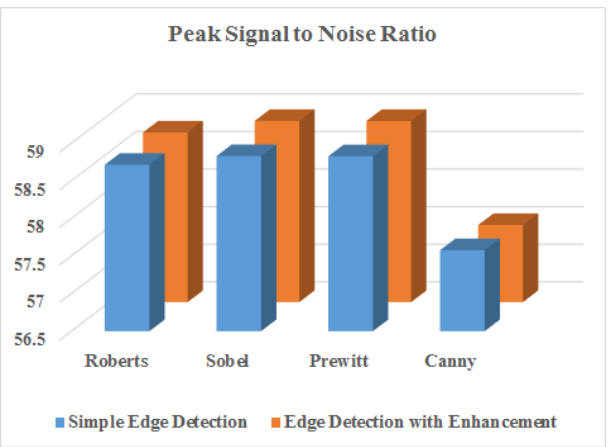

Figure 7. PSNR of Edge Detection Techniques

Table 3. Comparison between elimination methods

Image	Methods	Roberts	Sobel	Prewitt	Canny
3D Uimage (267 x 189)	PSNR	58.758	58.912	58.911	57.526
	SNR	0.087	0.0835	0.0836	0.1149
2D Uimage (225 x 225)	PSNR	58.464	58.766	58.765	57.380
	SNR	0.093	0.0864	0.0864	0.1189

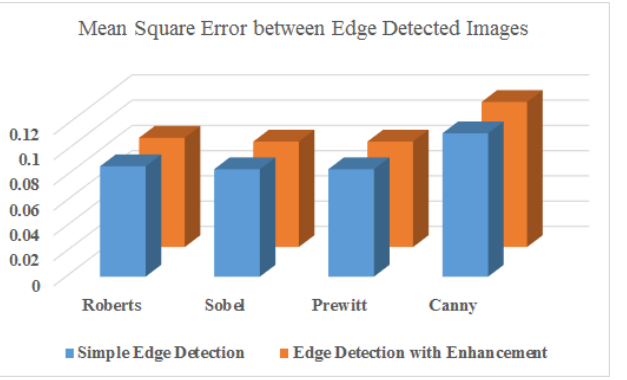

Figure 8. MSE of Edge Detection Techniques

Conclusion

In this research, PSNR and MSE values of 3D Ultrasound image are obtained among different techniques. PSNR value of enhancement and sharpening image is higher and MSE values lower than simple detected image. The observed values (PSNR and MSE) of different edge detection techniques and different Ultrasound images are compared in Table 3.

According to Table 3, PSNR and SNR values are nearly the same in Prewitt edge detector and Sobel edge detector form the experimental results. Among the detection techniques, Sobel edge detector gives the highest PSNR value in Table 1 and least MSE value on different image sizes in Table 2. From the point of experimental results, Sobel edge detector gives the best edge detector techniques. The experimental results and the

conclusion drawn from this paper will benefit the medical development in the field of ultrasound technology.

Acknowledgement

I would like to extend my sincere thanks to Dr Soe Mya Mya Aye, Professor, Head of Department of Computer Studies, University of Yangon, for her kind permission to carry out this work. I am utmost gratitude to Dr Pho Kaung, Rector, University of Yangon, for introducing me to the field of Parallel Processing.

References

Gonzalez, R.C and Woods., (2002), R.E, "*Digital Image Processing*", 2nd Edition, Prentice Hall, USA, New Jersey, ISBN: 0-130-94650-8/

Kutz,M., Thomenius, K. (2009). "Biomedical Engineering and Design Handbook", Volume 2, ISBN: 9780071498395, Page 251

Mehena,J., (2019), "Medical Image Edge Detection Using Modified Morphological Edge Detection Approach", *International Journal of Computer Sciences and Engineering*, Vol. 7(6), Page 523-528, E-ISSN: 2347-2693.

Nimrod M. T., (2005), "*Basic Physics of Ultrasound Graphic Imaging*", ISBN 92 41592990 , Page 13.

Ruba, A.,(2019), "Impact of Edge Detection Algorithms in Medical Image Processing", *Journal of World Scientific News*, Vol 118, Page 129-143, EISSN 2392-2192, January.

Stolojescu,C., (2012)"Edge detection techniques for X-ray image segmentation", *Proceedings of the 13th Symposium of Mathematics and its Applications*, "Politehnica", University of Timisoara, Page 1-4, November, 1-3.

Biodiversity Distribution Assessment of Some Order Lepidoptera on Study Area by Using R Language

Su Myo Swe[1] & Khin Myo Sett[2]

Abstract

Nowadays, although the technology is developing and moving forward fast, the nature of the value is getting reduce and biodiversity is being loss as a fast rate. Therefore, some creatures are need to be maintain for their natural life in the environment. The aim of this research is to assess the biodiversity distribution of some Order Lepidoptera in the area of Dagon University. 29 butterfly species were recorded from 13 genera, which belong to five families such as Nymphalidae, Nemeobidae, Papilionidae, Pieridae and Lycaenidae. Alpha index and beta index were calculated to designate Biodiversity. In this research, spread sheet software was used for data train, R programming language used for the statistical computing and graphics and PAST 4.03 software used for calculation of diversity profile of butterflies.

Keywords: Biodiversity, assessment method, R, statistical analysis, butterflies

Introduction

Butterflies and moths are insects are classified in the Kingdom: Animalia, Phylum: Arthropoda, and Order: Lepidoptera. In this research, Butterfly fauna is used as sampling item. Butterflies are the most well-known and beautiful creatures of all insects. They are the most conspicuous species on Earth' biodiversity.

Kingdom **Animalia** (animals)

Phylum **Arthropoda** (arthropods, invertebrate animals with an exoskeleton, a segmented body, and jointed legs)

Class **Insecta** (insects, arthropods with 6 legs, 2 antennae, and a 3-part body)

Order **optera** (butterflies and moths)

[1] Associate Professor, Department of Computer Studies, University of Mandalay

[2] Professor (Head), Department of Computer Studies, University of Mandalay

Due to disturbances in the environment caused by human activities, populations and species are threatened. Biodiversity refers to all of the natural world and all living organisms within it, including all living things such as plants, animals, bacteria and micro-organisms. Measures of biodiversity at the level of species or populations are directed towards the attainment of an index of the number of species and their relative abundances within a given landscape. Biodiversity Distribution Assessment is to investigate the spatial distribution of protected and unprotected areas that support animal and plant species.

Diversity index is a quantitative measure that reflects how many different types (such as species) there are in a dataset (a community) and that can simultaneously take into account the phylogenetic relations among the individuals distributed among those types, such as richness, divergence or evenness. In recent years, there are many biodiversity analysis packages software. Some of them which the researchers like are PAST, SPLAM, CANOCO, MVSP, Biodiversity Pro, Biodiversity R, AND Estimatie S etc.

R is a programming language and free software environment for statistical computing and graphics supported by the R Foundation for statistical computing. The R language is widely used among statisticians and data miners for developing statistical software and data analysis.

The objective of this research is biodiversity distribution assessment of butterflies across different Families of Order Lepidoptera. The assessment index is calculated by Shannon Diversity index and Simpson index. The diversity profile is created by using PAST 4.03 software and graph of species richness are created by R programming language.

Materials and Methods

Study Area

The study area was done in the Dagon University campus. Dagon University located in Dagon Myothit (East), Yangon, Myanmar and the total area is 1471.868 acre. Figure 1-A and Figure 1-B shows the campus of Dagon University from Google satellite and map representation.

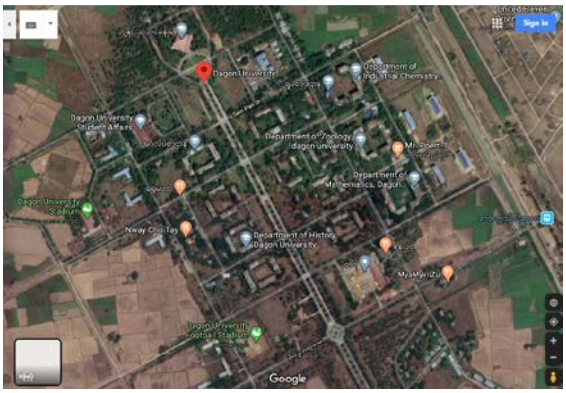

Figure 1-A. Google Satellite representation of Dagon University

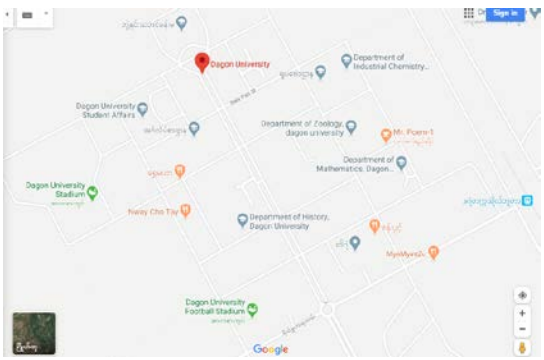

Figure 1-B. Google Map representation of Dagon University

Survey for Sampling

Sampling item (butterflies) are collected by ground survey. The classification and categorizing were carried out in stage of family, genus and species was carried out in the former research. There have total six families in Order Lepidoptera, among them five families are collected as survey for sampling. Family Hesperidae was not found as sampling. Table 1 shows the collected result of the survey sampling in Dagon University campus.

Table 1. Collected Result of the Survey Sampling

Sr.No	Family Name	Genus Name	Species Name	Species Richness
1	Nymphalidae	Danaus	chrysippus	15
			plexippus	18
		Mycalesis	gotama	10
		Orsotriaena	meda	5
		Cyllogenes	suradeva	15
		Euthalia	lubentina	12
			phemius	12
			acontius	10
2	Nemeobidae	Abisara	fylla	12
			echerius	7
3	Papilionidae	memnon	agenor	3
			polymnestoroides	3
			mayo	5
		Polytes	polyts	3
			pitmani	3
4	Pieridae	Delias	eucharis	10
			hierta	10
		Appias	nero	15
			libythea	12
			leis	13
			wardii	10
		Hebomoia	glaucippe	9
			roepstorff	9
		Catopsilia	crocale	12
			scylla	12
			pyranthe	12
			florella	10
5	Lycaenidae	Castalius	ananda	15
			rosimon	13
6	Hesperidae			0
Sum		13	29	295

Assessment Methods

In the research, biodiversity assessment provides the collected samplings are trained in the spread sheet first. For the calculation of diversity index, alpha diversity is used. Then the trained results are input in R programming language for statistical analysis and express the diagrammatic representation. Finally, trained results are input in the PAST 4.03 software for diversity profile.

Alpha Diversity

The majority of the proposed methods to quantify the biodiversity of species refer to the diversity within communities, namely as alpha diversity. These methods are based on the number of species (species richness), the information, the dominance and the equity of the community. In this research, habitat does not consider therefore the equity of the community does not contained.

Richness *R* simply quantifies how many different types the dataset of interest contains. For example, species richness (usually noted *S*) of a dataset is the number of different species in the corresponding species list. Species Richness (S) is and index based on the number of species.

Information or diversity index calculated by using Shannon diversity index formula. Shannon values generally vary between 1.3 and 3.5, and only rarely exceeds 4.5.

Shannon Index Fromula $$H = \sum[(p_i) \times ln(p_i)]$$

H = Shannon index

p_i = proportion of species in a Community ($p_i = n_i / n$)

n = total number of individuals

Simpson diversity index formula is used to calculate the dominance of the species in the communities. The Simpson index varies from 0 to 1, and the closer to 1 the more dominance.

Simpson Index Fromula $D = \sum p_i^2$

D = Simpson index

p_i = proportion of species in a Community ($p_i = n_i / n$)

n = total number of individuals

Beta Diversity

Beta diversity or among habitats represents the degree of change of species, as well as biotic change through environmental gradients. It is based in proportions or differences, that can be quantified based on indices or similarity coefficients of dissimilarity or distance between the plots, from quantitative or qualitative data. Therefore, beta diversity does not incorporate in this research for biodiversity distribution assessment of some Order Lepidoptera.

Implementation

Statistical Analysis with R Programming Language

R and its libraries implement a wide variety of statistical and graphical techniques, including linear and nonlinear modeling, classical statistical tests, time-series analysis, classification, clustering, and others. R is easily extensible through functions and extensions, and the R community is noted for its active contributions in terms of packages. Figure 2 shows the statistic the sampling of butterflies which are trained in spread sheet and input with the R language by using the **library(readxl)** in R language.

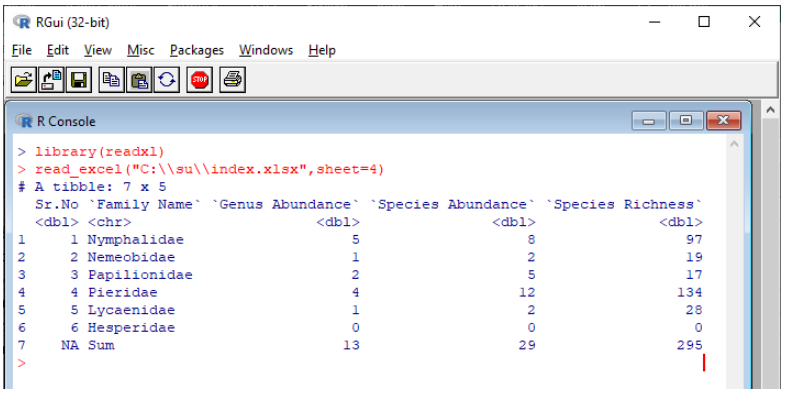

Figure 2. Survey Result with R Language

Figure 3 shows the result which are trained in spread sheet and input with the R language by using the **library(readxl)** in R language.

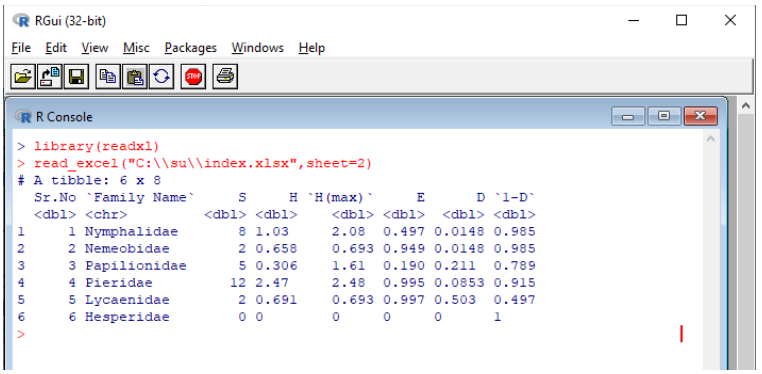

Figure 3. Trained Result in R Language

Figure 4 shows the code to produce the barplot for Shanon Index of biodiversity.

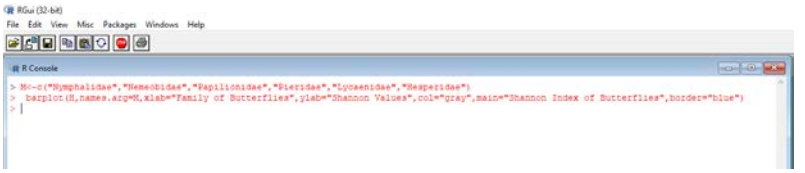

Figure 4: Code for Barplot for Shanon Index of Diodiversity with R Language

Figure 5 shows the code to produce the barplot for Simpson Index of biodiversity.

Figure 5. Code for Barplot for Simpson Index of Diodiversity with R Language

Calculation of Sampling Data for Diversity Profile with PAST 4.03

PAST is a software package for paleontological data analysis written by P.D. Ryan, D.A.T. Harper and J.S. Whalley (Ryan et al. 1995). Through continuous development for more than twenty years, PAST has grown into a comprehensive statistics package used not only by paleontologists, but in many fields of life science, earth science, engineering and economics. Figure 6 shows the input the sampling data into PAST 4.03 for calculation of diversity profile.

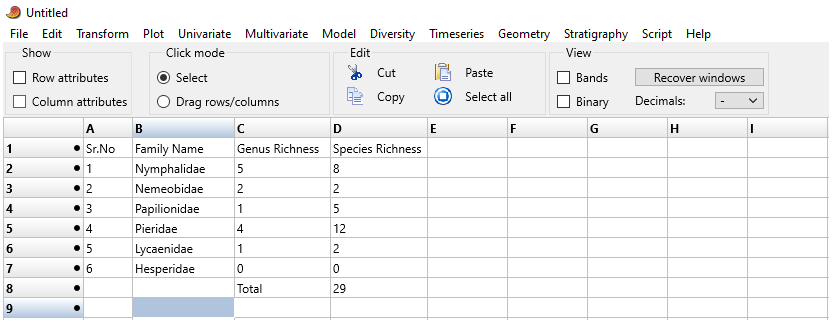

	A	B	C	D	E	F	G	H	I
1	Sr.No	Family Name	Genus Richness	Species Richness					
2	1	Nymphalidae	5	8					
3	2	Nemeobidae	2	2					
4	3	Papilionidae	1	5					
5	4	Pieridae	4	12					
6	5	Lycaenidae	1	2					
7	6	Hesperidae	0	0					
8			Total	29					
9									

Figure 6. Input the Sampling Data into PAST 4.03

Result and Discussion

Shannon index is used for species diversity and Simpson index is used for species dominance. Table 2. shows the calculated index for biodiversity and dominance of Order Lepidoptera (butterflies).

Table 2. Calculated Index for Biodiversity Distribution of Butterflies (Order Lepidoptera)

Sr.No	Family Name	Species Richness (S)	Shannon Index Species Diversity (H)	Simpson Index Species Dominance (D)
1	Nymphalidae	8	1.0327	0.0148
2	Nemeobidae	2	0.6581	0.0148
3	Papilionidae	5	0.3061	0.2111
4	Pieridae	12	2.4733	0.0853
5	Lycaenidae	2	0.6909	0.5026
6	Hesperidae	0	0	0

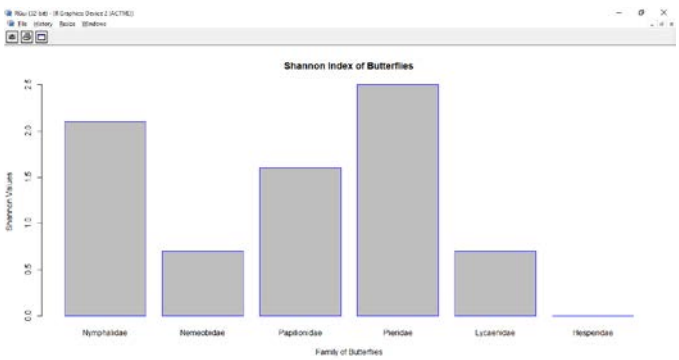

Figure 7. Species Diversity with Shannon Index

According Figure 7, Family Nemeobidae, Papilionidae and Lycaenidae are very low species diversity. Family Nymphalidae is low species diversity and Family Pieridae is medium diversity.

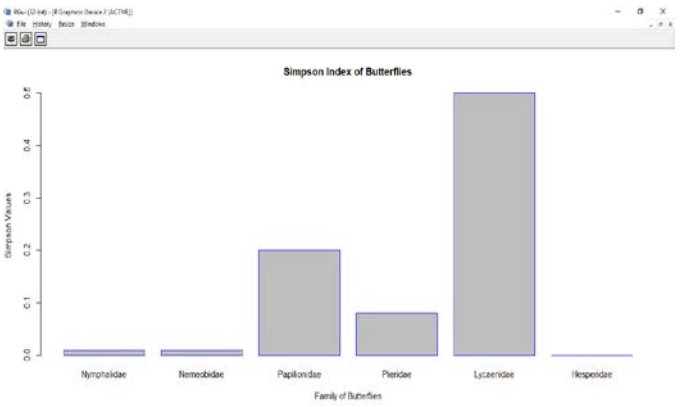

Figure 8. Species Dominance with Simpson Index

According Figure 8, Family Nymphalidae, Nemeobidae and Pieridae are very low dominance. Family Papilionidae is low dominance and Family Lycaenidae medium dominance.

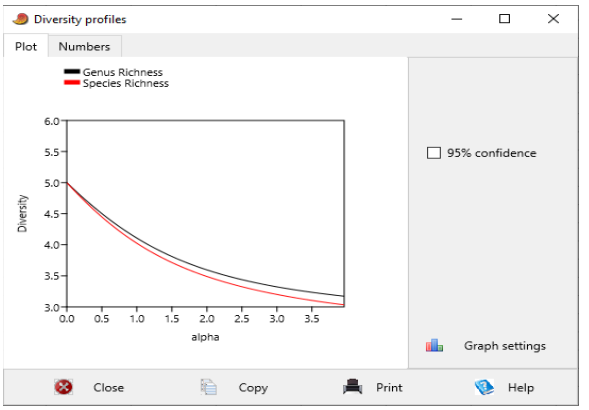

Figure 9. Diversity Profiles with PAST 4.03

Figure 9 shows diversity profiles of the Genus richness and Species richness of Order Lepidoptera of butterflies in Dagon University campus by using PAST 4.03 software. The biodiversity profile showed a decreasing trend of both Genus and Species but Species richness is more decrease then Genus richness.

Conclusion

Butterflies are the best-known and best group of insects for examining pattern of global biotic diversity and distribution. A total of 138 butterfly species from five lepidopteron families were collected as sampling in the Dagon University campus. For alpha diversity, Family Hesperidae was no species richness and Family Pieridae was best species richness. By using Shannon index, Family Papilionidae was very low diversity and Family Pieridae is medium diversity. By using Simpson index, Family Nymphalidae and Nemeobidae are very low dominance and Family Lycaenidae medium dominance. The presence of butterflies is very essential for pollinating different plant species within protected natural ecosystems. By making biodiversity distribution assessment of Order Lepidoptera will protect and sustain the natural environment.

Acknowledgements

First, I would like to thank Dr. Khin Myo Sett, Professor (Head), Department of Computer Studies, University of Mandalay, for her encouragement to prepare this research and review in details. Then, I grateful thank to Dr. Thet Mon Win, Professor, Faculty of Computing, Myanmar Institute of Information Technology, for her valuable suggestions. Finally, I also want to express very special thanks to my parents for their support and love.

References

Basavarajappa S., Gopi Krishna V. and S. Santhosh (2018). Butterfly species composition and diversity in a protected area of Karnataka, India.

Bingham. C.T, “The Fauna of British India, Ceylon and Burma. Butterflies, Vol. I Taylar and Francis, London”, 1905

Bingham. C.T, “The Fauna of British India, Ceylon and Burma. Butterflies, Vol. II Taylar and Francis, London”, 1907

Kanieski, Maria Raquel, Longhi, Solon Jonas and Soares P. R. Casemiro. (2018). Methods for Biodiversity Assessment: Case Study in an Area of Atlantic Forest in Southern Brazil.

Raut, Ninad, Dr. (2016). Biodiversity Assessment at GAIL Usar Complex: India.

Seefeld, K. (2007). Statistics Using R with Biological Examples.

Sreekanth, G. B., Lekshmi, N. Manju and Singh, N. P. (2015). BIODIVERSITY ASSESSMENT: IMPROVED METHODS AND APPROACHES.

Swe Su Myo. (2019). Classification of some Butterflies by Using Rules Induction: Cn2 Algorithm. MAAS, Vol. XVII, No.3.

Swe Su Myo and Sett Khin Myo. (2019). Approaching Rules Induction: CN2 Algorithm in Categorizing of Biodiversity. IJTSRD, Vol. 3, Issue. 4.

https://en.wikipedia.org

https://past.en.lo4d.com

www.dagonuniversity.edu.mm

www.google.com/maps

Monte Carlo Simulations of Spin Models on Graphics Processing Unit

Wint Pa Pa Kyaw [1] & Soe Mya Mya Aye[2]

Abstract

Monte Carlo simulations of classical spin (Ising) models are presented using the massively parallel architecture provided by graphics processing unit (GPU). GPU is able to perform massively parallel scientific computations at low cost. For performing scientific calculations, the compute unified device architecture (CUDA) is a programming approach as a data-parallel computing device. The checkerboard algorithm for the two dimensional spin model is implemented. The results of simulations are obtained up to 60 times faster on the GPU than on a current central processing unit (CPU) core. It is performed simulations for systems containing up to 4194304 spins on GeForce GT 750M GPU.

Keywords: Spin models, Monte Carlo Simulations, GPU, Ising model, CUDA

Introduction

Monte Carlo (MC) simulations have been studied since decades. It is continuously improved accuracy, which benefited from increasing computational resources. Such computing requirements necessary not only for MC simulations but also for various other tasks including, i.e., molecular dynamics simulations or stochastic optimization, need a large amount of high performance computing resources. Graphics processing unit (GPU) acceleration can be used significant savings of computing time by a huge variety of fields: in radio astronomy and astronomy, DNA sequence alignment, molecular dynamics simulations, quantum chemistry, MC simulations. Examples for the numerous applications in medicine are dose calculation, Soft tissue simulation, volume reconstruction from x-ray images, algorithms for image registration, and the optimization of intensity-modulated radiation therapy plans.

[1] Associate Professor, Dr., Department of Computer Studies, University of Yangon
[2] Professor and Head, Dr., Department of Computer Studies, University of Yangon

GPU are high-performance many-core processors. Computational power of recent graphics cards exceeds that of a central processing unit (CPU) by orders of magnitude. Anyone with knowledge about C/C++ can obtain significant results using standard C language with CUDA (Computing Unified Device Architecture) extensions developed in NVIDIA. Problems of parallel computation for working on CUDA kernels have to be taken into account. Then the optimal use of limited memory must be taken into account. In addition, memory transfers between host and device should be reduced to a minimum as they are often the slowest part of a CUDA program.

In this paper, the applicability of GPU to spin models, such as the Ising model is investigated. After having considered the models from the theoretical point of view, the spins are simulated by Monte Carlo methods. The CUDA programming model and the graphics (NVIDIA) are used. The two dimensional square lattice Ising model on a GPU and CPU are implemented. This implementation is able to accelerate the Ising model computation by migration to a GPU. GPU technologies for MC simulations of two dimensional square lattice Ising models are employed in this paper.

The Spin Model

The spin model is a simple lattice Ising model to apply the methods of statistical physics. It describes anti-ferromagnetism and ferromagnetism. It assumes a periodic *d*-dimensional lattice which is made up of magnetic dipoles, each of them associated with a spin s_i. The Ising model assumes all spins to point either in one direction or in the opposite, expressed by $s_i = \{+1,-1\}$ or $s_i = \{\text{'up', 'down'}\}$. The Ising model is described by the following Hamiltonian

$$H = -J\sum_{<ij>} s_i s_j - h\sum_i s_i, \qquad (1)$$

where *h* denotes to an external magnetic field, and the sum $\Sigma_{<ij>}$ is over nearest neighbours. J refers the strength of the coupling between adjacent spins. Ferromagnetism is $J > 0$, anti-ferromagnetism is $J < 0$. $J > 0$ is considered. The Ising model is a phase transition. There are two phases in zero external magnetic fields, separated by the transition temperature *Tc*. For temperatures T> *Tc*, the system is in a paramagnetic phase, whereas temperatures $T < Tc$ lead to a spontaneous magnetization.

GPU Implementation of Spin Models

As a first step of the GPU implementation, memory for the two dimensional spin field and the seed values are allocated on the global memory of GPU. Spins and seeds are transferred to the global memory of GPU after a random initialization of the spin field on the CPU and initialization of seed values. For each step, the energy difference $\Delta H = H_a - H_b$ between two subsequent states *a* and *b* is calculated. The probability for move a→ b is given by $W_{a\to b} = \exp(-\Delta H / k_B T)$ if $\Delta H > 0$ and $W_{a\to b} = 1$ if $\Delta H \leq 0$. Since only discrete values for this factor are possible, they should be pre-calculated on the CPU for each temperature and transferred to the GPU when the kernels are invoked.

The transition probability $W_{a\to b}$ depends on the temperature T which has to be passed to the GPU kernel function. In all simulations, the Boltzmann constant k_B is fixed to 1. A zero field (h = 0) and J = 1 are used. The system for MC trial moves to be executed in parallel has to be partitioned into non-interacting domains. Thus a checkerboard algorithm is applied for the update process of the spin lattice. After all spins on the 'white' squares of the checkerboard are updated and secondly all spins on the 'black' squares. The checkerboard algorithm is suitable for demonstrating the migration to the GPU architecture realizing non-interacting domains where the MC moves are performed in parallel.

It is possible to synchronize threads within a block on a GPU device and native block synchronization does not exist. Therefore the termination of this GPU kernel ensures that all blocks are executed. The spin update process on the lattice is divided into blocks on the GPU. A semi-lattice in a single GPU kernel is changed without creating conflicts.

The spin update process is subdivided into threads and blocks as shown in Figure (1) for n = 16. The spin field is split into strips where each stripe is handled by one block. For a square sub-cell of 2 * 2 spins, each thread is responsible. Thus, n/2 threads per block are used. The update process of the first semi-lattice is handled by a first GPU kernel, that is ϕ = n/2 threads in each block accomplish step (a) and (b) of Figure 1. In order to accomplish steps (c) and (d) a second kernel is started.

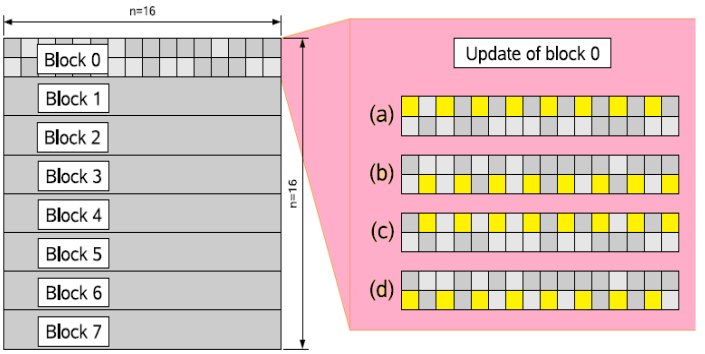

Figure 1. Schematic Visualization of the Implementation of a Two Dimensional Ising Model on a GPU for n = 16 Spins per Row

Each thread in one GPU kernel function needs up to two random numbers. For the reduction process of partial energies or magnetizations of the Ising lattice after two semi-lattice updates, this array is used. To increase memory speed, the seed values or current random numbers are transferred at the beginning of a GPU kernel to a shared memory array. The current value is transferred back to global memory after handling of the updating steps, i.e. after step (b) and after step (d). CUDA does not provide native reduction functions. Therefore, after step (d), the shared memory array is used. To be fast reduction of the partial values within a block, a binary tree structure is used. These partial results of each block are stored at block-dependent positions in global memory and then transferred to host's main memory. The final summation of the results of n=2 blocks is done by the CPU.

Results and Discussion

The CUDA architecture as an extension to the C language is used to implement the parallel algorithm. Table 1 shows different block sizes and their effect on the overall simulation speedup compared with the serial code. The results can be observed a huge performance improvement of up to 59.57 times faster than the CPU implementation for a relatively large system size.

Table1. Program Execution Times (seconds) and Speedup for Spins on i7 and GeForce GT 750M

Number of Spins	Serial Execution Times (seconds)	CUDA Execution Times (seconds)	Speedup	Block Size	Allocation Times (seconds)	Memory Transfer Times (seconds)
1024	0.0575	0.1652	0.3500	16	1.78	0.53
4096	0.2212	0.1869	1.1800	32	2.57	0.50
16384	0.8522	0.2040	4.1800	64	2.53	0.60
65536	3.9414	0.2269	17.3700	128	2.48	1.22
262144	17.0110	0.4455	38.1800	256	2.31	2.02
1048576	82.8262	1.5769	52.5200	512	2.64	5.31
4194304	381.9925	6.4121	59.5700	1024	2.71	19.09

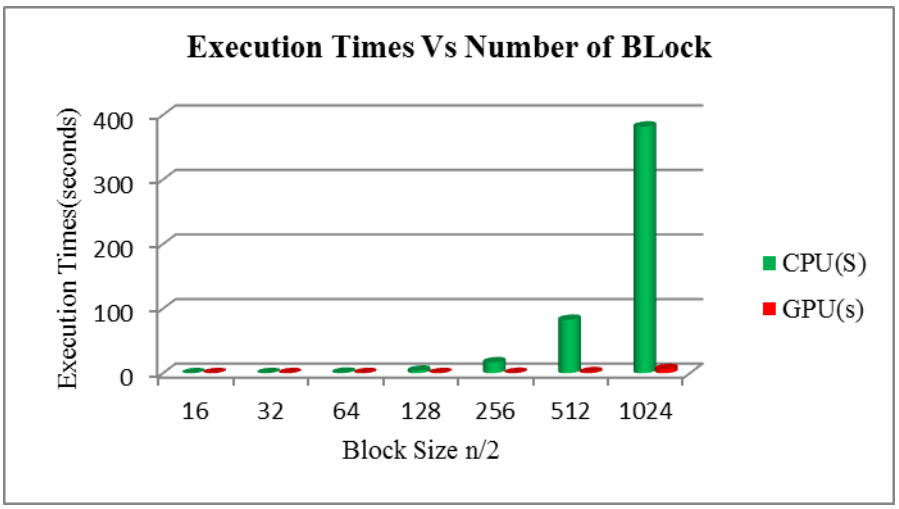

Figure 2. Processing Times for a Two Dimensional Ferromagnetic Square Lattice Ising Model

The processing times of the spin model implementation on the GPU are compared with the spin model implementation on CPU core in Figure 2. The processing time for both algorithms increases as the number of block increases. It can be concluded that parallel algorithm is executing entirely

on the GPU and keeping the overhead of executing on the CPU to a minimum.

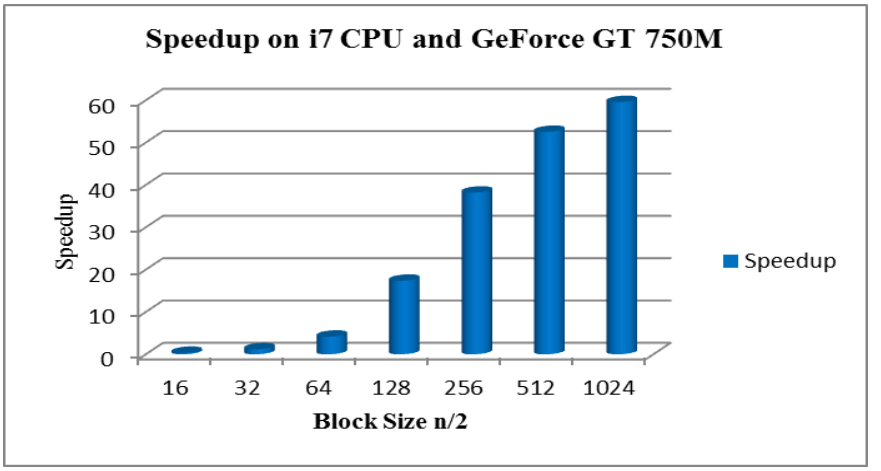

Figure 3. Plots of Speedup for Different Block Sizes

The speedup of the serial algorithm is compared with the parallel algorithm running on the GeForce GT 750M GPU in Figure 3 and Table 1. The speedup ratio seen in Figure 3 shows rapid improvement as the system size grows. For larger systems, more speedup can be observed. For the largest system, n = 1024, speedup of roughly 60 achieve. For very small systems, the speedup is smaller than 1 because for small thread numbers per block the GPU device is not used efficiently.

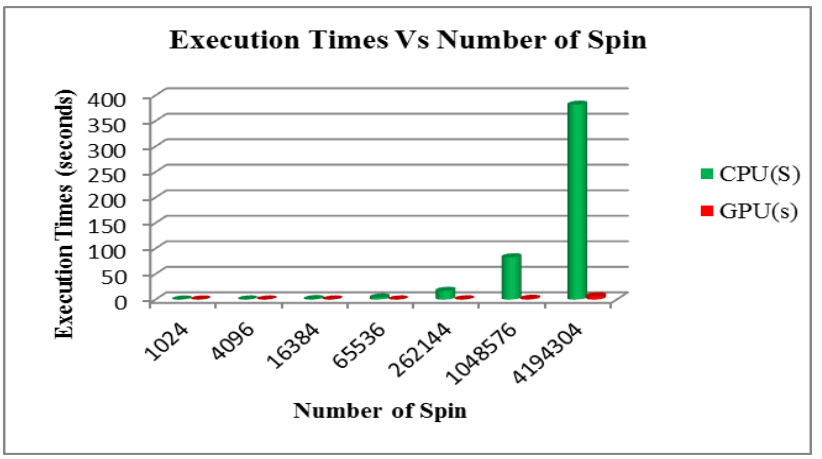

Figure 4. Serial Versus CUDA Execution Times for MC Simulation on i7 and GeForce GT 750M

The execution time for both algorithms increases as the number of spin increases. The execution time of the serial algorithm grows more than the parallel version. The GPU code starts to overcome the added overhead and shows better performance than the serial code as shown in Table 1 and Figure 4.

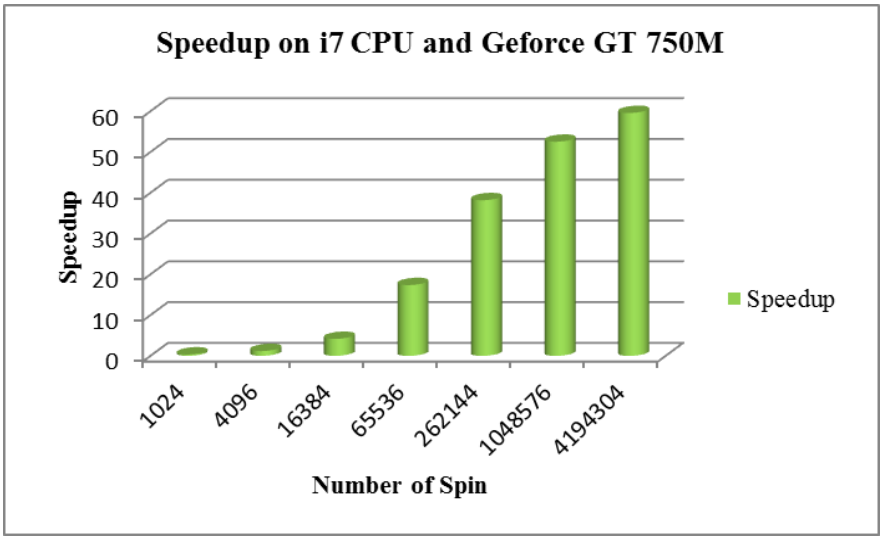

Figure 5. Serial Versus CUDA Speedup for MC Simulation on i7 and GeForce GT 750M.

The speed of the CPU (host) has a negligible impact on the execution time of the parallel algorithm. A detailed comparison between speedup and different spins can be observed looking at Table 1, plotted in Figure 5. The Speedup is increasing gradually with the number of spins and shows the best performance for the largest systems.

Conclusion

It takes time and effort to learn all important parts of CUDA programming and be able to use it well. If not used with proper planning, those methods would not lead to performance increase. It is as a special tool for parallel computation, not as a magical device that will speed up the program. It is important to consider dividing the procedure into many small, independent functions before trying to use it. If the current speed using CPU is not satisfying, CUDA for the problem should be used. The results can be astonishing as it is a powerful technology. As it has been shown, results can

be obtained much faster for bigger lattices, so it would be advisable to use for analysis of currently skipped system sizes because of the time of execution of simulations.

A GPU accelerated version of the two dimensional ferromagnetic square lattice Ising model is presented. The compute unified device architecture is employed for the GPU implementation. For general purpose computing, a recent GPU offers incredible resources by combination continuously increased number of cores and a high memory bandwidth. Results are obtained up to 60 times faster than on a current CPU core by GPU implementation of a checkerboard algorithm of the two dimensional spins model. The results of GPU are as precise as CPU and much faster than CPU for the Ising model when system sizes are sufficiently large.

Acknowledgement

I would like to extend my sincere thanks to Dr Soe Mya Mya Aye, Professor, Head of Department of Computer Studies, University of Yangon, for her kind permission to carry out this work. I am greatly indebted to Dr. Pho Kaung, Rector, and University of Yangon for his excellent help and creative ideas that have assisted me in broadening my research skills and his continuous guidance, devotion and perpetual encouragement.

References

Ferdinand, Arthur, Fisher, and Michael, E. (1969) "Bounded and Inhomogeneous Ising Models I. Specific-Heat Anomaly of a Finite Lattice.", Phys. Rev., 185(2):832–846.

Landau, D. and Binder, K. (2005) "A Guide to Monte Carlo Simulations in Statistical Physics.", second ed., Cambridge University Press, Cambridge

Nvidia Corp. (2008)"Nvidia CUDA Compute Unified Device Architecture-Programming Guide, v2.0". http://www.nvidia.com/object/cuda_develop.html.

Nvidia Corp. (2008) "Nvidia CUDA Compute Unified Device Architecture—Reference Manual,v2.0". http://www.nvidia.com/object/cuda_develop.html.

Preis, T. Virnau, P. Paul, W. and Schneider J. J. (2009) "GPU accelerated Monte Carlo simulation of the 2D and 3D Ising model." J. Comput. Phys., 228(12):4468–4477.

William, H. Press, Saul A. Teukolsky, William T. and Brian, P. Flannery. (2007) "Numerical Recipes-The Art of Scientific Computing." Cambridge University Press.

Some Oyster Fauna of Northern Rakhine Coastal Area

Naung Naung Oo*

Abstract

The distribution of oyster fauna in heterogenous soft bottoms and on various hard elements of the substrate in Nantha Island, Sittway Point and Myengu Island, Northern Rakhine Coastal Region was studied, a total of 3 species of *Crassostrea* Sacco, 1897, namely *C. belcheri* (G. B. Sowerby II, 1871), *C. gigas* (Thünberg, 1793) and *C. nippona* (Seki, 1934), and 1 species of *Dendostrea* Swainson, 1835, namely *D. folium* (Linnaeus, 1758), and 1 species of *Ostrea* Linnaeus, 1758, namely *O. denselamellosa* Lischke, 1869, and 3 species of *Saccostrea* Dollfus & Dautzenberg, 1920, namely *S. cucullata* (Born, 1778), *S. echinata* (Quoy & Gaimard, 1835) and *S. scyphophilla* (Peron & Lesueur, 1807), and 2 species of *Hyotissa* Stenzel, 1971, namely *H. hyotis* (Linnaeus, 1758) and *H. inermis* (G. B. Sowerby II, 1871) were recorded from December 2019 to August 2020. High intraspecific variation of morphological structures, the wide distribution and plasticity of these often sympatric species led to confusion regarding their identity. The geographical distribution of the studied species is recognized as intertidal and shallow subtidal waters of the Indo-West Pacific Region. This study provides the basic information necessary for further ecological and population studies on oyster species.

Keywords: Oysters, northern Rakhine coastal areas, distribution, habitats, ecological information.

Introduction

Oysters (Family Ostreidae) occupy nearshore marine and estuarine habitats in temperate to tropical latitudes worldwide (Ruesink *et al.* 2005). Being ecosystem engineers, they can provide many ecosystem goods and services by creating habitats then used by other species, and can modify the physical and chemical environment, with major consequences for estuarine populations, communities, and food webs (Ruesink *et al.* 2006). Oysters of the genus *Crassostrea* Sacco, 1897; *Ostrea* Linnaeus, 1758 and *Saccostrea* Dollfus & Dautzenberg, 1920 are widespread and commercially important groups of bivalves (Bussarawit *et al.* 2010).

* Lecturer, Dr., Department of Marine Science, Sittway University

Myanmar has a long coastal line along the Bay of Bengal and the Andaman Sea of the North Indian Ocean. A FAO document has reported that two oysters, *Crassostrea belcheri* and *Saccostrea cucullata*, are cultured in Myanmar (Lovatelli 1991). There has been no taxonomic classification except (Mar Lar Myo Sein 1982) or molecular confirmation of oysters from Myanmar in the English literature. Recently, the information regarding the molecular taxonomy of Myanmar oyster specimens such as *Crassostrea belcheri*, *Saccostrea malabonensis*, and a new subspecies *Crassostrea gryphoides tanintharyiensis* were collected and subjected to molecular classification and phylogenetic analysis with two mitochondrial genes, *cytochrome oxidase subunit I* (COI) and *16S rRNA* (16S) (Li *et al.* 2017).

The family Ostreidae has 12 species occurring in Myanmar waters. *Saxostrea parasitica commercialis* and *S. mordax* are flooded. *Crassostrea gigas* are common on Rakhine, Delta and Taninthayi coasts and flooded in Myeik Archipelago. *C. nippona* and *C. belcheri* are abundant in Myeik Archipelago. *Saxostrea echinata* is flooded and *Pretostrea affinis* is common on the Taninthayi coast. *Pycnodonta hyotis*, *P. musashiana*, *Pretostrea imbricata*, *Dendostrea folium* and *Ostrea denselamellosa* are rarely found in Myanmar waters. However, the family as a whole has a wide range in the Indo-Pacific region (Mar Lar Myo Sein 1982).

Little is known about the oyster population in Myanmar waters. Oyster shells are also one the important fisheries resources and they can easily be established as important commercial species in study areas. The aim of the study is to generate some information on the ecological habitat, taxonomy and distribution of the oyster shells in northern Rakhine coastal areas.

Materials and Methods

Studies on the distribution of oyster shells were conducted from Nantha Island, Sittway Point and Myengu Island in northern Rakhine coastal areas from December 2019 to August 2020 (Figure 1). Specimens of the oyster shell were manually collected using a hand scope from the study areas during low tide and transferred to the laboratory for further study. Shells were measured using a digital vernier calliper for total length and other shell morphometric characteristics. The identifications of the oyster

species were based on the conchological characters i.e; morphology of the shell, it is colour and lustre, absence or presence of denticles and shape, colour and position of adductor muscle scar. Some malacological features like the presence or absence of promyal chamber, the colour of the mantle folds and tentacles of the mantle folds were also examined. For the identification of the different morphological structures of oyster shell species, the works of Torigoe (1981), Harry (1985), Poutiers (1998), Siddiqui and Ahmed (2002), Lam and Morton (2003 & 2004) and Bussarawit *et al.* (2010) were followed.

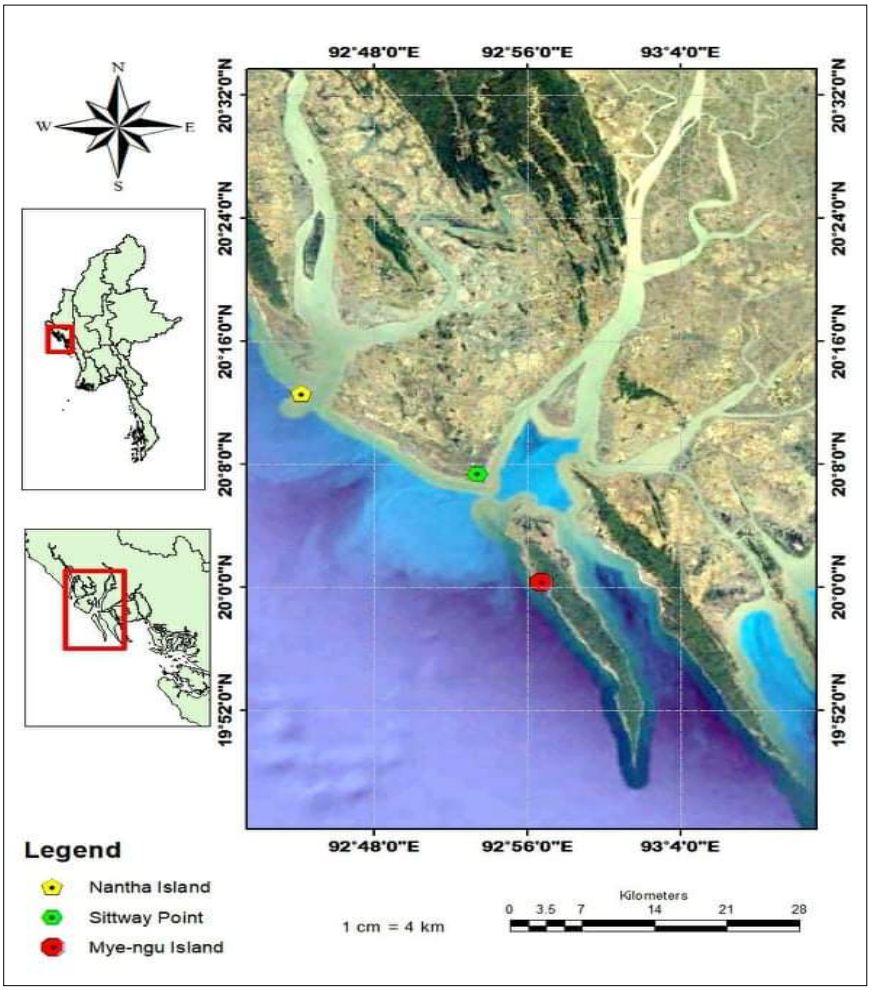

Figure 1. Map showing the collection sites in the Northern Rakhine coastal area

Results and Discussion

A total of 10 species of oyster fauna were recorded from Nantha Island, Sittway Point and Myengu Island in the northern Rakhine coastal area (Figure 2 and Table 1). These all species were abundantly found along the Myanmar coastal waters. The identification of the species was based on the external characteristics of the valves (Tables 2, 3 and 4). Among these species, *Crassostrea belcheri* (G. B. Sowerby II, 1871), *C. gigas* (Thünberg, 1793) and *Saccostrea cucullata* (Born, 1778) were highly consumption rates and demand by local people and markets.

Table 1. Systematic of some oysters in the northern Rakhine coastal area

Phylum	Mollusca Cuvier, 1795	
Class	Bivalvia (= Pelecypoda) Linnaeus, 1758	
Order	Ostreida Fèrussac, 1822	
Family	**Ostreidae Rafinesque, 1815**	
Genus	***Crassostrea* Sacco, 1897**	
Species	1	*C. belcheri* (G. B. Sowerby II, 1871) White scar oyster
	2	*C. gigas* (Thünberg, 1793) Giant cupped oyster
	3	*C. nippona* (Seki, 1934) Japanese oyster
Genus	***Dendostrea* Swainson, 1835**	
Species	4	*D. folium* (Linnaeus, 1758) Leaf oyster
Genus	***Ostrea* Linnaeus, 1758**	
Species	5	*O. denselamellosa* Lischke, 1869 Densely lamellated oyster
Genus	***Saccostrea* Dollfus & Dautzenberg, 1920**	
Species	6	*S. cucullata* (Born, 1778) Hooded oyster
	7	*S. echinata* (Quoy & Gaimard, 1835) Block edge oyster
	8	*S. scyphophilla* (Peron & Lesueur, 1807) Crenulate rock oyster

Family	**Gryphaeidae Vialov, 1936**	
Genus	***Hyotissa* Stenzel, 1971**	
Species	9	*H. hyotis* (Linnaeus, 1758) Honeycomb oyster
	10	*H. inermis* (G. B. Sowerby II, 1871) Saddle-shaped oyster

Family Ostreidae Rafinesque, 1815

Shell inequivalve cemented to substrate by the left valve, right valve quite flat. Ligamental area with a shallow median groove and 2 lateral thickenings. Hinge without teeth. A single adductor muscle scar, the median in position or nearer to the ventral margin. Internal margins are smooth or with simple short chomata.

Genus *Crassostrea* Sacco, 1897

The description of the genus as given by Thomson (1954) is as follows. “Shell elongate, very variable shape even within the species; lower valve deep, cup-shaped, recessed under hinge; the muscle scar displaced both towards the dorsolateral edge and towards the lip; upper valve opercular, flat except sometimes upraised at the rim, may or may not have a row of denticles along the rim laterally from the hinge. A promyal chamber on the right side. Non-incubatory”.

Habitat: Attached to hard objects or growing in bunches, on various soft bottoms, especially in bays and estuaries with somewhat reduced salinity. Intertidal and shallow subtidal water.

World distribution: Primarily restricted to the temperate and subtropical western Pacific, in Kamchatka to Japan and the South China Sea. This species has been introduced for culture, often successfully, in many parts of the world, including the western Pacific (Hawaii, Philippines, western Thailand, Australia, Tasmania, and New Zealand), the Indian Ocean (Mauritius), the eastern Pacific (Chile, Costa Rica, and the coasts of North America from British Columbia to California), the eastern Atlantic (from the British Islands to the Iberian Peninsula), and the western Mediterranean Sea.

Table 2. Comparison of the shell characteristics of genus *Crassostrea* in the study area

Shell characteristics	Species		
	C. belcheri	*C. gigas*	*C. nippona*
Upper valve	convex, dome-shaped	small	small
Lower valve	flat	cupped-shaped	large
Umbo	moderately small	deep	moderate
Adductor muscle scar	oblong-lunate	oval, postero-dorsal	oval, large

The genus *Crassostrea* Sacco, 1897 includes several commercially important species (Amaral and Simone 2014 and 2016). Species in this genus show a characteristic attachment mark on the left valve resulting from the cementation on mangrove roots (Sowerby II, 1870-1871) or on offshore or coastlines (Feng *et al.* 2015). They also lack denticles (chomata) near the inner edge of the shell, which are characteristic of other ostreids, such as *Ostrea* Linnaeus, 1758, *Saccostrea* Dollfus & Dautzenberg, 1920 and *Striostrea* Vyalov, 1936. In Brazil, *Crassostrea* species are popularly known as mangrove oysters. They can form banks both in the intertidal and subtidal zones, which are usually attached to rocky substrata and to the rhizomes of *Rhizophora mangle* Linnaeus, 1753, an estuarine tree (Amaral *et al.* 2020).

Genus *Dendostrea* Swainson, 1835

The description of the genus as given by Thomson (1954) is as follows. “Shell medium-sized, slightly inequivalve, variable in shape, irregularly subcircular or dorsoventrally elongate ovate in outline, “ on the substrate. The surface of valves, when not eroded, is roughened by low and irregular, concentric growth marks. Umbonal cavity of left valve shallow. Adductor muscle scar ovate and with the anterodorsal margin shallowly concave. Internal margins of both valves with slightly transverse chomata near the ligamental area, often supplemented in the right valve only by an irregular row of small pustules extending to the ventral margin”.

Habitat: On rocks or sea whip stems, in marine and estuarine waters. Common in mangrove areas. Lower intertidal zone and sublittoral to a depth of 5 m.

World distribution: Widespread in the Indo-West Pacific, from East Africa, including the Red Sea, to Melanesia; north to Japan and south to Queensland.

Sometimes, the species of *Hyotissa* may be confused with *Dendostrea folium*, especially in terms of external shell characters. Internal shell characters are more reliable in distinguishing these two species. For example, the shape of the adductor muscle scar is the most important feature for identification: that of *Hyotissa* is large and circular while that of *Dendostrea folium* is crescentic. Species of *Hyotissa* also have a well developed commissural shelf and are whitish internal whereas *Dendostrea* does not have an obvious commissural shelf and internally the basal witness is always patterned with dark yellowish-green patches showing the position of radial rays (Lam and Morton 2003).

Genus *Ostrea* Linnaeus, 1758

Description of the genus as listed by Thomson (1954). “Shell subcircular, relatively constant in shape within the species; lower valve shallow, not recessed under the hinge, muscle scar subcentral, the upper valve may be flat and opercular, or domed and subequal to the lower, and it may or may not have denticles along the margin laterally to the hinge which fit into pits in the lower valve. Anachomata is of small size present almost throughout the edge of the shell, with corresponding catachomata (pits) in the lower valve. Incubatory forms”.

Habitat: On various bottoms. Intertidal and shallow subtidal waters to a depth of 10 m.

World distribution: Indo-West Pacific, from India and Mauritius Island to the Philippines; north to the Yellow Sea and south to Indonesia.

The flat densely lamellated oyster *Ostrea denselamellosa* is considered to be one of the important bivalve resources in coastal shellfish fisheries, although its population density is known to be small (Lam and Morton 2004; Li, Wang and Guo 2017). The flat oyster occurs on rocks and gravel on sandy mud or muddy bottom in the study area. The flat oyster shell is irregularly sub-circular to sub-quadrate, and concave, with the right

valve flatter than the left. The valves are radially ribbed; those of the right valve is covered with fragile growth scales which are lacking on the left which may be purplish with radiating ribs (Noseworthy *et al.* 2016).

Genus *Saccostrea* Dollfus & Dautzenberg, 1920

Description of the genus as reported by Stenzel (1971). "Small to medium-sized, outline variable, but divisible into normal ostreiform ecomorphs with spatulate or vertical-oval to irregular form and abnormal rudistiform ecomorphs with small, operculiform right valve (upper valve) and large, slender conical to cornocupia-like. The left valve (lower valve) carries a very high, slender ligamental area, and has a large attachment area. Umbonal cavity on average very deep. Both valves with strong chomata, which commonly encircle the entire valve. The promyal chamber is present. Non-incubatory".

Habitat: Attached to various hard substrates, in marine, estuarine and mangrove areas, often in dense colonies. Intertidal and shallow subtidal levels to a depth of 5 m.

World distribution: Widespread in the Indo-West Pacific, from East and South Africa, including Madagascar, the Red Sea and the Persian Gulf, to eastern Polynesia; north to Japan and south to New South Wales and New Zealand. Also occurring in the tropical eastern Atlantic, from Cameroun to Angola. Introduced recently in the Mediterranean Sea for aquaculture.

Table 3. Comparison of the shell characteristics of genus *Saccostrea* in the study area

Shell characteristics	Species		
	S. cucullata	*S. echinata*	*S. scyphophilla*
Upper valve	flattish	small	small
Lower valve	generally deep	slightly large	large
Umbo	deep	deep	slight projection
Adductor muscle scar	kidney-shaped	elongate-reniform	well-defined, reniform

Species of the genus *Saccostrea* Dollfus and Dautzenberg, 1920 are oysters that live on rocky shores of the Indo-Pacific region. The taxonomy of this genus is unclear, and its morphological plasticity makes identification problematic (Morton 1990 and Klinbunga *et al.* 2005). They have small to medium-sized shells, and a left valve with a prominent ligament area, with projections in zigzag continuous and regular. The right valve is flat, bearing projections along its margin, with corresponding concavities on the left valve.

Family Gryphaeidae Vialov, 1936

Shell structure vesicular, distinguishable under a lens on an eroded part of the shell, or along the peripheral area of the interior; adductor muscle scar nearer to the hinge than to the ventral margin; chomata long, sinuous, and branched.

Genus *Hyotissa* Stenzel, 1971

Description of the genus as reported by Stenzel (1971). “Shell rather thick and heavy, of moderate size, roughly subcircular to irregularly trigonal in outline. The outer surface of valves is roughened by closely set, irregular concentric growth marks. The umbonal cavity of the left valve is rather deep. Adductor muscle scar large and somewhat obliquely elongated, rounded posteroventrally and straight to slightly depressed anterodorsally, situated near the posterior margin of the shell. Chomata forming in right valve 2 to 4 rows of numerous pustules all around the internal margins, and in left valve short transverse pits only present near the ligamental area”.

Habitat: Cemented on various hard substrates or objects. Intertidal and shallow subtidal waters to a depth of 5 m.

World distribution: Widespread in the Indo-West Pacific, from East Africa, including the Persian Gulf, to the Philippines; north to southern Japan and south to Indonesia. Exact distribution is not known because of frequent confusion with other species, notably *Alectryonella plicatula* and *Alectryonella haliotidea*.

Table 4. Comparison of the shell characteristics of genus *Hyotissa* in study area

Shell characteristics	Species	
	H. hyotis	*H. inermis*
Upper valve	convex, more flattened	small, slightly flattened
Lower valve	convex, rounded or angulate	more convex, large attachment
Umbo	left valve rather deep	shallow
Adductor muscle scar	large, obliquely elongated	large, circular, postero-dorsally

The shell morphology of the collected *Hyotissa* specimens also matches those of *O. imbricata* figured in Morris (1985) and *H. imbricata* figured in Torigoe (1981). *H. hyotis* has also been reported to occur in intertidal rock pools with corals on Ping Chau Island (Morton 1990). Whether *H. imbricata*, *H. hyotis* and *H. sinensis* either all co-occur locally or are synonymous is unknown.

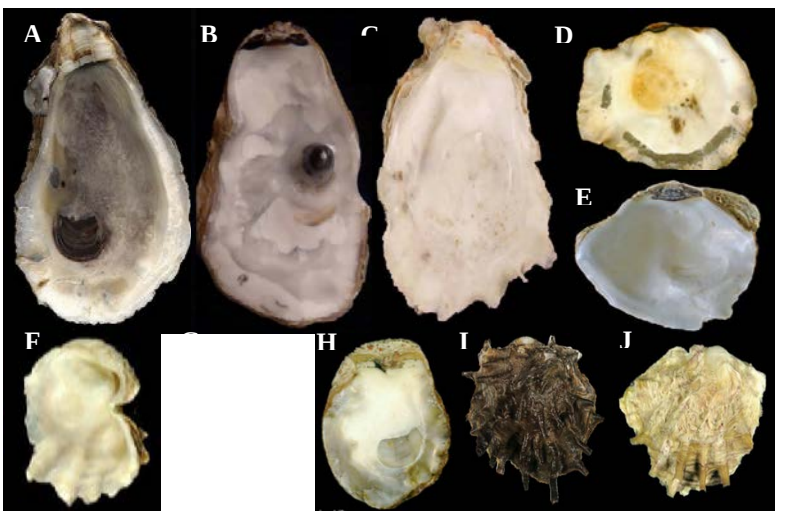

Figure. 2. A-J. Some oyster fauna of northern Rakhine coastal area. A) *Crassostrea belcheri*; B) *C. gigas*; C) *C. nippona*; D) *Dendostrea folium*; E) *Ostrea denselamellosa*; F) *Saccostrea cucullata*; G) *S. echinata*; H) *S. scyphophilla*; I) *Hyotissa hyotis*; J) *H. inermis*.

Conclusion

This paper presents a detailed morphotaxonomic study of the *Crassostrea*, *Dendostrea*, *Ostrea*, *Saccostrea* and *Hyotissa* species from the northern Rakhine coastal area, aiming at a better understanding of their identity. Specimens of the *C. belcheri*, *C. gigas* and *S. cucullata* are also investigated to widen the basis for reviewing the taxonomy and systematics of the genus and have been found to be the principal edible oyster species of Myanmar. Samples from the type locality of *S. scyphophilla*, *Hyotissa hyotis* and *H. inermis* are also studied in this manner for the first time. This study provided an analysis of the currently available data and made environmental and geographical inferences focused on supporting complementary activities, such as habitats and distribution of oysters.

Acknowledgements

I am indebted to Dr Win Naing, Rector of Sittway University and Dr Khin Maung Zaw, Pro-Rector of Sittway University, for their encouragement and support in preparing this work. I am very grateful to Dr Mya Kyawt Wai, Professor and Head of the Department of Marine Science, Sittway University, for her valuable suggestions and constructive criticisms of this study. I would like to express my sincere thanks to colleagues of Field Observation Group, Department of Marine Science, Sittway University, for their kindly helping me in many ways during the field trip. Many thanks go to Daw Lwin Lwin, Retired Lecturer of the Department of Marine Science, Mawlamyine University, for her assistance in the preparation of the manuscript. I would like to thank my beloved parents, U Win Maung and Daw Than Than Aye, for their physical, moral and financial support throughout this study.

References

Amaral, V. S. d. and Simone, L. R. L. (2014). Revision of genus *Crassostrea* (Bivalvia: Ostreidae) of Brazil. *Journal of the Marine Biological Association of the United Kingdom*. 1-26.

Amaral, V. S. d. and Simone, L. R. L. (2016). Comparative anatomy of five species of *Saccostrea* Dollfus and Dautzenberg, 1920 (Bivalvia: Ostreidae) from the Pacific Ocean. *The Nautilus*. **130**(2): 53-71.

Amaral, V. S. d., Simone, L. R. L., Tâmega, F. T. d. S., Barbieri, E., Calazans, S. H., Coutinho, R. and Spotorno-Oliveira, P. (2020). New records of the non-indigenous oyster *Saccostrea cucullata* (Bivalvia: Ostreidae) from the southeast and south Brazilian coast. *Regional Studies in Marine Science*. **33**: 1-6.

Bussarawit, S., Cedhagen, T., Shirayama, Y. and Torigoe, K. (2010). *Field Guide to The Oyster Fauna of Thailand*. Kyoto University Press, Japan, 47 pp.

Feng, D., Li, Q., Yu, H., Zhao, X. and Kong, L. (2015). Comparative Transcriptome Analysis of the Pacific Oyster *Crassostrea gigas* Characterized by Shell Colors: Identification of Genetic Bases Potentially Involved in Pigmentation. *PLoS ONE*. **10**(12): 1-17.

Harry, H. W. (1985). Synopsis of the supraspecific classification of living oysters (Bivalvia: Gryphaeidae and Ostreidae). Veliger. **28**(2): 121-158.

Klinbunga, S., Khamnamtong, B., Puanglarp, N., Jarayabhand, P., Yoosukh, W. and Menasveta, P. (2005). Molecular Taxonomy of Cupped Oysters (*Crassostrea*, *Saccostrea*, and *Striostrea*) in Thailand Based on COI, 16S, and 18S rDNA Polymorphism. Marine Biotechnology. **7**: 306-317.

Lam, K. and Morton, B. (2003). Hong Kong's subtidal oysters (Bivalvia: Ostreidae and Gryphaeidae). *In*: Morton, B. (Ed). Perspectives on Marine Environmental Change in Hong Kong, 1977-2001. *Hong Kong University Press.* pp. 311-327.

Lam, K. and Morton, B. (2004). The oysters of Hong Kong (Bivalvia: Ostreidae and Gryphaeidae). *The Raffles Bulletin of Zoology*. **52**(1): 11-28.

Li, C., Haws, M., Wang, H. and Guo, X. (2017). Taxonomic classification of three oyster (Ostreidae) species from Myanmar. *Journal of Shellfish Research*. **36**(2): 365-371.

Li, C., Wang, H. and Guo, X. (2017). Classification and taxonomic revision of two oyster species from Peru: *Ostrea megodon* (Hanley, 1846) and *Crassostrea talonata* (Li & Qi, 1994). *Journal of Shellfish Research*. **36**(2): 359-364.

Lovatelli, A. (1991). *Regional seafarming resources atlas* (*Vol. II*). Bangkok, Thailand: FAO/UNDP Regional Seafarming Development and Demonstration Project (RAS/90/002).

Mar Lar Myo Sein. (1982). The taxonomy and distribution of Burmese marine bivalves. Unpublished MSc Thesis, Department of Zoology, Art and Science University, Rangoon. Burma.

Morris, S. (1985). Preliminary guide to the oysters of Hong Kong. *Asian Mar. Biol*. **2**: 119-138.

Morton, B. S. (1990). Life cycle and sexual strategy of *Saccostrea cucullata* (Bivalvia: Ostreidae) from a Hong Kong mangrove. *Am. Malac. Bull*. **8**(1): 1-8.

Noseworthy, R. G., Hee-Jung, L., Sang-Duk, C. and Kwang-Sik, C. (2016). Unique substrate preference of *Ostrea denselamellosa* Lischke, 1869 (Mollusca: Ostreidae) at Haechang Bay, on the south coast of Korea. *Korean J. Malacol*. **32**(1): 31-36.

Poutiers, J. M. (1998). Bivalves. *In*: Carpenter, K. E. and Niem, V. H. (Eds). FAO Species Identification Guide for Fishery Purposes. The Living Marine Resources of the Western Central Pacific. Volume 1. Seaweeds, Corals, Bivalves and Gastropods. *Food and Agriculture Organization, Rome*. pp. 123-362.

Ruesink, J. L., Feist, B. E., Harvey, C. J., Hong, J. S., Trimble, A. C. and Wisehart, L. M. (2006). Change in productivity associated with four introduced species: ecosystem transformation of a "pristine" estuary. *Mar. Ecol. Prog. Ser*. **311**: 203-215.

Ruesink, J. L., Lenihan, H. S., Trimble, A. C. Heiman, K. W., Micheli, F., Byers, J. E. and Kay, M. C. (2005). Introduction of nonnative oysters: ecosystem effects and restoration implications. *Ann. Rev. Ecol. Evol. Syst*. **36**: 643-689.

Siddiqui, G. and Ahmed, M. (2002). Oyster species of the sub tropical coast of Pakistan (northern Arabian Sea). *Indian Journal of Marine Sciences*. **31**(2): 108-118.

Stenzel, H. B. (1971). Oysters. *In*: Moore, R. C. (Ed.). Treatise on invertebrate paleontology. *Lawrence, K.S: Geological Society of America and University of Kansas*, pp. iv + 953-1224.

Thomson, J. M. (1954). The genera of oysters and the Australian species. *Aust. J. Mar. Freshw. Res*. **5**: 132-168.

Torigoe, K. (1981). Oysters in Japan. *J. Sci. Hiroshima University*. **29**(2): 291-419.

Estimating Time Series Biovolume and Carbon Biomass of Phytoplankton in the Coastal Water of Tateyama Bay, Japan

Khin Khin Gyi*

Abstract

Time series distributions of phytoplankton biovolume and carbon biomass were monitored every 4 h interval from 12 h of 12 May 2017 to 8 h on 13 May 2017 in a coastal area of Tateyama Bay, Japan. The vertical patterns of phytoplankton carbon biomass changed with tidal events which modulate periods of water stratification and mixing. In the low tide samplings, a heterogeneous pattern in phytoplankton carbon biomass distribution was detected related to thermal stratification. In contrast, phytoplankton carbon biomass showed a more homogenous pattern in distribution during deep-mixing periods. Throughout the whole samplings, the distribution pattern of phytoplankton carbon biomass was generated by the dominant dinoflagellates *Prorocentrum micans* and *Scrippsiella trochoidea*. The carbon biomass of phytoplankton was high in the day-time samplings 12 and 16 h due to high temperature and light intensity which may create suitable conditions for high phytoplankton abundance. At night-time samplings, which were during the high tide, the water mass changed, and the low temperature and light intensity may induce a decrease in phytoplankton abundance and carbon biomass.

Keywords: carbon biomass, light, mixing, stratification, temperature, tide

Introduction

The structure of the planktonic community characterized by its species composition, size spectra, or trophic relationship among its components is one of the main determinants of the ecosystem's functioning and dynamics (Tilman 1999). The size structure of plankton assemblages, understood as the partitioning of biomass among species of different cell sizes as it affects the abundance and diversity of organisms is a key characteristic of pelagic ecosystems (Marañón 2015). Plankton cell size ranges over several orders of magnitude: from less than 2 µm in equivalent spherical diameter for the picoplankton, 2-20 µm for the nanoplankton, 20-200 µm for the microplankton, and up to 20-200 cm for the megaplankton (Wotton 1994). The relative abundance of small and large cells of plankton

* Lecturer, Dr., Department of Marine Science, Mawlamyine University

can influence the ecosystem stability, productivity, and the global biogeochemical cycles of major elements (Acevedo-Trejos 2015). Most of the biomass produced by small phytoplankton is thought to be quickly recycled within the euphotic zone, while large phytoplankton cells drive the biological pump by rapidly transporting carbon to the ocean interior (Marañón 2015).

Phytoplankton cell size affects numerous other functional traits and crucial physiological and ecological processes, including light absorption, nutrient uptake, sinking, and grazing (Litchman and Klausmeier 2008, Finkel *et al*. 2010). A complex interplay of environmental conditions (e.g., temperature and nutrient concentrations), interspecific relationships (e.g., predation and competition), and dispersal contribute to creating heterogeneous patterns of phytoplankton community size structures (Follows *et al*. 2007, Ward *et al*. 2012). Thus, assessment of the structural aspects of phytoplankton (i.e., size-specific species composition, abundance, and biomass) is one of the important approaches in aquatic ecology studies. Phytoplankton size measurement and reliable conversion of cell volume (biovolume) into species and community carbon biomass are key components of the phytoplankton monitoring programs.

Materials and Methods

Sampling site and sample collection

Phytoplankton samples were collected at a coastal site (35º00.06′ N, 139º49.87′ E; 23 m depth) of Tateyama Bay, Japan (Fig.1), using a submersible pump from 0 to 14 m at 0.5 m interval, and at 2 m interval below 14 to 20 m depth. The samplings were performed from a training ship Seiyo-maru (Tokyo University of Marine Science and Technology) while anchoring and water samples were collected from the faucet connected to the water intake pipe which was set to the prescribed sampling depths by lowering it with the help of a shipboard crane. A total of six samplings were done every 4h of predetermined times (12, 16, 20, 00, 04, and 08 h) on 12-13 May 2017. Water samples of 500 mL were collected for phytoplankton analysis and stored in 500 mL polyethylene bottles and fixed with formalin (final concentration 1%). During each time of sampling, the surface to bottom CTD (JFE Advantech, AAQ-PRO 2) observation was done to record the vertical profile of the water column conditions.

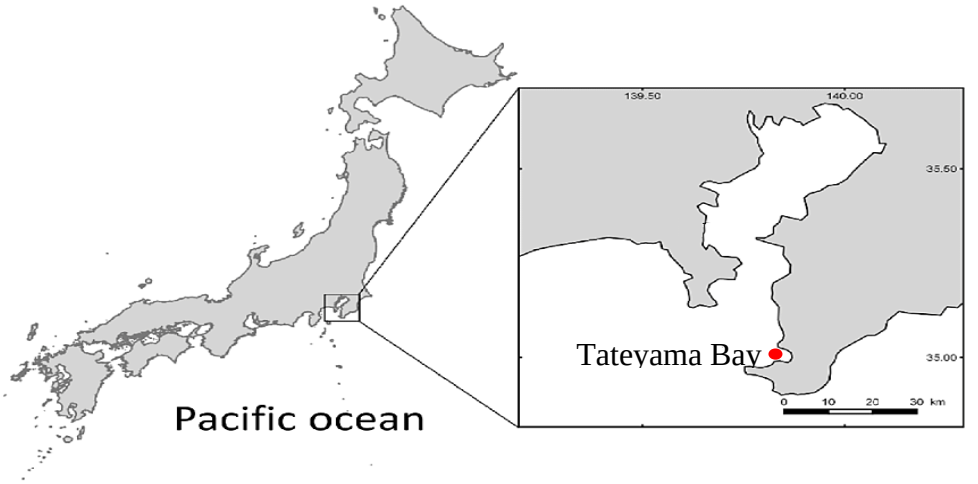

Figure 1. Sampling site in Tateyama Bay, Japan.

Phytoplankton analysis

Phytoplankton samples were analyzed with a FlowCAM® (Fluid Imaging Technologies, Yarmouth, ME, USA, Fig. 2) in triplicate under the autoimage mode with 10x objective lens and 100 µm flowcell (FC-100).

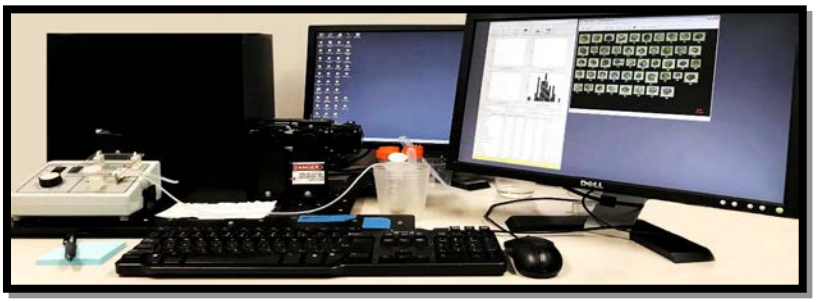

Figure 2. Flow Cytometer and Microscope (FlowCAM®).

Estimation of phytoplankton biovolume and carbon biomass

Biovolume was calculated using the mean linear dimension of each phytoplankton taxon (at least 20 individuals of FlowCAM® length and width measurements were used for the manual calculation) and converted into biovolume according to the shape manually assigned (i.e., shape-based)

which is described in detail below. For low cell density taxa (e.g., *Alexandrium* sp. and *Ceratium fusus*), the calculation of the mean dimension was based on the number of cells observed during sampling. In the case of chain-forming taxa, the single-cell dimension was considered rather than the chain length. After that, each phytoplankton taxon was separated into 12 morphological groups (box, cylinder, cone, and 3 cylinders, cone and half-sphere, 2 cones, ellipsoid, half sphere, prism on elliptic-base girdle view, prism on parallelogram-base, prolate spheroid or rotational ellipsoid, sphere, 2 truncated cones, and 2 cylinders) using a geometrical approximation of its form from the literature (Hillebrand *et al*. 1999, Sun and Liu 2003, Olenina *et al*. 2006, Baek *et al*. 2009) for the biovolume estimation. Since the FlowCAM® provides 2-dimensional measurements (length and width), the estimation of height for each taxon was taken from the literature (Olenina *et al*. 2006). Biovolume was converted into carbon biomass according to the functional classes described by Menden-Deuer and Lessard (2000).

Results

Hydrological conditions

During 12 and 16 h, before lower high tide, the vertical structure of the water column was relatively stable, and the upper layer (top 6 m) was heated by the solar radiation (850-150 µmol photons $m^{-2}s^{-1}$) with certain temperature gradients (18.5-17.0°C) resulting in the formation of density discontinuity water layers. During flood flow (lower high tide 20 h), the water column condition changed due to the intrusion of colder and saltier water from the bottom. This intrusion mixed vertically the water column but was not strong enough to break a shallow layer thermocline at 1-6 m depth. The following sampling (00 h) took place during the higher low tide when the water intrusion of the flood tide moved downward, and a thermocline was found at a deeper depth of 16-19 m. At 04 and 08 h, as the higher high tide approached, the water column was well-mixed (Fig. 3).

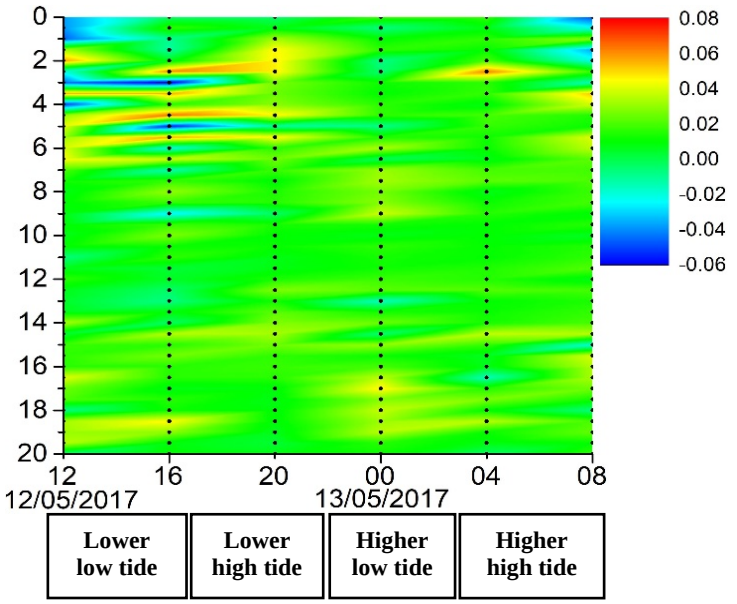

Figure 3. Brunt-Väisälä frequency (s^{-1}).

Phytoplankton community

In the present study, a total of 22 phytoplankton taxa, including 9 diatoms (Bacillariophyceae), 10 dinoflagellates (Dinophyceae), and 3 species belong to Raphidophyceae, Dictyochophyceae, and Haptophyceae were identified. Hence, the phytoplankton community was mainly dominated by diatoms and dinoflagellates (51% and 41% of the total phytoplankton). Other phytoplankton classes including Raphidophyceae, Dictyochophyceae, Haptophyceae, and the unidentified phytoplankton were altogether accounted for only 8% of the total phytoplankton abundance. The dominant species in the sampling period were *Dactyliosolen fragilissimus* 13.9%, *Pseudo-nitzschia* sp. 7.2%, *Thalassiosira* sp. 27.5%, *Prorocentrum minimum* 20.5%, *Scrippsiella trochoidea* 12.6%, and *Gyrodinium spirale* 3.9%, respectively.

Phytoplankton carbon biomass

A taxonomic list of phytoplankton expressed either as biovolume or carbon biomass was given in Table 1. The carbon content of *Noctiluca scintillans* was excluded in the calculation of total phytoplankton carbon

biomass because this heterotrophic species with extensive vacuoles occupies huge cell volume and carbon biomass. Also, *N. scintillans* ingested

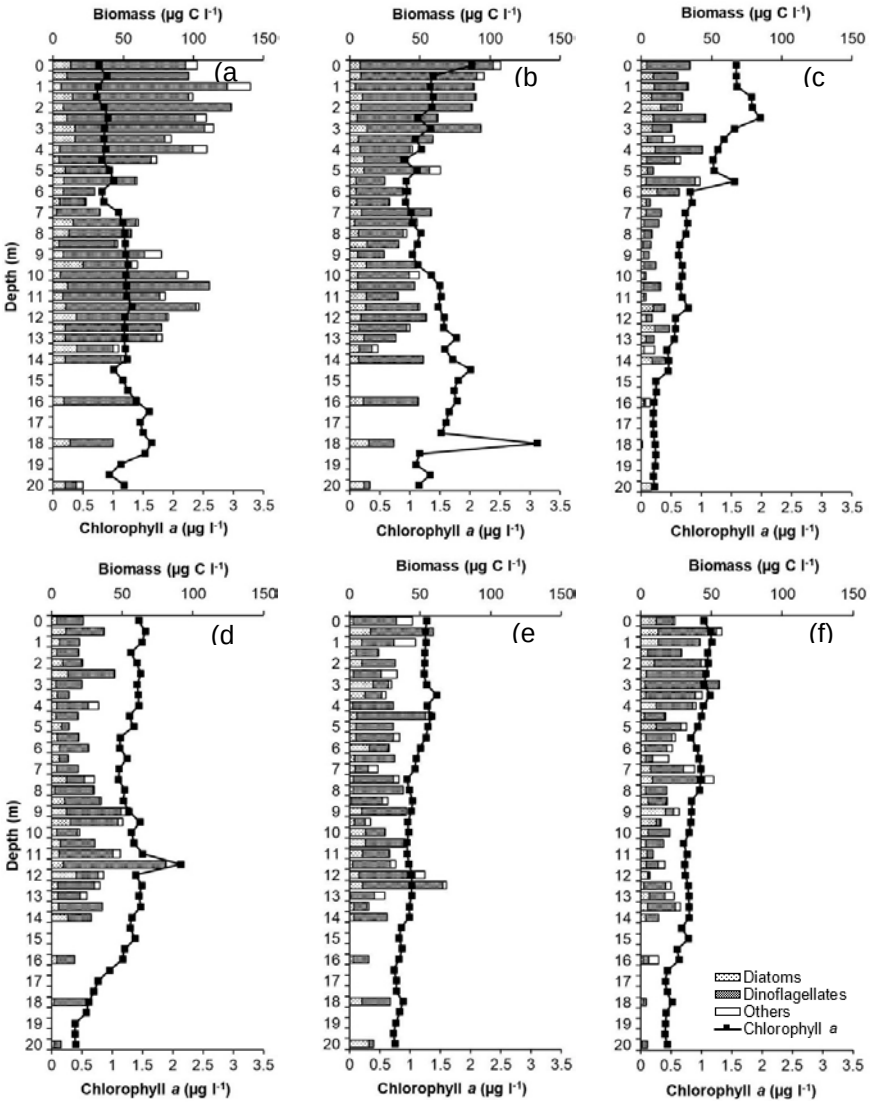

Figure 4. Vertical distributions of total phytoplankton carbon biomass (µg Cl^{-1}) during six sampling times (a: 12, b: 16, c: 20, d: 00, e: 04 and f: 08 h). Biomass illustrated by stacked bars (diatoms, dinoflagellates and others) and lines with markers (Chl-*a*).

many prey items (including phytoplankton and zooplankton species, etc.) and it is difficult to estimate how much percentage of carbon biomass they grazed from these prey items in field-collected *Noctiluca* samples. Therefore, *N. scintillans* was considered an exception in the calculation of biovolume and total phytoplankton carbon biomass.

During the study period, the bulk of the carbon biomass 76% was dominated by the dinoflagellates with a major contribution of *S. trochoidea* (36.45%), *Gyrodinium spirale* (17.96%), and *P. minimum* (13.35%). Diatoms and other phytoplankton groups accounted for only 18% and 6%. Indeed, the distribution of total phytoplankton carbon biomass was influenced by the dominant dinoflagellate species *P. minimum*, *S. trochoidea,* and *Gyrodinium spirale*. The total phytoplankton biomass was higher in the first two sampling times (12 and 16 h, before lower high tide), ranging from 14.3 to 140.4 µg C l^{-1}, with higher biomass in the upper layers but a relatively low carbon concentration was noted at a depth of chl-*a* peak 18 m (Figs. 4a, 4b). After the lower high tide, at 20 h, the biomass distribution pattern changed, and a high concentration of carbon (up to 40 µg C l^{-1}) was observed in the thermal layers (1-6 m) where chl-*a* showed the maximum, but suddenly decreased to half of the concentration (less than 20 µg C l^{-1}) below the thermocline towards the bottom (Fig. 4c). At 00 h, carbon biomass was higher above the thermal layers (16-19 m) and reached the maximum value (80.8 µg C l^{-1}) at a high chl-*a* depth of 11.5 m (Fig. 4d). During 04 and 08 h, the biomass was more uniform in the water column due to the increased water mixing generated by higher tidal current (Figs. 4e, 4f).

Discussion

In this study, water stratification and mixing associated with periodic changes in tidal currents played major physical factors influencing the vertical patterns of phytoplankton biomass distribution. Dinoflagellates dominated the total phytoplankton carbon biomass due to their higher carbon content (Menden-Deuer and Lessard 2000) and the vertical pattern of biomass distribution was influenced by the predominant dinoflagellates *P. minimum* and *S. trochoidea*. A great difference in phytoplankton biomass was found before (14.3-140.4 µg C l^{-1}) and after high tide (0.6-80.8 µg C l^{-1}) due to the changes of these dominant species' abundance and distribution related to the tidal-induced stratification and mixing and species-specific

Table 1. A taxonomic list of phytoplankton taxa from Tateyama Bay with total abundance and percentage distribution, linear dimensions (µm), biovolume (µm^3), carbon biomass (pgC cell^{-1}) and total carbon biomass (µgC l^{-1}) and percentage distribution.

Phytoplankton	Total abundance		Length	Width	Shape code	Biovolume	Carbon	Total carbon	
	cells ml^{-1}	%	(µm)	(µm)		(µm^3)	(pgC cell^{-1})	µgC l^{-1}	%
Bacillariophyceae									
Coscinodiscus sp.	183	1.4	50	37.7	C[a]	55785.6	2036.2	373.3	5.0
Dactyliosolen fragilissimus	1776	13.9	23	12	C[a]	2599.9	169.4	300.9	4.03
Lauderia annulata	37	0.3	23.7	16.9	C[a]	5313.6	302.5	11.1	0.15
Meuniera membranacea	6	0.05	57.8	31.1	PEB[b]	40711.3	1577.1	10	0.13
Pleurosigma sp.	49	0.4	150.6	20.2	PPB[a]	30725.4	1255.3	61.1	0.82
Pseudo-nitzschia spp.	927	7.2	30.3	4.6	PPB[a]	250.8	25.4	23.6	0.32
Rhizosolenia setigera	17	0.1	379	5.2	C[a]	8044.8	423.4	7.1	0.09
Thalassionema nitzschioides	13	0.1	25	2.9	B[a]	210.25	22	0.3	0.004
Thalassiosira sp.	3520	27.5	18.9	12.5	C[a]	2318.2	154.4	544.1	7.29
Dinophyceae									
Alexandrium sp.	7	0.05	41.1	37.2	PS[c]	29575.4	3487.4	23.2	0.31
Ceratium furca	23	0.2	153.6	34.2	CO3C[b]	31271.9	3650.4	85.2	1.14
Ceratium fusus	7	0.05	343.7	30.5	2TCO2C[d]	29077.8	3439.3	22.9	0.31
Gonyaulax spinifera	10	0.1	29.6	23.1	COHS[b]	12410.3	1712.5	17.1	0.23
Gyrodinium spirale	501	3.9	60.9	36.8	E[a]	21443	2680	1340.9	17.96
Heterocapsa sp.	177	1.4	30.7	21.1	2CO[c]	3553.7	614.9	109	1.46
Oxyphysis oxytoxoides	76	0.6	56.9	19.4	PS[b]	11135.7	1567	119.6	1.60

Phytoplankton	Total abundance		Length	Width	Shape code	Biovolume	Carbon	Total carbon	
	cells ml^{-1}	%	(µm)	(µm)		($µm^3$)	(pgC $cell^{-1}$)	µg C l^{-1}	%
Prorocentrum minimum	2622	20.5	22.2	18.5	E[a]	1975.5	380.2	996.8	13.35
Protoperidinium quinquecrone	253	2.0	23.7	18.7	COHS[b]	6505.8	1009	255.6	3.42
Scrippsiella trochoidea	1612	12.6	29.1	23.1	COHS[b]	12189.5	1687.5	2721.4	36.45
Dictyochophyceae									
Dictyocha speculum	10	0.1	29.5	21.3	HS[c]	2516.1	337.1	3.5	0.05
Haptophyceae									
Coccolithophorid	468	3.7	13.2	12.3	S	967.7	137.4	64.3	0.86
Raphidophyceae									
Heterosigma akashiwo	303	2.4	29.8	24.3	PS[c]	9150.2	1133	343.7	4.60
Unidentified phytoplankton	205	1.5	13.9	11.9	S	876.3	195.4	21.5	0.29

C=cylinder, PPB=prism on parallelogram-base, PEB=prism on elliptic-base, E= ellipsoid, CO3C=cone+3 cylinder, COHS=cone+half sphere, PS=prolate spheroid or rotational ellipsoid, HS= half sphere, 2CO= 2 cones, S=sphere, B=box, 2TCO2C=2 truncated cones+2 cylinder. (a: Hillebrand *et al*. 1999, b: Sun and Liu 2003, c: Olenina *et al*. 2006, d: Baek *et al*. 2009)

responsiveness to the hydrodynamic gradients. Indeed, *S. trochoidea* contains much more carbon 1687.5 pgC cell^{-1} than *P. minimum* 380.2 pgC cell^{-1}, which most contributed to the total phytoplankton biomass and drove the general distribution pattern. Many studies suggested that chl-*a* concentration is the best proxy for the estimation of phytoplankton biomass, but it is not always consistent that chl-*a* maximum may coincide with high phytoplankton biomass. In this study, phytoplankton biomass maximum was not always matched with chl-*a* peak, especially at 12 and 16 h (Figs. 4a, 4b). At these sampling times, the chl-*a* peak was observed at the bottom layer, 18 m, but the phytoplankton biomass was relatively low with the higher contribution of small-sized diatoms (e.g., *Pseudo-nitzschia* sp., *Thalassiosira* sp.). Hence, a research question occurs why chl-*a* showed a peak? According to Khin Khin Gyi *et al*. (2019), the high value of chl-*a* in the bottom layer was related to the whirling-up of the deposited aggregated particles which still keep chl-*a* pigment in their cells. Therefore, chl- *a* concentration sometimes shows a high value in the bottom layer even though the phytoplankton carbon biomass was lower.

Conclusions

Time series vertical patterns of phytoplankton carbon biomass distribution are related to the water stratification and mixing processes influenced by the periodic changes of tidal currents observed in the sampling site of the Tateyama Bay coastal area. In the low tide samplings, phytoplankton biomass showed fluctuations through the vertical water column resulting from the influence of thermal stratification. Moreover, an increase in the phytoplankton abundance and carbon biomass was recorded probably due to high temperature and light availability. Conversely, vertical mixing modulates homogeneity in phytoplankton carbon biomass distribution in the water column, especially in deep-mixing periods generated by the high tidal current. Additionally, a decrease in carbon biomass was observed during the mixing period characterized by low water temperature and low solar radiation. Furthermore, the fluctuations in the phytoplankton carbon biomass were related to the species-specific distributions because each phytoplankton responds differently depending on their preferred environmental variables.

Acknowledgments

The author's sincere thanks are extended to the academic supervisor Professor Dr. Yuji Tanaka and co-supervisor Dr. Takuo Omura for their kind supervision and supportive help throughout the research. Special thanks are also to the Laboratory of Aquatic Science Consultant Co., Ltd. which provided the use of a FlowCAM® and lab facilities, the captains, and crew members of a training ship "Seiyo-maru" and students of Plankton Lab who helped during field sampling. This research was partially supported by the Monbukagakusho Scholarship for K.K.G, and also by JSPS KAKEN-HI Grant Numbers JP18H02263 for YT. Finally, the author would like to express the deepest gratitude and appreciation to the Ministry of Education, Myanmar, and the Department of Marine Science, Mawlamyine University, and the Rector of Mawlamyine University, Dr. Aung Myat Kyaw Sein for permitting me to study abroad in Japan.

References

Acevedo-Trejos, E., Brandt, G., Bruggeman, J. and Merico, A. (2015). Mechanisms shaping size structure and functional diversity of phytoplankton communities in the ocean. Scientific Reports, 5: 8918, 1-8.

Baek, S.H., Shimode, S., Shin, K., Han, M.S. and Kikuchi, T. (2009). Growth of dinoflagellates, *Ceratium furca* and *Ceratium fusus* in Sagami Bay, Japan: the role of vertical migration and cell division. Harmful Algae 8: 843-856.

Finkel, Z.V., Beardall, J., Flynn, K.J., Quigg, A., Rees, T.A.V. and Raven, J.A. (2010). Phytoplankton in a changing world: cell size and elemental stoichiometry. J. Plankton Res. 32, 119-137.

Follows, M.J., Dutkiewicz, S., Grant, S. and Chisholm, S.W. (2007). Emergent biogeography of microbial communities in a model ocean. Science 315, 1843-1846.

Hillebrand, H., Dürselen, C.D., Kirschtel, D., Pollingher, D. and Zohary, T. (1999). Biovolume calculation for pelagic and benthic microalgae. J. Phycol., 35: 403-424.

Khin Khin Gyi, Omura, T., Nakamura, R. and Yuji, T. (2019): High-resolution observation on fine-scale spatial and temporal heterogeneity of phytoplankton community using FlowCAM. La mer, 57 (3-4): 73-87.

Litchman, E. and Klausmeier, C.A. (2008). Trait-based community ecology of phytoplankton. Annu. Rev. Ecol. Evol. Syst. 39: 615-39.

Marañón, E. (2015). Cell size as a key determinant of phytoplankton metabolism and community structure. Ann. Rev. Mar. Sci. 7: 241-264.

Menden-Deuer, S. and Lessard, E.J. (2000). Carbon to volume relationships for dinoflagellates, diatoms, and other protist plankton, Limnol. Oceanogr., 45: 569-579.

Olenina, I., Hajdu, S., Edler, L., Andersson, A., Wasmund, N., Busch, S., Göbel, J., Gromisz, S., Huseby, S., Huttunen, M., Jaanus, A., Kokkonen, P., Ledaine, I. and Niemkiewicz, E. (2006). Biovolumes and size-classes of phytoplankton in the Baltic Sea. HELCOM Balt. Sea Environ. Proc. No. 106, 144 pp.

Sun, J. and Liu, D. (2003). Geometric models for calculating cell biovolume and surface area for phytoplankton. Journal of Plankton Research, 25 (11): 1331-1346.

Tilman, D. (1999). The ecological consequences of changes in biodiversity: a search for general principles. Ecology 80, 1455–1474.

Ward, B.A., Dutkiewicz, S., Jahn, O. and Follows, M.J. (2012). A size-structured food-web model for the global ocean. Limnol. Oceanogr. 57, 1877-1891.

Wotton, R.S. (1994). The biology of particles in aquatic ecosystems. Second Edition. Lewis Publishers. 325 pp.

Study on the Genus *Hypnea* J. V. Lamouroux (1813) (Gigartinales, Rhodophyta) of Myanmar

Sein Moh Moh Khaing[1] & Jar San[2]

Abstract

The plants of the genus *Hypnea* J. V. Lamouroux **(**1813) from 25 stations along three Coastal Regions of Myanmar are composed of 11 species belonging to family Cystocloniaceae falling under the order Gigartinales collected from field observation from 2013 to 2017, were identified using liquid-preserved and living specimens in the field, based on the external morphology of the vegetative and reproductive structures of these species. The species comprised *H. saidana* Holmes, *H. pannosa* J. Agardh, *H. esperi* Bory, *H. charoides* J. V. Lamouroux, *H. spinella* (C. Agardh) Kützing, *H. musciformis* (Wulfen) J. V. Lamouroux, *H. cenomyce* J. Agardh, *H. valentiae* (Turner) Montagne, *H. hamulosa* (Esper) J. V. Lamouroux, *H. boergesenii* Tanaka, and *H. flagelliformis* Greville ex J. Agardh. Moreover, descriptions, habitats and distribution of these species along three coastal regions of Myanmar were described.

Keywords: external, *Hypnea*, morphology, Myanmar, ocean, world.

Introduction

The genus *Hypnea* J. V. Lamouroux **(**1813) is well known within the family Cystocloniaceae of the order Gigartinales by its wide geographic distribution, a large number of species and economic importance for the production of carrageenan. One hundred and twelve names have been assigned to *Hypnea* J. V. Lamouroux **(**1813) of which fifty-five are currently listed as accepted in AlgaeBase (Guiry and Guiry 2020).

Of these species, 13 species of *Hypnea* namely, *H. hippuroides* Kützing, *H. cervicornis* J. Agardh, *H. hamulosa* (Turner) Montagne, *H. spinella* (C. Agardh) Kützing, *H. chordacea* Kützing, *H. valentiae* (Turner) Montagne, *H. flagelliformis* Tanaka, *H. boergesenii* Tanaka, *H. charoides* Lamouroux, *H. saidana* Holmes, *H. pannosa* J. Agardh, *H. esperi* Bory, and *H. cenomyce* J. Agardh were recorded from three coastal regions of

[1] Lecturer, Dr., Department of Marine Science, Mawlamyine University
[2] Lecturer, Dr., Department of Marine Science, Mawlamyine University

Myanmar by Aung Myint 1975, Kyaw Soe and Kyi Win 1977, Soe-Htun 1998, Soe-Htun *et al*. 2009 a, Soe-Htun *et al*. 2009 b, Hlaing Hlaing Htoon 2009, Zayar Aung 2012, Myo Min Tun 2013 and Thet Htwe Aung 2013. Moreover, eleven species of *Hypnea* J. V. Lamouroux **(**1813) are recorded for the Myanmar coast after Thet Htwe Aung 2013 by Sein Moh Moh Khaing 2017. According to worldwide literatures, taxonomic and phytogeographic relationships of *Hypnea* along the tropical and subtropical coasts around the world were studied by Tanaka 1941, Lucas and Perrin 1947, Durairatnam 1961, Silva, Basson & Moe 1996, Coppejans *et al.* 2009 and 2010, Braune and Guiry 2011. The main objectives of this study are: 1) to identify the diversified species of the genus *Hypnea* and 2) to investigate the species distribution of *Hypnea* from three coastal regions of Myanmar.

Materials and Methods

The live and herbarium specimens of the genus *Hypnea* J. V. Lamouroux **(**1813) were collected from 1972 to 2017 from the following (25) collection sites: 1. Sittwe Point, 2. Kyauk Phyu, 3. Nat Kyauk, 4. Adams Point, 5. Thamihla Island, 6. Mazin, 7. Ngapali, 8. A Paw Ye Island, 9. Gyeik Taw, 10. Leik Tet Gyaing, 11. Maung Shwe Lay Gyaing, 12. Moe Gyoe Pyit Gyaing, 13. Sin Phyu Gyaing, 14. Wetthay Gyaing, 15. Makyee, 16. Ngwe Saung, 17. Pashyu Gyaing, 18. Zeagyaing, 19. Mawtin Point, 20. Setse, 21. Kalegauk Island, 22. Maungmagun, 23. Thabawseik, 24. Kampani and 25. Wa Maw (Fig. 1). All collections were preserved in 4% formaldehyde in seawater and also mounted on the herbarium sheets. Herbarium sheets, mounted slide, liquid-preserved and living specimens were used for detailed investigations that emphasized on external structures such as height of thallus, color, holdfast, branches and branchlets. All materials prepared for observations are deposited in the Herbarium of the Department of Marine Science, Mawlamyine University.

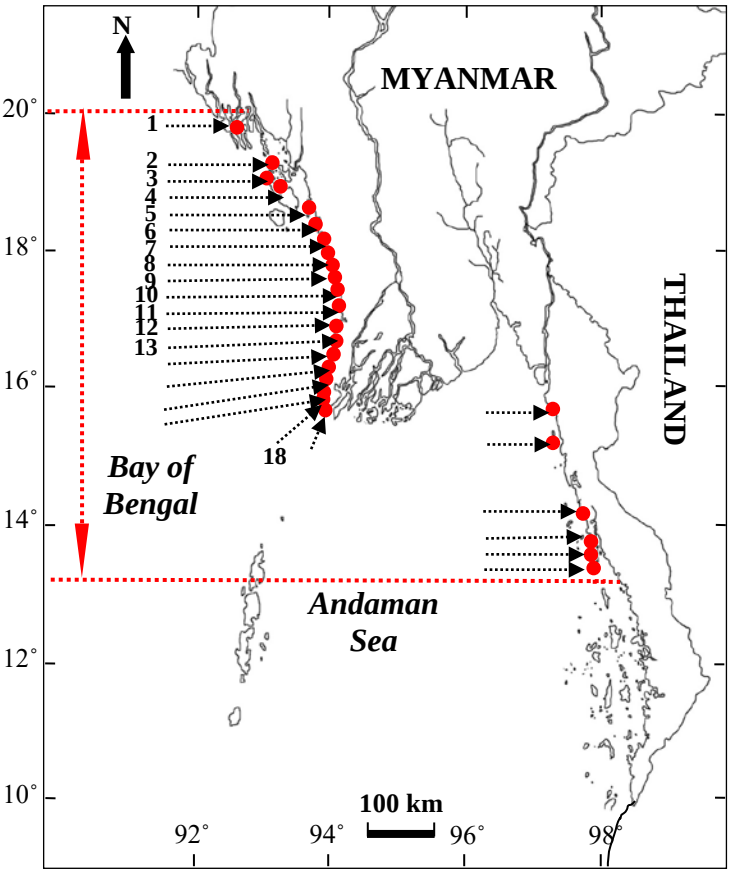

Figure 1. Map showing the collection sites of the eleven species of the genus *Hypnea* J. V. Lamouroux **(**1813) along three Coastal Regions of Myanmar. Distribution range of the genus *Hypnea* J. V. Lamouroux **(**1813).

Results and Discussion

A classification system of the genus *Hypnea* J. V. Lamouroux (1813)

Phylum: Rhodophyta

Class: Florideophyceae

Order: Gigartinales

Family: Cystocloniaceae Kützing 1843

Genus: *Hypnea* J. V. Lamouroux 1813

Species: 1. *H. saidana* Holmes 1896

2. *H. pannosa* J. Agardh 1847

3. *H. esperi* Bory 1828

4. *H. charoides* J. V. Lamouroux 1813

5. *H. spinella* (C. Agardh) Kützing 1847

6. *H. musciformis* (Wulfen) J. V. Lamouroux 1813

7. *H. cenomyce* J. Agardh 1851

8. *H. valentiae* (Turner) Montagne 1841

9. *H. hamulosa* (Esper) J. V. Lamouroux 1813

10. *H. boergesenii* Tanaka 1941

11. *H. flagelliformis* Greville ex J. Agardh 1851

Key to the species of *Hypnea* from Myanmar

1a. Thalli compressed, with curved branches.....***H. saidana***

1b. Thalli terete, without curved branches.....**2**

2a. Thalli with compound spinulose branchlets…….....***H. pannosa***

2b. Thalli soft without compound spinulose branchlets.....**3**

3a. Distinct main branch absent, irregular branches.....***H. esperi***

3b. Distinct main branch present and alternate branches.....**4**

4a. Branchlets mostly occur throughout the branches……..***H. charoides***

4b. Branchlets mostly occur in the basal portion of the branches……...**5**

5a. Thalli with many spines and pulviniformis fronds.....***H. spinella***

5b. Thalli without many spines and pulviniformis fronds.....**6**

6a. Branches with crozier-like hooks.....***H. musciformis***

6b. Branches without crozier-like hooks.....**7**

7a. Small discs on the apical portions of branchlets.....***H. cenomyce***

7b. Small discs on the entire portions of branchlets.....**8**

8a. Main branches with densely branchlets…….....***H. valentiae***

8b. Main branches without densely secondary branchlets.....**9**

9a. Branchlets with short spinous throughout the frond……..***H. hamulosa***

9b. Branchlets without short spinous throughout the frond.....**10**

10a. Branches with acuminate branchlets.....***H. boergesenii***

10b. Branches with divaricate branchlets.....***H. flagelliformis***

Description of the species of *Hypnea* from Myanmar

Hypnea saidana Holmes 1896 (Figs. 2-3)

Thallus compressed, growing roundish mass and intricate by irregularly compressed branches to form a cushion, up to 2 cm high, cherry red to bright red in color, subcartilaginous, attached by accessory holdfast. Primary branches are alternately in opposite directions, dichotomous with

alternate branches which are mostly directly upward and innate-like branchlets form laterally on both margins of the flattened thallus. Plants live as roundish network at the streams and intertidal zones, and epiphytically on other algae.

Hypnea pannosa J. Agardh 1847 (Fig. 4)

Thalli forming encrusted mass with loosely intricate branches, up to 3-5 cm high and 1 mm in diameter, pale red slightly tinged with purple in color, terete, subcartilaginous, attached by accessory discs which occur from the basal portions of branches and sometimes these come from the apical portion of thallus. Distinct main branch is present and branchlets occur throughout the branches of thallus. Thallus grows on rocks and in the low intertidal continuously wave-swept and attached in crevices.

Hypnea esperi Bory 1828 (Fig. 5)

Thalli forming in loose tufts, with intricate caespitose branches, attached by means of small numerous accessory holdfasts which occur throughout the main branches of thallus. Thallus is soft or dainty in texture, thread-like, minute, terete, up to 5 mm high, 280-550 µm in diameter and pale red in color. Distinct main branches are absent and long cylindrical branchlets form on the entire branches. Plants grow on exposed rocks in the intertidal zone.

Hypnea charoides J. V. Lamouroux 1813 (Fig. 6)

Thalli growing in company but not united or matted together, up to 5-7 cm high, bright red slightly tinged with brown in color, terete, subcartilaginous, attached by accessory disc and sometimes creeping branches forming secondary accessory holdfasts. Distinct main branch is present, the laterals are alternately and branchlets form on the entire branches. Thalli grow on rocks in shallow water near the shore in areas somewhat exposed to waves surf.

Hypnea spinella (C. Agardh) Kützing 1847 (Fig. 7)

Thallus purple to dark red in color, 3 cm in high, forming as intricate cushion, pulviniformis fronds, texture firm fleshy alternately

branches are freely erect, branches occur prostrate with tip rising upwards by accessory holdfast. Thallus is covered with many spines or branchlets, acutes originated from the primary branches, and more frequent in the basal parts of the plants. Plants occur as an intricate cushion or mats on rocks densely intertwined at the streams and tidal pools of intertidal zones.

Hypnea musciformis (Wulfen) J. V. Lamouroux 1813 (Fig. 8)

Thalli forming in tufts, erect and intertwined with other algae. These thalli attached to the substrata by numerous accessory disciformis holdfast, which mostly form laterally on the mature portion of the thallus. Thallus somewhat subcartilaginous, up to 10 cm tall, terete, 1-2 mm in diameter and is indutus strongly pinkish red in color. Distinct main branch absence and branchlets occur throughout the thallus. Thalli grow on submerge exposed rocks, old corals and some debris of subtidal zone.

Hypnea cenomyce J. Agardh 1851 (Fig. 9)

Thallus growing basal pulviniformis with some upper erect branches, up to 3-4 cm in high, 0.5-1 mm in width and yellowish red to greenish red in color. Their accessory holdfasts occur abundantly on the thallus, especially on the apical portions of branchlets. Thallus soft in texture, primary branch ramified dichotomously or subdichotomously, approximately 1-2 mm long and 0.5 mm broad, gradually attenuate to the growing apices, mostly end in sharp points and branchlets which occur abundantly on the entire branch. Plants form in mid to low intertidal water, shallow in rock pools, continuously wave swept.

Hypnea valentiae (Turner) Montagne 1841 (Fig. 10)

Thallus forming in tufts or patches, loosely branched, up to 6-9 cm in high, 1-2 mm in diameter, reddish brown in color, terete, subcartilaginous to soft in texture, attaching with their finer branches, on which accessory discs occur to serve as holdfast. Main branches percurrent along thallus with laterally ramifying secondary branches which occur alternately or sometimes radially and branchlets occur densely on the entire frond. Thalli live in mid to low intertidal water, shallow in rock pools, continuously wave swept.

Hypnea hamulosa (Esper) J. V. Lamouroux 1813 (Fig. 11)

Thallus densely growing in tufts or caespitose forming as cushion-like basal portion, forms in an intricate manner with decumbent branches, some erect branches ramify freely, attached by numerous accessory holdfast, most of the lower branches are anastomosing with one another. Frond rigid texture, subcartilaginous, up to 5-6 cm in high, terete, 3 mm in diameter and is reddish brown in color. Distinct main branch is absent and branchlets occur densely on the branches of thallus. Thallus grows tufts or caespitose in intertidal zones, sometimes plants attached to gravel or shell fragments.

Hypnea boergesenii Tanaka 1941 (Fig. 12)

Thalli growing caespitose, freely erect branches, up to 7-10 cm high, purplish red to reddish brown in color, terete, subcartilaginous, attached by accessory holdfast but original accessory holdfast mostly unclear because densely growing in tufts. Distinct main branch is present; the laterals are alternately in opposite directions. Simple, stout and acuminate branchlets formed along the entire branches. Plants form in mid to low intertidal water, shallow in rock pools, continuously wave swept.

Hypnea flagelliformis Greville ex J. Agardh 1851 (Fig. 13)

Thallus is erect, caespitose or bushy, attached by primary holdfast and laterally produced accessory discs which are made up of rhizoidal filamentous cells. Thallus is subcartilaginous, up to 4 cm high, approximately 1mm broad and is pale reddish brown in color. The main branch is percurrent throughout the frond. The secondary branches are generally alternative on the main branches and densely branchlets which are formed along the thallus. Plants grow as roundish network at the streams and intertidal zones.

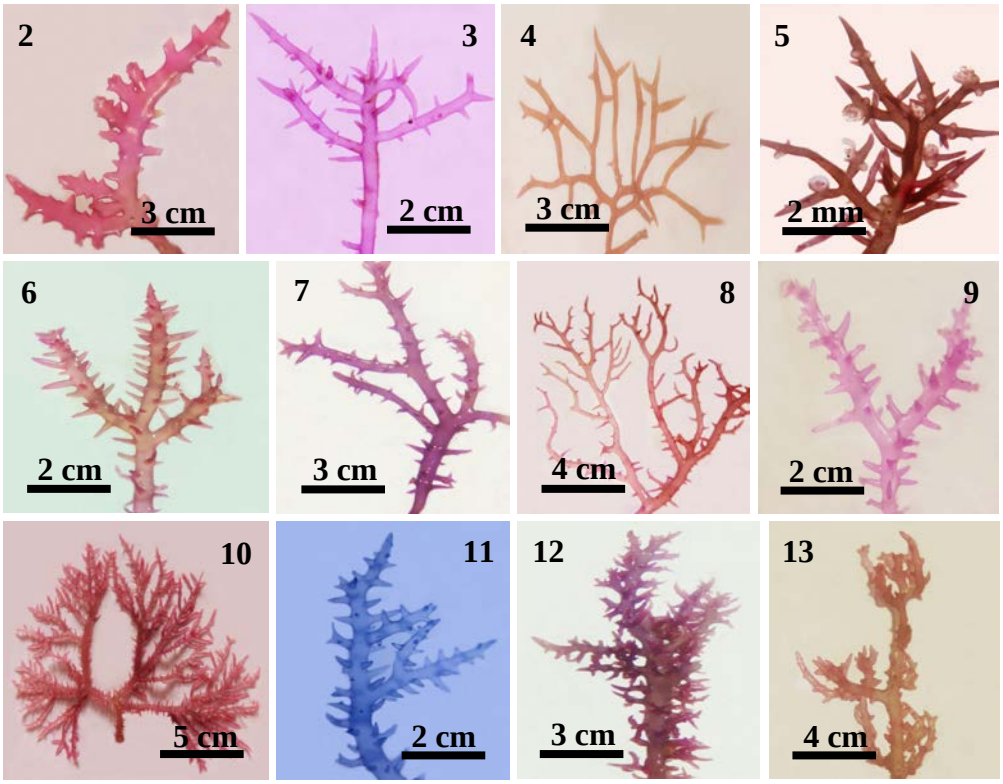

Figure 2-13. Habits of the genus *Hypnea* J. V. Lamouroux **(**1813) of Myanmar. 2-3) *H. saidana* Holmes (vegetative); 4) *H. pannosa* J. Agardh (tetrasporophyte); 5) *H. esperi* Bory (carposporophyte); 6) *H. charoides* J. V. Lamouroux (tetrasporophyte); 7) *H. spinella* (C. Agardh) Kützing (tetrasporophyte); 8) *H. musciformis* (Wulfen) J. V. Lamouroux (tetrasporophyte); 9) *H. cenomyce* J. Agardh (tetrasporophyte); 10) *H. valentiae* (Turner) Montagne (vegetative); 11) *H. hamulosa* (Esper) J. V. Lamouroux (tetrasporophyte); 12) *H. boergesenii* Tanaka (tetrasporophyte); 13) *H. flagelliformis* Greville ex J. Agardh (tetrasporophyte).

Table 1. Distribution of *Hypnea* along three coastal regions of Myanmar.

Sr No.	Name of location		***Hypnea* species**											
			H. saidana	*H. pannosa*	*H. esperi*	*H. choroides*	*H. spinella*	*H. musciformis*	*H. coenomyce*	*H. valentiae*	*H. hamulosa*	*H. boergesenii*	*H. flagelliformis*	
1.	Sittwe Point	RCR		+										
2.	Kyauk Phyu	RCR				+								
3.	Nat Kyauk	RCR				+					+	+		
4.	Adoms Point	RCR				+		+						
5.	Thamihla Island	RCR				+					+			
6.	Mazin	RCR	+				+	+			+			
7.	Ngapali	RCR			+			+			+			
8.	A Paw Ye Lel Island	RCR	+			+	+	+	+	+	+	+		
9.	Gyeik Taw	RCR	+	+								+		
10.	Leik Tet Gyaing	RCR									+			
11.	Maung Shwe Lay Gyaing	RCR		+	+	+	+	+	+	+	+	+	+	
12.	Moe Gyo Pyit Gyaing	RCR									+	+		
13.	Sin Phyu Gyaing	RCR								+			+	
14.	Wethey Gyaing	RCR		+				+	+	+				
15.	Makyee	RCR		+	+	+	+				+		+	

Sr No.	Name of location		*Hypnea* species										
			H. saidana	*H. pannosa*	*H. esperi*	*H. choroides*	*H. spinella*	*H. musciformis*	*H. coenomyce*	*H. valentiae*	*H. hamulosa*	*H. boergesenii*	*H. flagelliformis*
16.	Ngwe Saung	RCR		+	+	+	+	+	+	+	+	+	+
17.	Pashyu Gyaing	RCR									+		
18.	Zeagyaing	RCR									+		
19.	Mawtin Point	RCR	+	+		+	+	+	+	+	+	+	
20.	Setse	ACR					+						
21.	Kalegauk Island	ACR		+									
22.	Maungmagun	TCR		+	+		+	+		+			
23.	Thebawseik	TCR		+	+		+	+		+			
24.	Kampani	TCR		+				+					
25.	Wa Maw	TCR					+						
	Total occurrence		4	11	6	9	12	11	5	8	13	7	4

RCR = Rakhine Coastal Region, ACR = Ayeyarwady Delta and Gulf of Martaban Coastal Region, TCR = Tanintharyi Coastal Region.

In this study, compressed features of thallus are observed only *H. saidana*, not like in other species of *Hypnea* with terete thallus. Pinnate-like branchlets form laterally on both margins of the flattened thallus and some thorn-like branchlets occur six to eight times those compound spinulose branchlets are generally larger than the branchlets of other species of the genus *Hypnea.* Tanaka (1941) studied these thalli from Japan

are 6-10 cm, frond caespitose, blood red and yellowish red in color and more or less dichotomous branched and thallus subcartilaginous in texture. So, the length of thallus from Japan is absolutely higher than thallus of the present study from Myanmar.

In this research, the tetrasporophyte *H. pannosa* is similar to *H. esperi* in being small, but the former can be distinguished compactly caespitose form, more delicately branching, possessing cylindrical, longer, slender, and more attenuate branches. Some thorn-like branchlets are created two-five times these compound spinulose branchlets are generally larger than the simple branchlets. *Hypnea esperi* not possessed these spinulose branchlets as in *H. pannosa*.

The carposporophyte *H. esperi* are the smallest plant and slender species and shows some resemblance to *H. spinella* but the frond of the former is not so rigid as that of the latter. The tetrasporophyte *H. spinella* can be found abundantly in three coastal areas of Myanmar, but *H. esperi* are rare than other species in this study. Branchlets of *H. spinella* are spinous as in the tetrasporophyte *H. hamulosa*, but the branchlets of the former species are distinctly longer than the later. Repeatedly dividing branchlets are common in *H. hamulosa* and these are not found in *H. spinella*. The color of plants from Setse coastal areas is darker and the size of plant is smaller than Rakhine coastal regions. *H. spinella* are growing abundantly in three coastal areas of Myanmar during the study period.

H. musciformis can be recognized as the occurrence of hooked branches in the specimens. The tetrasporophyte of *H. musciformis* are found and carposprophyte are not found during the study period. The branching system found in thalli from Myanmar, these are subdichotomously or irregularly branches agreed well with the illustrations of this species given by Durairatnam (1961). In the present observation, there is no difficulting in separating *H. cenomyce* from *H. spinella* and *H. hamulosa*. In fact, the sizes of *H. cenomyce* and *H. hamulosa* in this study are relatively larger than *H. spinella.*

The vegetative thalli of *H. valentiae* are found more abundantly in Wetthay Gyaing than in other stations during field period. In mature portions, most of the branchlets are more elongated than other species of the genus *Hypnea*, cylindrical, and acute at the apices. Jha *et al*. (2009) identified the branches system of these thalli is alternately, but they not described the measurement of their thalli. Therefore, the branching system

of these thalli given by Trono and Gronier (2002), Jha *et al*. (2009) and the present study are almost the same but different from the result of Durairatnam (1961). In this study, the tetrasporophyte *H. flagelliformis* is closely related to *H. valentiae* in having distinct main branches. However, long and cylindrical branchlets of *H. valentiae* are not found in *H. flagelliformis* which has intricate and much divided branchlets. In this study, all thalli were attached by accessory holdfasts but original accessory holdfasts were mostly unclear because densely growing in tufts except *H. cenomyce* J. Agardh.

Conclusion

In the present research, *H. saidana* Holmes, *H. charoides* J. V. Lamouroux, *H. cenomyce* J. Agardh, *H. hamulosa* (Esper) J. V. Lamouroux, *H. boergesenii* Tanaka, and *H. flagelliformis* Greville ex J. Agardh were observed from Rakhine coastal region, *H. esperi* Bory, *H. pannosa* J. Agardh, and *H. spinella* (C. Agardh) Kützing were found from three coastal regions, but *H. musciformis* (Wulfen) J. V. Lamouroux, and *H. valentiae* (Turner) Montagne were not found in Ayeyarwady Delta and Gulf of Martaban coastal region.

Acknowledgements

We are thankful to Dr. Aung Myat Kyaw Sein, Rector of Mawlamyine University and Dr. San San Aye, Pro-Rector of Mawlamyine University, for their encouragement and supports in preparing this work. We are very grateful to Dr. San Tha Tun, Professor and Head of the Department of Marine Science, Mawlamyine University, for his valuable suggestions and advice throughout our research. We are also thankful to Dr. War War Nwe, Lecturer of the Department of Marine Science, Pathein University for her assistance during Ngwe Saung field collection. In addition, funding for this work from the Department of Higher Education, the Ministry of Education and the Department of Marine Science, Mawlamyine Univerity is also most appreciated.

References

Aung Myint. (1975). Studies on the Hypneaceae (Gigartinales, Rhodophyta) of Burma. M.Sc Thesis, Department of Marine Biology, Moulmein College, Myanmar.

Braune, W. and Guiry, M. D. (2011). *Seaweeds.* A.R. G. Ganter Verlag K. G. 604pp.

Coppejans, E., Leliaert, F., Dargent, O., Gunasekara, R. and Cleck, O. D. (2009). *Sri Lankan Seaweeds*. Abc Taxa, Belgian Development Cooperation. **6**: 265pp.

Coppejans, E., Prathep, A., Leliaert, F., Lewmanomont, K. and De Clerck, O. (2010). *Seaweeds of Mu Ko Tha Lae Tai* (*SE Thailand*)*: Methodologies and Field guide to the dominant species.* Biodiversity research and training program. Thailand. 274 pp.

Du Durairatnam, M. (1961). Contribution to the study of the marine algae of Ceylon. *Fish. Res. Sta.* Ceylon. **10**: 55-57.

Guiry M. D. and Guiry, G. M. (2020). *AlgaeBase*.World-wide electronic publication, National University of Ireland, Galway [http://www.algaebase.org.]

Hlaing Hlaing Htoon. (2009). Studies on the marine algae of Setse coastal area. Unpublished Master of Research Thesis, Department of Marine Science, University of Mawlamyine, Myanmar.

Jha, B., Reddy, C.R.K, Thakur, M.C. and Rao, M.U. (2009). *Seaweeds of India.* The diversity and distribution of seaweeds of Gujarat Coast. Springer Dordrecht Heidelberg London New York. 215 pp.

Kyaw Soe and Kyi Win. (1977). Seaweeds for utilization. *University Translation and Publication Department.* **2**(168): 502 pp (*in Myanmar*)

Lucas, A.H.S. and Perrin, F. (1947). *The seaweeds of south Australia. Part II. The red seweeds.* K.M. stevenson, government printer, Adelaide. 458 pp.

Myo Min Tun. (2013). The Flora and ecology and marine algae in Kampani coastal areas. Unpublished MRes Thesis Department of Marine Science. Mawlamyine University.

Sein Moh Moh Khaing. (2017). Morphotaxonomy of the carrageenophyte species of the family Cystocloniaceace (Gigartinales, Rhodophyta) of Myanmar. Unpublished PhD Thesis, Department of Marine Science, University of Mawlamyine, Myanmar.

Silva, P.C., Meñez, E.G. and Moe, R.L. (1996). *Catalogue of the benthic marine algae of the Indian Ocean*. University of California Publication in Botany. 1261 pp.

Soe-Htun, U. (1998). The seaweed resources of Myanmar. *In*: Critchley, A.T and Ohno, M. (Eds), Seaweed resources of the world. *Kanakawa International Fisheries Training Center, Japan International Cooperation Agency* (*JICA*): pp. 99-105.

Soe-Htun, Mya Kyawt Wai, Thida Nyunt, Soe Pa Pa Kyaw and Mu Mu Aye. (2009a). Notes on some marine benthic red algae of Gwa Coastal Areas II. Rhodophyta (Cryptonemiales, Gigartinales, Gracilariales, Rhodymeniales and Ceramiales). *Jour. Mya. Acad. Arts & Sc.* **7** (5): 143-181.

Soe-Htun, Mya Kyawt Wai, Thida Nyunt, Soe Pa Pa Kyaw, Yin Yin Htay and Mu Mu Aye. (2009b). Checklist, distribution and potential utilization of marine algae of Myanmar II. Rhodophyta (Red algae). *Jour. Myan. Acad. Arts & Sci*. **7**(5): 279-305.

Tanaka, T. (1941). *The genus Hypnea from Japan*. Hokkido University. 250 pp.

Thet Htwe Aung. (2013). A study on the benthic algal flora of Kalagauk Island. Unpublished Master of Science Thesis. Department of Marine Science, Mawlamyine University.

Trono, G. C. and Gronier, P. (2002). *Hypnea* J. V. Lamour. *In*: Trono, G. C. and Reine, W. F. P. (Eds), Plant resources of South East Asia. *Prosea Foundation, Bogor, Indonesia*: pp. 208-212.

Zayar Aung. (2012). Study on the marine benthic red algae of Kampani coastal areas. Unpublished MSc Thesis. Department of Marine Science. Mawlamyine University.

Species, Size and Catch Composition of Rays Landed in Myeik Areas

Khin May Chit Maung[1], Ei Thal Phyu[2] & Nyo Nyo Tun[3]

Abstract

Rays landed in Myeik areas were studied to know the species, size, and catch composition from February 2019 to January 2020. There were 16 ray species of 12 genera belonging to 5 families landed in Tha-Kay-Ta and Naukle fish landing sites. Ray species (*Brevitrygon imbricata*, *B. heterura*, *Neotrygon orientalis*, *Taeniurops meyeni*, *Rhinoptera javanica* and *Mobula thurstoni*) landed in those sites were immature during the study period. High landed species were *Neotrygon orientalis* and *Brevitrygon heterura*, comprising with 60.4% and 24.2% of all landed individuals. The highest and lowest landed number of rays was found in October and April respectively.

Keywords: Catch composition, fish landing site, myeik, rays, species composition.

Introduction

Rays belong to the Batoidea group which is characterized by dorso-ventrally flattened body. They are widely distributed in shallow continental waters of tropical and warm-temperate seas (Compagno and Last 1999). Ahmad *et al*. (2014) recorded 148 species belonging to 5 orders of rays and skates in the Southeast Asia Region, including 44 species of 10 families in Myanmar. According to the ray species of Myanmar, 71 species of rays were found and recognized by Howard *et al*. (2015).

Rays are being caught as bycatch in trawl, gill net, drift net, purse seine. Hook longline fishermen targeted rays due to their high prices of dried meat, dried skin, and gill rakers. The trunk area of ray skins was valued as quality leather for the manufacture of wallets, keychains, phone covers, handbags, and belts. Due to the increasing demand for marine products for local markets and export, there is considerable pressure on fishing efforts leading to a decrease in the fish population. Zin Lin Khine and Hnin Hnin Maw (2016) stated that more than 60% of fishermen

[1] Lecturer, Department of Marine Science, Myeik University
[2] Demonstrator, Department of Marine Science, Myeik University
[3] Professor, Department of Marine Science, Myeik University

perceived a decline in rays catch and fishery in Kyauk-Phyar and Thit-Yar-Wa Villages in Myeik.

Rays have limited capacity to recover from overfishing due to slow growth rate, late maturity, and low fecundity. So, it is essential to know the information of landing data for the successful management of rays. Thus, the present study aimed to record the list of ray species, size, and catch composition landed in Myeik areas.

Materials and methods

Surveys were conducted at the two landing sites (Tha-Kay-Ta and Naukle) in Myeik from February 2019 to January 2020 (Fig 1). Taxonomic classifications of rays were mainly followed on the system of Compagno and Last (1999) and Ahmad *et al*. (2013-2014, 2017). Species identification was mainly based on their external morphological features: body profile, coloration, the presence or absence of denticle band, stinging spine, and thorns.

Disc width (the extremities of the left and right pectoral fins) was measured by measuring tape to the nearest centimeter. Some samples were photographed during the survey. All species observed from the survey were checked against the IUCN Red List categories of 2017.

Figure 1. Map showing the study area

Results

A total of 16 species of rays belonging to the 12genera of the 5 families: Dasyatidae, Gymnuridae, Myliobatidae, Rhinopteridae and Mobulidae were recorded in the present study (Figure 2).

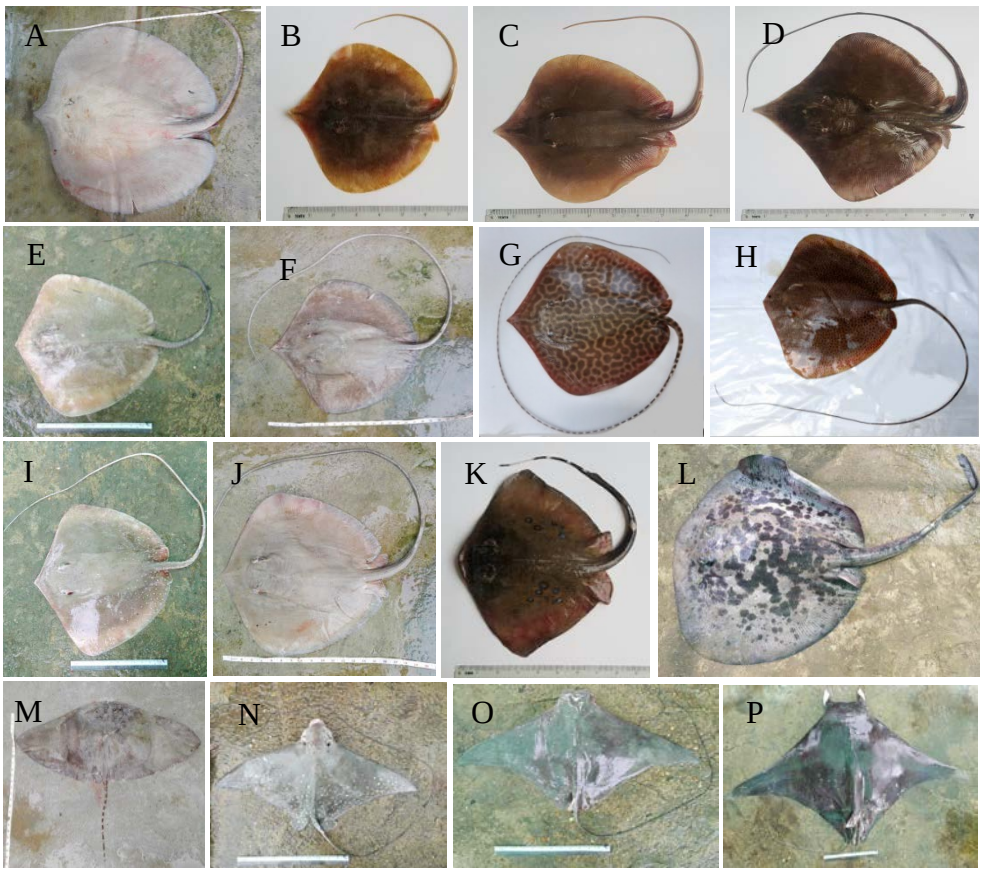

Figure 2. A-P. Landed rays species of two sampling sites: A) *Urogymnus polylepis* (Bleeker 1852); B) *Brevitrygon imbricata* (Bloch & Schneider 1801); C) *B. heterura*; D) *Telatrygon zugei* (Muller and Henle 1839); E) *Pateobatis jenkinsii* (Annandale 1909); F) *P. uarnacoides* (Bleeker 1852); G) *Himantura undulata* (Bleeker 1852); H) *H. uarnak* (Forsskal 1775); I) *Maculabatis gerrardi* (Gray 1851); J)*M. pastinacoides* (Bleeker 1852); K) *Neotrygon orientalis* Last, White and Seret 2016; L) *Taeniurops meyeni* Muller and Henle 1841; M) *Gymnura poecilura* (Shaw 1804); N) *Aetobatus ocellatus* (Kuhl 1823); O) *Rhinoptera javanica* Muller and Henle 1841 and P) *Mobula thurstoni* (Lloyd 1908)

Species and Catch Composition

Among the 16 species landed in the two sampling sites, 15 species (985 individuals) were recorded in Tha Kay Ta fish landing site and 10 species (651 individuals) were recorded in Naukle fish landing site (Table 1 and Figure 3).

Table 1. Total number of recorded species and their IUCN Red List status (NE: Not Evaluated, DD: Data Deficient, NT: Near Threatened, VU: Vulnerable, En: Endangered) Site1= Tar Kay Ta and Site2= Naukle

Species name	Common name	Number		IUCN Red List
		Site 1	Site 2	
Urogymnus polylepis	Giant freshwater whipray	9	16	EN
Brevitrygon imbricata	Bengal whipray	42	-	NE
B. heterura	Dwarf whipray	280	116	DD
Telatrygon zugei	Sharpnose stingray	18	-	NT
Pateobatis jenkinsii	Jenkins' whipray	14	-	VU
P. uarnacoides	Bleeker's whipary	10	5	VU
Himantura undulata	Honeycomb whipray	10	15	VU
H. uarnak	Reticulate whipray	8	1	VU
Maculabatis gerrardi	Whitespotted whipray	6	4	VU
M. pastinacoides	Round whipray	4	17	VU
Neotrygon orientalis	Oriental bluespotted maskray	529	459	NE
Taeniurops meyeni	Blotched fantail stingray	2	-	VU
Gymnura poecilura	Longtail butterfly ray	-	3	NT
Aetobatus ocellatus	Spotted eagle ray	23	-	VU
Rhinoptera javanica	Javanese cownose ray	8	-	VU
Mobula thurstoni	Smoothtail devilray	22	15	NT

The high diversity of rays was recorded from the family Dasyatidae belonging to twelve species, followed by the families Gymnuridae, Myliobatidae, Rhinopteridae, and Mobulidae with one species. For both sampling sites, the dominant ray species was *Neotrygon orientalis* composed of 60.4 % of total landed rays, followed by *Brevitrygon heterura* with 24.2%.

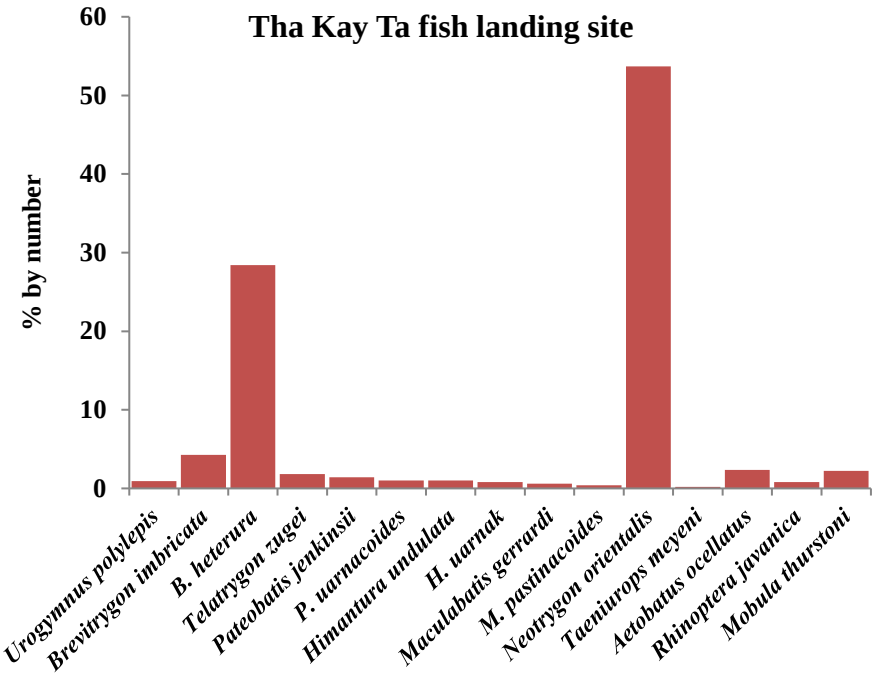

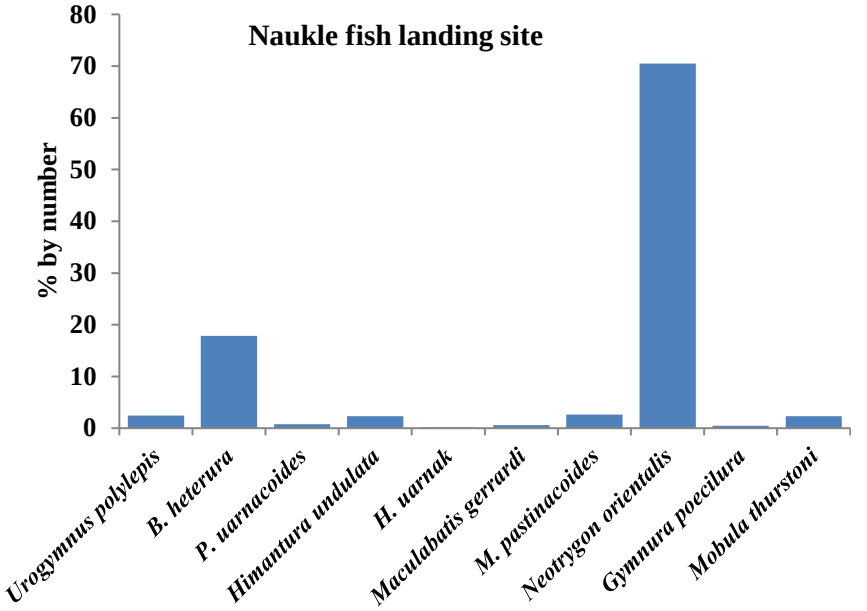

Figure 3. Species composition (%) of ray landed in Myeik

A total of 16 ray species were assessed against the IUCN Red List categories (Table 1). Vulnerable species accounted for 56.3% of rays landed in two sites (9 species), followed by 18.8% of Near Threatened rays (3 species), 12.5% of Not Evaluated rays (2 species), 6.2% of Data Deficient rays (1 species) and 6.2% of Endangered rays (1 species).

With regards to the monthly landed number of rays (Figure 4), the highest number of individuals were recorded in October (363 individuals), followed by February (293 individuals), September (274 individuals), and June (259 individuals). The number of ray catches was low in April (35 individuals), July (37 individuals), and May (39 individuals).

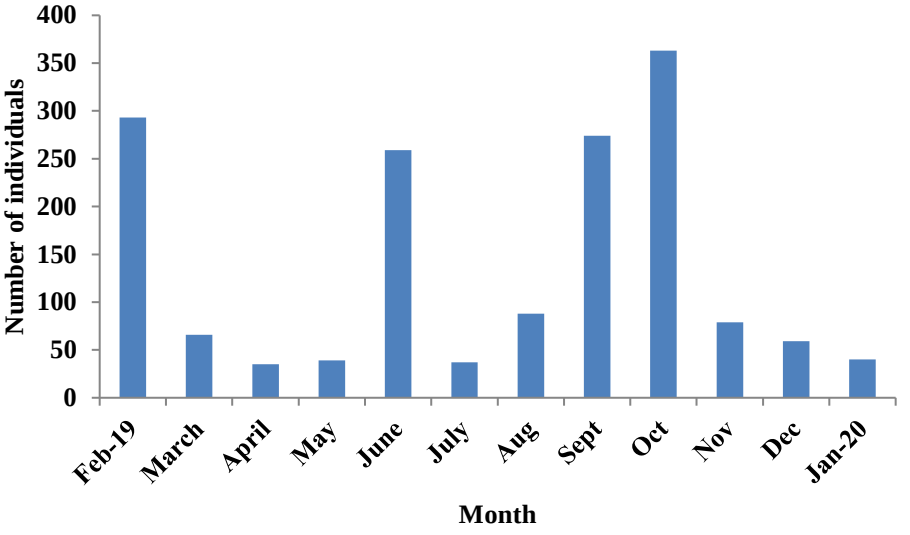

Figure 4. Monthly recorded numbers of rays in two landing sites

Size composition

The landed size range of rays were 142-160 cm DW in *Urogymnus lobistoma*, 53.3-58.4 cm DW in *Brevitrygon imbricata*, 15.2-30.5 cm DW in *Brevitrygon heterura*, 55.8-58.4 cm DW in *Pateobatis uamacoides*, 121.9-130 cm DW in *Himantura uarnak*, 91.4-92 cm DW in *Taeniurops meyeni* in July, 60.9- 66.4 cm DW in *Gymnura poecilura*, 86.4-198 cm DW in *Rhinoptera javanica*, 21.6-26.7 cm DW in *Telatrygon zugei*, 88.9-104.1 cm DW in *Pateobatis jenkinsii*, 90.2- 116.8 cm DW in *Himantura undulata*, 16.5- 45.7 cm DW in *Neotrygon orientalis*, 162.6-185.4 cm DW in *Maculabatis gerrardi*, 93.9-104.1 cm DW in *Maculabatis pastinacoides*, 167.6-289.6 cm DW in *Aetobatus ocellatus*, 53.3- 228.6 cm DW in *Mobula thurstoni*.

Species of *Brevitrygon heterura* and *Neotrygon orientalis* were recorded in all months of the study period. The size composition of these two species was presented in Figure 5.

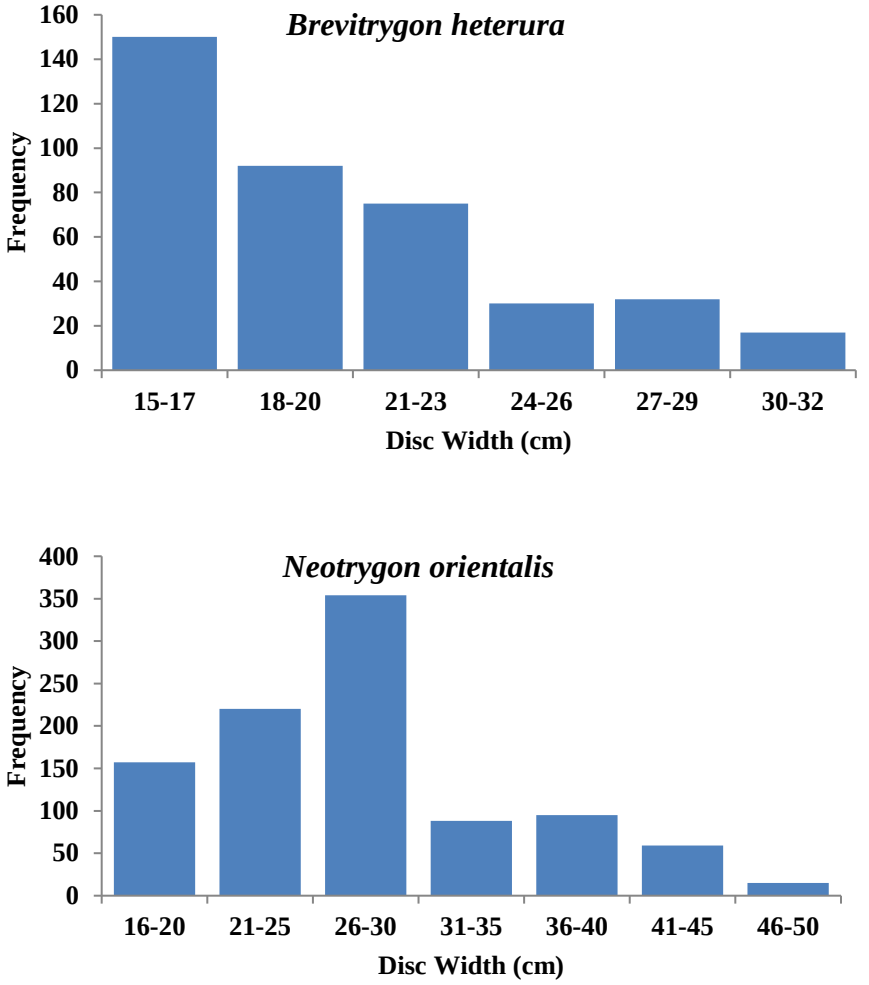

Figure 5. Length frequency of *Brevitrygon heterura* and *Neotrygon orientalis*

Discussion

There are sixteen species of rays: namely *Urogymnus lobistoma*, *Brevitrygon imbricata*, *B. heterura*, *Telatrygon zugei*, *Pateobatis jenkinsii*, *P. uamacoides*, *Hemantura undulata*, *H. uarnak*, *Maculabatis gerrardi*, *M. pastinacoides*, *Neotrygon orientalis*, *Taeniurops meyeni*, *Gymnura*

poecilura, *Aetobatus ocellatus*, *Rhinoptera javanica*, and *Mobula thurstoni* landed in the two landing sites during February 2019 to February 2020.

Compagno and Last (1999) listed 66 rays species under the order Myliobatiformes in the western central pacific. Ahmad *et al*. (2014) reported 44 species of rays belonging to 10 families from Myanmar. According to the recent data, Howard *et al*. (2015) recorded 71 species of rays in Myanmar.

The dominant family of ray landed was Dasyatidae (Stingrays) with 12 species, which is about 75% of the total recorded ray species. Only one species recorded from the families in the present study were Gymnuridae (Butterfly rays), Myliobatidae (Eagle rays), Rhinopteridae (Cownose rays), and Mobulidae (Devil rays). Ray landing from the two landing sites dominated by *Neotrygon orientalis* (previously identified as *Neotrygon kuhlii*) and *Brevitrygon heterura* (previously identified as *Himantura walga*), which contribute 60.4% and 24.2% of the total number of rays recorded. Similarly, Krajangdara (2014) reported that common rays of Thailand were *Neotrygon kuhlii* and *Himantura walga*. Howard *et al.* (2015) also described that the most common market species in Myanmar were *Neotrygon kuhlii, Himantura imbricate,* and *H. gerrardi.* Nyo Nyo Tun (2016) also reported that 9 species of rays were recorded from the Aleman Island with the abundant species of *Himantura walga* and *Neotrygon kuhlii*. But Kizhakudan *et al.* (2010) reported that the dominant species of *Himantura jenkinsii* (36%) and *Rhinoptera javanica* (12.7%) in Chennai. *Brevitrygon imbricata* contributes only a small percentage (8%) of landed ray species.

According to Ahmad *et al*. (2014), the mature disc width was 110 cm for *Urogymnus polylepis*, 16-18 cm for *Brevitrygon imbricata*, 16-18 cm for *Brevitrygon heterura*, 16-19 cm for *Telatrygon zugei*, 70-85 cm for *Pateobatis jenkinsii*, 50-60 cm for *P. uarnacoides*, 60-70 cm for *Himantura undulate*, 82-84 cm for *H. uarnak*, 46-64 cm for *Maculabatis gerrardi*, 43-58 cm for *M. pastinacoides*, 26 cm for *Neotrygon orientails*, 100-110 cm for *Taeniurops meyeni*, 45 cm for *Gymnura poecilura*, 100-110 cm for *Aetobatus ocellatus*, 90 cm for *Rhinoptera javanica* and 198-205 cm for *Mobula thurstoni*. Most of the landed species were mature but some were immature.

According to the monthly recorded samples, the highest individual of rays was landed in October, February and September. Low catches were recorded in April, July, and May during the present study period. Nyo Nyo Tun (2016) reported that the catches of rays in Aleman Island were high in October, November, and December and low in the rainy season.

Conclusion

Ray fishery is profitable for small and large scale fishermen because of the high market price of meat, skin, and gill rakers. Rays are being caught as a target in hook longline and by catch in trawl, gill net, drift net, purse seine. Sixteen rays species were landed in the Tha Kay Ta and Naukle landing sites during the study period. Landed ray species of *Brevitrygon imbricata, Brevitrygon heterura, Neotrygon orientails*, *Taeniurops meyeni*, *Rhinoptera javanica,* and *Mobula thurstoni* were immature. The present catch data can still support for the objectives of Myanmar's National Plan of Action for Sharks and rays. So, regular data collections are still needed for future stock assessments and management plans.

Acknowledgements

We would like to express our special thanks, to Dr. Ni Ni Oo, Rector, and Dr. Win Win Than, Pro-Rectors of Myeik University for their permission to carry out this research. Thanks are also due to the fourth-year students of Marine Science in 2018-2019 Academic year for helping during the samples and data collection of ray species.

References

Ahmad, A., Lim, A.P.K., Fahmi and Dharmadi. (2013). Field guide to look-alike sharks and rays species of the Southeast Asia Region. SEAFDEC/MFRDMD/SP/22, pp: 71-95.

Ahmad, A., Lim, A.P.K., Fahmi, Dharmadi and Krajangdara, T. (2014). Field Guide to Rays, Skates and Chimaeras of the Southeast Asia Region. SEAFDEC/MFRDMD/SP/25, pp: 146-248.

Ahmad, A., Lim, A.P.K., Fahmi, Dharmadi and Krajangdara, T. (2017). Identification guide to sharks, rays and skates of the Southeast Asian region. SEAFDEC/MFRDMD/SP:22-33.

Compagno, L.J.V. and Last, P.R. (1999). Order Myliobatiformes. In:Carpenter, K.E. and Niem, V.H.(eds) FAO species identification guide for fishery purposes. The living Marine Resources of the Western Central Pacific. Volume. 3: Batoid Fishes, Chimaeras and Bony Fishes Part I (Elopidae and Linophrynidae). Rome, FAO. pp: 1479-1529.

Howard, R., Ahmad, A. and U Saw Han Shein. (2015). Shark and ray fisheries of Myanmar-Status and Socio-Economic Importance. Report No.12 of the Tanintharyi Conservation Programme, a joint initiative of Fauna and Flora International and Myanmar Forest Department, FFI, Yangon and the Bay of Bengal Large Marine Ecosystem project (BOBLME). 36pp.

Kizhakudan, S. J., Mohanraj, G., Hameed Batcha, T. and Rajapackiam, S. (2010). Ray fishery by trawlers off Chennai and some aspects of biology of the scaly whipray *Himantura imbricate* (Bloch & Schneider, 1801). *J. Mar. Biol. Ass. Indian*, 52 (1): 92-95.

Krajangdara, T. (2014). Sharks and Rays in Thailand. Country report of Andaman Sea Fisheries Research and Development Center. 10pp.

Nyo Nyo Tun. (2016). Study on Ray Fishery near Aleman Island, Myeik Archipelago. *University Research Journal*. 9 (4): 87-98.www.redlist.com. (2017)

Zin Lin Khine and Hnin Hnin Maw. (2016). Socio-economic assessment on fishing communities in Kyauk-Phyar and Thit-Yar-Wa villages, Tanintharyi Region *Myeik University Research Journal*, vol 1):130-142pp.

Reproductive Biology of *Cynoglossus lingua* in Myeik Coastal Waters

Sabai Soe*

Abstract

Cynoglossus lingua was collected monthly from fish landing site during October 2018 to September 2019. The GSI values of *C. lingua* showed wide variations between sexes and it was higher for females throughout the sampling period. Higher GSI for females during January (2.95%) and August (4.41%) also confirmed the two spawning peaks. The overall male: female ratio of *C. lingua* was 1: 0.6. There was an overall predominance of males in the population of *C. lingua* in all the months except August and September during the present study. In *C. lingua*, 50% of fish attained maturity at cm 28.5TL for males and 34.1cm TL for females. The fecundity of *C. lingua* ranged from 5970-303750 in fish at 32-45 cm TL.

Keywords: long tongue sole, *Cynoglossus lingua*, fecundity, gonad maturity, spawning.

Introduction

The fisheries sector is a very important component of Myanmar's economy. Tongue sole is also important marine fishery resources for Myanmar (Psomadakis, *et al*. 2019). They are locally known as "Nga Khway Shar". Tongue sole are small flatfishes with a small, curved mouth and united caudal, dorsal and anal fins. *Cynoglossus lingua* belonging to family *Cynoglossidae* and commonly known as long tongue sole. This species is found in all Myanmar's Coastal Waters inhabiting estuarine habitat.

The reproductive biology study provides information on the species life history, is an important component for fishery science and useful to fishery management.

* Lecturer, Department of Marine Science, Myeik University

Identification of tongue soles was reported by Mya Than Tun (2001), Hla Win *et al.* (2008), Thet Htwe Aung (2015) and Psomadakis, *et al*. (2019) in Myanmar Waters. Moreover, some biological studies of tongue soles from Myeik Coastal Waters were conducted by Sabai Soe (2012) and Iris *et al*. (2021). However, there is a gap in the knowledge of the reproductive biology of *C. lingua* in this region. The present study dealt with reproductive biology encompassing various aspects of gonad maturity level, gonadosomatic index, sex ratio, length at sexual maturity and fecundity of this species in Myeik.

Material and Methods

Samples were collected monthly from October 2018 to November 2019. Fish were dissected for visual observation of testes and ovaries which can indicate maturity and spawning season. According to (Ghaffari 2015), the maturity stages were classified into five stages. The gonadosomatic index (GSI) was calculated by using the formula,

$$GSI = \frac{\text{weight of gonad}}{\text{weight of fish}} \times 100 \quad \text{(Strum, 1978)}$$

Sex ratio was calculated for different months and was tested for the expected ratio 1:1 by the method of Chi-square (χ^2) test according to the formula:

$$\chi^2 = \frac{\Sigma (O - E)^2}{E} \quad \text{(Banerjee, 2004)}$$

where, O = observed outcomes, E = expected outcomes

Length at first maturity was estimated using the standard methodology described by King(1997).

To determine fecundity, a sub-sample of 1.0 g was taken out from the mature ovary. The sub-sample ovary was counted under the stereomicroscope for the numbers of ova and the fecundity was determined by using the formula,

$$\text{Fecundity} = \frac{\text{total weight of gonad}}{\text{sub} - \text{sample weight}} \times \quad \text{No. of ova in the sub-sample}$$

Results

Stages of maturity

According to Ghaffari (2015), the maturity stages of *Cynoglossus lingua* were classified into five stages as follows:

Stages	Macroscopic Characteristics
Stage-I (Immature)	Very thin ovaries not extending more than 4cm down the side of the body. Pinkish ovaries with very thin walls and easily broken. No visible oocytes (Female). Testis minute, pale white (Male).
Stage-I I (Maturing)	The ovaries increase in length and in width; they become thicker and opaque. Small opaque speck is visible (Female). Testis slightly enlarged, pale white (Male).
Stage-III (Mature)	The ovaries increase considerably in volume and usually distend the body. Many opaque and a few hydrated oocytes are visible (Female). Testis enlarged, sac-like, creamy white (Male).
Stage-IV (Ripe)	Full ovary with hydrated oocytes visible. In the running stage, the oocytes are extruded copiously under light pressure of the ovary (Female). Testis enlarged, sac-like, creamy white; whitish milt running from a vent on slight pressure (Male).
Stage-V (Spent)	Ovaries are empty or partially empty, flaccid with mainly opaque oocytes in a state of reabsorption with a lot of slimes. Gonads are highly vascularized with some ruptured capillaries, bloodshot in appearance (Female). Not found during the present study (Male).

Percentage occurrence of different maturity stages

In this study, a total of 672 samples of *Cynoglossus lingua* (407 males and 240 females) were collected from October 2018 to September 2019. The monthly percentage occurrence of different maturity stages is illustrated in Table 2 and 3. In male *C. lingua,* Stage I (immature) occurred throughout the study period and Stage II (Maturing) was observed in all months except October. Stage III (Mature) occurred occasionally throughout the study period. Those fish at Stage IV (Ripe) and Stage V (spent) were not observed during the present study. The females at Stage I were observed in all months. Stage II (Maturing) was observed in the months of October, January, March, May, and September. Mature females (Stage III) were observed in all months of the study period except December. The highest value (32%) was observed in August. The ripe females (at Stage VI) were firstly recorded in December, their numbers increased after March. The spent females occurred occasionally during the study period.

Gonadosomatic Index (GSI)

The monthly variation of GSI for *C. lingua* was shown in Table1 and Figure 1. In *C. lingua*, the GSI values of males and females varied from 0.04-0.13% and 1.27- 4.41% respectively. For females, the highest average GSI value was observed in September (4.15%) and the lowest in June (1.27%). The monthly GSI values of females were always higher than those of males in all months.

Table 1. Monthly variation in the GSI values of males and females of *C. lingua* during the study period.

	Oct	Nov	Dec	Jan	Feb	Mar	Apr	May	Jun	Jul	Aug	Sep
Male	0.05	0.04	0.04	0.07	0.06	0.05	0.07	0.05	0.04	0.07	0.07	0.13
Female	1.74	1.41	1.39	2.95	2.34	1.67	2.24	2.55	1.27	3.45	4.41	4.15

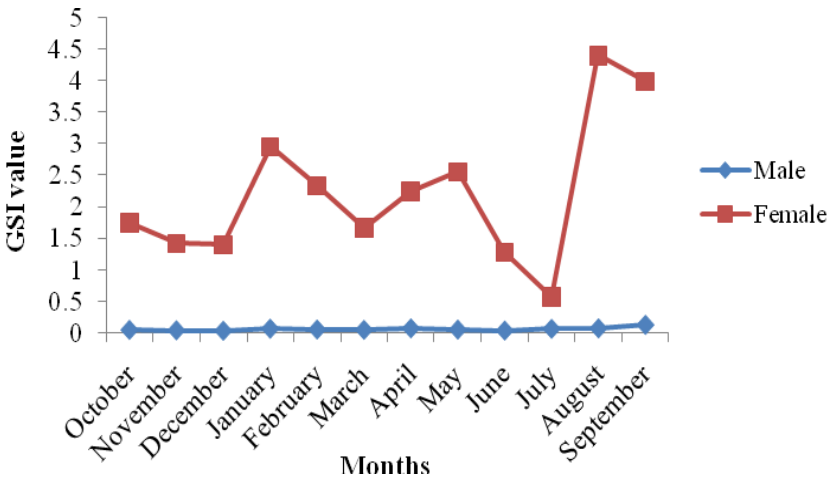

Figure 1. Monthly average GSI values of males and females *C. lingua*

Table 2. Monthly percentage occurrence of the gonads of *C. lingua* in the different maturity stages (Males).

Months	Stages of maturity (%)				
	I (Immature)	II (Maturing)	III (Mature)	IV (Ripe)	V (Spent)
Oct-2018	96.6	-	3.4	-	-
Nov	97.2	2.8	-	-	-
Dec	86.7	13.3	-	-	-
Jan	69	31.0	-	-	-
Feb	65.8	28.9	5.3	-	-
Mar	35.9	50.0	14.0	-	-
Apr	64.6	27.1	8.3	-	-
May	91.1	8.9	-	-	-

Months	Stages of maturity (%)				
	I (Immature)	II (Maturing)	III (Mature)	IV (Ripe)	V (Spent)
Jun	96.2	3.8	-	-	-
Jul	96.0	4.0	-	-	-
Aug	56.3	18.8	25.0	-	-
Sep-2019	50.0	35.0	15.0	-	-

Table 3. Monthly percentage occurrence of the gonads of *C. lingua* in the different maturity stages (Females).

Months	Stages of maturity (%)				
	I (Immature)	II (Maturing)	III (Mature)	IV (Ripe)	V (Spent)
Oct-2018	68.7	12.5	18.8	-	-
Nov	80	-	20	-	-
Dec	90.9	-	-	9.1	-
Jan	20	10	25	40	5
Feb	63	-	29.6	3.7	3.7
Mar	60	25	15	-	-
Apr	50	-	15.38	30.77	3.85
May	50	16.67	16.67	16.67	-
Jun	72.72	-	9.09	18.18	-
July	33.3	-	26.7	33.3	6.7
Aug	31.82	-	31.82	36.36	-
Sept-2019	11.11	37.78	13.33	35.56	2.22

Sex ratio

A total of 647 specimens of *C. lingua* were sexed, of which 407 (62.9%) were males and 240 (37.1%) were females giving a sex ratio of 1:0.59. The highest proportion of females occurred in September and the lowest in May. The chi-square test indicated a significant difference from 1:1 ratio ($P<0.05$), except in October-December, February, July, and August (Table 4). The highest proportion of females occurred in November and the lowest, in September. Females were dominant almost all the months; the Chi-square test applied for monthly sample indicates that no significant difference was noted at 5% probability level in seven months of the study period.

Table 4. Monthly variation in the sex ratio of *C. lingua*.

Months	Total	Male	Female	M:F	Chi-square
October	45	29	16	1:0.55	3.76
November	22	12	10	1:0.83	0.18
December	26	15	11	1:0.73	0.62
January	62	42	20	1:0.48	7.80*
February	65	38	27	1:0.71	1.86
March	84	64	20	1:0.31	23.0*
April	74	48	26	1:0.54	6.54*
May	51	45	6	1:0.13	29.82*
June	75	53	22	1:0.41	12.82*
July	40	25	15	1:0.60	2.5
August	38	16	22	1:1.38	0.94
September	65	20	45	1:2.25	9.62*
	647	407	240	1:0.59	43*
		62.9%	37.1%		

*Significant at 5% level (Tabulated value 3.841)

Length at first maturity

In the present study, the fish belonging to Stage I and II were considered immature. Stage III and above were grouped under a mature category. In *C. lingua* which has the size at first sexual maturity (L_{50}) for males occurred at 28.5 cm and for females at 34.1 cm in total length.

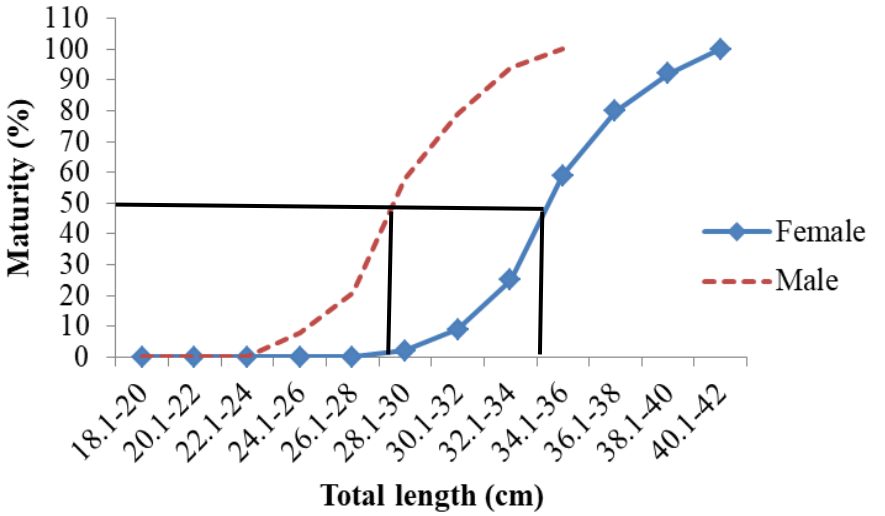

Figure 2. Length at first maturity of males and females *C. lingua*

The fecundity of *C. lingua* was investigated based on eighteen females of stages III and IV. The fecundity of *C. lingua* ranged from 5970-303750 ova in fish lengths that ranged from 32cm to 45cm. The average fecundity was 82174± 17,054.

The regression equations of fecundity in relation to fish length, fish weight and gonad weight were given as:

$$\text{Log } F = -1.4302 + 3.89 \text{ Log } L \ (r = 0.3)$$

$$\text{Log } F = 0.566 + 1.89 \text{ Log } W \ (r = 0.6)$$

$$\text{Log } F = 3.478 + 1.46 \text{ Log } Wg \ (r = 0.9)$$

where F = fecundity, L = total length of fish, W = body weight of fish, Wg = weight of the gonad.

The correlation coefficient ‘ r ’value 0.3 indicated that there was a low correlation between the fecundity and total length. The r value of 0.6 showed that the relationship between fecundity and body weight is in agreement. The fecundity increased as the fish grew in weight. The value of the correlation coefficient was 0.9; the relationship between fecundity and gonad weight also revealed a strong agreement. The fecundity increased with increasing gonad weight.

Discussion

Samples of *C. lingua* were collected monthly from fish landing sites for reproductive studies. Reproduction involves changes in the growth and development of oocytes during the process of gonad maturation. In *C. lingua,* both mature males and females occurred throughout the study period. In most months, the availability of gravid females in the fishery suggests that the spawning season is extended with two peaks, one during December-February and one during July-September. The spawning takes place in August with more mature individuals present, and subsequent observation of spent females in September supports the finding as well. Pradhan (1964) revealed that the presence of mature and spent individuals is an indicator of the spawning season.

In *C. lingua,* a higher gonado-somatic index was reported in females during August (4.41) and September (4.15), showing the occurrence of more ripe individuals. GSI for males was highest in September (0.13) and lowest in December and June (0.04). The female's GSI value was always higher than that of males. According to Osman *et al.* (2011), the GSI values for females in teleosts were always higher than that of males especially in the breeding season because the ovaries were several times larger than the testes.

Observations of the fish sex ratio are important for population structure studies. The sex ratio of males and females from the total sample of *C. lingua* was 1:0.59. The Chi-square test indicated a significant difference during January, May, June, and September ($P< 0.05$). Males were dominated in all the months except August and September,

In fish, length at sexual maturity might be determined by a combination of exploitation and environmental condition (King, 1997). Kamal and Sunarno (2009) described the first sexual maturity of *C. lingua*

as 9.4 cm for males and 8.5 cm for females. Sulistiono, *et al*. (2009) reported the first gonad maturity of males and females for this species was 9.4 and 12.2 cm respectively. In the present study, the size at sexual maturity observed in male and female *C. lingua* was 28.5 cm TL and 34.1 cm TL respectively.

The fecundity of the fish is determined by the number of ova of the mature group in the ovary (just before the spawning stage). Hence, in the present study, mature ovaries were taken into consideration for fecundity estimation. In the present study, the fecundity of *C. lingua* ranged from 5970-303750 eggs in fish with a total length of 32-45 cm. The average fecundity was 82174± 17,054. Kamal and Sulistiono *et al.* (2009) stated that the fecundity of *C. lingua* ranged from 360 to 35926 eggs from the Ujung Pangkah Estuary. Bhalekar *et al.* 2018 revealed that the fecundity of *C. macrostomus* was 3280-29480 ova for sizes of 9-15.9 cm from the Ratnagiri coast of Maharashtra. Compared with other results in previous studies the fecundity of *C. lingua* in the present study appears to be high indicating the presence of highly productive stock. In *C. lingua,* the fecundity against total length, body weight, and gonad weight were positively correlated. However, the relationship of the fecundity of *C. lingua* revealed that fecundity was more related to body weight and gonad weight than that of total length.

Hence, it is concluded that the gonad weight is a better index of fecundity than total length and body weight. Higher fecundity recorded for *C. lingua* could be a result of the size of fish and the variations in environmental conditions and food intake by the individual.

Conclusion

Cynoglossus lingua exhibited two spawning seasons from December to February and July to September. The female's GSI value was always higher than that of males. The sex ratio of males to females *C. lingua* was 1:0.59. The first sexual maturity in male and female *C. lingua* was 28.5 cm TL and 34.1 cm TL, this indicated that the male was faster mature than that of the female.

Acknowledgments

I would like to express my gratitude to Dr. Ni Ni Oo, Rector, and Dr. Win Win Than, Pro-Rector of Myeik University, for permitting me to conduct this research. I am grateful to Professor Dr. Nyo Nyo Tun, Head of Marine Science Department, Myeik University, for her provision of laboratory facilities.

References

Banerjee, P. K. (2004). Introduction to Biostatistics (A Textbook of Biometry). S. Chand & Company Ltd. Ram Nagar, New Delhi, 200 pp.

Bhalekar, P, V., Nirmale, V. H., Metar, S, Y. Pawar, R. A. and Kende, D. R. (2018). Studies on feeding and reproductive biology of Malabar tongue sole, *Cynoglossus macrostomus* along the Ratnagiri coast of Maharashtra. Indian Journal of Geo Marine Sciences, **47** (6): 1217-1221.

Ghaffari, H., Sahafi, H. H., Engelhard, G.H., and Babaei, M. M. (2015). Reproductive biolo of large scale tonguesole *Cynoglossus arel* in coastal waters of Bandar Abbas, Persian Gulf, Iran. Animal Reproduction Science **154**: 142-157.

Hla Win, Shwe Thwin, Myint Pe and Maung Myint. (2008). Commercial fishes of Myanmar. Fishery Products Processes and Exporters Association, 248pp.

Iris, S. G., Sabai Soe, Nyo Nyo Tun and Stephen B. (2021). Beyond Bycatch: The Species Diversity of Tonguesole (Pleuronectiformes: Cynoglossidae) in Coastal Fisheries of the Tanintharyi Region, Southern Myanmar. *Asian Fisheries Science.* **34**: 23-33.

Kamal, M. M. and Sunarno, M. T. D. (2009). Biological Reproductive of estuarine fish comparing between demersal (Long Tongue Sole, *Cynoglossus lingua*) and pelagic (Mustached Thryssa, *Thryssa mystax*) assemblages. In. Fish. Res.J.**15**(1):37-42.

King, M. (1997). Fisheries Biology, Assessment, and Management. Fishing News Books. Blackwell Science Inc. USA, Canada, and Australia. 341pp.

Mya Than Tun (2001). *Marine fishes of Myanmar (Pelagic and Demersal)*. Marine Fisheries Resources Survey Unit. Department of Fisheries. Yangon: 276 pp.

Osman, A. G., Akel, E. S., Farrage, M. M. and Moustafa, M. A. (2011). Reproductive biology of round herring *Etrumeru teres* (Dekay, 1842) from the Egyptian Mediterranean water at Alexandra. 12pp.hattp: //www.isrn. com/ journals/ zoology/2011/215950.

Pradhan, M. J. (1964). Observations on the maturity and spawning of *Psettodes erumei* (Schneider). *Indian J. Fish.,* **9**(2):580-589.

Psomadakis, P. N., Htun Thein, Russell, B. C. and Mya Than Tun (2019). *Field Identification Guide to the living Marine Resources of Myanmar*. FAO species identification field guide for fishery purposes. Rome, FAO and MOALI.

Sabai Soe. (2012). Some aspects of biological measures of tonguesole (Family-Cynoglossidae) found in Myeik Area. Unpublished MSc (Thesis). Department of Marine Science, Myeik University, Myanmar.

Strum, L. M. G. (1978). Aspects of the biology of *Scombermous maculates* (Mitchill) in Trinidad. *J. Fish Biol*., **13**: 155-157.

Sulistiono, Soenanthi, K. D. and Ernawati, D. Y. (2009). Reproductive aspect of long tonguesole, *Cynoglossus lingua* H. B. 1822. in Ujung Pangkah Waters, East Java. *J. Iktiologi Indonesia,* **9**(2): 175-185.

Thet Htwe Aung. (2015). Observation on Pleuronectiformes (flatfishes) in Mon State. Unpublished M.Res. (Thesis). Department of Marine Science, University of Mawlamyine. Myanmar.